Full-duplex Transceivers: Architectures and Performance Analysis

Bilal Alauldeen Jebur

Newcastle University

Newcastle upon Tyne, UK.

A thesis submitted for the degree of

Doctor of Philosophy

December 2017

To my loving parents and siblings for their support and encouragement.

Declaration

NEWCASTLE UNIVERSITY

SCHOOL OF ELECTRICAL AND ELECTRONIC ENGINEERING

I, Bilal Alauldeen Jebur, declare that this thesis is my own work and it has not been previously submitted, either by me or by anyone else, for a degree or diploma at any educational institute, school or university. To the best of my knowledge, this thesis does not contain any previously published work, except where another persons work used has been cited and included in the list of references.

Signature:

Student: Bilal Alauldeen Jebur

Date:

SUPERVISOR'S CERTIFICATE

This is to certify that the entitled thesis "Full-duplex Transceivers: Architecture and Performance" has been prepared under my supervision at the school of Electrical and Electronic Engineering / Newcastle University for the degree of PhD in Electrical and Electronic Engineering.

Signature:

Supervisor: Dr. Charalampos Tsimenidis

Date:

Acknowledgements

First of all, I must start by thanking Almighty Allah for giving me the opportunity to fulfil my dream, and giving me the patience and strength throughout my life to be what I am today. All thanks and praise are due to Allah for his blessings, which have given me the courage and persistence to carry out this work.

I would like to take this opportunity to express my sincere gratitude and thanks to Dr. Charalampos Tsimenidis, for his help, guidance, and support throughout my PhD journey. I am extremely grateful for his contribution to this thesis and my scientific development without his encouragement and constructive criticism this work would not be the same.

I have been extremely lucky to have a good friend such as Omar Al-Janabi who has made this experience much easier, many thanks for your support. I would like to thank all my friends at Newcastle University, Sinan, Mohamad, Wael, Yasir, Harith, Safaa, Ahmad, Zaid, Mohammed, Ali and Sanker for all their support and motivating discussions.

Next, I would like to express my thanks to my country, Iraq, and the Ministry of Higher Education and Scientific Research (MOHSR) for the fully-funded scholarship that provided the necessary financial support for this research. I also would like to thank Iraqi Cultural Attache/London for the appreciated support and help throughout my PhD study.

Moreover, I am very grateful for help and support of the nice Postgraduate Research Coordinator, Gillian Webber and the wonderful Receptionist, Deborah Alexander.

Additionally, my thanks go to all the people who have helped throughout my life. I cannot mention all the names here, however, they all deserve my sincere gratitude.

Last but by no means least, I thank my parents and my siblings. I would like to express my sincere gratitude to my loving parents for their unconditional care, continuous help, and support. Without your prayers, nice words, encouragement,

motivation and sound advice, I would not achieve anything in my life, I owe you everything and to you, I dedicate this thesis.

Abstract

The revolution of the 5G communication systems will result in 10,000 times increase in the total mobile broadband traffic in the 2020s, which will increase the demand on the limited wireless spectrum. This has highlighted the need for an efficient frequency-reuse technique that can meet the ever-increasing demand on the available frequency resources. In-band full-duplex (FD) wireless technology that enables the transceiver nodes to transmit and receive simultaneously over the same frequency band, has gained tremendous attention as a promising technology to double the spectral efficiency of the traditional half-duplex (HD) systems. However, this technology faces a formidable challenge, that is the large power difference between the self-interference (SI) signal and the signal of interest from a remote transceiver node. In this thesis, we focus on the architecture of the FD transceivers and investigate their ability to approximately double the throughput and the spectral efficiency of the conventional HD systems. Moreover, this thesis is concerned with the design of efficient self-interference cancellation schemes that can be combined with the architecture of the FD transceiver nodes in order to effectively suppress the SI signal and enable the FD mode. In particular, an orthogonal frequency-division multiplexing (OFDM) based amplify-and-forward (AF) FD physical-layer network coding (PLNC) system is proposed. To enable the FD mode in the proposed system, a hybrid SIC scheme that is a combination of passive SIC mechanism and active SIC technique is exploited at each transceiver node of that system. Next, we propose an adaptive SIC scheme, which utilizes the normalized least-mean-square (NLMS) algorithm to effectively suppress the SI signal to the level of the noise floor. The proposed adaptive SIC is then utilized in a denoise-and-forward (DNF) FD-PLNC system to enable the FD mode. Finally, we introduce a novel over-the-air SIC scheme that can effectively mitigate the SI signal before it arrives the local analog-to-digital converter (ADC) of the FD transceiver nodes. Furthermore, the impact of the hardware impairments on the performance of the introduced SIC scheme is examined and characterized.

Contents

List of Figures

List of Tables

Nomenclature

Acronyms

4G	Fourth generation
5G	Fifth generation
ADC	Analogue-to-digital converter
AF	Amplify-and-forward
$ASER$	Average-symbol-error rate
$AWGN$	Additive while Gaussian noise
BD	Bi-directional
BER	Bit-error rate
$BPSK$	Binary phase shift keying
CDF	Cumulative distribution function
CSI	Channel state information
$D_p(.)$	Parabolic cylinder function
DF	Decode-and-forward
DoF	Degree of freedom
DNF	Denoise-and-forward
DF	Decode-and-forward
DAC	Digital-to-analogue conversion
dB	Decibel

$E2E$	End-to-end
FD	Full-duplex
FDD	Frequency domain duplex
FDM	Frequency division multiplexing
FF	Filter-and-forward
FFT	Fast Fourier transform
$GNEP$	Generalized nonsymmetric eigenproblem (GNEP)
HD	Half-duplex
IDD	Iterative detection and decoding
$IDFT$	Inverse discrete Fourier transform
$IFFT$	Fast Fourier transform
$i.i.d.$	Independent and identically distributed
ISI	Inter-symbol interference
I/Q	In-phase/Quadrature
LI	Loop-interference
LoS	Line-of-sight
LNA	Low noise amplifier
LO	Local oscillator
$MIMO$	Multiple-input multiple-output
$MISO$	Multiple-input single-output
$MMSE$	Minimum mean-square error
MAP	Maximum *a posteriori*
MRC	Maximum-ratio combining
ML	Maximum-likelihood

MSE Mean square error

MGF Moment generation function

NSP Null-space projection

NSC Non-systematic convolutional encoder

$OFDM$ Orthogonal frequency division multiplexing

$OWRC$ One-way relay channel

P Precoded

PDF Probability density function

PSK Phase-shift keying

PA Power amplifier

PEP Pairwise error probability

PIC Parallel interference cancellation

$PLNC$ Physical-layer network coding

$QPSK$ Quadrature Phase Shift Keying

QAM Quadrature amplitude modulation

RF Radio frequency

SI Self-interference

SIC Self-interference cancellation

$SISO$ Single-input single-output

$SIMO$ Single-input multiple-output

$SINR$ Signal-to-interference-plus-noise ratio

SVD Singular-value decomposition

$STBC$ Space-time block coding

SNR Signal-to-noise ratio

$SiSo$ Soft-in soft-out

$SiSo$ Soft-in soft-out

TDD Time domain duplex

TDC Time-domain cancellation

$TWRC$ Tne-way relay channel

ZF Zero-forcing

Notations

$\mathbf{A}$	Uppercase boldface characters for matrices
$\mathbf{a}$	Lowercase boldface characters for vectors
$\mathbf{A}^T$	Transpose of the matrix **A**
$\mathbf{A}^*$	Conjugate the matrix **A**
$\mathbf{A}^H$	Hermitian the matrix **A**
$\|\mathbf{a}\|$	The Euclidean norm of the vector **a**
$\|\mathbf{A}\|$	The Euclidean norm of the matrix **A**
$\|\mathbf{A}\|$	The determinant of the matrix **A**
$\Gamma(a)$	The complete Gamma function of the variable a
$\mathbf{E}\{\mathbf{a}\}$	The statistical expectation of the random vector **a**
$\Re[A]$	The real part of the complex number A
$\Im[A]$	The imaginary part of the complex number A
$a!$	The factorial of the integer number a
$\binom{a}{b}$	The binomial coefficient which is evaluated as $\frac{a!}{b!(a-b)!}$
$W_{\lambda,\mu}(a)$	Whittaker function
$M_{\lambda,\pm\mu}(a)$	Whittaker function
$\mathrm{Ei}(a)$	Exponential integral function
$\mathrm{erf}(a)$	Error function
$\mathrm{B}(a, b)$	Beta function
$\Gamma(a, b)$	Incomplete gamma functions
$\Phi(a, b; c)$	hypergeometric function

Chapter 1

Introduction

1.1 Motivation and Challenges

The development of the anticipated 5G communication systems, which aims to attain a 100 times more throughput than that of the 4G systems, has immensely increased the demand for higher spectral efficiency networks. The existing conventional half-duplex (HD) networks utilize separate time slots in the time division duplex (TDD) technique, while orthogonal frequency bands are used in the frequency division duplex (FDD) technique, to separate the transmit and receive signals as illustrated in Figs. 1.1 and Figs. 1.2, respectively, [1–3]. Hence, the HD networks exploit only half of the spectral resources for the actual signal transmission. To improve the HD networks' spectral efficiency, some communication schemes, such as multiple-inputmultiple output (MIMO) [4, 5], and orthogonal frequency division multiplexing (OFDM) have been introduced [6]. However, these schemes alone do not meet the spectral requirements of the 5G wireless communication networks. Thus, in-band full-duplex (FD) communication mode has emerged as a promising solution to double the capacity and ameliorate the spectral efficiency of the existing HD systems by enabling the transceiver nodes to concurrently transmit and receive over the same frequency band as shown in Fig. 1.3.

It is worth pointing out that the key challenge associated with the FD mode of communication is the self-interference (SI) signal. In essence, the power of the SI signal is much higher than that of the signal of interest, which is coming from the far transceiver node. This power differential between the SI signal and the signal of interest along with the limited dynamic range of the analog-to-digital converter (ADC) can dramatically increase the signal of interest quantization noise and degrade the performance of the system. Consequently, to attain the aim of the FD

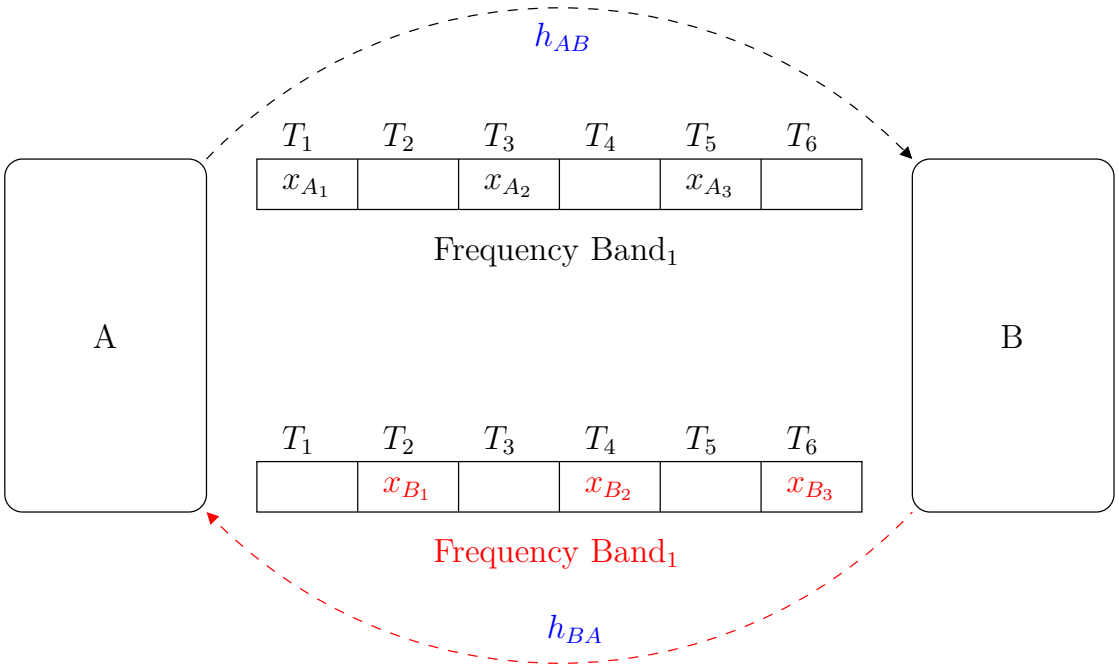

Figure 1.1: Time division duplex (TDD) scheme.

mode, i.e. double the throughput of the conventional HD communication systems, the SI signal should be effectively suppressed to the level of the noise floor before the ADC. Motivated by this fact, various self-interference cancellation (SIC) techniques have been introduced to tackle the SI challenge. The proposed schemes can be categorized into two major types: passive and active SIC schemes. The passive SIC mechanism exploits the distance between the local TX and RX antennas, some antennas settings and RF shielding materials to improve the isolation between the transmit and receive chains, subsequently, mitigate the SI signal. In contrast, the active SIC techniques utilize various signal processing methods both in the analog and digital domains to suppress the SI signal. These signal processing methods are exploited to construct a replica of the SI signal, which is then subtracted from the total received signal to diminish the actual SI signal. Furthermore, digital filtering methods have been proposed to mitigate the SI signal. In essence, these methods utilize transmit and receive filters in the local transmitting and receiving chains to cancel the SI signal. Various mechanisms are exploited to design these filters such as null-space projection (NSP), singular value decomposition (SVD), minimum mean square error (MMSE) and zero-forcing (ZF). The aforementioned SIC techniques will be meticulously discussed in Chapter 2.

Owing to the tremendous challenge induced by the FD mode, i.e the SI signal mitigation and impact of the SI signal on the performance of the wireless communication systems, most of the research only considers HD mode to avoid SI signal. However, the evolution of the 5G wireless communication systems and the throughput requirements of these systems cannot be

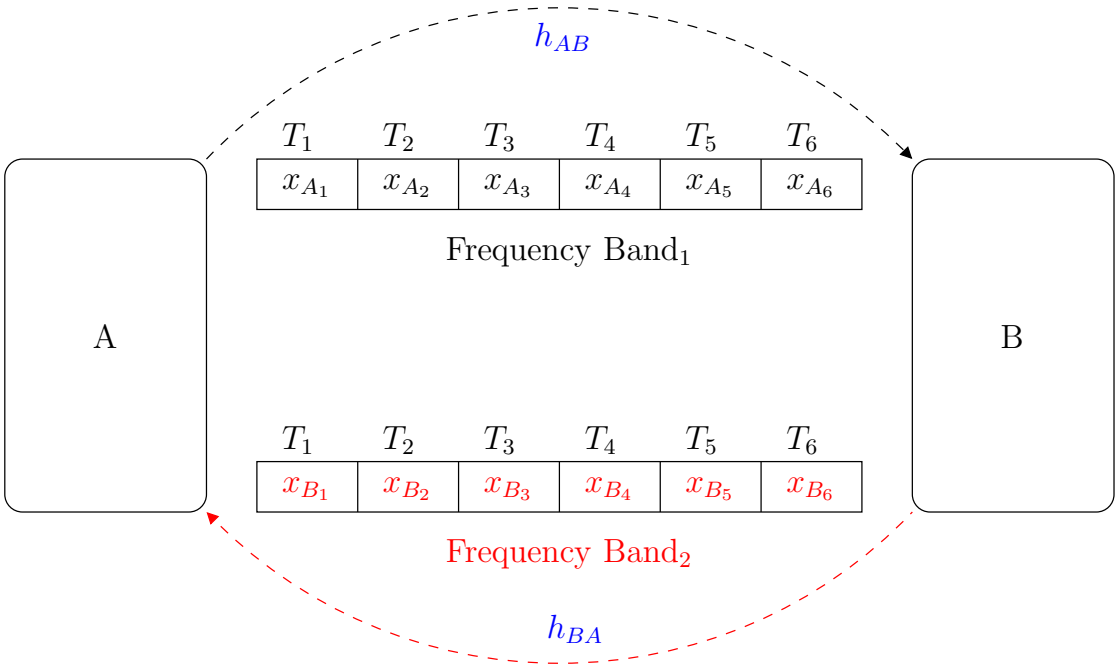

Figure 1.2: Frequency division duplex (FDD) scheme.

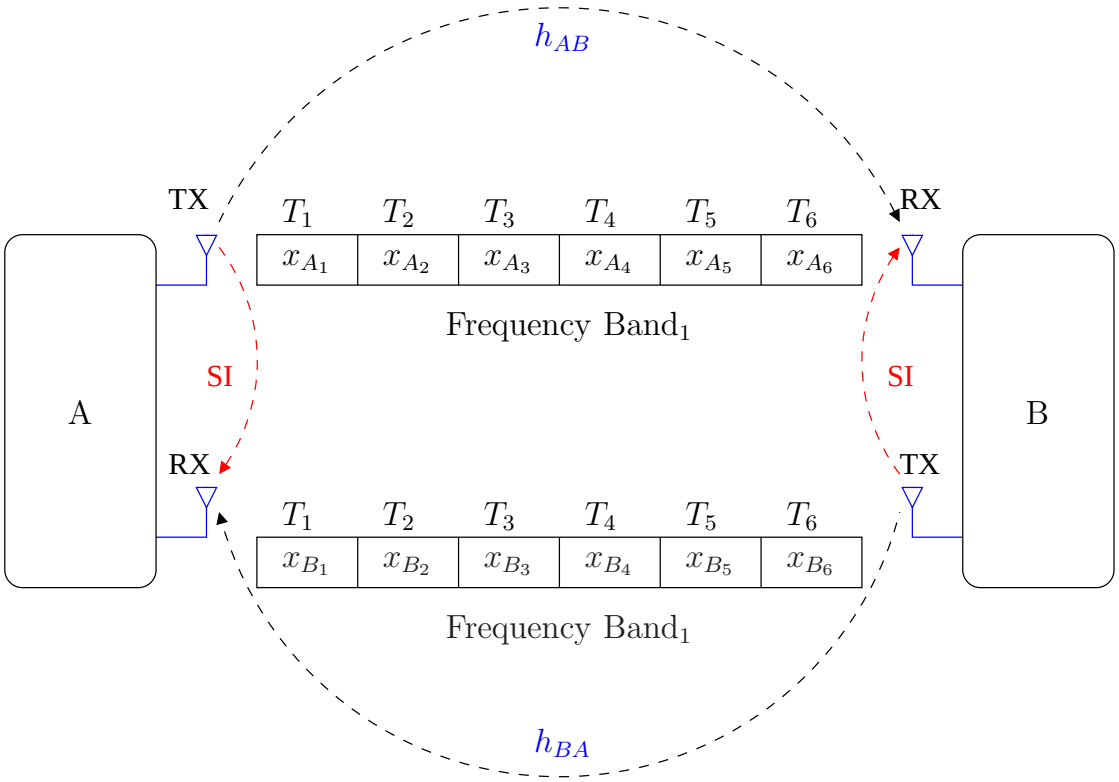

Figure 1.3: In-band full-duplex (FD) scheme.

satisfied using the HD mode of communication. Hence, recently, some researchers have investigated designing effective SIC schemes, which can enable the FD mode by diminishing the SI signal [7–11]. The promising results of these research works have indicated the feasibility of implementing a pragmatic FD wireless communication systems. In general, the obtained results have shown that the SI signal can be effectively mitigated using various SIC techniques. Thus,

recent work has considered implementing FD wireless communication networks and investigated their attained gain over the traditional HD wireless communication networks. Furthermore, some research work has studied the impact of the residual SI signal on the performance of the FD wireless communication networks.

In [12], the feasibility of utilizing FD relay node in a one-way relay channel (OWRC) network, , which comprises one HD source node (S), one HD destination node (D) and one FD relay node, was investigated in the presence of residual self-interference by evaluating the attained end-to-end (E2E) capacity. Moreover, this E2E capacity of the FD mode was compared with that of the HD mode, which exploits HD relay node. This comparison was used to study the amount of the residual SI that can be tolerated by the FD mode. Furthermore, it was assumed in this work that the received signal at the FD relay node is affected by the SI signal resulting from the FD mode. A compact relay antenna node was developed in [13]. This relay antenna node was exploited to aid the communication between outdoor base stations and indoor users, and was utilized for the SI channel measurement, where the SI interference channels were measured and modelled for outdoor-to-indoor communications. The empirical results in this work have shown that the compact relay antenna can achieve up to 51 dB isolation in an anechoic chamber, whilst 48 dB isolation was attained in the multipath environment. Nevertheless, these results can be further improved by placing antenna in different positions

A three nodes OWRC network, where the source node in the network transmits information to the destination node with the help of an FD relay node in [14]. Moreover, in this work, an adaptive FD/HD relaying scheme, which utilizes a combination of FD orthogonal reception and transmission at the relay, was introduced to maximize the spectral efficiency of the two-hop communication network. This relaying scheme was formulated as an optimization problem subject to the condition that the accomplished throughput is higher than that of the FD and HD schemes. In [15], an hybrid relaying scheme was developed. This developed scheme opportunistically switches FD and HD relaying schemes to maximize the throughput and spectral efficiency of the two-hop communication network. Moreover, a transmit power adaptation technique was combined with proposed relaying scheme to further improve the performance of the considered three nodes relay network. The benefit of opportunistic switching between relaying schemes is examined and discussed. Furthermore, the explicit conditions under which the FD relaying scheme outperforms the HD relaying scheme and vice versa were provided in this work. The FD relay selection problem was investigated in [16]. A two-hop relay network, which consists of one source node, one destination node and N FD relays is considered. The source and the destination nodes are assumed to have no direct link connecting them. Moreover,

different relay selection policies were considered to maximize the instantaneous E2E FD relay channel capacity. The performance of these relaying schemes was examined in terms of outage probability in the presence of SI signal. A two-hop relay network, which consists of one source node, one destination node and N FD relays is considered. The source and the destination nodes are assumed to have no direct link connecting them.

In [17], different antenna selection (AS) mechanisms were proposed for MIMO FD two-hop relay networks, which consist of one source node, one destination node and N FD relays is considered. The source and the destination nodes are assumed to have no direct link connecting them.. The main idea of the posed AS technique is utilizing less radio frequency chains than the equipped antennas to decrease the implementation complexity MIMO system. Moreover, the outage probability performance of the proposed AS schemes was studied in this work. A simple power allocation (PA) scheme was proposed to tackle the zero-diversity limitation associated with FD mode at the relay. Furthermore, the optimal PA value for the proposed AS schemes was analytically derived and presented. Next, a joint AS and relay selection scheme was introduced in [18] to optimize the E2E error performance of the general FD multiple-relay network. In the proposed scheme the channel condition is used to adaptively selects the TX antenna and RX antenna at the FD relay nodes, whilst the relay that can maximize the E2E performance of the FD relay network is selected. Furthermore, closed-form expressions for the outage probability and average symbol error rate of the considered network were derived and validated using simulation studies. As a result of the antenna selection at the relay nodes, the proposed scheme can attain an extra space diversity at the destination. Hence, the proposed system outperforms the traditional FD relay selection scheme. However, proposed scheme exhibits error floor at high SNR region.

In [19], an optimal relay assignment and power allocation (ORAPA) scheme, which utilizes bipartite matching approach, was proposed to maximize the attained sum rate of the FD relaying network. The Hungarian algorithm was exploited to solve the sum rate maximization problem. This problem was presented as a mixed-integer nonlinear programming (MINLP) problem. The proposed scheme was employed in an FD relay network, which comprises multiple source and destination nodes connected via multiple relay nodes. Khafagy et al. [20] studied the performance of an FD cooperative network with opportunistic relay selection, which comprises one source node and one destination communication over Nakagami-m fading channels with aid of N FD relay nodes. In particular, the outage probability and the throughput of the considered FD network were investigated. Moreover, a closed-form expression of the cumulative distribution function (CDF) of the E2E signal-to-interference and noise ratio (SINR) in the presence of a di-

rect source-destination link was derived and presented. Next, an MIMO FD relay network with a source node transmits data to a destination node with assistance of FD amplify-and-forward (AF) relay node was considered in [21]. Moreover, the source node and the destination node in the considered system are equipped with N_S and N_D antennas, respectively, while the relay node is equipped with two antennas one dedicated fro transmission and the other one for reception. The E2E outage probability performance of the considered network was investigated. Furthermore, improve the E2E performance of the FD relay network maximum ratio combining (MRC) technique was exploited at the destination node. On the other hand, transmit antenna selection (TAS) technique was used at the source node.

Exact outage probability expressions of the FD two-way relay channel (TWRC) network were derived and presented in [22], under the assumption that perfect channel state information (CSI) should be available at the relay node to accomplish a correct decoding. . Furthermore, to improve the outage performance for the FD-TWRC network, optimal power allocation techniques along with optimal relay node placement strategies were introduced. Next, The performance of an AF-FD-MIMO relay channel network was analyzed in [23]. The considered MIMO channel network comprises one source node and one destination node both equipped with a single antenna. The source node in this network intends to transmit data to the destination node via an AF-FD-MIMO relay node, which equipped with N_R and N_T antennas dedicated for reception and transmission, respectively. Moreover, the impact of the residual SI, imperfect CSI and spatial fading correlation on the performance of the system under consideration was studied. Furthermore, an exact expression in conjunction with a simpler lower band expression for the outage probability of the considered system were derived and presented. Finally, maximum and ratio transmission (MRT) and MRC techniques were considered to improve the E2E system performance.

It is worth pointing out that the main focus of the discussed literature was investigating the performance of the FD cooperative networks and presenting some AS and relay selection techniques along with some PA algorithms. Moreover, the discussed literature did not present or discussed any SIC technique, which is considered as the crucial stage in any pragmatic FD system. This comes from the fact that without the SIC stage the SI signal will swamp the signal of interest at the local ADC. Motivated by this fact several SIC techniques have been presented in the last decade to effectively diminish the SI signal before the ADC. In [24], MIMO nodes were exploited in conjunction with simultaneous transmission and reception can improve the efficiency of the ad hoc networks. Moreover, interference suppression techniques that can solve the simultaneous link problem in the ad hoc networks and enable the FD mode were utilized.

In particular, using the null-space projection to suppress the SI signal was discussed in this work. Moreover, the feasibility of mitigating SI signal using signal processing techniques, which can enable the concurrent transmission and reception, was demonstrated. A three node FD relay channel network in which the relay node is equipped with two antennas both are simultaneously used to transmit and receive data was considered is [25]. Moreover, the singular value decomposition (SVD) techniques was used to effectively diminish the SI signal and enable the FD mode, which improve the spectral effecnicy of the tow-hobs relay channel network. Next, transmit and receive filters were employed in a MIMO-FD relay channel network to effectively mitigate the SI signal [26]. These filters were designed using null-space projection and minimum mean square error techniques. Moreover, the channel estimation error of the SI channels was considered as the key limitation of the proposed SIC technique.

An FD bi-directional communication system was proposed and implemented using off-the-shelf MIMO Radios in [27]. Moreover, an effective SIC scheme, which comprises a combination of Antenna Separation, Analog Cancellation, and Digital Cancellation was introduced and empirically tested. The proposed SIC scheme constructs a replica of the SI signal and subtracts this replica from the received signal before it reaches the front end of the local receiver. The proposed SIC scheme can achieve up to 80 dB SI signal suppression. Moreover, the availability of the perfect CSI was identified as the key limitation of the proposed SIC scheme. Next, Achieving FD wireless communication was investigated in [7]. In particular, a SIC scheme, which used a combination of a novel antenna, RF, and digital cancellation techniques, was proposed. Three antennas were used to enable the antenna cancellation technique, one RX antenna, and two TX antennas. The idea behind using two TX antennas is to use one antenna for the actual transmission while using the other antenna to transmit a destructive copy of the SI signal. It is worth pointing out that the TX antennas should be placed such that the distance between them and the RX antenna should be d and $d+\lambda$. In [28], directional antennas are used to minimize the overlap in the antennas coverage patterns, which passively mitigate SI signal and enable the FD mode in a FD base station. The performance of the FD mode was characterized as a function of the angel between the directional antennas. At 10 m distance, the FD mode can achieve up to 90% and no lower than 60% gain over the HD mode when the antennas were separated by 45 or more.

An experiment-based characterization of passive SI mitigation and active SIC techniques, which includes analog and digital mechanisms, in FD wireless communication was presented in [9]. The amount of the SI suppression that is attained due to the distance between the local TX and RX antennas at each node was determined as a function of the distance between the

antennas. The experimental results demonstrated that the performance of the digital SIC stage varies as a function of the performance of the analog SIC stage and the combination of the passive and active SCI techniques can accomplish up 74 dB SI suppression. Moreover, the probability distribution of the SI channel was empirically determined and given. A combination of RF cancellation and digital cancellation techniques was considered in [29] to diminish the SI signal. The aim of the using the RF cancellation was to suppress the SI signal before the ADC to a level, which enables the receive chine to detect the signal of interest after the ADC. Next, the digital cancellation was exploited to further mitigate the SI signal in the digital domain. Moreover, the impact of the nonlinear distortion induced by the receive chain was studied in this work The nonlinear distortion produced by the PA at the transmit side was identified as a key limitation of the existing linear SIC mechanisms. Next, a pragmatic SIC scheme with practical imperfect radio frequency (RF) components was presented in [30]. Furthermore, the key RF imperfections were considered in this work. Moreover, novel widely linear digital SIC processing, which can effectively suppress the nonlinear SI resulting from the PA and the image components of the SI signal produced by the imperfections IQ mixers was introduced. It is noteworthy that this is the first time the problem of the image component of SI signal, resulting from the imbalances in IQ mixers was addressed.

A bi-directional FD-MIMO communication system was presented in [31]. Moreover, a pricing-based precoding algorithm was introduced to effectively mitigate the SI signal. Due to the fact that the proposed precoding is implemented prior to the LNA and ADC, the linearity of the system can be ensured. Next, three passive SIC mechanism were presented and their performance was characterized in [10]. First, directional antennas with 90° were used to mitigate the SI signal by minimizing the placing the TX and RX antennas such that the coverage pattern intersection is minimized. Second, dual-polarized antennas were exploited such that one antenna excites in a horizontally polarized mode, and the other in a vertically polarized mode to diminish the SI signal. Finally, an RF absorber was placed between the TX and RX antennas to suppress the SI signal. The attained SI suppression was experimentally obtained both in a reflective environment and in a nonreflective environment. The combination of the proposed SIC mechanisms can achieve up to 73.8 dB SI suppression.

A mobile single-antenna in-band FD transceiver architecture was presented in [32]. Moreover, an adaptive digital SIC algorithms with the ability to track the SI channel changing due the mobile transceiver movement was introduced. Furthermore, LMS-based learning algorithm was exploited to implemented the proposed SIC mechanism. The proposed adaptive SIC algorithms can attain 100 dB SI cancellation using a 20 MHz LTE waveform and over 110 dB with a nar-

rower bandwidth of 1.4 MHz. Next, Ahmed et al. [11] presented an active digital SIC scheme. The main idea of the proposed scheme is to exploit an auxiliary receiver chain to acquire a copy of the SI signal in the digital domain, which includes all the impairments induced by the transmit chain. Then, this copy is subtracted from the received signal to cancel the SI signal along with the transmitter impairments. Moreover, a common oscillator is shared between the auxiliary and ordinary receive chains to mitigate the phase noise of the receive chain. The proposed SIC mechanism can attain approximately 117 dB SI cancellation. An integrated wideband RF domain SIC technique was proposed in [33]. The proposed SIC mechanism utilized multiple RF bandpass filters to echo the the magnitude, phase of the SI signal.

An electrical balance duplexing technique was proposed in [34], to suppress the SI signal in a single antenna mobile devices. Hybrid junctions with electrical balance duplexer have been exploited to apply significant isolation between the transmit and receive terminals. This technique is proposed for small size devices and one antenna is used for transmission. Furthermore, the performance of this mechanism is affected by the antenna impedance variation in both the frequency domain and time domain. Next, an multitap RF cancellation scheme with multiple pre-weighted taps was introduced in [35]. The proposed scheme used fixed delay and adaptive algorithm to track the amplitude and the phase of the direct path between the local TX and RX antennas and the recollections from the surrounding environment. Moreover, this SIC can accomplish up to 90 dB analog cancellation before the signal reaches the ADC. A shared antenna full-duplex transceiver was introduced in [36], this transceiver exploits adaptive RF cancellation along with adaptive digital SIC scheme to suppress the SI signal at digital baseband. The adaptive RF cancellation circuit in this work tracks the changes in the amplitude and phase of the SI signal to construct a copy of it and then subtract this copy from the received signal. The power of the SI signal after the adaptive RF cancellation can still be stronger than the signal of interest from the other nodes due to the nonlinear low-cost RF components. Thus, the adaptive digital SIC is exploited to suppress the residual SI in the digital domain after the adaptive RF cancellation.

An SIC mechanism, which comprises a combination of Iterative detection and decoding (IDD) with MMSE filtering were proposed in [37], to further diminish the residual SI signal after passive and active SIC stages. Moreover, the proposed SIC scheme was exploited in an FD single-input multiple-output (SIMO) bi-directional communication system. The proposed SIC technique in conjunction with passive, and analog and digital active SIC stages can enhance the performance of the considered FD-SIMO bi-directional system. The obtained results showed a close match with the SI free scenario. Next, a frequency domain SIC scheme that can remove

all the SI components in a generalized frequency-division multiplexing (GFDM) system was designed and presented in [38]. This was done by generating a replica of the SI signal and subtract this replica from the received signal. The performance of the FD-GFDM can be enhanced without increasing the computational complexity of the system. Korpi et at. [39], introduced a new SIC scheme, which comprises passive SI suppression attained using a novel antenna design followed by multitap RF cancellation and nonlinear digital cancellation to further suppress the SI signal to the level of the receiver noise floor. The utilized antenna design uses wavetraps to attain passive isolation of up to 70 dB between the TX and RX antenna ports. Then, feeding the SI signal into the multitap RF cancellation and nonlinear digital cancellation can achieve over a 100 dB SI cancellation even when 80 MHz bandwidth is assumed.

A novel RF SIC scheme that exploits phase modulation and optical sideband filtering was introduced in [40]. The SI signal was suppressed by tuning the delay time and amplitude in the optical domain. There are mainly two issues associated with this SIC approach, which can be investigated in the future. First, how to optimize the phase modulators and the optical filter to improve the SIC over a wide bandwidth. Second, exploit an adaptive algorithm to efficiently track the amplitude and phase of the SI signal. Next, a novel digital SIC mechanism for in-band FD MIMO transceivers was introduced in [41]. Moreover, a general signal model for the observed SI in the digital domain was presented in this. This SI signal model can capture all the distortions induced by the transmit and receive chains such as IQ imbalance, the nonlinearity of the PA, and the crosstalk between the transmitters. Furthermore, a novel principal component analysis based scheme was proposed to reduce the complexity of the cancellation scheme by controlling the number of parameters in the signal model. It is worth pointing out that the proposed complexity reduction scheme can remove up to 65% of the parameters in the digital canceller, hence formidable computational requirements reduction can be attained.

1.2 Contributions

This research aims to design a pragmatic transceiver node that can enable the FD mode of communication, i.e. simultaneously transmit and receive in the same frequency band. Moreover, in this thesis, meticulous performance analysis of the proposed FD systems is done to investigate the ability of these systems to improve the throughput and the spectral efficiency of the traditional HD systems. To tackle the formidable challenge induced by the FD mode, i.e. the SI signal, three SIC schemes are presented in this work. The performance of these SIC schemes is thoroughly examined and their performance limitations are addressed in this work.

The contribution of this thesis can be summarized as follows

- In Chapter 3, a new orthogonal frequency-division multiplexing (OFDM) based FD physical-layer network coding (PLNC) system with a hybrid SIC scheme, which is a combination of passive and active SIC techniques, is introduced in this work.
- In Chapter 4, an adaptive SIC scheme which exploits the normalized least-mean-square (NLMS) algorithm to suppress the SI signal to the level of the noise floor is developed and presented.
- Furthermore, the proposed adaptive SIC is exploited in a denoise-and-forward (DNF) FD-PLNC system.
- In Chapter 5, a novel over-the-air SIC scheme that exploits the generalized nonsymmetric eigenproblem (GNEP) to effectively diminish the SI signal before it reaches the ADC of the local receive chain is introduced in this work.
- Closed-form expressions for various performance evaluation metrics of the proposed FD wireless communication systems are derived and presented in this work. Moreover, the derived expressions are validated using extensive simulation studies.
- The effect of the imperfect CSI and residual SI on the performance of the FD wireless communication systems is meticulously studied.
- The impact of the hardware impairments on the performance of the considered FD systems is investigated in this work.

1.3 Publications Arising From This Research

- Conference Papers

1. **B. A. Jebur**, C. C. Tsimenidis and J. Chambers, "Tight Upper Bound Ergodic Capacity of an AF Full-Duplex Physical-Layer Network Coding System," in *IEEE 27th Annual International Symposium on Personal, Indoor, and Mobile Radio Communications (PIMRC)*, pp. 1-6, Sept 2016, Valencia, Spain.
2. **B. A. Jebur**, C. C. Tsimenidis, M. Johnston, and J. Chambers, "Outage probability of an AF full-duplex physical-layer network coding system," in *24th European Signal Processing Conference (EUSIPCO)*, pp. 1828-1832, Aug 2016, Budapest, Hungary.

3. **B. A. Jebur**, and C. C. Tsimenidis, "Performance analysis of OFDM-Based denoise-and-forward full-duplex PLNC with imperfect CSI," in *IEEE International Conference on Communication Workshop (ICCW)*, pp. 997-1002, June 2015, London, United Kingdom.

1.4 Thesis Outline

The rest of the thesis is organized as follows:

Chapter 2 discusses the evolution of the 5G wireless communication networks and the challenges that are associated with these networks. Next, the PLNC scheme is presented as a promising technique to improve the throughput of the TWRC networks. Furthermore, the relaying schemes that are used in the cooperative systems are outlined in this chapter. Moreover, this chapter introduces the in-band FD mode and the challenges associated with this mode. Additionally, various SIC mechanisms are illustrated in this chapter such as passive SIC techniques, analog, and digital active SIC schemes, and spatial SIC methods.

Chapter 3 presents an amplify-and-forward (AF) OFDM based FD-PLNC system that is combined with a hybrid SIC scheme to effectively mitigate the SI signal. Moreover, closed-form expressions for the E2E average symbol error rate (ASER), outage probability and ergodic capacity of the proposed AF-FD-PLNC system are derived and presented in this chapter. Furthermore, the impact of the residual SI signal on the performance of the proposed system is meticulously studied. The estimation error of the SI channel and the imperfect synchronization between the constructed replica of the SI signal and the actual SI signal are identified as the key limitation of the proposed SIC scheme.

Chapter 4 focuses on the design of an adaptive SIC scheme that exploits the NLMS algorithm to effectively suppress the SI signal. Moreover, a DNF-FD-PLNC system, which exploits the proposed adaptive SIC scheme, is presented in this chapter. Exact E2E expressions for the outage probability, ASER and ergodic capacity of the proposed system are derived and validated using Monte Carlo simulations. Furthermore, the E2E performance of the proposed DNF-FD-PLNC system is thoroughly analyzed in the presence of the residual SI and imperfect CSI.

Chapter 5 introduces a novel SIC scheme that utilizes Generalized Nonsymmetric Eigenproblem (GNEP) to effectively suppress the SI signal over-the-air before it reaches the local ADC. Moreover, a precoded full-duplex bi-directional (P-FD-BD) wireless communication system is presented. Furthermore, the impact of the hardware impairments on the performance of the proposed SIC scheme is investigated in this chapter.

Finally, the conclusions of this thesis along with the potential future work are presented in Chapter 6.

Chapter 2

Evolution of Full-Duplex Architectures

2.1 Introduction

The evolution of the fifth-generation (5G) wireless communication systems, which will be deployed in 2020, has introduced a number of challenges and different research topics [42]. These challenges can be summarized as follows; higher capacity and performance requirements, higher spectrum efficiency, more spectrum resources, low cost and low latency [43]. Moreover, 5G networks should enable mobile broadband (MBB) service, machine type communications (MTC), and vehicular to anything (V2X) communications [44,45]. Thus, a number of research topics such as cooperative communication and FD systems have been proposed to address these challenges. The cooperative communication systems are one of the solutions to extend the coverage and improve the throughput of the 5G communication systems due to its diversity gain [46–49]. In general, the cooperative communication systems comprises two main types of networks: one-way relay channel (OWRC) network and two-way relay channel (TWRC) network, booth will be thoroughly discussed in this chapter. In both types, i.e. OWRC and TWRC, one or more nodes are exploited as a relay to extend the network coverage and/or to provide diversity gain [50].

Furthermore, FD communication mode is a promising technology that can double spectral efficiency and capacity of the conventional half-duplex (HD) communication system by enabling each transceiver node in this system to transmit and receive simultaneously over the same frequency band [51, 52]. Hence, exploiting the FD mode can meet the 5G throughput requirements, however, FD systems suffer from SI, which can dramatically degrade the throughput performance of these systems [53, 54]. This degradation comes from the fact that the power of the SI signal is much larger than that of the signal of interest that is coming from the far

transceiver nodes, subsequently, the signal of interest can be swamped by the SI signal in the ADC [55, 56]. Thus, to enable the FD communication systems and enhance the capacity of the conventional HD systems by approximately a factor of 2, an efficient self-interference cancellation (SIC) scheme is required at each transceiver node [57]. The aim of the SIC is to suppress the SI signal to approximately the noise floor level before the ADC [3]. In the recent years, a number of different SIC schemes have been presented such as; passive SIC exploiting the propagation suppression and isolation materials, and active SIC, which is implemented in the analog and digital domain. Furthermore, a spatial SIC which exploits zero-forcing (ZF), minimum mean square error (MMSE) filtering and null space projection (NSP) to diminish the SI signal, has been presented an effective technique to mitigate the SI signal. These SIC schemes will be thoroughly discussed in the rest of this chapter.

This chapter presents a background and theoretical overview of the cooperative communication systems in general along with a comprehensive description of the OWRC and TWRC networks. Moreover, a detailed discussion of the relaying schemes that can be utilized in the cooperative systems is included in this chapter. Finally, a theoretical overview and comprehensive discussion of the different SIC schemes that have been presented thus far in the existing research work.

2.2 Cooperative Wireless Communication Systems

A cooperative wireless communication system is defined to be a system, in which all or some of the wireless nodes cooperate to relay other nodes' data [58], as illustrated in Fig 2.1. It is worth noting that some of these nodes do not have any data to transmit and act only as a relay to facilitate the communication between the nodes in the cooperative networks. In essence, these systems can improve the spectral efficiency, enhance transmission capacity, extend the coverage and exploit distributed spatial diversity [59]. The main idea of the cooperative communication systems was introduced in [60], which studied the capacity of a simple cooperative wireless communication system that comprises three nodes, i.e. source node, a relay node and destination node. In general, the cooperative wireless communication systems include two main network categories: OWRC network and TWRC network. These network categories will be discussed in detail in this section.

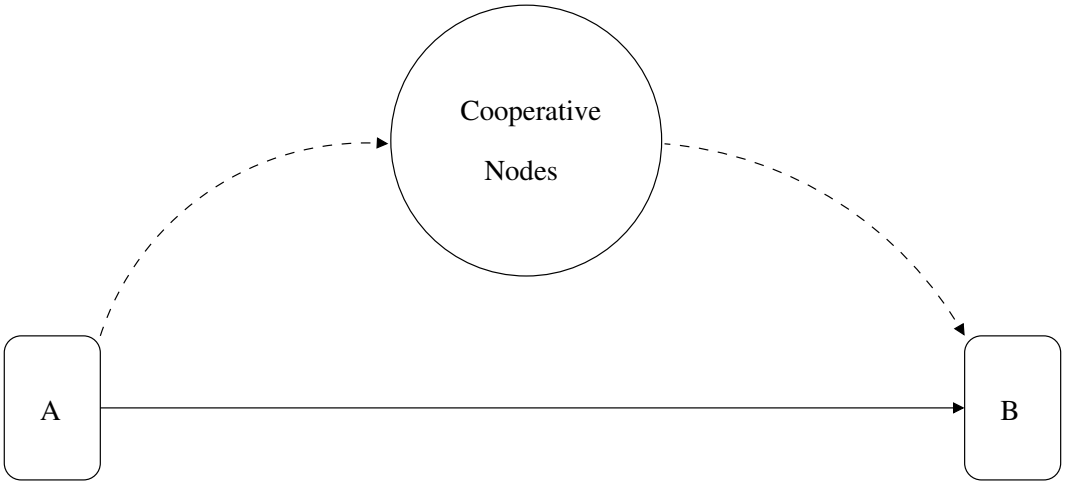

Figure 2.1: A cooperative communication system.

2.2.1 One-Way Relay Channel (OWRC) Network

The OWRC network consists of one source node, S, one destination node, D, and one or more intermediate nodes that act as relay nodes as depicted in Figs. 2.2, 2.3 and 2.5. These relay nodes facilitate the communication between the source and destination nodes. Figs. 2.2 and

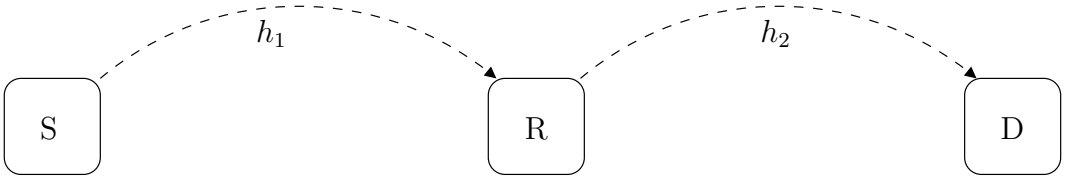

Figure 2.2: Two-hop one-way relay channel network.

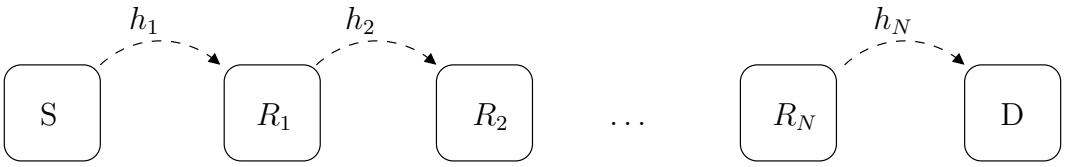

Figure 2.3: Multi-hop one-way relay channel network.

2.3 illustrate a two-hop and multi-hop relay channel network, respectively, in which there is no direct path connecting the source and a destination nodes, hence, they communicate with aid of the relay nodes. The main role of the relay nodes in these networks is facilitating the communication between the source and destination nodes, S and D, in the absence of a direct link between these nodes [61, 62]. It can be observed from Fig. 2.2 that two time slots are required to deliver the source node signal to the destination node. In the first time slot, the relay

node receives the signal transmitted by the source node, while in the second time slot, the relay forwards the source node signal to the destination node. Furthermore, it is clear that the network in Fig. 2.3 is an extension of the network shown in Fig. 2.2, thus, $N + 1$ are needed to convey the source node signal to the destination node, where N denotes the number of relay nodes.

Fig. 2.4 shows an OWRC network which exploits the relay node to enhance the diversity gain as the destination node receives two copies of the source node signal. Hence, in the first time slot, the received signal at the relay is given as

$$y_R = h_1 x_S + w_R, \tag{2.1}$$

while the signal received from the source node at the destination node can be expressed as

$$y_D = h_3 x_S + w_D, \tag{2.2}$$

where x_S is the signal transmitted from the source node, h_1 and h_3 denote the channels between the source node and the relay and the source node and the destination, respectively. Moreover, w_R and w_D are the additive white Gaussian noise (AWGN) terms at the relay and destination nodes, respectively. In the second time slot, the received signal at the destination node can be written as

$$y_D = h_2 x_R + w_D, \tag{2.3}$$

where h_2 represents the channel coefficients between the relay and the destination node, and x_R is the signal transmitted from the relay node. This signal, i.e. x_R, is obtained from the received signal at the relay node in the first time slot by applying one the relaying schemes. These relaying schemes will be explained in this chapter.

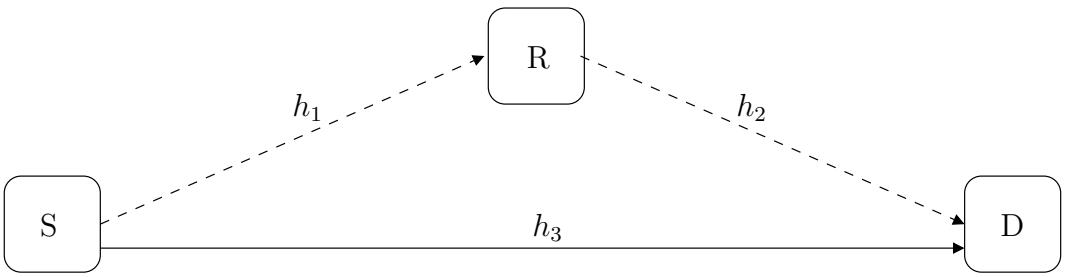

Figure 2.4: Two-hop one-way relay channel network with a direct link between the source and destination nodes.

Fig. 2.5 illustrates an OWRC, which comprises one source node, S, one destination node, D,and N relays. The multiple relays in this network can enhance the diversity gain and improve

the achievable throughput of the OWRC. In the first time slot, the received signal at the n-th relay is given as

$$y_{R_n} = h_{1_n} x_S + w_{R_n}, \tag{2.4}$$

where h_{1_n} is the channel coefficients between the source node, S, and the n-th relay, R_n, and w_{R_n} represents the AWGN term at the n-th relay node. During the second time slot, all the relay nodes transmit the signal that was received from the source in the first time slot to the destination node. Thus, the received signal at the destination node is modelled as

$$y_D = \sum_{n=1}^{N} h_{2_n} x_{R_n} + w_D, \tag{2.5}$$

where h_{2_n} denotes the channel between the n-th relay and the destination node, and x_{R_n} represents the signal transmitted from the n-th relay node. The destination node combines all the received signal using one of the combining technique that can attain the maximum diversity gain such as the Maximum Ratio Combining (MRC).

2.2.2 Two-Way Relay Channel (TWRC) Network

The TWRC networks have been presented to overcome the half-duplex (HD) capacity loss in the OWRC systems [63]. In essence, a TWRC network comprises two end nodes, A and B, intending to exchange information with aid of one or more intermediate nodes. Fig. 2.6 illustrates a simple TWRC network which consists of two end nodes, A and B, with no direct link connecting them, and one relay node, R. The end nodes in this network exchange information with the assistance of the relay node, R, in four time slots. In the first time slot, T_1, node A transmits its data to the relay node, which retransmit this data to node B in the second time slot, T_2. Furthermore, node B sends its data to the relay node in the third time slot, T_3, while the relay forwards the data received from node B to node A during the fourth time slot, T_4.

The received signal in the first time slot at the relay node can be given as

$$y_R = h_A x_A + w_R, \tag{2.6}$$

where h_A represents the channel coefficients between node A and the relay, x_A is the signal transmitted by node A, and w_R denotes the AWGN samples at the relay node. Moreover, during

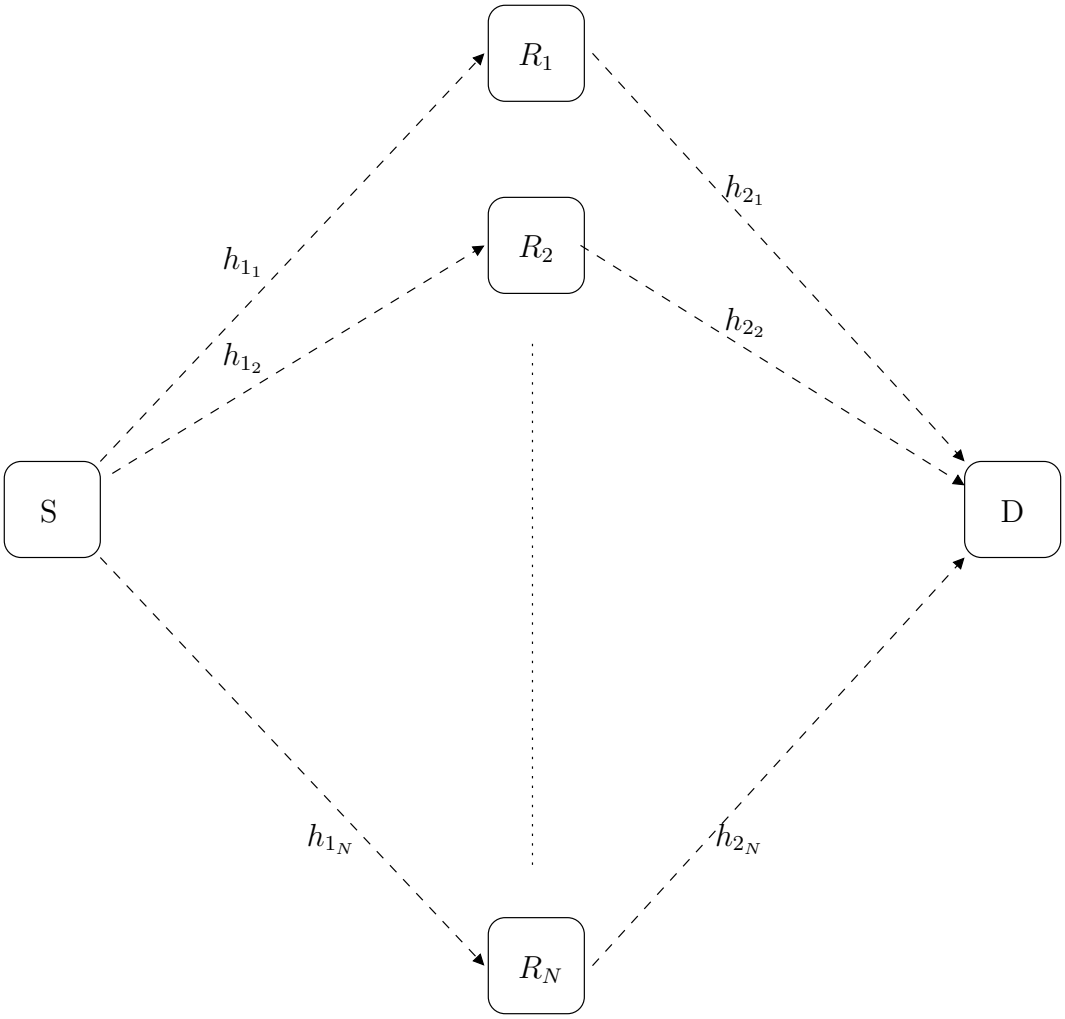

Figure 2.5: Two-hop one-way relay channel network with multiple relay nodes.

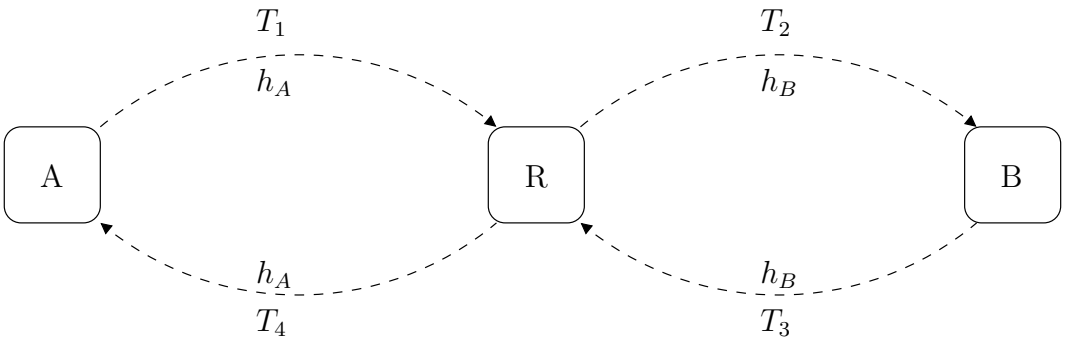

Figure 2.6: Two-hop two-way relay channel network.

the second time slot, T_2, the received signal at node B is modelled such that

$$y_B = h_B x_R + w_B, \tag{2.7}$$

where w_B denotes the AWGN term at node B, x_R represents the relay transmitted signal and

h_B indicates the channel coefficients between the relay and node B. Furthermore, in the third time slot, T_3, the received signal at the relay can be expressed as

$$y_R = h_B x_B + w_R, \tag{2.8}$$

while the received signal at node A in the fourth time slot, T_4, can be written such that

$$y_A = h_A x_R + w_A, \tag{2.9}$$

where x_B denotes node B transmitted signal and w_A represents the AWGN samples at node A.

Analogous to the OWRC network, multiple relays can be utilized in the TWRC network to maximize the achievable throughput as depicted in Fig. 2.7. A closer inspection of Fig. 2.7

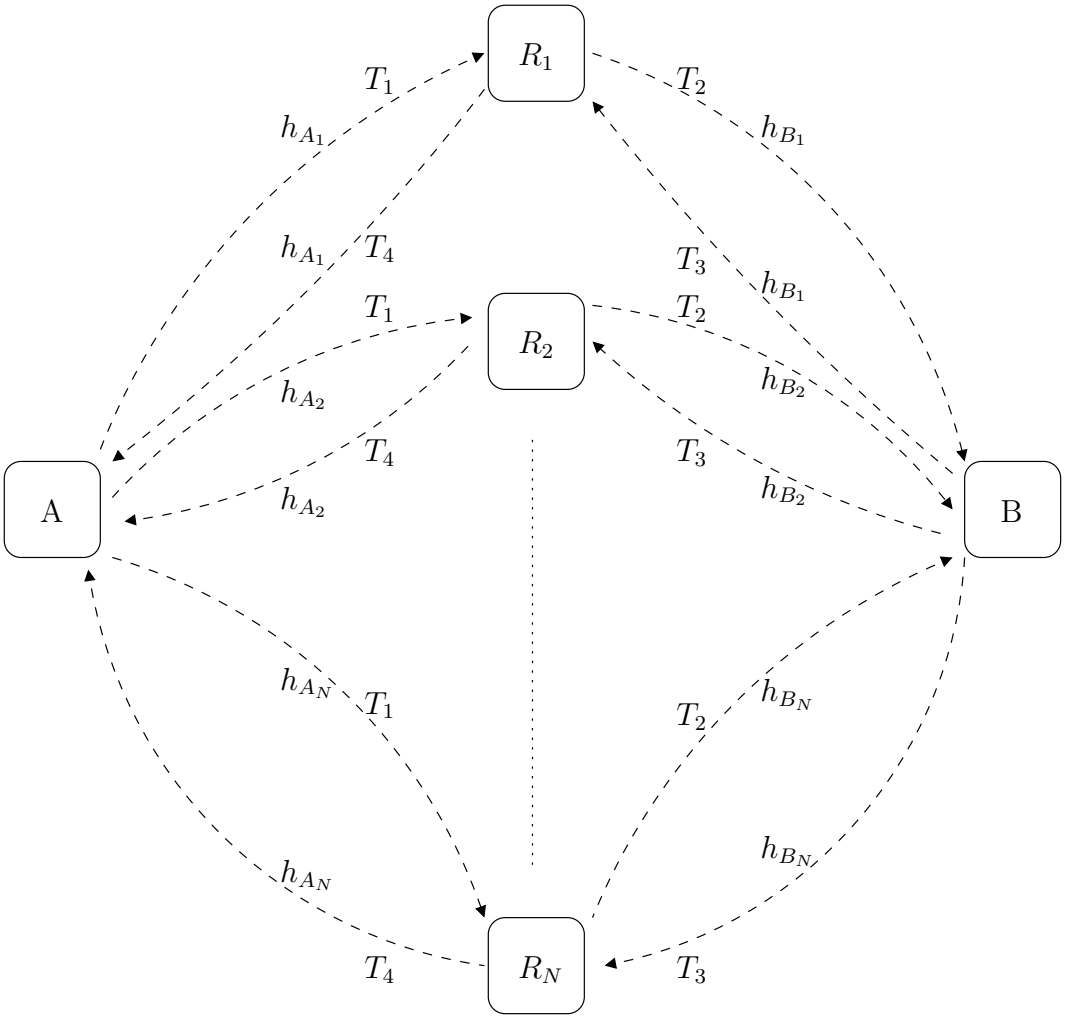

Figure 2.7: Two-hop one-way relay channel network.

shows that four time slots are sufficient for the end nodes to exchange information. In the first time slot, node A transmits its signal to all the relay nodes, subsequently, the received signal at

the n-th relay node in this time slot, T_1, can be expressed as

$$y_{R_n} = h_{A_n} x_A + w_{Rn}, \tag{2.10}$$

where h_{A_n} indicates the channel connecting node A with the m-th relay node, R_n. Moreover, during the second time slot, T_2, the relay nodes forward the signal transmitted by node A in the first time slot to node B. The received signal at node B in the second time slot can be modelled as

$$y_B = \sum_{n=1}^{N} h_{B_n} x_{R_n} + w_B, \tag{2.11}$$

where h_{B_n} denotes the channel between the n-th relay and node B. Furthermore, node B transmits its signal to the relay nodes in the third time slot, T_3, hence, the signal observed by the m-the relay node in this time slot can be written as

$$y_{R_n} = h_{B_n} x_B + w_{Rn}. \tag{2.12}$$

Finally, the relay nodes transmit the signal received during the third time slot to node A in the fourth time slot, T_4. Thus, in this time slot node A receives the signals transmitted from all of the relay nodes, which can be expressed as

$$y_A = \sum_{n=1}^{N} h_{A_n} x_{R_n} + w_A. \tag{2.13}$$

The end nodes, A and B , combine the signals received from the relay nodes to maximize the signal-to-noise ratio (SNR).

2.3 Relaying Techniques

In the cooperative wireless communication networks, the relay node plays a crucial role to facilitate the communication between the end nodes utilizing one the relaying techniques. In essence, the relaying technique indicates the signal processing that is performed by the relay node on the received signal before forwarding the processed signal to destination node [64]. In practice, there are different relaying techniques.

2.3.1 Amplify-and-Forward (AF) Relaying

The amplify-and-forward (AF) relaying technique is a simple relaying approach, with low hardware complexity [65]. In this relaying strategy, the relay multiplies the signal received from the source node by a scaling factor, β_{co}, before transmitting the scaled version of the received signal to the destination node [66]. Given that the received signal at the relay is expressed as

$$y_R = h_{S,R}x_s + w_R, \tag{2.14}$$

where $h_{S,R}$ denotes the channel connecting the source node and the relay, x_s represents the source node signal, and w_R is the additive white Gaussian noise (AWGN) samples at the relay node exhibiting a complex-valued circular Gaussian distribution, whose PDF is $\mathcal{CN}(0, N_0)$. The scale factor at the relay node can be expressed as

$$\beta_{co} = \sqrt{\frac{E_R}{|h_{S,R}|^2 + N_0}}, \tag{2.15}$$

where E_R denotes the relay's average transmit energy [67]. It can be observed from (2.15) that the key reason behind using the scaling factor is to meet the relay's average transmit power constraint. Consequently, the relay's transmitted signal can be written as

$$x_R = \beta_{co}y_R, \tag{2.16}$$

which can be expanded such that

$$x_R = \beta_{co}h_{S,R}x_s + \beta_{co}w_R. \tag{2.17}$$

A closer inspection of (2.17) reveals that in addition to the desired signal, i.e. the source node signal, the AF relaying technique forwards a scaled version of the AWGN. Subsequently, utilizing this relaying approach in the multiple hop cooperative networks can result in performance desegregation [65, 68].

2.3.2 Decode-and-Forward (DF) Relaying

In the decode-and-forward (DF) relaying technique, the relay decodes the message received from the source node before using the decoded message to generate a new message, which is then sent to the destination node [69]. Hence, this relaying approach is also called regenerative

relaying technique. It is noteworthy that the hardware requirements for the DF relaying are more complex than those of the AF method [70]. Moreover, due to the fact that the relay has to explicitly decode the message received from the source node before forwarding this message to the destination node, the source node should transmit at a rate that allows the relay to decode the source node message and forward it to the destination node [71]. Consequently, in this relying scheme, the relay nodes usually operate in HD mode as the full message have to be received by the relay before it can be decoded and then transmitted to the destination node.

2.3.3 Compress-and-Forward (CF)

In this method, the relay quantizes and compresses the signal received from the source node, then this quantized version of the received signal is forwarded to the destination node [65, 69–71], thus the compress-and-forward (CF) method is also called quantize-and-forward relaying scheme. In the quantization process at the relay, the message received from the source node is modelled as a sequence of quantized symbols, which are transmitted to the destination node [71]. Then, these quantized symbols are decoded at the destination node to retrieve the source transmitted message.

2.4 Physical-Layer Network Coding (PLNC)

The physical-layer network coding (PLNC) scheme was introduced in [72] as a promising technique to improve the throughput and enhance the spectral efficiency of the TWRC networks. In essence, the PLNC scheme exploits the superimposition of the electromagnetic (EM) waves that occurs naturally when these EM waves come together in the same physical space [73]. The EM waves superimposition is considered as a form of network coding that occurs naturally [74]. A simple TWRC network can be utilized to illustrate the concept of the PLNC. Consider a three nodes TWRC network with two end nodes, A and B, and one relay node, R, as depicted in Fig. 2.8.

In general, the PLNC scheme consists of two phases [72, 73, 75, 76]. During the first phase, which is called the multiple access (MAC) phase, both of the source nodes A and B transmit their information concurrently to the relay node as depicted in Fig. 2.8, therefore, the received signal at the relay node is given as

$$y_R = x_A + x_B + w_R, \tag{2.18}$$

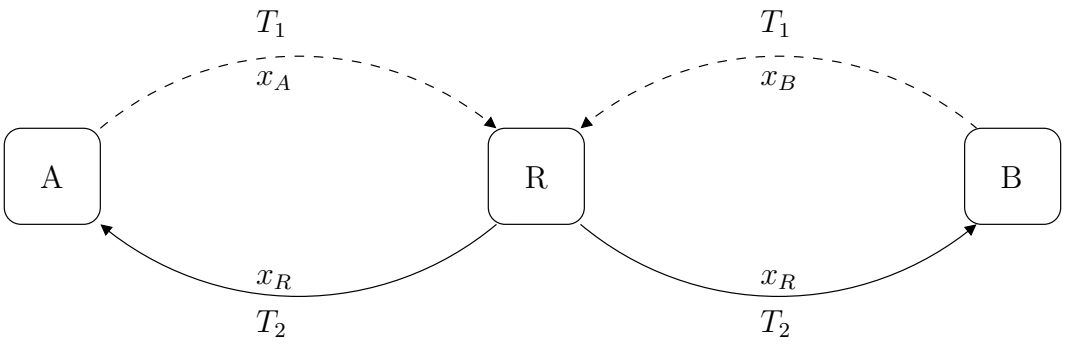

Figure 2.8: Physical-layer network coding system.

where x_A and x_B denote the signal transmitted by node A and B, respectively. These signals can be expressed as

$$x_A = \mathcal{C}\left(S_A\right), \tag{2.19}$$

$$x_B = \mathcal{C}\left(S_B\right), \tag{2.20}$$

where S_A and S_B are the binary data at node A and B, respectively, and $\mathcal{C}$ represents the Gray mapper, which maps the binary data input to the modulation symbols. Moreover, in the second phase, which is called the broadcast (BC) phase, the relay broadcasts its signal to both of the end nodes. Hence, the observed signal at node A can be given as

$$y_A = x_R + w_A, \tag{2.21}$$

while the received signal at node B can be written as

$$y_B = x_R + w_B, \tag{2.22}$$

where x_R is the signal transmitted from the relay node, which can be obtained using one of the relaying schemes.

2.5 Relaying Schemes for Physical-Layer Network coding (PLNC)

The relaying schemes that are utilized at the relay nodes in the PLNC scheme to obtain the signal to be broadcasted from the relay to the end nodes are similar to those explained in Section 2.3. However, in the PLNC relaying schemes, the resulting signal at the relay node should

be constructed in a manner that enables both the end nodes to decode it and extract the signal transmitted by the far end node using the knowledge of its own transmitted signal in the previous time slot. Different relaying techniques can be applied to realize the PLNC scheme such as AF and denoise-and-forward (DNF) schemes [77].

2.5.1 Amplify-and-Forward Relaying Scheme for the Physical-Layer Network Coding

In this scheme, the superimposed signal at the relay node is scaled by an amplification factor, β_{PL}, which can be given as [78]

$$\beta_{PL} = \sqrt{\frac{E_R}{E_A + E_B + N_0}}, \tag{2.23}$$

where E_A, E_B and E_R are the average transmit energy at node A, B and the relay, respectively. Therefore, the received signal at node A can be expressed as

$$y_A = \beta_{PL} y_R + w_A, \tag{2.24}$$

and that of node B can be given such that

$$y_B = \beta_{PL} y_R + w_B. \tag{2.25}$$

Substituting (2.18) in (2.24) and (2.25) yields

$$y_A = \beta_{PL} x_A + \beta_{PL} x_B + \beta_{PL} w_R + w_A, \tag{2.26}$$

$$y_B = \beta_{PL} x_A + \beta_{PL} x_B + \beta_{PL} w_R + w_B. \tag{2.27}$$

To this end, nodes A and B exploit their knowledge of the scaling factor in conduction with their transmitted signal in the previous time slot to estimate the signal transmitted by the far end node. Thus, the signal transmitted by node B can be estimated at node A such that

$$\hat{x}_B = \frac{\beta_{PL} x_A + \beta_{PL} x_B + \beta_{PL} w_R + w_A - \beta_{PL} x_A}{\beta_{PL}}, \tag{2.28}$$

while the estimated version of x_A at node B can be obtained as follows

$$\hat{x}_A = \frac{\beta_{PL}x_A + \beta_{PL}x_B + \beta_{PL}w_R + w_B - \beta_{PL}x_B}{\beta_{PL}}. \tag{2.29}$$

Moreover, (2.28) and (2.29) can be simplified such that

$$\hat{x}_B = x_B + w_R + \frac{w_A}{\beta_{PL}}, \tag{2.30}$$

$$\hat{x}_A = x_A + w_R + \frac{w_B}{\beta_{PL}}. \tag{2.31}$$

It can be observed from (2.30) and (2.31) that the main drawback in this relaying scheme is the propagating noise from the relay node.

2.5.2 Denoise-and-Forward Relaying Scheme for the Physical-Layer Network Coding

This relaying scheme was introduced in [79] and further developed in [80,81]. The main advantage of this scheme is the ability to improve the achievable throughput of the PLNC system [76]. It is worth pointing out that for simplicity reason we consider an uncoded quadrature amplitude modulation (QAM) PLNC network to explain the denoising operation at the relay node. The relay node in this scheme performs the denoising operation on the received superimposed signals to construct x_R, which is then broadcasted to end nodes [82]. The denoising operation starts with maximum-likelihood (ML) detection and followed by two mappers, i.e. denoising mapper $\mathcal{DMA}$ and constellation mapper $\mathcal{CMA}$. The ML detection is performed as follows

$$\hat{X}_{AB} = \underset{(q_1,q_2)\in\mathbb{Z}_4\times\mathbb{Z}_4}{\operatorname{argmin}} \mid y_R - (\mathcal{C}(q_1) + \mathcal{C}(q_2)) \mid^2, \tag{2.32}$$

where $\mathcal{C}$ denotes the mapper that maps the binary data to the modulation symbols. Moreover, (2.32) yields the estimated version of superimposed signal, which is given as

$$x_{AB} = x_A + x_B, \tag{2.33}$$

where $x_{AB} \in \{\pm 2 \pm 2j, 0, \pm 2, \pm 2j\}$. Next, the ML output is mapped to a QAM signal, x_R, using the constellation mapper $\mathcal{CMA}$. The relay QAM signal, x_R, is selected from a well-designed finite mapping book as depicted in Table 2.1 [73]. This mapping book was designed to enable the end nodes to exploit their own transmitted data to extract the data transmitted by

the far end node [83]. Node A uses its transmitted data during the previous time slot to extract the data transmitted by node B such that

$$S_B(i-1) = S_R(i) \oplus S_A(i-1). \tag{2.34}$$

Furthermore, the data transmitted by node A is extracted from the relay signal received at node B using the data transmitted by node B in the previous time slot as follows

$$S_A(i-1) = S_R(i) \oplus A_B(i-1), \tag{2.35}$$

where i denotes the time slot index and S_R represents the binary data corresponding to the signal x_R.

Table 2.1: The constellation mapping operation at the relay

Node A signal	Node B signal	The superimposed signal (x_{AB})	QPSK Mapping, X_R
-1+ 1j	1- 1j	0	-1-1j
1+ 1j	-1- 1j	0	-1-1j
1- 1j	-1+ 1j	0	-1-1j
-1- 1j	1+ 1j	0	-1-1j
1- 1j	1+ 1j	2	1-1j
-1+ 1j	-1- 1j	-2	1-1j
-1+ 1j	1+ 1j	2j	-1+1j
1- 1j	-1- 1j	-2j	-1+1j
1+ 1j	1+ 1j	2+2j	1+1j
-1+ 1j	-1+ 1j	-2+2j	1+1j
1- 1j	1- 1j	2-2j	1+1j
-1- 1j	-1- 1j	-2-2j	1+1j

2.6 In-Band Full-Duplex Wireless Systems

Recent developments in the communication devices and the substantially increased number of these devices have increased the demand on the limited wireless spectrum resources [84]. Moreover, the 5G communication systems high-throughput requirements have highlighted the demand for efficient wireless systems. Hence, in-band FD high spectral efficiency systems that

can meet the 5G throughput requirements have been presented. The main idea of the in-band FD mode is enabling the wireless transceiver nodes to transmit and receive concurrently over the same frequency band. Thus, theoretically, the spectral efficiency of this wireless technology is double that of the well-known time-division duplexing (TDD) and frequency-division duplexing (FDD) systems. Furthermore, the in-band FD system can double the throughput of the conventional HD systems. As a result, the in-band FD technology has been considered in a vast variety of wireless communication systems [85].

2.6.1 Full-Duplex One-Way Relay Channel

To improve the throughput of a two-hop OWRC network, which comprises a source node, destination node, and relay node, the FD-OWRC has been introduced [12, 86]. Analogous to the conventional HD-OWRC, the FD-OWRC consists of an HD source node that transmits information contentiously to an HD destination node with the help of an FD relay node as illustrated in Fig. 2.9. It can be observed from Fig. 2.9 that unlike the HD-OWRC, in the FD-

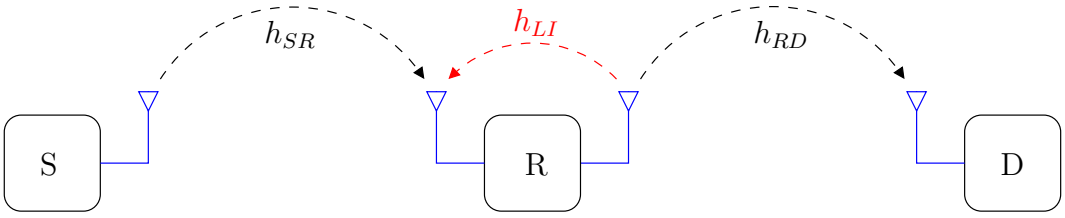

Figure 2.9: Full-duplex two-hop one-way relay channel network.

OWRC, the source node, S, transmits continuously, the destination node, D, receives all the time, and the relay node, R, transmits and receives concurrently all the time. Thus the received signal at the relay can be given as

$$y_R = h_{SR}x_S + h_{RR}x_R + w_R, \tag{2.36}$$

where h_{RR} and h_{SR} denote the self-interference channel at the relay, and the channel between the source node and the relay, respectively. Moreover, the observed signal at the end node can be expressed as

$$y_R = h_{RD}x_R + w_D, \tag{2.37}$$

where h_{RD} represents the channel between the relay and the end node. Moreover, since the relay node operates in FD mode the source node in the FD-OWRC can transmit $(I-1)$ information

packets to the destination node in I time slots.

2.6.2 Full-Duplex Physical-Layer Network Coding

As was discussed in Section 2.4, the PLNC scheme has doubled the throughput of the traditional TWRC network. Nevertheless, the work in [87–91] has introduced an FD-PLNC system to further ameliorate the throughput of the TWRC network. In general, the FD-PLNC system consists of two FD end nodes, A and B, and one FD relay node as shown in Fig. 2.10. The end nodes in this system communicate with the help of the relay node. Due to the fact that all the nodes in this system operate in FD mode, i.e. transmit and receive simultaneously, both of the PLNC phases, i.e. MA and BC phase, occur in one time slot as depicted in Fig. 2.10. Thus, the end nodes A and B in the FD-PLNC scheme can exchange $2(I-1)$ packets in I time slots. In contrast, I information packets can be exchanged between the end nodes in I time slots in the conventional PLNC system.

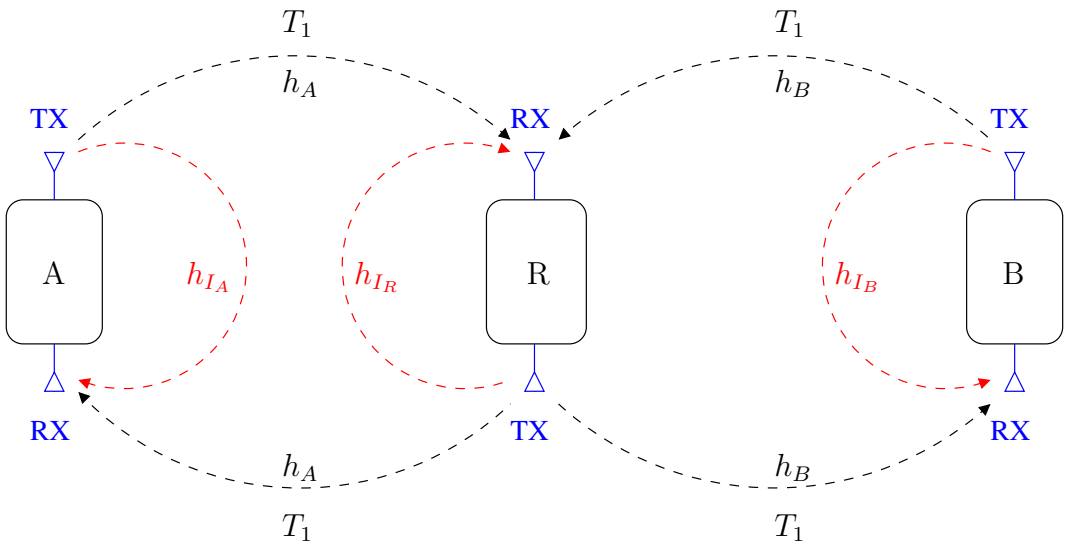

Figure 2.10: Full-duplex two-hop one-way relay channel network.

It can be noticed from Fig. 2.10 that all the nodes in this system will be affected by the self-interference (SI) signal that needs to be included in the description of the received signal at each node. Hence, The observed signal at the relay can be given as

$$y_R = h_A x_A + h_B x_B + h_{I_R} x_R + w_R, \tag{2.38}$$

where h_{I_R} is the self-interference channel at the relay. Moreover, the received signal at both of

the end nodes, A and B, can be expressed as

$$y_A = h_A x_R + h_{I_A} + w_A, \tag{2.39}$$

and

$$y_B = h_B x_R + h_{I_B} + w_B, \tag{2.40}$$

where h_{I_A} and h_{I_B} represent the SI channels at node A and B, respectively.

2.6.3 Full-Duplex Bi-Directional Wireless Communication System

The FD bi-directional (BD) wireless communication system consists of two transceiver nodes exchange information in FD mode as depicted in Fig. 2.11. A closer examination of Fig. 2.11

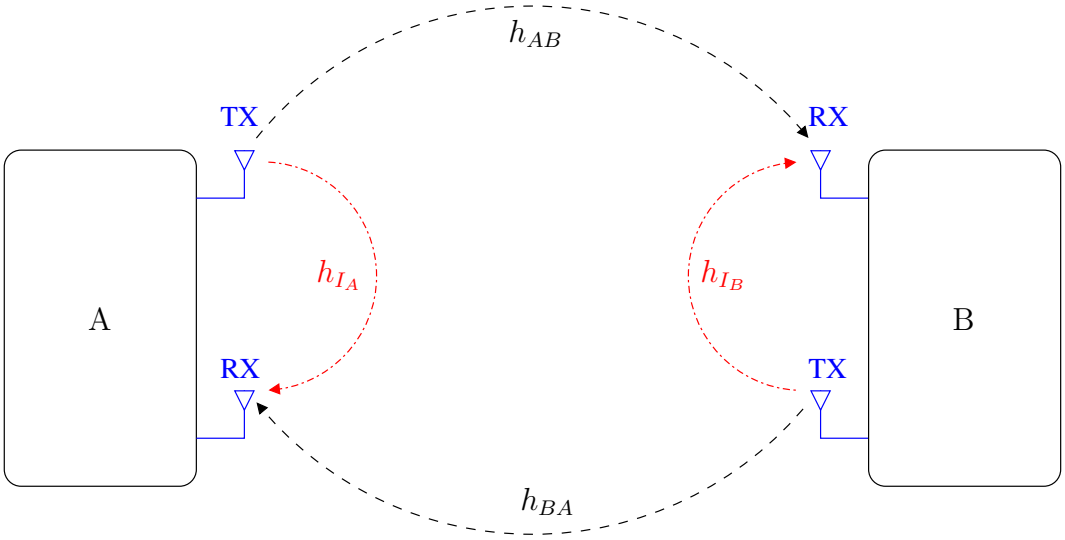

Figure 2.11: Full-duplex two-hop one-way relay channel network.

reveals that each node in the FD-BD system receives two signals, i.e. the signal from the far node and the SI signal. Therefore, the received signal at node A can be given as

$$y_A = h_{BA} x_B + h_{I_A} x_A + w_A, \tag{2.41}$$

while the observed signal at node B can written as

$$y_B = h_{AB} x_A + h_{I_B} x_B + w_B, \tag{2.42}$$

where h_{AB} and h_{BA} denote the channels between node A and B.

2.7 Self-Interference Cancellation Schemes

This section focuses on the most challenging problem that is associated with the FD mode, i.e. the SI signal. To thoroughly address this challenging issue, we consider the following example. Consider a wireless communication system in which the nodes transmit at 20 dBm, the power of the received signal of interest is -75 dBm and the noise floor is -90 dBm. Moreover, assume that all the nodes in the proposed system are equipped with two antennas dedicated for transmission and reception, respectively. This is a relatively low complexity approach and more practical solution to mitigate SI than using a single antenna. Furthermore, if we assume that the isolation between the local TX and RX antennas can result in a 40 dB SI signal suppression [9,92,93]. To this end, the SI signal power is 55 dB higher than that of the signal received from the far node and the gap between the SI signal at the input of the RX antenna and the noise floor is 70 dB (see Fig.2.12). As a result, the signal of interest will be swamped by the SI signal at the ADC due to the dynamic range limitation of the ADC. To protect the signal of interest from being lost

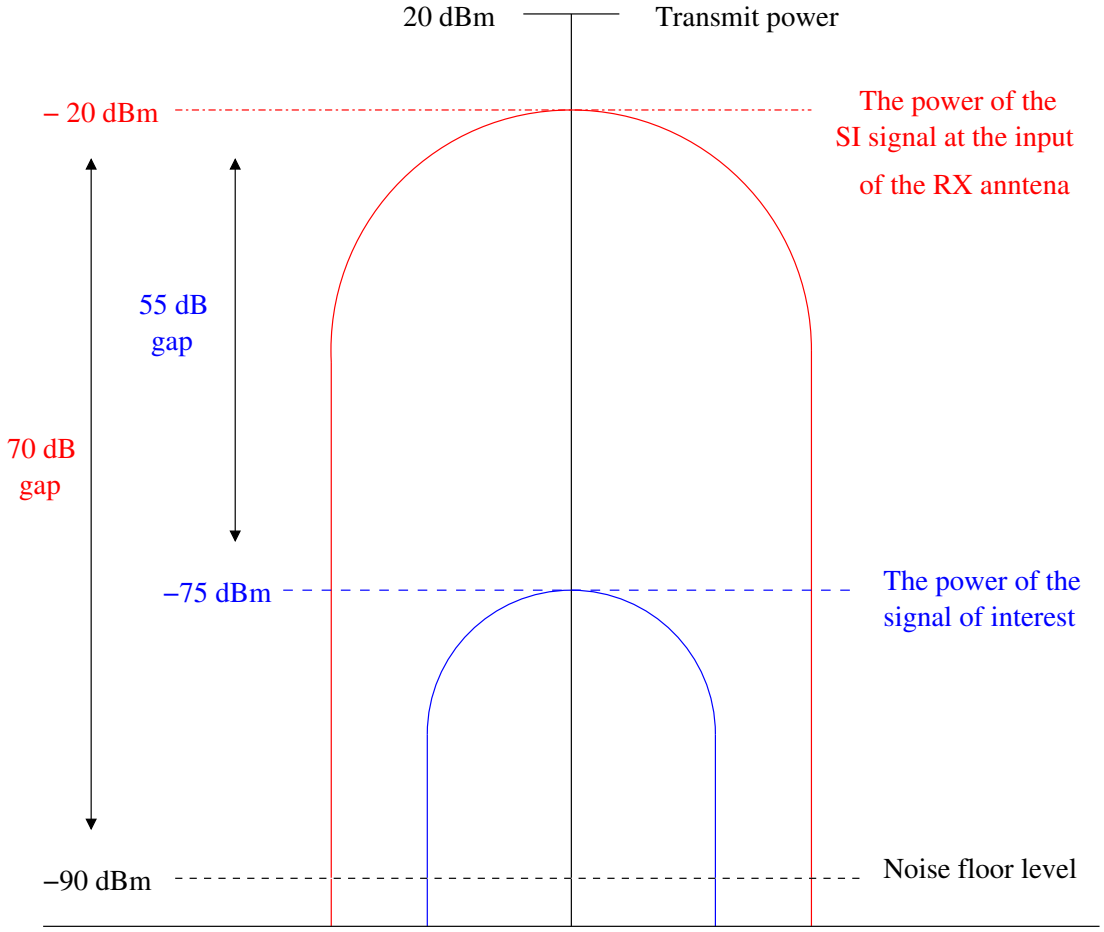

Figure 2.12: Illustration of the impact of the SI signal.

at the ADC and attain an SNR level approximately equal to that of the HD mode, the SI signal

should be effectively suppressed to the level of the noise floor, i.e. in the considered example, the SI signal should be suppressed by 70 dB, before the ADC. This has highlighted the need to an effective self-interference cancellation (SIC) scheme. Consequently, a number of different SIC techniques have been presented such as wireless-propagation domain SIC techniques, radio frequency (RF) domain mechanisms, analog domain and digital-domain techniques [85].

2.7.1 Passive Self-Interference Cancellation

This SIC technique was presented as a way to suppress the SI signal before it reaches the local receiver front-end. To attain this several approaches have been presented such as antenna separation, antenna cancellation, directional isolation, absorptive shielding, cross-polarization, and transmit beamforming [10, 94–98]. First, the antenna separation has been considered in [9, 10] to simply exploit the isolation that appears naturally due to the distance between the local transmit chain and receive chain antennas. Hence, increasing the distance between the local TX and RX antennas boosts the free-space path loss, which is given as [99]

$$L_S = \left(\frac{c}{4\pi f}\right)^2, \tag{2.43}$$

where $c = 3 \times 10^8$ is the speed of light in a vacuum, f is the transmitted signal frequency, and d is the distance between the TX and RX antennas. A closer inspection of (2.43) reveals that the path loss is inversely proportional to the distance between the TX and RX antennas. However, this approach is limited by the size of the transceiver node, i.e. the smaller the node the less the distance between the local TX and Rx antennas. Moreover, the amount of the path loss can be enhanced by placing an RF absorber material, which acts as a radiation shield, between the two antennas as depicted in Fig. 2.14. It is noteworthy that the key point behind using this RF absorber shield is to block the LOS path between the TX and RX antennas [88].

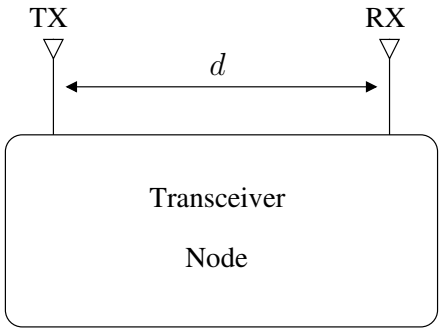

Figure 2.13: Full-duplex transceiver node with antenna separation.

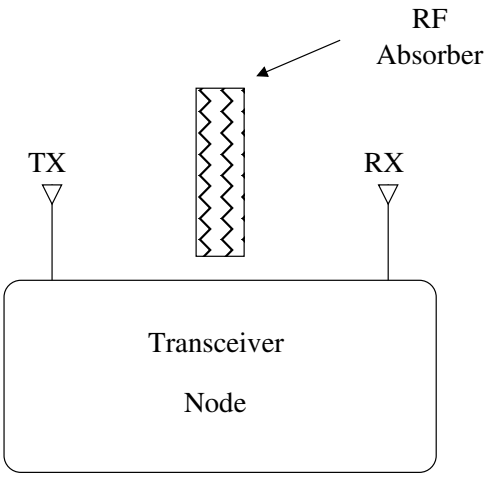

Figure 2.14: Full-duplex transceiver node with RF absorber.

Furthermore, utilizing 90° beamwidth antennas can improve the attained SI suppression in the wireless-propagation domain [10]. For example, using two 90° beamwidth antennas in the TX and RX chains that are pointed with 90° beam separation can minimize the overlap between the antennas coverage pattern as depicted in Fig. 2.15. Consequently, this TX-RX arrangement can mitigate the SI. Further improvement can be achieved by exploiting dual-

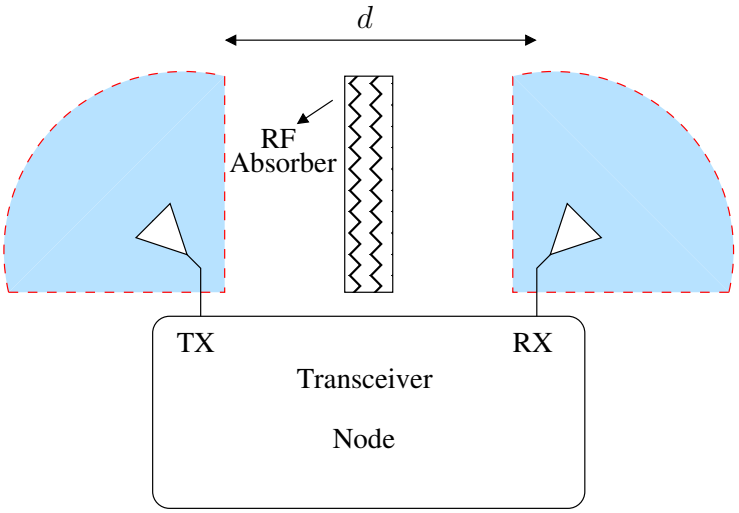

Figure 2.15: Full-duplex transceiver node 90° beamwidth antennas.

polarized antennas, which have two ports operate in an orthogonally polarized mode, to separate the TX and RX signal. This can be done by using these antennas in an orthogonally polarized mode in the TX and RX chains to minimize the self-interference. For example, a transceiver node can be designed to receive only horizontally polarized signal and transmit only vertically polarized signal to prevent the interference between the transmitted and received signals. The empirical results in [10] have demonstrated that combining these approaches as depicted in

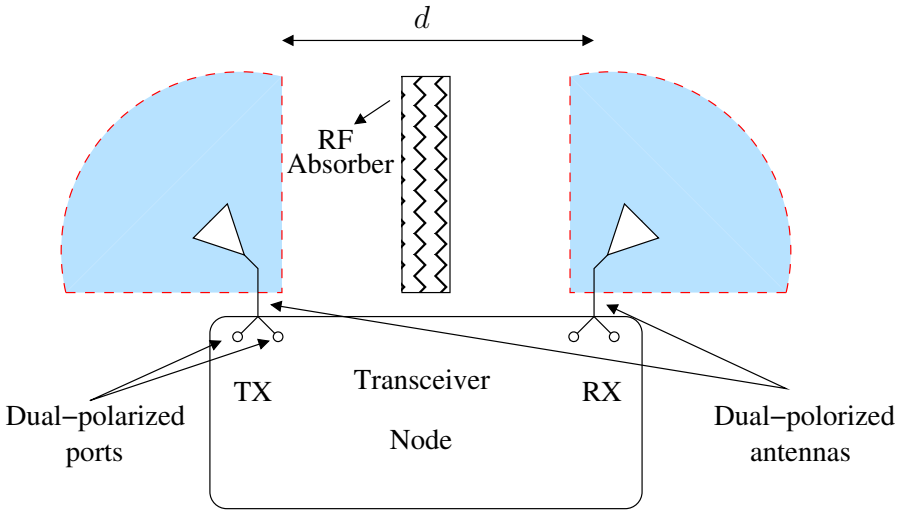

Figure 2.16: Full-duplex transceiver node with separated dual-polarized antennas and RF absorber.

Fig. 2.16 can achieve up to 73.8 dB of SI suppression.

Moreover, symmetric antenna cancellation technique was introduced in [94], which comprises RX and TX antenna cancellation schemes as depicted in Figs. 2.17 and 2.18, respectively. TThe RX antenna cancellation consists of one TX antenna and two RX antennas that are po-

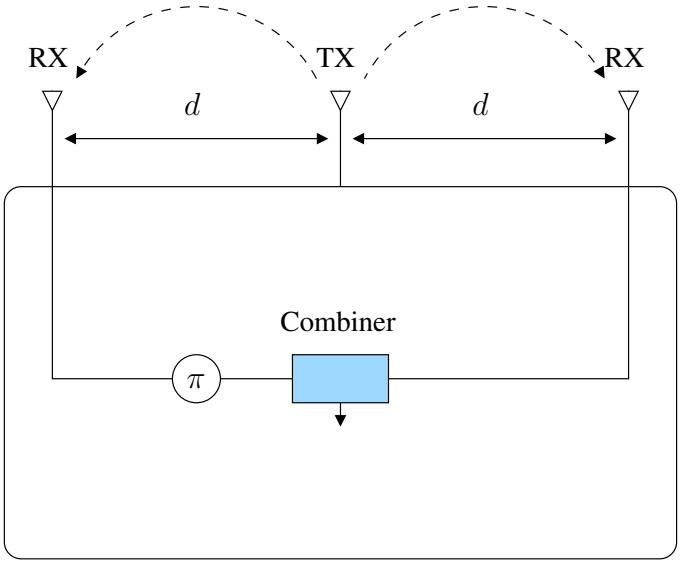

Figure 2.17: Receive antenna cancellation.

sitioned at a d distance from the TX antenna as illustrated in Fig. 2.17. Moreover, to diminish the SI signal, a fixed π phase shifter is exploited in this cancellation technique to phase shift the signal received by one of the RX, then the shifted signal is combined with the signal received by the other RX antenna. Ideally, this combination will result canceling out both of the signals. Analogous to the RX antenna cancellation, TX antenna cancellation scheme comprises one RX

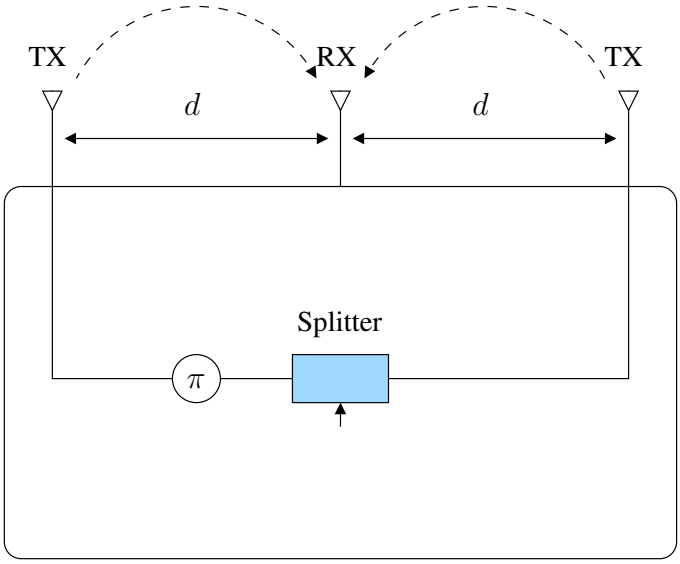

Figure 2.18: Transmit antenna cancellation.

antenna and two TX antennas as illustrated in Fig. 2.18. It can be observed from Fig. 2.18 that the signal to be transmitted is fed into a splitter, then one of the splitter's output signal is phase shifted by a fixed π phase shifter before being transmitted by one of the TX antennas, while the other output of the splitter is transmitted directly by the other TX antenna. However, this approach might have an impact on the quality of the signal received by the far node. In general, the passive SIC techniques can effectively suppress the SI signal. Yet, the attained SI suppression using the passive approaches depends on the surrounding environment and can be severely degraded by this environment. This has highlighted the need for active SIC techniques.

2.7.2 Active Self-Interference Cancellation

The concept of the active SIC has been proposed to exploit active signal processing techniques to sufficiently suppress the SI signal to the level of the noise floor. In general, this SIC approach can be performed before and after the downconverter in the analog domain and/or in the digital domain. The key idea of the active SIC approach is to exploit the transceiver node knowledge of its own transmitted signal to construct a replica of the SI signal and subtract this replica from the received signal in order to diminish the SI signal [9, 27, 100].

2.7.2.1 Analog Domain Self-Interference

Analog domain SIC techniques aim to perform the active SIC and suppress the SI signal before the received signal reaches the ADC [1, 7, 9, 27, 101]. This can be done by generating a copy of the SI signal and then combining this copy with total received signal before the ADC as

depicted in Fig. 2.19. A closer inspection of Fig. 2.19 shows that the received signal can be

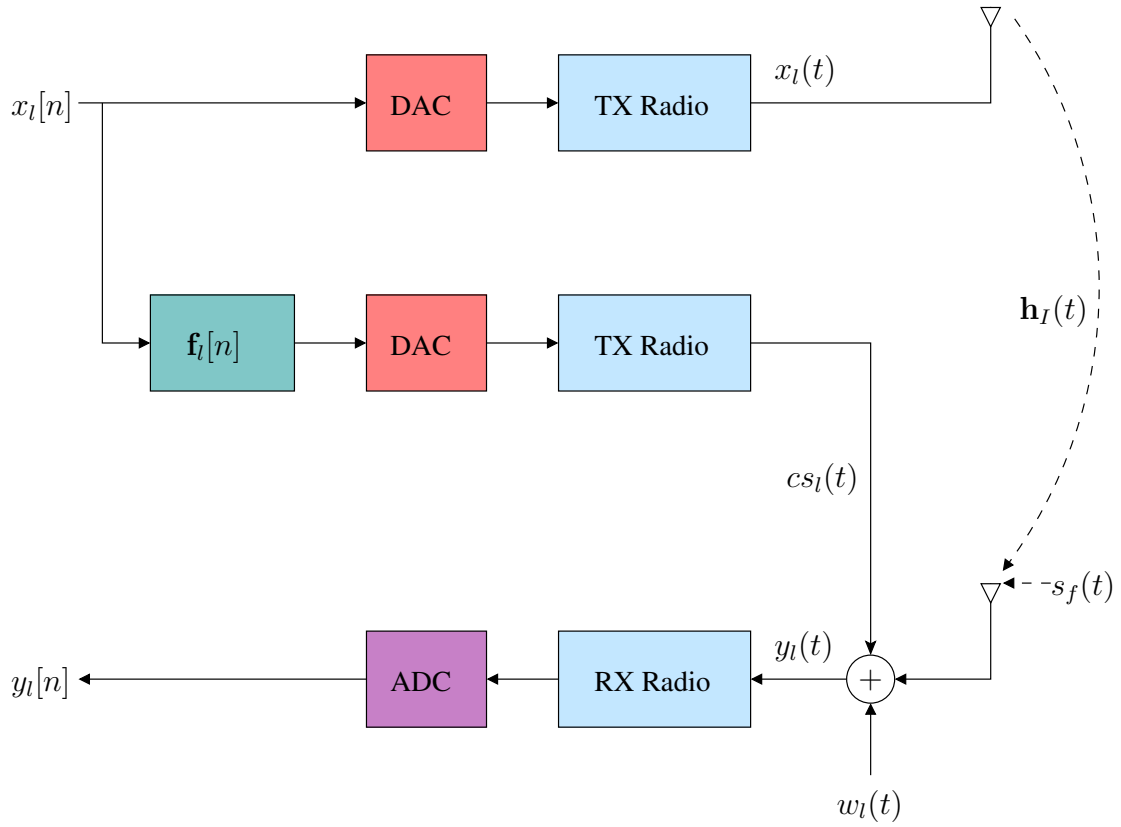

Figure 2.19: Full-duplex transceiver node with active analog self-interference cancellation.

given as

$$y_l[n] = s_f[n] + \mathbf{h}_I[n] * x_l[n] + \mathbf{f}_l[n] * x_l[n] + w_l[n], \tag{2.44}$$

where $*$ represents the convolution operation, $s_f[n]$ denotes the signal of interest from the far node, $x_l[n]$ indicates the local SI signal and $\mathbf{h}_I[n]$ is the self-interference multipath channel between the TX and RX antennas. It is noteworthy that due to the fact that the SI signal comprises the signal that propagates directly from the local TX antenna to the local RX antenna in addition to the signal components that are reflected from the surrounding environment, the self-interference channel is modelled as a multipath channel. Moreover, $\mathbf{f}_l[n]x_l[n]$ represents the self-interference cancellation term, in which $\mathbf{f}_l[n]$ denotes the filter that is used to construct a replica of the SI signal, while $w_l[n]$ is the AWGN term. Theoretically, to cancel the SI signal, the addition of the self-interference cancellation and SI terms should yield zero such that

$$\mathbf{h}_I[n] * x_l[n] + \mathbf{f}_l[n] * x_l[n] = 0. \tag{2.45}$$

It can be easily shown that to fulfil (2.45), $\mathbf{f}_l[n]$ should be given as

$$\mathbf{f}_l[n] = -\mathbf{h}_I[n]. \tag{2.46}$$

Consequently, the transceiver node should obtain $\mathbf{h}_I[n]$ using channel estimation. Thus, $\mathbf{f}_l[n]$ can be expressed as

$$\mathbf{f}_l[n] = -\hat{\mathbf{h}}_I[n], \tag{2.47}$$

where $\hat{\mathbf{h}}_I[n]$ denotes the estimated version of $\mathbf{h}_I[n]$. It is worth pointing out that the performance of this approach is limited by the precision of $\hat{\mathbf{h}}_I[n]$. Furthermore, obtaining the perfect channel state information (CSI) of $\mathbf{h}_I[n]$ is very challenging.

Moreover, an active RF SIC can be exploited to cancel the SI signal by creating a cancellation signal, $cs_l(t)$, in the RF domain [32, 35, 102–107] as depicted in Fig. 2.20. Then, this cancellation signal is injected at the front-end of the receiving chain resulting in effectively suppressing the SI signal before the ADC. It can be noticed from Fig. 2.20 that the output of the power amplifier (PA) is exploited as a reference input to the RF SIC, subsequently, all the transmit chain imperfections will be captured in the RF SIC reference signal. The received signal at the input of the local receive chain before injecting the cancellation signal can be given as

$$r_l(t) = s_f(t) + \mathbf{h}_I(t) * x_l(t) + w_l(t), \tag{2.48}$$

where $\mathbf{h}_I(t)$ is the multipath self-interference channel which can be modelled as

$$\mathbf{h}_I(t) = \sum_{i=0}^{L} h_{I_i}(t). \tag{2.49}$$

Moreover, the received signal after the RF SIC can be expressed as

$$y_l(t) = s_f(t) + \mathbf{h}_I(t) * x_l(t) - cs_l(t) + w_l(t). \tag{2.50}$$

Furthermore, the architecture of the RF self-interference cancellation that is used to construct $cs_l(t)$ is illustrated in Fig. 2.20. A closer look at Fig. 2.20 shows that $cs_l(t)$ can be expressed as

$$cs_l(t) = \sum_{i=0}^{L} f_{l_i} x_l(t - \tau_i), \tag{2.51}$$

where τ_i denotes the fixed delay of the i-th tap and f_{l_i} represents a complex-valued coefficient

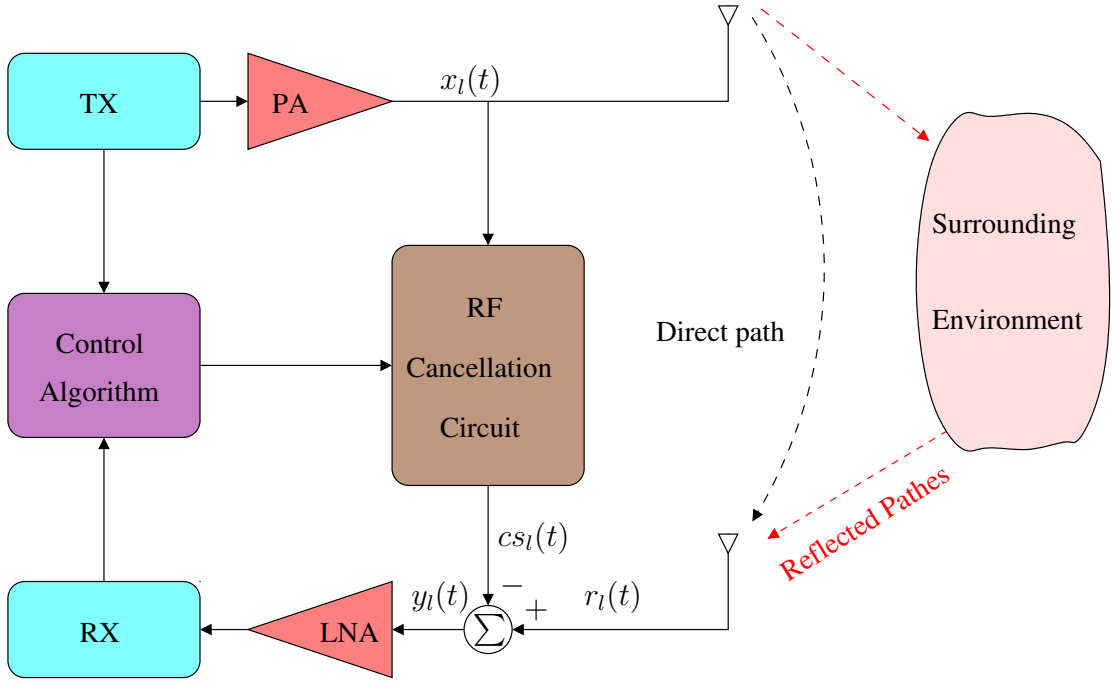

Figure 2.20: Full-duplex transceiver node with RF self-interference cancellation.

modelling the amplitude and phase of the i-th path. It is intuitive that in order to perfectly diminish the SI signal the constructed cancellation signal, $cs_l(t)$, should perfectly mimic the SI signal. To attain this an effective self-tuning technique is required to control the amplitudes and phases of the RF SIC scheme. The well-known least mean square algorithm was exploited in [104, 105] to minimize the difference between the SI signal and the output of the RF SIC by tuning the amplitudes and phases of the RF SIC scheme. The self-tuning operation of f_{l_i} is performed as follows

$$f_{l_i}(k+1) = f_{l_i}(k) + \mu \int x^*_{l_{IQ}}(t-\tau_i) y_{l_{IQ}(t)} dt, \tag{2.52}$$

where μ represents the tracking step-size, $x^*_{l_{IQ}}(t-\tau_i)$ and $y_{l_{IQ}(t)}$ denote the IQ demodulated baseband version of the delayed transmitted signal and the signal after the RF SIC, respectively. Moreover, (2.52) can be presented in terms of the IQ signals such that

$$f_{l_i,I}(k+1) = f_{l_i,I}(k) + \mu \int \left(x_{l_I}(t-\tau_i) y_{l_I(t)} + x_{l_Q}(t-\tau_i) y_{l_Q(t)} \right) dt, \tag{2.53}$$

$$f_{l_i,Q}(k+1) = f_{l_i,Q}(k) + \mu \int \left(x_{l_I}(t-\tau_i) y_{l_I(t)} - x_{l_Q}(t-\tau_i) y_{l_Q(t)} \right) dt. \tag{2.54}$$

It is worth mentioning that owing to the fact that the power level of SI signal is very high, the RF SIC alone is not sufficient to suppress the SI signal to the level of the noise floor [36, 108].

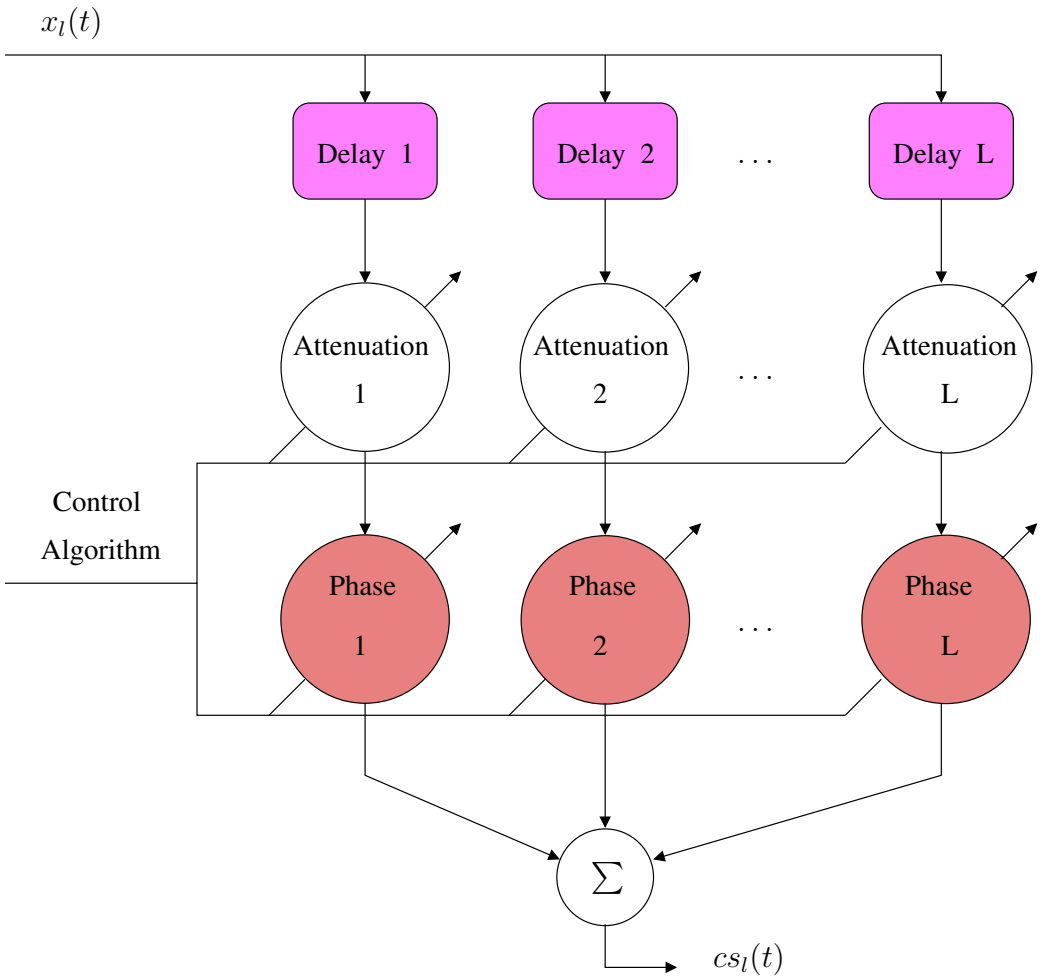

Figure 2.21: Simplified block diagram of the RF self-interference cancellation.

Consequently, the received signal after the RF SIC contains residual SI component [109]. This residual SI is further mitigated using various techniques in the digital domain [110].

2.7.2.2 Digital Self-Interference Cancellation

Several self-interference cancellation techniques that are implemented in the digital domain have been presented to diminish the residual SI and further improve the overall self-interference cancellation [11, 111, 112]. In general, the digital SIC is cascaded with the analog SIC and/or the RF SIC stages to suppress the residual SI after these stages to the level of the noise floor. Analogous to the analog SIC concept, the digital SIC composes a digital cancellation signal, which is an estimated copy of the actual SI signal and combines it with the received signal to cancel the residual SI as depicted in Fig. 2.22. It can be noticed form Fig. 2.22 that the received signal after applying the analog SIC can be expressed as

$$r_l[n] = s_f[n] + \mathbf{h}_I[n] * x_l[n] + \mathbf{f}_l[n] * x_l[n] + w_l[n]. \tag{2.55}$$

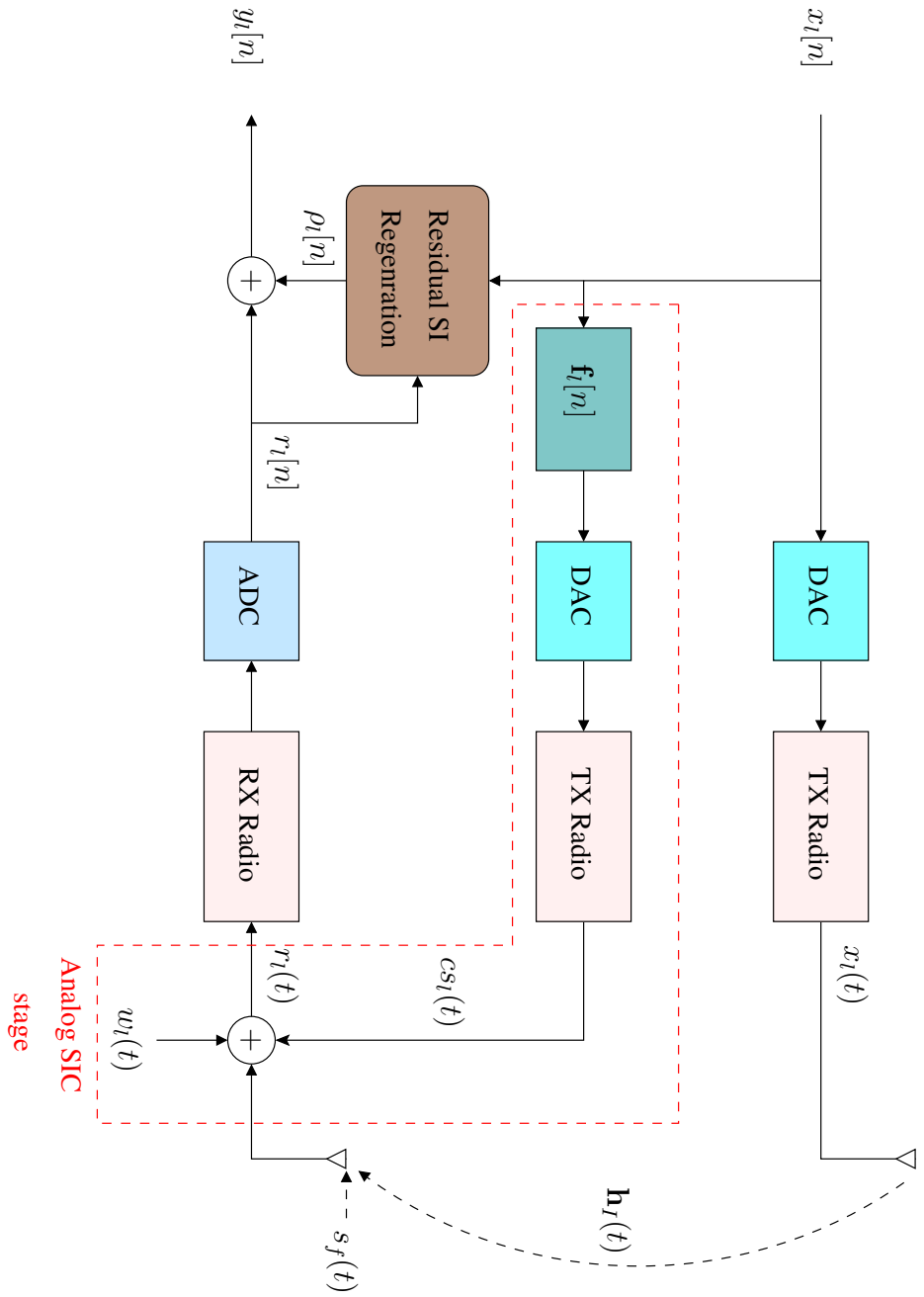

Figure 2.22: Full-duplex transceiver node with analog and digital self-interference cancellation.

The aim of the analog SIC is to cancel the SI signal such that

$$\mathbf{h}_I[n] * x_l[n] + \mathbf{f}_l[n] * x_l[n] = 0. \tag{2.56}$$

Ideally $\mathbf{f}_l(t)$ is given as

$$\mathbf{f}_l[n] = -\mathbf{h}_I[n], \tag{2.57}$$

However, in practice the perfect CSI of $\mathbf{h}_I[n]$ cannot be obtained due to AWGN and other distortions. Subsequently, the analog SIC cannot completely remove the SI signal. To tackle

this issue and further suppress the SI signal, the analog SIC is followed by a digital SIC satge as shown in Fig. 2.22.

The received signal after the analog and digital cancellation can be modelled as

$$y_l[n] = s_f[n] + \mathbf{h}_I[n] * x_l[n] + \mathbf{f}_l[n] * x_l[n] + \rho_l[n] + w_l[n], \tag{2.58}$$

where $\rho_l[n]$ denotes the digital cancellation signal. It has been shown in [9, 27] that this digital cancellation signal, i.e. $\rho_l[n]$, can be given as

$$\rho_l[n] = -\left(\mathbf{h}_I[n] * x_l[n] + \mathbf{f}_l[n] * x_l[n]\right). \tag{2.59}$$

Furthermore digital filters can be exploited in the transmitting and receiving chains at each node to suppress the SI signal as illustrated in Fig. 2.23. Different techniques can be used to

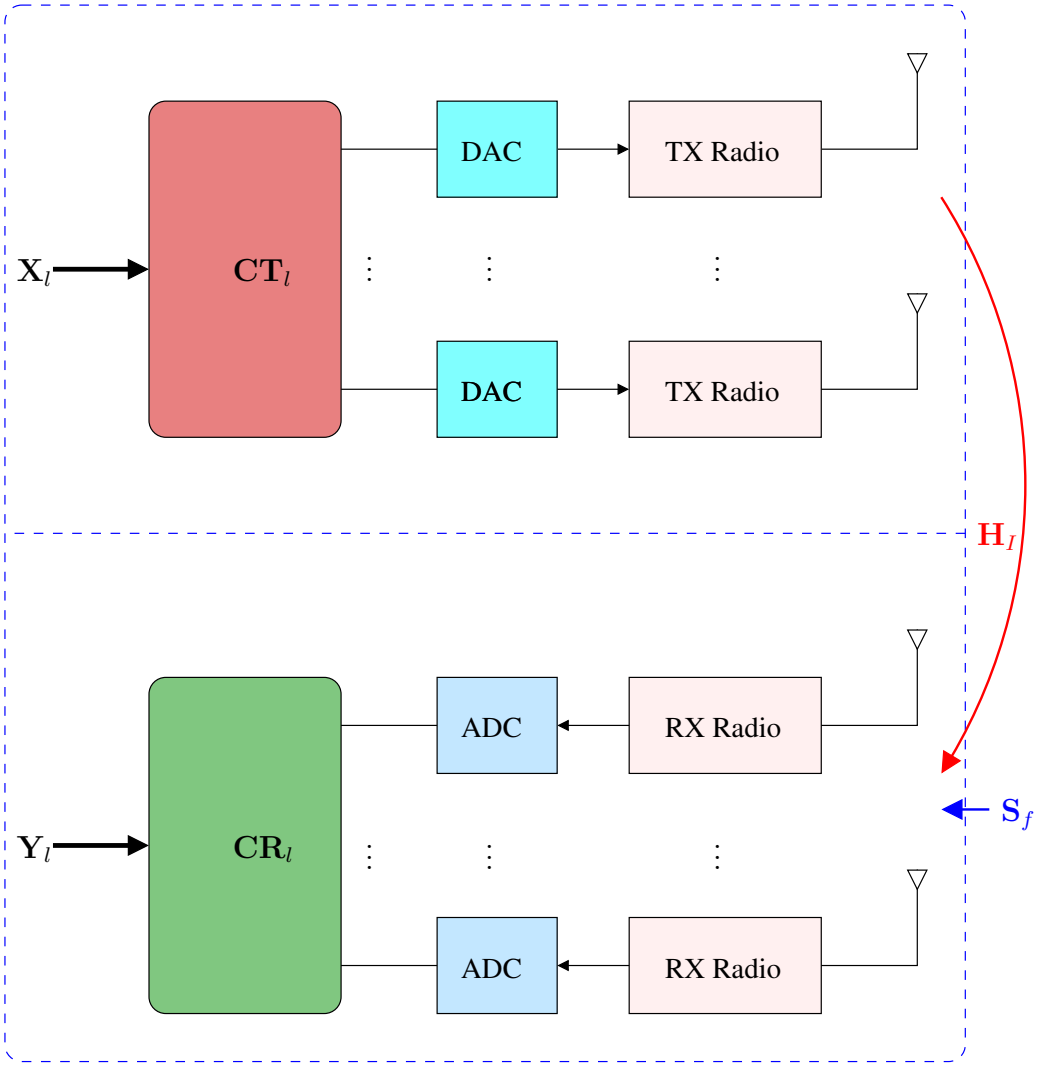

Figure 2.23: Full-duplex transceiver node with spatial self-interference cancellation.

construct these digital filters, i.e. $\mathbf{CT}_l$ and $\mathbf{CR}_l$, such as MMSE, null-space projection (NSP), and singular value decomposition (SVD) [97, 113, 114]. A closer look at Fig. 2.23 reveals that the SI signal can be modelled as

$$\mathbf{SI}_l = \mathbf{CT}_l \, \mathbf{H}_I \, \mathbf{CR}_l, \tag{2.60}$$

where $\mathbf{H}_I \in \mathbb{C}^{N_{rx} \times N_{tx}}$, $\mathbf{CT}_l \in \mathbb{C}^{N_{tx} \times 1}$ and $\mathbf{CR}_l \in \mathbb{C}^{1 \times N_{rx}}$ denote the self-interference channel, the transmitting chain filter and receiving chain filter, respectively. Moreover, N_{tx} and N_{rx} represent the number of transmit and receive antennas, respectively. The self-interference channel can be factorized using SVD to give

$$\mathbf{H}_I = \mathbf{U}_I \mathbf{\Sigma}_I \mathbf{V}_I^H, \tag{2.61}$$

where $\mathbf{U}_I \in \mathbb{C}^{N_{rx} \times N_{rx}}$ and $\mathbf{H}_I \in \mathbb{C}^{N_{tx} \times N_{tx}}$ are orthogonal matrices, i.e. $\mathbf{U}_I \mathbf{U}_I^H = \mathbf{I}$ and $\mathbf{V}_I \mathbf{V}_I^H = \mathbf{I}$, and $\mathbf{\Sigma}_I \in \mathbb{R}^{N_{rx} \times N_{tx}}$ is a diagonal matrix that comprises the self-interference channel eigenvalues. substituting (2.61) in (2.60) yields

$$\mathbf{SI}_l = \mathbf{CT}_l \, \mathbf{U}_I \mathbf{\Sigma}_I \mathbf{V}_I \, \mathbf{CR}_l. \tag{2.62}$$

The ultimate goal of utilizing the digital filters in the transmitting and receiving chains, i.e. $\mathbf{CT}_l$ and $\mathbf{CR}_l$, is to attain

$$\mathbf{SI}_l = \mathbf{CT}_l \, \mathbf{U}_I \mathbf{\Sigma}_I \mathbf{V}_I \, \mathbf{CR}_l = \mathbf{0}. \tag{2.63}$$

To fulfil this an NSP technique was presented in [115], in which the $\mathbf{CT}_l$ and $\mathbf{CR}_l$ are given such that

$$\mathbf{CT}_l = \mathbf{V}_I \boldsymbol{\Xi}_I, \tag{2.64}$$

and

$$\mathbf{CR}_l = \mathbf{T}_I \mathbf{U}_I^H, \tag{2.65}$$

where Ξ_I and $\mathbf{T}_I$ denote binary row and column matrices, respectively, which satisfy $\boldsymbol{\Xi}_I^T \boldsymbol{\Xi}_I = \mathbf{I}$, $\mathbf{T}_I \mathbf{T}_I^T = \mathbf{I}$ and $\mathbf{T}_I \Xi_I = \mathbf{0}$. Substituting 2.64 and 2.65 in 2.62 yields

$$\mathbf{SI}_l = \mathbf{T}_I \mathbf{\Sigma}_I \boldsymbol{\Xi}_I, \tag{2.66}$$

which meets the aim of the SIC mechanism.

2.8 Chapter Summary

In this chapter, the background theory of the evolution of the 5G communication networks has been presented. In particular, 5G systems requirements and challenges have been discussed in this chapter. Then, cooperative communication networks, i.e. OWRC and TWRC, and their ability to meet the 5G system requirements have been investigated. Next, the PLNC scheme was presented as a solution to enhance the throughput and the spectral efficiency of the cooperative networks. Moreover, the FD communication mode has been discussed as a promising technique to attain the capacity requirements of 5G communication systems and enhance the spectral efficiency of the traditional HD networks. The challenges that are associated with the FD mode such as SI signal have been addressed. Furthermore, different SIC techniques that are used to suppress the SI signal and enable the FD mode of communication have been discussed and presented. In particular, passive and active SIC schemes have been discussed. Finally, the performance limitations of each SIC technique have been investigated.

Chapter 3

AF Full-Duplex Physical-Layer Network Coding System Utilizing Active Self-Interference Cancellation

3.1 Introduction

The physical-layer network coding (PLNC) system has been the center of the research interest due to its ability to improve the throughput of a two-way relay channel (TWRC) network [73]. In essence, a PLNC system consists of two end nodes, denoted A and B, which communicate with the assistance of one relay node R. The relay facilitate the communication between the end nodes using three different relaying schemes, i.e. amplify-and-forward (AF), decode-and-forward (DF) and denoise-and-forward (DNF) [77]. In this chapter, we consider AF relaying scheme, whose transmission schedule comprises two phases, i.e. multiple access (MA) phase, and broadcast (BC) phase. During the MA phase, the end nodes transmit their data concurrently to the relay; in contrast, during the BC phase, the relay broadcasts a scaled version of the signal received in the MA phase to both of the end nodes [116]. Moreover, due to the 5G systems throughput requirements, the full-duplex (FD) mode has been combined with PLNC systems to further improve the throughput of the TWRC networks. In this chapter, we present a TWRC network that utilizes an FD-PLNC scheme in conjunction with AF relaying technique and orthogonal frequency-division multiplexing (OFDM) scheme. Moreover, this chapter investigates the performance of the proposed AF-FD-PLNC system over reciprocal, asymmetric, and frequency-selective Rayleigh fading channels. Furthermore, in order to cope with the self-interference (SI) induced by the FD mode of operation, an active self-interference cancellation

(SIC) scheme is utilized at each transceiver node in the proposed system.

The performance of the proposed system is thoroughly investigated in the presence of residual SI by deriving a closed-form expression for the distribution of the tight upper bound end-to-end (E2E) signal-to-interference-and-noise ratio (SINR). Moreover, an E2E outage probability expression of the proposed system is derived and presented in this chapter. Next, a closed-form expression of the E2E tight lower bound average symbol error rate for the AF-FD-PLNC is derived in this chapter. Furthermore, an exact expression for the tight upper bound ergodic capacity is derived and used to evaluate the E2E upper bound ergodic capacity of the proposed AF-FD-PLNC system. All the derived theoretical expressions are validated using extensive simulation studies. The results of this chapter confirm the feasibility of the proposed AF-FD-PLNC and its capability to double the throughput of conventional amplify-and-forward half-duplex physical-layer network coding (AF-HD-PLNC).

The rest of the chapter is organized as follows: Section 3.1 presents the design of the proposed AF-FD-PLNC system. Section 3.3 introduces the architecture of the active SIC scheme. Section 3.4 presents the E2E SINR of the AF-FD-PLNC. Moreover, the statistical analysis of the E2E SINR is derived in Section 3.5. Section 3.6 presents the Performance evaluation metrics of the proposed system. Section 3.7 presents the results, and finally, Section 3.8 presents the chapter summary.

3.2 The Design of the Amplify-and-Forward Full-Duplex Physical-Layer Network Coding System

This section presents the OFDM-based AF-FD-PLNC system. Consider an uncoded TWRC network with three nodes, two FD end nodes, A and B, and one FD relay node, R. We assume that there is no direct path connecting the end nodes due to the deep fading. Therefore, the end nodes communicate with the aid of the node R as depicted in Fig. 3.1. It is worth pointing out that in this work we assume that the distances between both of the end nodes and the relay node are equal. Due to the fact that all the nodes in the proposed AF-FD-PLNC can transmit and receive simultaneously, the end nodes can exchange up to $2(I-1)$ packets in I time slots, while the end nodes in AF-HD-PLNC system can exchange I information packets in I time slots.

A closer look at Fig. 3.1 reveals that there are two types of channels in the proposed system; the channels between the nodes' own TX and RX antennas, and the channels between the end nodes and the relay. These channels are assumed to be quasi-static asymmet-

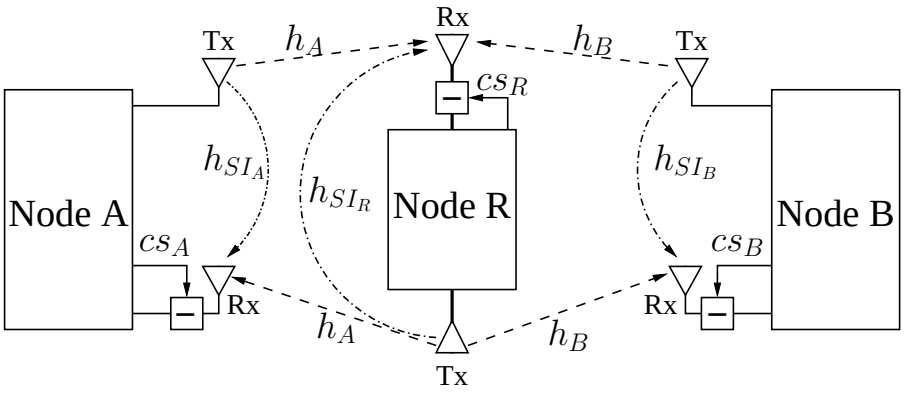

Figure 3.1: Full-duplex physical_layer network coding (FD-PLNC) system.

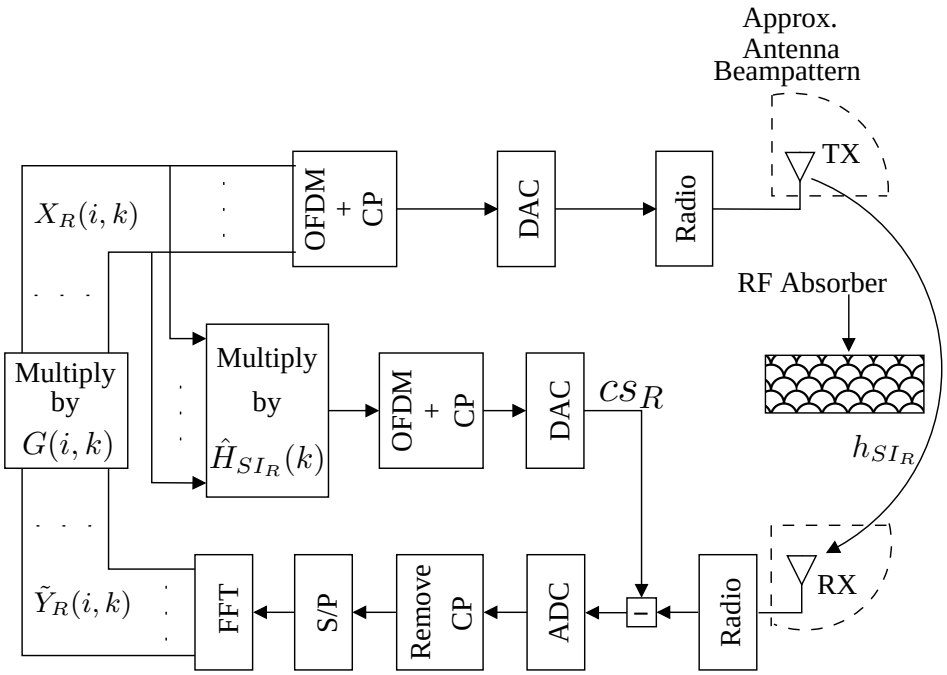

Figure 3.2: Architecture of OFDM-based AF full-duplex PLNC relay node combined with active self-interference cancellation scheme.

ric and reciprocal Rayleigh-fading channels. Since all the channels are frequency-selective, the OFDM scheme is applied at each node to cope with the intersymbol interference (ISI) induced by these channels. The cyclic prefix (CP) length in the proposed system is chosen such that $L_{CP} \geqslant \max\{L_A, L_B, L_{SI_J}\}$, where, L_A and L_B represent the excess delay spreads of the multipath channels, $\mathbf{h}_A$ and $\mathbf{h}_B$, between the end nodes, A and B, and the relay nod. $L_{SI_J} \in \{L_{SI_A}, L_{SI_B}, L_{SI_R}\}$, represents the set of excess delay spreads of the self-interference channels.

After removing the CP and performing the fast Fourier transform (FFT) demodulation, the received signal at the relay node is given as

$$Y_R(i,k) = X_A(i,k)H_A(k) + X_B(i,k)H_B(k) + X_R(i,k)H_{SI_R}(k) + W_R(k), \tag{3.1}$$

while the received signal at the end nodes is given as

$$Y_D(i,k) = X_R(i,k)H_D(k) + X_D(i,k)H_{SI_D}(k) + W_D(k), \tag{3.2}$$

where $D \in \{A, B\}$, X_A, X_B and X_R are the transmitted signals from nodes A, B and R, respectively, W_D and W_R represent the AWGN samples at each node following a complex-valued circular Gaussian distribution, whose PDFs are $\mathcal{CN}(0, N_0^D)$ and $\mathcal{CN}(0, N_0^R)$, respectively. Furthermore, $H_A(k)$ and $H_B(k)$ denote the frequency responses of the multipath channels between node A and R, and B and R, respectively, while H_{SI_A}, H_{SI_B} and H_{SI_R} represent the self-interference channels between the TX and RX antennas at each node. Finally, $k = 1, 2, \ldots, K$ and $i = 1, 2, \ldots, I$ denote the subcarrier and the time slot indices, respectively. As illustrated in Fig. 3.2 the transmitted signal from node R, X_R, is obtained by multiplying the received superimposed signal by an amplification factor G, subsequently, the received signal at the end nodes can be written as

$$\begin{aligned} Y_D(i,k) =& G(i,k)Y_R(i-1,k)H_D(k) + X_D(i,k)H_{SI_D}(k) \\ &+ W_D(k). \end{aligned} \tag{3.3}$$

The amplification factor is given as

$$G(i,k) = \sqrt{\frac{E_{b_R}}{E_{b_A}|H_A(k)|^2 + E_{b_B}|H_B(k)|^2 + \sigma_{SI_R}^2 E_{b_R} + N_0^R}}, \tag{3.4}$$

where E_{b_A}, E_{b_B} and E_{b_R} are the average transmitted bit energies, respectively, whilst the product $\sigma_{SI_R}^2 E_{b_R}$ denotes the power of the residual SI.

The end nodes utilize a maximum-likelihood (ML) detector to extract the data transmitted by the other node from the received signal as depicted in Fig. 3.3. This operation is performed by the end nodes, A and B, by exploiting the perfect knowledge of their transmitted signal during the previous time slot, $X_D(i-1)$, to obtain the ML estimate of the signal transmitted by the other end node as follows

$$\hat{X}_B(i-1,k) = \underset{(q)\in\mathbb{Z}_M}{\operatorname{argmin}} \mid Y_{A(i,k)} - G(i,k)H_A(k) \times (H_A(k)X_A(i-1,k) + H_B(k)\mathcal{C}(q)) \mid^2, \tag{3.5}$$

$$\hat{X}_A(i-1,k) = \underset{(q)\in\mathbb{Z}_M}{\operatorname{argmin}} \mid Y_{B(i,k)} - G(i,k)H_B(k) \times (H_A(k)\mathcal{C}(q)) + H_B(k)X_B(i-1,k)) \mid^2, \tag{3.6}$$

where $\mathcal{C}$ represents the constellation mapper.

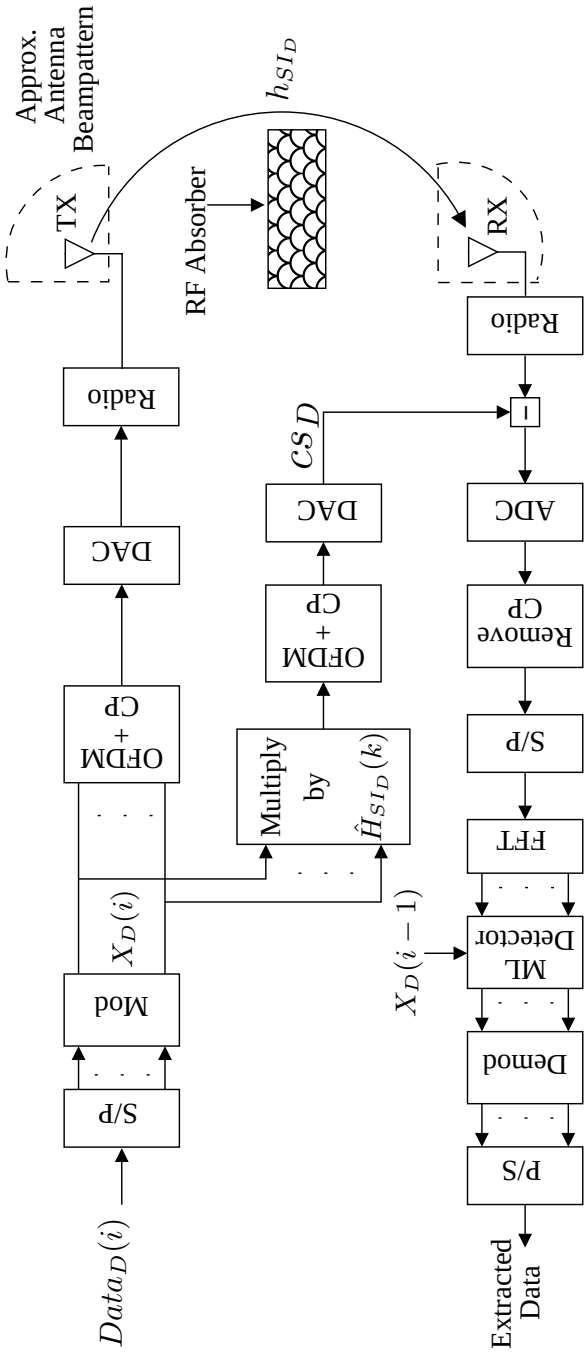

Figure 3.3: Architecture of OFDM-based full-duplex PLNC end node combined with active self-interference cancellation scheme.

3.3 Active Self-Interference Cancellation

This section presents the architecture of the OFDM based AF-FD-PLNC system, which is combined with an active SIC scheme. As depicted in Figs. 3.2 and 3.3, each transceiver node in the proposed system contains two 90° beamwidth antennas, which are pointed with 90° beam separation to minimize the overlap in the coverage patterns, and RF absorptive shielding, which is placed between the TX and RX antennas, to block the line-of-sight (LOS) path present in this

transmission link, and to attenuate the SI signal. Moreover, each transceiver node comprises one transmit and one receive chain in addition to an extra circuitry dedicated to generate the canceller signal (CS), which is generated using the node's perfect knowledge of its own transmitted signal. This CS signal is subtracted from the received signal in the waveform domain (time-domain IF) to minimize the effect of the SI signal before the analog-to-digital converter (ADC). The CS signal is given in the frequency domain as

$$CS_J(i,k) = \hat{H}_{SI_J}(k) X_J(i,k). \tag{3.7}$$

where $J \in \{A, B, R\}$, $\hat{H}_{SI_J}$ represents the estimated version of H_{SI_J}, for $k = 1, 2, ..., K$. H_{SI_J} denotes the frequency response of the SI channel, which is given as

$$H_{SI_J} \;\; = \;\; \hat{H}_{SI_J} + \xi_{SI_J}, \tag{3.8}$$

where ξ_{SI_J} is the uncorrelated channel estimation error exhibiting a complex Gaussian distribution, i.e., $\mathcal{CN}(0, \sigma^2_{\xi_{SI_J}})$.

The received signal at the relay node after the active SIC is given as

$$\begin{aligned}\tilde{Y}_R(i,k) =& \Big(H_{SI_R}(k) - \hat{H}_{SI_R}(k) \Big) X_R(i,k) + X_A(i,k) H_A(k) \\ &+ X_B(i,k) H_B(k) + W_R(k),\end{aligned} \tag{3.9}$$

while the received signal at the end nodes after the active SIC is given as

$$\begin{aligned}\tilde{Y}_D(i,k) =& \Big(H_{SI_D}(k) - \hat{H}_{SI_D}(k) \Big) X_D(i,k) + G(i,k) \tilde{Y}_R(i-1,k) H_D(k) \\ &+ W_D(k).\end{aligned} \tag{3.10}$$

A further inspection of (3.9) and (3.10) reveals that the SI can be entirely eliminated if the perfect channel state information (CSI) of H_{SI_J} is available. It is noteworthy that the error of the self-interference channel estimation, which results from the AWGN, is expected to be very small as the power of the SI signal is much larger the power of the AWGN. Thus, the residual SI is also expected to be rather small. Moreover, (3.9) and (3.10) can be simplified by using (3.8) to substitute H_{SI_J} followed by replacing the residual SI terms by $SI_J(k) X_J(i,k)$, subsequently, (3.9) and (3.10) can be written as

$$\tilde{Y}_R(i,k) = X_A(i,k) H_A(k) + X_B(i,k) H_B(k) + SI_R(k) x_R(i,k) + W_R(k). \tag{3.11}$$

$$\tilde{Y}_D(i,k) = G(i,k)\tilde{Y}_R(i-1,k)H_D(k) + SI_D(k)X_D(i,k) + W_D(k). \tag{3.12}$$

where SI_J is modelled using a zero-mean complex Gaussian PDF, i.e. $\mathcal{CN}(0, \sigma^2_{SI_J})$ [117, 118].

3.4 The End-to-End Signal-to-Interference-and-Noise Ratio (SINR)

The examination of (3.12) shows that the first term is the desired term, and the rest are unwanted interference and noise terms. Subsequently, the E2E SINR can be given as

$$\gamma_{E2E} = \frac{\gamma_R \gamma_D}{\gamma_R + \gamma_D + 1}, \tag{3.13}$$

where γ_R is the SINR at the relay node and is given as

$$\gamma_R = \frac{\Lambda_R(|H_A|^2 + |H_B|^2)}{\Lambda_{IR} + 1}, \tag{3.14}$$

while, γ_D represents the SINR at the end nodes and can be expressed as

$$\gamma_D = \frac{\Lambda_D |H_D|^2}{\Lambda_{ID} + 1}. \tag{3.15}$$

Moreover, $\Lambda_D = \frac{E_{b_R}}{N_0^D}$ and $\Lambda_R = \frac{E_{b_D}}{N_0^R}$, are constants denoting the signal to noise ratio (SNR) at the end nodes and the relay, respectively, while Λ_{I_D} and Λ_{I_R}, are random variables representing the interference to noise ratio (INR) at the end nodes and the relay, respectively, which are given as $\Lambda_{I_D} = \frac{\sigma^2_{SI_D} E_{b_D}}{N_0^D}$, $\Lambda_{I_R} = \frac{\sigma^2_{SI_R} E_{b_R}}{N_0^R}$. Further inspection of (3.14) and (3.15) reveals that they can be given as the ratio of two random variables. Therefore, the SINR at the relay node is given

$$\gamma_R = \frac{\omega_R}{\psi_R + 1}, \tag{3.16}$$

in contrast, at the end nodes the SINR is given as

$$\gamma_D = \frac{\omega_D}{\psi_D + 1}, \tag{3.17}$$

where $\omega_D = \Lambda_D |H_D|^2$ and $\omega_R = \Lambda_R(|H_A|^2 + |H_B|^2)$ denote the SNR terms at the end nodes and the relay, respectively, while $\psi_D = \Lambda_{ID}$ and $\psi_R = \Lambda_{IR}$ represent the INR terms at the end nodes and the relay, respectively.

It is worth pointing out that using the exact E2E, i.e. (3.13), in the analytical studies is mathematically challenging. Thus, to evaluate the PDF of the E2E SINR, we exploit the tight upper bound of the E2E SINR that was presented in [119] as

$$\gamma_{E2E} \leqq \gamma_{E2E_{up}} = \min(\gamma_R, \gamma_D), \tag{3.18}$$

where γ_R and γ_D are assumed to be independent.

3.5 Statistical Analysis of the SINR

3.5.1 Probability Density Function (PDF) of the Tight Upper Bound of the End-to-End (E2E) SINR

The PDF of the tight upper bound of the E2E SINR for the proposed AF-FD-PLNC system is given as [119]

$$p_{\gamma_{E2E_{up}}}(\gamma) = p_{\gamma_R}(\gamma) + p_{\gamma_D}(\gamma) - \left[p_{\gamma_R}(\gamma)P_{\gamma_D}(\gamma) + p_{\gamma_D}(\gamma)P_{\gamma_R}(\gamma)\right], \tag{3.19}$$

where $p_{\gamma_R}(\gamma)$ and $p_{\gamma_D}(\gamma)$ represent the PDF of the SINR at the relay and the end nodes, respectively, whilst $P_{\gamma_R}(\gamma)$ and $P_{\gamma_D}(\gamma)$ are the CDF of the SINR at the relay and the end nodes, respectively. Since all the channels are assumed to be Rayleigh fading and the residual SI follow a complex Gaussian distribution distributions [91, 120, 121], these random variables, i.e. ω_R, ψ_R, ω_D and ψ_D follow a Gamma distribution. Thus, PDF of these random variables can be expressed as

$$p_{\omega_R}(\omega_R) = \frac{\omega_R}{{\varepsilon_R}^2} e^{-\frac{\omega_R}{\varepsilon_R}}, \tag{3.20}$$

$$p_{\omega_D}(\omega_D) = \frac{e^{-\frac{\omega_D}{\varepsilon_D}}}{\varepsilon_D}, \tag{3.21}$$

$$p_{\psi_J}(\psi_J) = \frac{e^{-\frac{\psi_J}{\varsigma_J}}}{\varsigma_J}, \tag{3.22}$$

where $\varepsilon_R = \frac{1}{2}E\{\omega_R\}$, $\varepsilon_D = E\{\omega_D\}$ and $\varsigma_J = E\{\psi_J\}$ for $J \in \{A, B, R\}$, whilst $D \in \{A, B\}$. Furthermore, as the SINR at the relay and end nodes consists of the ratio of two independent random variables, the PDF of these SINRs can be evaluated using the result [122, Eq. (4.6)],

which is given as

$$p_{\gamma_J}(\gamma) = \int_0^\infty (1+\psi_J) p_{\omega_J}\big((1+\psi_J)\gamma\big) p_{\psi_J}(\psi_J) d\psi_J. \tag{3.23}$$

Hence, the PDF of the SINR at the relay can be computed by using (3.20) and (4.30) to substitute $p_{\omega_J}(\omega_J)$ and $p_{\psi_J}(\psi_J)$ in (3.23), which results in

$$p_{\gamma_R}(\gamma) = \frac{\gamma e^{-\frac{\gamma}{\varepsilon_R}}}{{\varepsilon_R}^2 \varsigma_R} \int_0^\infty (1+\psi_R)^2 e^{-\frac{\gamma\varsigma_R+\varepsilon_R}{\varepsilon_R\varsigma_R}\psi_R} d\psi_R. \tag{3.24}$$

This integral can be solved by exploiting the results of $\int_{x=0}^{\infty} x^n e^{-\mu x} dx = n!\mu^{-n-1}$ for $[\mathbf{Re}\ \mu > 0]$ [123, Eq. (3.351.3)] to give

$$p_{\gamma_R}(\gamma) = \frac{\gamma e^{-\frac{\gamma}{\varepsilon_R}}}{\varepsilon_R^2 \varsigma_R} \left[\frac{\varepsilon_R\varsigma_R}{\gamma\varsigma_R + \varepsilon_R} + 2\left(\frac{\varepsilon_R\varsigma_R}{\gamma\varsigma_R + \varepsilon_R}\right)^2 + 2\left(\frac{\varepsilon_R\varsigma_R}{\gamma\varsigma_R + \varepsilon_R}\right)^3 \right]. \tag{3.25}$$

Moreover, the PDF of the SINR at the end nodes can be evaluated using (3.21) and (4.30) to substitute $p_{\omega_J}(\omega_J)$ and $p_{\psi_J}(\psi_J)$ in (3.23), which yields

$$p_{\gamma_D}(\gamma) = \frac{e^{-\frac{\gamma}{\varepsilon_D}}}{\varepsilon_D \varsigma_D} \int_0^\infty (1+\psi) e^{-\frac{\gamma\varsigma_D+\varepsilon_D}{\varepsilon_D\varsigma_D}\psi} d\psi_D. \tag{3.26}$$

Using the result of $\int_{x=0}^{\infty} x^n e^{-\mu x} dx = n!\mu^{-n-1}$ for $[\mathbf{Re}\ \mu > 0]$ [123, Eq. (3.351.3)] to solve (3.26) results in the PDF of the SINR at the end nodes, which is given as

$$p_{\gamma_D}(\gamma) = \frac{e^{-\frac{\gamma}{\varepsilon_D}}}{\varepsilon_D \varsigma_D} \left[\frac{\varepsilon_D\varsigma_D}{\gamma\varsigma_D + \varepsilon_D} + \left(\frac{\varepsilon_D\varsigma_D}{\gamma\varsigma_D + \varepsilon_D}\right)^2 \right]. \tag{3.27}$$

On the other hand, the CDF of the SINR can be computed using [122, Eq. (4.5)] as

$$P_{\gamma_J}(\gamma) = \int_0^\infty P_{\omega_J}\big((1+\psi_J)\gamma\big) p_{\psi_J}(\psi_J) d\psi_J, \tag{3.28}$$

where, the CDF of ω_R, i.e. $P_{\omega_R}(\omega_J)$, is given as

$$P_{\omega_R}(\omega_R) = 1 - e^{-\frac{\omega_R}{\varepsilon_R}} \left(1 + \frac{\omega_R}{\varepsilon_R}\right), \tag{3.29}$$

while the CDF of ω_D is expressed as

$$P_{\omega_D}(\omega_D) = 1 - e^{-\frac{\omega_D}{\varepsilon_D}}. \tag{3.30}$$

Using (3.22) and (3.29) to substitute $p_{\psi_J}(\psi_J)$ and $P_{\omega_J}(\omega_J)$ in (3.28), respectively, results in the CDF of the SINR at the relay node, which is given as

$$P_{\gamma_R}(\gamma) = \int_0^\infty \frac{1}{\varsigma_R} e^{-\frac{\psi_R}{\varsigma_R}} d\psi_R - \frac{e^{-\frac{\gamma}{\varepsilon_R}}}{\varsigma_R} \int_0^\infty e^{-\frac{\varepsilon_R+\gamma\varsigma_R}{\varepsilon_R\varsigma_R}\psi_R} d\psi_R - \frac{\gamma e^{-\frac{\gamma}{\varepsilon_R}}}{\varepsilon_R\varsigma_R} \int_0^\infty e^{-\frac{\varepsilon_R+\gamma\varsigma_R}{\varepsilon_R\varsigma_R}\psi_R} d\psi_R - \frac{\gamma e^{-\frac{\gamma}{\varepsilon_R}}}{\varepsilon_R\varsigma_R} \times \int_0^\infty \psi_R e^{-\frac{\varepsilon_R+\gamma\varsigma_R}{\varepsilon_R\varsigma_R}\psi_R} d\psi_R. \tag{3.31}$$

Thus, the CDF of the SINR at the relay can be obtained by solving these integrals using [123, Eq. (3.351.3)], which yields

$$P_{\gamma_R}(\gamma) = 1 - \frac{\varepsilon_R e^{-\frac{\gamma}{\varepsilon_R}}}{\varepsilon_R + \gamma\varsigma_R} - \frac{\gamma e^{-\frac{\gamma}{\varepsilon_R}}}{\varepsilon_R + \gamma\varsigma_R} - \frac{\gamma\varepsilon_R\varsigma_R e^{-\frac{\gamma}{\varepsilon_R}}}{(\varepsilon_R + \gamma\varsigma_R)^2}. \tag{3.32}$$

Moreover, using (4.30) and (3.30) to substitute $p_{\psi_J}(\psi_J)$ and $P_{\omega_J}(\omega_J)$ in (3.28), respectively, gives the CDF of the SINR at the end nodes, which can be expressed as

$$P_{\gamma_D}(\gamma) = \int_0^\infty \frac{1}{\varsigma_D} e^{-\frac{\psi_D}{\varsigma_D}} d\psi_D - \frac{e^{-\frac{\gamma}{\varepsilon_D}}}{\varsigma_D} \int_0^\infty e^{-\frac{\varepsilon_D+\gamma\varsigma_D}{\varepsilon_D\varsigma_D}\psi_D} d\psi_D. \tag{3.33}$$

The CDF of the SINR at the end nodes is computed by solving these integrals, which results in

$$P_{\gamma_D}(\gamma) = 1 - \frac{\varepsilon_D e^{-\frac{\gamma}{\varepsilon_D}}}{\gamma\varsigma_D + \varepsilon_D}. \tag{3.34}$$

Finally, the PDF of the tight upper bound of the E2E SINR is evaluated by using (3.25), (3.27), (3.32) and (3.34) to substitute $p_{\gamma_R}(\gamma)$, $p_{\gamma_D}(\gamma)$, $P_{\gamma_R}(\gamma)$ and $P_{\gamma_D}(\gamma)$, respectively, which yields

$$\begin{aligned} p_{\gamma_{E2E_{up}}}(\gamma) =& \frac{\gamma\varepsilon_D e^{-\frac{\varepsilon_R+\varepsilon_D}{\varepsilon_R\varepsilon_D}\gamma}}{{\varepsilon_R}^2\varsigma_R(\gamma\varsigma_D + \varepsilon_D)} \left[\frac{\varepsilon_R\varsigma_R}{\gamma\varsigma_R + \varepsilon_R} + 2\left(\frac{\varepsilon_R\varsigma_R}{\gamma\varsigma_R + \varepsilon_R}\right)^2 + 2\left(\frac{\varepsilon_R\varsigma_R}{\gamma\varsigma_R + \varepsilon_R}\right)^3 \right] \\ &+ \frac{e^{-\frac{\varepsilon_R+\varepsilon_D}{\varepsilon_R\varepsilon_D}\gamma}}{\varepsilon_D\varsigma_D} \left[\frac{\varepsilon_D\varsigma_D}{\gamma\varsigma_D + \varepsilon_D} + \left(\frac{\varepsilon_D\varsigma_D}{\gamma\varsigma_D + \varepsilon_D}\right)^2 \right] \times \left[\frac{\varepsilon_R}{\varepsilon_R + \gamma\varsigma_R} + \frac{\gamma}{\varepsilon_R + \gamma\varsigma_R} \right. \\ &\left. + \frac{\gamma\varepsilon_R\varsigma_R}{(\varepsilon_R + \gamma\varsigma_R)^2} \right]. \end{aligned} \tag{3.35}$$

The PDF expressions that are presented in this section will be exploited in the next section to derive a closed-form expression for the tight upper bound of the E2E ergodic capacity of the proposed AF-FD-PLNC system.

3.5.2 Cumulative Distribution Function (CDF) of the Tight Upper Bound of the End-to-End (E2E) SINR

The CDF of the E2E SINR for the AF-FD-PLNC can be evaluated using the results of [124] as

$$P_{\gamma_{E2E_{up}}}(\gamma) = P_{\gamma_R}(\gamma) + P_{\gamma_D}(\gamma) - P_{\gamma_R}(\gamma)P_{\gamma_D}(\gamma), \tag{3.36}$$

where $P_{\gamma_R}(\gamma)$ and $P_{\gamma_D}(\gamma)$ are the CDF of the SINR at the relay and the end nodes, respectively. Substituting, (3.32) and (3.34) in (3.36) results in

$$P_{\gamma_{E2E_{up}}}(\gamma) = 1 - \frac{e^{-\frac{\varepsilon_R+\varepsilon_D}{\varepsilon_R\varepsilon_D}\gamma}\varepsilon_D}{\gamma\varsigma_D + \varepsilon_D}\left[\frac{\varepsilon_R}{\varepsilon_R+\gamma\varsigma_R} + \frac{\gamma}{\varepsilon_R+\gamma\varsigma_R} + \frac{\gamma\varepsilon_R\varsigma_R}{(\varepsilon_R+\gamma\varsigma_R)^2}\right]. \tag{3.37}$$

This expression will be utilized in the next section to derive closed-form expression for the E2E outage probability along with the E2E ASER of the proposed AF-FD-PLNC system.

3.6 Performance Evaluation Metrics

This section presents closed-form expressions for the performance evaluation metrics of the proposed AF-FD-PLNC system, i.e. E2E outage probability, E2E ASER and E2E ergodic capacity. The derived expression will be used in the next section to thoroughly study the performance of the proposed AF-FD-PLNC and the impact of the residual SI on the performance of that system.

3.6.1 End-to-end Outage Probability

Here we present a closed-form expression for the outage probability of the proposed system. The outage probability is an important performance evaluation metric that is used to measure the quality of the communication and defined as the probability that the SINR falls below a specific threshold, γ_{th} [125]. Thus, the E2E outage probability is given as

$$\begin{aligned} P_{out}^{E2E}(\gamma_{E2E_{th}}) &\triangleq Pr\{\gamma_{E2E} \leq \gamma_{E2E_{th}}\} \\ &= \int_0^{\gamma_{E2E_{th}}} p_{\gamma_{E2E}}(\gamma)d\gamma. \end{aligned} \tag{3.38}$$

A closer inspection of (3.38) reveals that the E2E outage probability definition is similar to that of the CDF of the SINR, thus the outage probability can also be expressed as

$$P_{out}^{E2E}(\gamma_{E2E_{th}}) = P_{\gamma_{E2E}}(\gamma_{E2E_{th}}). \tag{3.39}$$

Therefore, utilizing $\gamma_{E2E_{th}}$ rather than γ to evaluate (3.37) yields the E2E outage probability of the proposed AF-FD-PLNC, which is expressed as

$$P_{\gamma_{E2E_{up}}}(\gamma_{E2E_{th}}) = 1 - \frac{e^{-\frac{\varepsilon_R+\varepsilon_D}{\varepsilon_R\varepsilon_D}\gamma_{E2E_{th}}}\varepsilon_D}{\gamma_{E2E_{th}}\varsigma_D + \varepsilon_D}\left[\frac{\varepsilon_R}{\varepsilon_R + \gamma_{E2E_{th}}\varsigma_R} + \frac{\gamma_{E2E_{th}}}{\varepsilon_R + \gamma_{E2E_{th}}\varsigma_R} + \frac{\gamma_{E2E_{th}}\varepsilon_R\varsigma_R}{(\varepsilon_R + \gamma_{E2E_{th}}\varsigma_R)^2}\right]. \tag{3.40}$$

Next, we derive the E2E outage probability expression of the AF-HD-PLNC system. The results of the E2E outage probability of the AF-HD-PLNC will be used as a reference to study the effect of the residual SI after the active SIC on the E2E outage probability results of the AF-FD-PLNC system. In order to obtain the E2E outage probability expression of the AF-HD-PLNC, we need to derive the E2E CDF of the SNR for that system first. Due to the fact that the AF-HD-PLNC system is SI free, the SNR expression of that system at the relay and the end nodes are given as

$$\gamma_R^{HD} = \omega_R, \tag{3.41}$$

and

$$\gamma_D^{HD} = \omega_D, \tag{3.42}$$

respectively, where $\omega_R = \Lambda_R\left(|H_A|^2 + |H_B|^2\right)$ and $\omega_D = \Lambda_D|H_D|^2$. Moreover the CDF expressions of ω_R and ω_D are given in (3.29) and (3.30), respectively. Hence, the CDF expression of the E2E SNR for the AF-HD-PLNC can be computed by substituting (3.29) and (3.30) in (3.36), which yields

$$P_{\gamma_{E2E_{up}}^{HD}}(\gamma^{HD}) = 1 - e^{-\frac{\varepsilon_R+\varepsilon_D}{\varepsilon_R\varepsilon_D}\gamma} - \frac{\gamma e^{-\frac{\varepsilon_R+\varepsilon_D}{\varepsilon_R\varepsilon_D}\gamma}}{\varepsilon_R}. \tag{3.43}$$

Since the definition of the outage probability is similar to that of the SNR CDF, the E2E outage probability of the AF-HD-PLNC can be obtained by evaluating (3.43) at $\gamma_{E2E_{th}}^{HD}$ to give

$$P_{\gamma_{E2E_{up}}^{HD}}(\gamma_{E2E_{th}}^{HD}) = 1 - e^{-\frac{\varepsilon_R+\varepsilon_D}{\varepsilon_R\varepsilon_D}\gamma_{E2E_{th}}^{HD}} - \frac{\gamma_{E2E_{th}}^{HD} e^{-\frac{\varepsilon_R+\varepsilon_D}{\varepsilon_R\varepsilon_D}\gamma_{E2E_{th}}^{HD}}}{\varepsilon_R}. \tag{3.44}$$

3.6.2 Lower Bound End-to-end Average Symbol Error Rate (ASER)

This subsection presents the derivation of the lower bound E2E ASER of the proposed Af-FD-PLNC for two different scenarios. First, the average SNR and INR at the relay and the end nodes are assumed to be different, i.e. $\varepsilon_R \neq \varepsilon_D$ and $\varsigma_R \neq \varsigma_D$; the second considered scenario is when both of the average SNR and INR at the relay and the end nodes are equal, $\varepsilon_R = \varepsilon_D$ and $\varsigma_R = \varsigma_D$.

3.6.2.1 First scenario ($\varepsilon_R \neq \varepsilon_D$ and $\varsigma_R \neq \varsigma_D$)

In general, the ASER can be evaluated using the formula that was introduced in [126] as

$$\bar{P}_{e_{E2E}} = \frac{\varrho}{2}\sqrt{\frac{\nu}{\pi}}\int_0^\infty \frac{e^{-\nu\gamma}}{\sqrt{\gamma}} P_{\gamma_{E2E_{up}}}(\gamma)d\gamma, \tag{3.45}$$

which exploits the CDF of the SINR that was evaluated in Section 3.5, $P_{\gamma_{E2E_{up}}}(\gamma)$. Thus, substituting (3.37) in (3.45) yields

$$\bar{P}^1_{e_{E2E}} = \frac{\varrho}{2}\sqrt{\frac{\nu}{\pi}}\int_0^\infty \frac{e^{-\nu\gamma}}{\sqrt{\gamma}} d\gamma \tag{3.46a}$$

$$- \frac{\varrho}{2}\sqrt{\frac{\nu}{\pi}}\int_0^\infty \frac{\varepsilon_D\varepsilon_R}{(\varepsilon_R+\gamma\varsigma_R)(\varepsilon_D+\gamma\varsigma_D)\sqrt{\gamma}} e^{-\frac{\varepsilon_R+\varepsilon_D+\nu\varepsilon_R\varepsilon_D}{\varepsilon_R\varepsilon_D}} d\gamma \tag{3.46b}$$

$$- \frac{\varrho}{2}\sqrt{\frac{\nu}{\pi}}\int_0^\infty \frac{\varepsilon_D\sqrt{\gamma}}{(\varepsilon_R+\gamma\varsigma_R)(\varepsilon_D+\gamma\varsigma_D)} e^{-\frac{\varepsilon_R+\varepsilon_D+\nu\varepsilon_R\varepsilon_D}{\varepsilon_R\varepsilon_D}} d\gamma \tag{3.46c}$$

$$- \frac{\varrho}{2}\sqrt{\frac{\nu}{\pi}}\int_0^\infty \frac{\varepsilon_R\varepsilon_D\varsigma_R\sqrt{\gamma}}{(\varepsilon_R+\gamma\varsigma_R)^2(\varepsilon_D+\gamma\varsigma_D)} e^{-\frac{\varepsilon_R+\varepsilon_D+\nu\varepsilon_R\varepsilon_D}{\varepsilon_R\varepsilon_D}} d\gamma. \tag{3.46d}$$

The the last three integrals in (3.46), (3.46b) - (3.46d), are mathematically challenging to solve, hence, we exploit the partial fraction decomposition technique to present these integrals in a

simpler and mathematically tractable form. Subsequently, the ASER can be rewritten as

$$\bar{P}^1_{e_{E2E}} = \frac{\varrho}{2}\sqrt{\frac{\nu}{\pi}}\int_0^\infty \frac{e^{-\nu\gamma}}{\sqrt{\gamma}}d\gamma \tag{3.47a}$$

$$+ \frac{\varrho}{2}\sqrt{\frac{\nu}{\pi}}\frac{\varepsilon_R\varepsilon_D}{(\varepsilon_D\varsigma_R - \varepsilon_R\varsigma_D)}\left[\int_0^\infty \frac{e^{-\frac{\varepsilon_R+\varepsilon_D+\nu\varepsilon_R\varepsilon_D}{\varepsilon_R\varepsilon_D}}}{\sqrt{\gamma}\left(\frac{\varepsilon_D}{\varsigma_D}+\gamma\right)}d\gamma - \int_0^\infty \frac{e^{-\frac{\varepsilon_R+\varepsilon_D+\nu\varepsilon_R\varepsilon_D}{\varepsilon_R\varepsilon_D}}}{\sqrt{\gamma}\left(\frac{\varepsilon_R}{\varsigma_R}+\gamma\right)}d\gamma\right] \tag{3.47b}$$

$$+ \frac{\varrho}{2}\sqrt{\frac{\nu}{\pi}}\frac{\varepsilon_D}{(\varepsilon_D\varsigma_R - \varepsilon_R\varsigma_D)}\left[\int_0^\infty \frac{\sqrt{\gamma}e^{-\frac{\varepsilon_R+\varepsilon_D+\nu\varepsilon_R\varepsilon_D}{\varepsilon_R\varepsilon_D}}}{\left(\frac{\varepsilon_D}{\varsigma_D}+\gamma\right)}d\gamma - \int_0^\infty \frac{\sqrt{\gamma}e^{-\frac{\varepsilon_R+\varepsilon_D+\nu\varepsilon_R\varepsilon_D}{\varepsilon_R\varepsilon_D}}}{\left(\frac{\varepsilon_R}{\varsigma_R}+\gamma\right)}d\gamma\right] \tag{3.47c}$$

$$+ \frac{\varrho}{2}\sqrt{\frac{\nu}{\pi}}\Bigg[\frac{\varepsilon_R\varepsilon_D}{\varsigma_R\varsigma_D\left(\frac{\varepsilon_R}{\varsigma_R}-\frac{\varepsilon_D}{\varsigma_D}\right)^2}\left(\int_0^\infty \frac{\sqrt{\gamma}e^{-\frac{\varepsilon_R+\varepsilon_D+\nu\varepsilon_R\varepsilon_D}{\varepsilon_R\varepsilon_D}}}{\left(\frac{\varepsilon_R}{\varsigma_R}+\gamma\right)}d\gamma - \int_0^\infty \frac{\sqrt{\gamma}e^{-\frac{\varepsilon_R+\varepsilon_D+\nu\varepsilon_R\varepsilon_D}{\varepsilon_R\varepsilon_D}}}{\left(\frac{\varepsilon_D}{\varsigma_D}+\gamma\right)}d\gamma\right)$$

$$+ \frac{\varepsilon_R\varepsilon_D}{(\varepsilon_R\varsigma_D - \varepsilon_D\varsigma_R)}\int_0^\infty \frac{\sqrt{\gamma}e^{-\frac{\varepsilon_R+\varepsilon_D+\nu\varepsilon_R\varepsilon_D}{\varepsilon_R\varepsilon_D}}}{\left(\frac{\varepsilon_R}{\varsigma_R}+\gamma\right)^2}d\gamma\Bigg]. \tag{3.47d}$$

Furthermore, (3.47) can be presented as

$$\bar{P}^1_{e_{E2E}} = \bar{P}^1_{e_1} + \bar{P}^1_{e_2} + \bar{P}^1_{e_3} + \bar{P}^1_{e_4} + \bar{P}^1_{e_5}, \tag{3.48}$$

where

$$\bar{P}^1_{e_1} = \frac{\varrho}{2}\sqrt{\frac{\nu}{\pi}}\int_0^\infty \frac{e^{-\nu\gamma}}{\sqrt{\gamma}}d\gamma, \tag{3.49}$$

$$\bar{P}^1_{e_2} = \frac{\varrho}{2}\sqrt{\frac{\nu}{\pi}}\frac{\varepsilon_R\varepsilon_D}{(\varepsilon_D\varsigma_R - \varepsilon_R\varsigma_D)}\left[\int_0^\infty \frac{e^{-\frac{\varepsilon_R+\varepsilon_D+\nu\varepsilon_R\varepsilon_D}{\varepsilon_R\varepsilon_D}}}{\sqrt{\gamma}\left(\frac{\varepsilon_D}{\varsigma_D}+\gamma\right)}d\gamma - \int_0^\infty \frac{e^{-\frac{\varepsilon_R+\varepsilon_D+\nu\varepsilon_R\varepsilon_D}{\varepsilon_R\varepsilon_D}}}{\sqrt{\gamma}\left(\frac{\varepsilon_R}{\varsigma_R}+\gamma\right)}d\gamma\right], \tag{3.50}$$

$$\bar{P}^1_{e_3} = \frac{\varrho}{2}\sqrt{\frac{\nu}{\pi}}\frac{\varepsilon_D}{(\varepsilon_D\varsigma_R - \varepsilon_R\varsigma_D)}\left[\int_0^\infty \frac{\sqrt{\gamma}e^{-\frac{\varepsilon_R+\varepsilon_D+\nu\varepsilon_R\varepsilon_D}{\varepsilon_R\varepsilon_D}}}{\left(\frac{\varepsilon_D}{\varsigma_D}+\gamma\right)}d\gamma - \int_0^\infty \frac{\sqrt{\gamma}e^{-\frac{\varepsilon_R+\varepsilon_D+\nu\varepsilon_R\varepsilon_D}{\varepsilon_R\varepsilon_D}}}{\left(\frac{\varepsilon_R}{\varsigma_R}+\gamma\right)}d\gamma\right], \tag{3.51}$$

$$\bar{P}^1_{e_4} = \frac{\varrho}{2}\sqrt{\frac{\nu}{\pi}}\frac{\varepsilon_R\varepsilon_D}{\varsigma_R\varsigma_D\left(\frac{\varepsilon_R}{\varsigma_R}-\frac{\varepsilon_D}{\varsigma_D}\right)^2}\left(\int_0^\infty \frac{\sqrt{\gamma}e^{-\frac{\varepsilon_R+\varepsilon_D+\nu\varepsilon_R\varepsilon_D}{\varepsilon_R\varepsilon_D}}}{\left(\frac{\varepsilon_R}{\varsigma_R}+\gamma\right)}d\gamma - \int_0^\infty \frac{\sqrt{\gamma}e^{-\frac{\varepsilon_R+\varepsilon_D+\nu\varepsilon_R\varepsilon_D}{\varepsilon_R\varepsilon_D}}}{\left(\frac{\varepsilon_D}{\varsigma_D}+\gamma\right)}d\gamma\right), \tag{3.52}$$

and

$$\bar{P}^1_{e_5} = \frac{\varrho}{2}\sqrt{\frac{\nu}{\pi}}\frac{\varepsilon_R\varepsilon_D}{(\varepsilon_R\varsigma_D - \varepsilon_D\varsigma_R)}\int_0^\infty \frac{\sqrt{\gamma}e^{-\frac{\varepsilon_R+\varepsilon_D+\nu\varepsilon_R\varepsilon_D}{\varepsilon_R\varepsilon_D}}}{\left(\frac{\varepsilon_R}{\varsigma_R}+\gamma\right)^2}d\gamma. \tag{3.53}$$

The integral in (3.49) can be solved using the result in [123, Eq. (3.361.2)] to give

$$\bar{P}^1_{e_1} = \frac{\varrho}{2}. \tag{3.54}$$

Next, [123, Eq. (3.383.10)] can be exploited to solve the integrals in (3.50), which results in

$$\bar{P}_{e_2}^1 = \frac{\varrho}{2}\sqrt{\frac{\nu}{\pi}}\frac{\varepsilon_R\varepsilon_D}{(\varepsilon_D\varsigma_R - \varepsilon_R\varsigma_D)}\left[\sqrt{\frac{\varsigma_D}{\varepsilon_D}}e^{\frac{\varepsilon_R+\varepsilon_D+\nu\varepsilon_R\varepsilon_D}{\varepsilon_R\varsigma_D}}\Gamma\left(\frac{1}{2}\right)\Gamma\left(\frac{1}{2},\ \frac{\varepsilon_R+\varepsilon_D+\nu\varepsilon_R\varepsilon_D}{\varepsilon_R\varsigma_D}\right)\right.$$
$$\left. - \sqrt{\frac{\varsigma_R}{\varepsilon_R}}e^{\frac{\varepsilon_R+\varepsilon_D+\nu\varepsilon_R\varepsilon_D}{\varepsilon_D\varsigma_R}}\Gamma\left(\frac{1}{2}\right)\Gamma\left(\frac{1}{2},\ \frac{\varepsilon_R+\varepsilon_D+\nu\varepsilon_R\varepsilon_D}{\varepsilon_D\varsigma_R}\right)\right], \tag{3.55}$$

where $\Gamma(\alpha, x)$ denotes the incomplete gamma function, which is defined in [123, Eq. (8.350.2)] as

$$\Gamma(\alpha, x) = \int_x^\infty e^{-t}t^{\alpha-1}dt. \tag{3.56}$$

Moreover, the integrals in (3.51) are solved by exploiting the result in [123, Eq. (3.383.10)], which yields

$$\bar{P}_{e_3}^1 = \frac{\varrho}{2}\sqrt{\frac{\nu}{\pi}}\frac{\varepsilon_D}{(\varepsilon_D\varsigma_R - \varepsilon_R\varsigma_D)}\left[\sqrt{\frac{\varepsilon_D}{\varsigma_D}}e^{\frac{\varepsilon_R+\varepsilon_D+\nu\varepsilon_R\varepsilon_D}{\varepsilon_R\varsigma_D}}\Gamma\left(\frac{3}{2}\right)\Gamma\left(-\frac{1}{2},\ \frac{\varepsilon_R+\varepsilon_D+\nu\varepsilon_R\varepsilon_D}{\varepsilon_R\varsigma_D}\right)\right.$$
$$\left. - \sqrt{\frac{\varepsilon_R}{\varsigma_R}}e^{\frac{\varepsilon_R+\varepsilon_D+\nu\varepsilon_R\varepsilon_D}{\varepsilon_D\varsigma_R}}\Gamma\left(\frac{3}{2}\right)\Gamma\left(-\frac{1}{2},\ \frac{\varepsilon_R+\varepsilon_D+\nu\varepsilon_R\varepsilon_D}{\varepsilon_D\varsigma_R}\right)\right]. \tag{3.57}$$

Furthermore, [123, Eq. (4.383.10)] is utilized to solve the integrals in (3.52), which gives

$$\bar{P}_{e_4}^1 = \frac{\varrho}{2}\sqrt{\frac{\nu}{\pi}}\frac{\varepsilon_R\varepsilon_D}{\varsigma_R\varsigma_D\left(\frac{\varepsilon_R}{\varsigma_R} - \frac{\varepsilon_D}{\varsigma_D}\right)^2}\left[\sqrt{\frac{\varepsilon_R}{\varsigma_R}}e^{\frac{\varepsilon_R+\varepsilon_D+\nu\varepsilon_R\varepsilon_D}{\varepsilon_D\varsigma_R}}\Gamma\left(\frac{3}{2}\right)\Gamma\left(-\frac{1}{2},\ \frac{\varepsilon_R+\varepsilon_D+\nu\varepsilon_R\varepsilon_D}{\varepsilon_D\varsigma_R}\right)\right.$$
$$\left. - \sqrt{\frac{\varepsilon_D}{\varsigma_D}}e^{\frac{\varepsilon_R+\varepsilon_D+\nu\varepsilon_R\varepsilon_D}{\varepsilon_R\varsigma_D}}\Gamma\left(\frac{3}{2}\right)\Gamma\left(-\frac{1}{2},\ \frac{\varepsilon_R+\varepsilon_D+\nu\varepsilon_R\varepsilon_D}{\varepsilon_R\varsigma_D}\right)\right]. \tag{3.58}$$

Finally, (3.53) can be solved using [123, Eq. (3.383.7)], which results in

$$\bar{P}_{e_5}^1 = \frac{\varrho}{2}\sqrt{\frac{\nu}{\pi}}\frac{\varepsilon_R\varepsilon_D}{(\varepsilon_R\varsigma_D - \varepsilon_D\varsigma_R)}(2)^{\frac{3}{2}}\Gamma\left(\frac{3}{2}\right)\frac{e^{\frac{\varepsilon_R+\varepsilon_D+\nu\varepsilon_R\varepsilon_D}{2\varepsilon_D\varsigma_R}}}{\sqrt{\frac{\varepsilon_R}{\varsigma_R}}}D_{-3}\left(\sqrt{2\frac{\varepsilon_R+\varepsilon_D+\nu\varepsilon_R\varepsilon_D}{\varepsilon_D\varsigma_R}}\right), \tag{3.59}$$

where $D_p(z)$ is the parabolic cylinder function that is defined in [123, Eq. (9.241.2)] as

$$D_p(z) = \frac{e^{-\frac{z^2}{4}}}{\Gamma(-p)}\int_0^\infty e^{-xz-\frac{x^2}{2}}x^{-p-1}dx, [\mathbf{Re}\ p < 0]. \tag{3.60}$$

Finally, the lower bound E2E ASER of the proposed AF-FD-PLNC system can be obtained

by substituting (3.54), (3.55), (3.57), (3.58) and (3.59) in (3.48), which yields

$$\bar{P}^{1}_{e_{E2E}} = \frac{\varrho}{2}\Bigg(1+\sqrt{\frac{\nu}{\pi}}\frac{\varepsilon_R\varepsilon_D}{(\varepsilon_D\varsigma_R-\varepsilon_R\varsigma_D)}\Bigg[\sqrt{\frac{\varsigma_D}{\varepsilon_D}}e^{\frac{\varepsilon_R+\varepsilon_D+\nu\varepsilon_R\varepsilon_D}{\varepsilon_R\varsigma_D}}\Gamma\left(\frac{1}{2}\right)\Gamma\left(\frac{1}{2},\ \frac{\varepsilon_R+\varepsilon_D+\nu\varepsilon_R\varepsilon_D}{\varepsilon_R\varsigma_D}\right)$$
$$-\sqrt{\frac{\varsigma_R}{\varepsilon_R}}e^{\frac{\varepsilon_R+\varepsilon_D+\nu\varepsilon_R\varepsilon_D}{\varepsilon_D\varsigma_R}}\Gamma\left(\frac{1}{2}\right)\Gamma\left(\frac{1}{2},\ \frac{\varepsilon_R+\varepsilon_D+\nu\varepsilon_R\varepsilon_D}{\varepsilon_D\varsigma_R}\right)\Bigg]+\sqrt{\frac{\nu}{\pi}}\frac{\varepsilon_D}{(\varepsilon_D\varsigma_R-\varepsilon_R\varsigma_D)}$$
$$\times\Bigg[\sqrt{\frac{\varepsilon_D}{\varsigma_D}}e^{\frac{\varepsilon_R+\varepsilon_D+\nu\varepsilon_R\varepsilon_D}{\varepsilon_R\varsigma_D}}\Gamma\left(\frac{3}{2}\right)\Gamma\left(-\frac{1}{2},\ \frac{\varepsilon_R+\varepsilon_D+\nu\varepsilon_R\varepsilon_D}{\varepsilon_R\varsigma_D}\right)-\sqrt{\frac{\varepsilon_R}{\varsigma_R}}e^{\frac{\varepsilon_R+\varepsilon_D+\nu\varepsilon_R\varepsilon_D}{\varepsilon_D\varsigma_R}}$$
$$\times\Gamma\left(\frac{3}{2}\right)\Gamma\left(-\frac{1}{2},\ \frac{\varepsilon_R+\varepsilon_D+\nu\varepsilon_R\varepsilon_D}{\varepsilon_D\varsigma_R}\right)\Bigg]+\sqrt{\frac{\nu}{\pi}}\frac{\varepsilon_R\varepsilon_D}{\varsigma_R\varsigma_D\left(\frac{\varepsilon_R}{\varsigma_R}-\frac{\varepsilon_D}{\varsigma_D}\right)^2}\Bigg[\sqrt{\frac{\varepsilon_R}{\varsigma_R}}$$
$$\times e^{\frac{\varepsilon_R+\varepsilon_D+\nu\varepsilon_R\varepsilon_D}{\varepsilon_D\varsigma_R}}\Gamma\left(\frac{3}{2}\right)\Gamma\left(-\frac{1}{2},\ \frac{\varepsilon_R+\varepsilon_D+\nu\varepsilon_R\varepsilon_D}{\varepsilon_D\varsigma_R}\right)-\sqrt{\frac{\varepsilon_D}{\varsigma_D}}e^{\frac{\varepsilon_R+\varepsilon_D+\nu\varepsilon_R\varepsilon_D}{\varepsilon_R\varsigma_D}}\Gamma\left(\frac{3}{2}\right)$$
$$\times\Gamma\left(-\frac{1}{2},\ \frac{\varepsilon_R+\varepsilon_D+\nu\varepsilon_R\varepsilon_D}{\varepsilon_R\varsigma_D}\right)\Bigg]-\sqrt{\frac{\nu}{\pi}}\frac{\varepsilon_R\varepsilon_D}{(\varepsilon_D\varsigma_R-\varepsilon_R\varsigma_D)}(2)^{\frac{3}{2}}\Gamma\left(\frac{3}{2}\right)\frac{e^{\frac{\varepsilon_R+\varepsilon_D+\nu\varepsilon_R\varepsilon_D}{2\varepsilon_D\varsigma_R}}}{\sqrt{\frac{\varepsilon_R}{\varsigma_R}}}$$
$$\times D_{-3}\left(\sqrt{2\frac{\varepsilon_R+\varepsilon_D+\nu\varepsilon_R\varepsilon_D}{\varepsilon_D\varsigma_R}}\right)\Bigg). \tag{3.61}$$

3.6.2.2 Second scenario ($\varepsilon_R = \varepsilon_D$ and $\varsigma_R = \varsigma_D$)

A closer look at equations (3.55)-(3.59) reveals that when $\varepsilon_R = \varepsilon_D$ and $\varsigma_R = \varsigma_D$ these expressions yield zero. Hence, to thoroughly investigate the ASER results of the proposed AF-FD-PLNC, we need to drive the ASER for this scenario. First, we need to evaluate the CDF of the upper bound SINR for the considered scenario. To this end when $\varepsilon_R = \varepsilon_D$ and $\varsigma_R = \varsigma_D$ are assumed the CDF of the SINR in (3.37) can be rewritten as

$$P_{\gamma_{E2E_{up}}}(\gamma) = 1 - e^{-\frac{2}{\varepsilon_J}\gamma}\left[\frac{\varepsilon_J^2}{(\varepsilon_J+\gamma\varsigma_J)^2}+\frac{\varepsilon_J\gamma}{(\varepsilon_J+\gamma\varsigma_J)^2}+\frac{\gamma\varepsilon_J^2\varsigma_J}{(\varepsilon_J+\gamma\varsigma_J)^3}\right]. \tag{3.62}$$

Recall (3.45), the lower bound ASER of the proposed AF-FD-PLNC in this scenario can be obtained by using (3.62) to substitute $P_{\gamma_{E2E_{up}}}(\gamma)$ in (3.45) such that

$$\bar{P}^2_{e_{E2E}} = \frac{\varrho}{2}\sqrt{\frac{\nu}{\pi}}\int_0^\infty \frac{e^{-\nu\gamma}}{\sqrt{\gamma}}d\gamma \tag{3.63a}$$

$$- \frac{\varrho\varepsilon_J^2}{2}\sqrt{\frac{\nu}{\pi}}\int_0^\infty \frac{e^{-\frac{2+\nu\varepsilon_J}{\varepsilon_J}\gamma}}{\sqrt{\gamma}\left(\varepsilon_J+\gamma\varsigma_J\right)^2}d\gamma \tag{3.63b}$$

$$- \frac{\varrho\varepsilon_J}{2}\sqrt{\frac{\nu}{\pi}}\int_0^\infty \frac{\sqrt{\gamma}e^{-\frac{2+\nu\varepsilon_J}{\varepsilon_J}\gamma}}{\left(\varepsilon_J+\gamma\varsigma_J\right)^2}d\gamma \tag{3.63c}$$

$$- \frac{\varrho\varepsilon_J^2\varsigma_J}{2}\sqrt{\frac{\nu}{\pi}}\int_0^\infty \frac{\sqrt{\gamma}e^{-\frac{2+\nu\varepsilon_J}{\varepsilon_J}\gamma}}{\left(\varepsilon_J+\gamma\varsigma_J\right)^3}d\gamma \tag{3.63d}$$

The above expression can be simplified as

$$\bar{P}^2_{e_{E2E}} = \bar{P}^2_{e_1} + \bar{P}^2_{e_2} + \bar{P}^2_{e_3} + \bar{P}^2_{e_4}, \tag{3.64}$$

where

$$\bar{P}^2_{e_1} = \frac{\varrho}{2}\sqrt{\frac{\nu}{\pi}}\int_0^\infty \frac{e^{-\nu\gamma}}{\sqrt{\gamma}}d\gamma, \tag{3.65}$$

$$\bar{P}^2_{e_2} = -\frac{\varrho\varepsilon_J^2}{2\varsigma_J^2}\sqrt{\frac{\nu}{\pi}}\int_0^\infty \frac{e^{-\frac{2+\nu\varepsilon_J}{\varepsilon_J}\gamma}}{\sqrt{\gamma}\left(\frac{\varepsilon_J}{\varsigma_J}+\gamma\right)^2}d\gamma, \tag{3.66}$$

$$\bar{P}^2_{e_3} = -\frac{\varrho\varepsilon_J}{2\varsigma_J^2}\sqrt{\frac{\nu}{\pi}}\int_0^\infty \frac{\sqrt{\gamma}e^{-\frac{2+\nu\varepsilon_J}{\varepsilon_J}\gamma}}{\left(\frac{\varepsilon_J}{\varsigma_J}+\gamma\right)^2}d\gamma, \tag{3.67}$$

and

$$\bar{P}^2_{e_4} = -\frac{\varrho\varepsilon_J^2}{2\varsigma_J}\sqrt{\frac{\nu}{\pi}}\int_0^\infty \frac{\sqrt{\gamma}e^{-\frac{2+\nu\varepsilon_J}{\varepsilon_J}\gamma}}{\left(\frac{\varepsilon_J}{\varsigma_J}+\gamma\right)^3}d\gamma. \tag{3.68}$$

The lower bound E2E ASER expression can be obtained by solving the integrals in (3.65)-(3.68). First, the integral in (3.65) can be solved using [123, Eq. (3.361.2)] such that

$$\bar{P}^2_{e_1} = \frac{\varrho}{2}. \tag{3.69}$$

Moreover, (3.66) can be simplified using the partial fraction decomposition technique such that

$$\bar{P}_{e_2}^2 = \frac{\varrho\varepsilon_J}{2\varsigma_J}\sqrt{\frac{\nu}{\pi}}\int_0^\infty \frac{\sqrt{\gamma}e^{-\frac{2+\nu\varepsilon_J}{\varepsilon_J}\gamma}}{\left(\frac{\varepsilon_J}{\varsigma_J}+\gamma\right)^2}d\gamma \tag{3.70a}$$

$$+\frac{\varrho}{2}\sqrt{\frac{\nu}{\pi}}\int_0^\infty \frac{\sqrt{\gamma}e^{-\frac{2+\nu\varepsilon_J}{\varepsilon_J}\gamma}}{\left(\frac{\varepsilon_J}{\varsigma_J}+\gamma\right)}d\gamma \tag{3.70b}$$

$$-\frac{\varrho}{2}\sqrt{\frac{\nu}{\pi}}\int_0^\infty \frac{e^{-\frac{2+\nu\varepsilon_J}{\varepsilon_J}\gamma}}{\sqrt{\gamma}}d\gamma. \tag{3.70c}$$

Furthermore, $\bar{P}_{e_2}^2$, i.e. (3.70), can be expressed as

$$\bar{P}_{e_2}^2 = \mathbf{I}_1 + \mathbf{I}_2 + \mathbf{I}_3, \tag{3.71}$$

where $\mathbf{I}_1$ is given as

$$\mathbf{I}_1 = \frac{\varrho\varepsilon_J}{2\varsigma_J}\sqrt{\frac{\nu}{\pi}}\int_0^\infty \frac{\sqrt{\gamma}e^{-\frac{2+\nu\varepsilon_J}{\varepsilon_J}\gamma}}{\left(\frac{\varepsilon_J}{\varsigma_J}+\gamma\right)^2}d\gamma, \tag{3.72}$$

while $\mathbf{I}_2$ is given as

$$\mathbf{I}_2 = \frac{\varrho}{2}\sqrt{\frac{\nu}{\pi}}\int_0^\infty \frac{\sqrt{\gamma}e^{-\frac{2+\nu\varepsilon_J}{\varepsilon_J}\gamma}}{\left(\frac{\varepsilon_J}{\varsigma_J}+\gamma\right)}d\gamma, \tag{3.73}$$

and $\mathbf{I}_3$ is expressed such that

$$\mathbf{I}_3 = -\frac{\varrho}{2}\sqrt{\frac{\nu}{\pi}}\int_0^\infty \frac{e^{-\frac{2+\nu\varepsilon_J}{\varepsilon_J}\gamma}}{\sqrt{\gamma}}d\gamma. \tag{3.74}$$

The integral in (3.72) can be solved by exploiting [123, Eq. (3.383.7)], which produces

$$\mathbf{I}_1 = \varrho\sqrt{\frac{\nu}{\pi}}\sqrt{\frac{2\varepsilon_J}{\varsigma_J}}\Gamma(\frac{3}{2})e^{\frac{2+\nu\varepsilon_J}{2\varsigma_J}}D_{-3}\left(\sqrt{2\frac{2+\nu\varepsilon_J}{\varsigma_J}}\right). \tag{3.75}$$

Next, [123, Eq. (3.383.10)] is utilized to evaluate the integral in (3.73) such that

$$\mathbf{I}_2 = \frac{\varrho}{2}\sqrt{\frac{\nu}{\pi}}\sqrt{\frac{\varepsilon_J}{\varsigma_J}}e^{\frac{2+\nu\varepsilon_J}{\varsigma_J}}\Gamma\left(\frac{3}{2}\right)\Gamma\left(-\frac{1}{2},\frac{2+\nu\varepsilon_J}{\varsigma_J}\right). \tag{3.76}$$

Finally, the integral in (3.74) is solved using [123, Eq. (3.361.2)], which yields

$$\mathbf{I}_3 = -\frac{\varrho}{2}\sqrt{\frac{\nu\varepsilon_J}{2+\nu\varepsilon_J}}. \tag{3.77}$$

Therefore, $\bar{P}_{e_2}^2$ is evaluated by using (3.75), (3.76) and (3.77) to substitute $\mathbf{I}_1$, $\mathbf{I}_2$ and $\mathbf{I}_3$ in (3.71),

respective, which results in

$$\bar{P}_{e_2}^2 = \varrho\sqrt{\frac{\nu}{\pi}}\sqrt{\frac{2\varepsilon_J}{\varsigma_J}}\Gamma(\frac{3}{2})e^{\frac{2+\nu\varepsilon_J}{2\varsigma_J}}D_{-3}\left(\sqrt{2\frac{2+\nu\varepsilon_J}{\varsigma_J}}\right) + \frac{\varrho}{2}\sqrt{\frac{\nu}{\pi}}\sqrt{\frac{\varepsilon_J}{\varsigma_J}}e^{\frac{2+\nu\varepsilon_J}{\varsigma_J}}\Gamma\left(\frac{3}{2}\right) \times \Gamma\left(-\frac{1}{2}, \frac{2+\nu\varepsilon_J}{\varsigma_J}\right) - \frac{\varrho}{2}\sqrt{\frac{\nu\varepsilon_J}{2+\nu\varepsilon_J}}. \tag{3.78}$$

Furthermore, the result of the integral in (3.67) is obtained using [123, Eq. (3.383.7)] such that

$$\bar{P}_{e_3}^2 = -\frac{\varrho\sqrt{\varepsilon_J}}{2\varsigma_J^{\frac{3}{2}}}\sqrt{\frac{\nu}{\pi}}2^{\frac{3}{2}}\Gamma\left(\frac{3}{2}\right)e^{\frac{2+\nu\varepsilon_J}{2\varsigma_J}}D_{-3}\left(\sqrt{2\frac{2+\nu\varepsilon_J}{\varsigma_J}}\right). \tag{3.79}$$

Due to that fact that the integral (3.68) is mathematically challenging to solve, a straightforward manipulation is performed on this integral in order to present it in a more mathematically tractable form such that

$$\bar{P}_{e_4}^2 = -\frac{\varrho\varepsilon_J^2}{2\varsigma_J}\sqrt{\frac{\nu}{\pi}}e^{\frac{2+\nu\varepsilon_J}{\varsigma_J}}\int_{\frac{\varepsilon_J}{\varsigma_J}}^{\infty}\frac{\sqrt{\gamma-\frac{\varepsilon_J}{\varsigma_J}}e^{-\frac{2+\nu\varepsilon_J}{\varepsilon_J}\gamma}}{\gamma^3}d\gamma. \tag{3.80}$$

The above integral can be solved by exploiting the result of [123, Eq. (3.383.4)], which yields

$$\bar{P}_{e_4}^2 = -\frac{\varrho}{2}\sqrt{\frac{\nu}{\pi}}e^{-\frac{2+\nu\varepsilon_J}{2\varsigma_J}}\left(\frac{2+\nu\varepsilon_J}{\varepsilon_J}\right)^{\frac{1}{4}}\varepsilon_J^{\frac{3}{4}}\varsigma_J^{\frac{1}{4}}\Gamma\left(\frac{3}{2}\right)W_{-\frac{7}{4},\,\frac{3}{4}}\left(\frac{2+\nu\varepsilon_J}{\varsigma_J}\right), \tag{3.81}$$

where $W_{\lambda,\mu}(z)$ denotes the Whittakers function that is defined in [123, Eq. (9.220.4)] as

$$W_{\lambda,\mu}(x) = \frac{\Gamma(-2\mu)}{\Gamma\left(\frac{1}{2}-\mu-\lambda\right)}M_{\lambda,\mu}(x) + \frac{\Gamma(2\mu)}{\Gamma\left(\frac{1}{2}+\mu-\lambda\right)}M_{\lambda,-\mu}(x). \tag{3.82}$$

Moreover, $M_{\lambda,\pm\mu}(x)$ denotes the other Whittaker function that is defined in [123, Eq. (9.220.2)] and [123, Eq. (9.220.2)] such that

$$M_{\lambda,\mu}(x) = x^{\mu+\frac{1}{2}}e^{\frac{-x}{2}}\Phi\left(\mu-\lambda+\frac{1}{2}, 2\mu+1; x\right), \tag{3.83}$$

$$M_{\lambda,-\mu}(x) = x^{-\mu+\frac{1}{2}}e^{\frac{-x}{2}}\Phi\left(-\mu-\lambda+\frac{1}{2}, -2\mu+1; x\right), \tag{3.84}$$

where $\Phi(\alpha,\gamma;x)$ is the confluent hypergeometric function, which is given in [123, Eq. (9.220.2)] as

$$\Phi(\alpha,\gamma;x) = \frac{2^{1-\gamma}e^{\frac{1}{2}x}}{B(\alpha,\gamma-\alpha)}\int_{-1}^{1}(1-t)^{\gamma-\alpha-1}(1+t)^{\alpha-1}e^{\frac{1}{2}xt}dt, \tag{3.85}$$

and $B\left(x,y\right)$ denotes the beta function that is defined in [123, Eq. (8.380.1)] such that

$$B\left(x,y\right)=\int_{0}^{1}t^{x-1}\left(1-t\right)^{y-1}dt. \tag{3.86}$$

Finally, the lower bound E2E ASER of the proposed AF-FD-PLNC for the second scenario can be computed by using (3.69), (3.78), (3.79) and (3.81) to substitute $\bar{P}_{e_1}^2$, $\bar{P}_{e_2}^2$, $\bar{P}_{e_3}^2$ and $\bar{P}_{e_4}^2$ in (3.64), respectively, to give

$$\begin{aligned}\bar{P}_{e_{E2E}}^2=\frac{\varrho}{2}\Bigg[1+(2)^{\frac{3}{2}}\sqrt{\frac{\nu}{\pi}}\sqrt{\frac{\varepsilon_J}{\varsigma_J}}\Gamma(\frac{3}{2})e^{\frac{2+\nu\varepsilon_J}{2\varsigma_J}}D_{-3}\left(\sqrt{2\frac{2+\nu\varepsilon_J}{\varsigma_J}}\right)+\sqrt{\frac{\nu}{\pi}}\sqrt{\frac{\varepsilon_J}{\varsigma_J}}e^{\frac{2+\nu\varepsilon_J}{\varsigma_J}}\Gamma\left(\frac{3}{2}\right)\\ \times\Gamma\left(-\frac{1}{2},\frac{2+\nu\varepsilon_J}{\varsigma_J}\right)-\sqrt{\frac{\nu\varepsilon_J}{2+\nu\varepsilon_J}}-2^{\frac{3}{2}}\frac{\sqrt{\varepsilon_J}}{\varsigma_J^{\frac{3}{2}}}\sqrt{\frac{\nu}{\pi}}\Gamma\left(\frac{3}{2}\right)e^{\frac{2+\nu\varepsilon_J}{2\varsigma_J}}D_{-3}\left(\sqrt{2\frac{2+\nu\varepsilon_J}{\varsigma_J}}\right)\\ -\sqrt{\frac{\nu}{\pi}}e^{-\frac{2+\nu\varepsilon_J}{2\varsigma_J}}\left(\frac{2+\nu\varepsilon_J}{\varepsilon_J}\right)^{\frac{1}{4}}\varepsilon_J^{\frac{3}{4}}\varsigma_J^{\frac{1}{4}}\Gamma\left(\frac{3}{2}\right)W_{-\frac{7}{4},\,\frac{3}{4}}\left(\frac{2+\nu\varepsilon_J}{\varsigma_J}\right)\Bigg].\end{aligned} \tag{3.87}$$

The derivations that have been presented in this subsection will be exploited in Section 3.7 to evaluate the E2E lower bound ASER of the proposed Af-FD-PLNC, which will enable us to meticulously investigate the ASER performance in the presence of the residual SI after the active SIC.

Next, the E2E lower bound ASER expression for the AF-HD-PLNC system is derived and presented in this subsection. The ASER results of the AF-HD-PLNC will be used as a benchmark to investigate the impact of the residual SI after the active SIC on the E2E ASER performance of the AF-FD-PLNC. The lower bound E2E ASER of the Af-HD-PLNC can be computed by substituting (3.43) in (3.45), which results in

$$\begin{aligned}\bar{P}_{e_{E2E}}^{HD}=\frac{\varrho}{2}\sqrt{\frac{\nu}{\pi}}\Bigg[\int_{0}^{\infty}\frac{e^{-\nu\gamma^{HD}}}{\sqrt{\gamma^{HD}}}d\gamma^{HD}+\int_{0}^{\infty}\frac{e^{-\frac{\varepsilon_R+\varepsilon_D+\nu\varepsilon_R\varepsilon_D}{\varepsilon_R\varepsilon_D}\gamma^{HD}}}{\sqrt{\gamma^{HD}}}d\gamma^{HD}\\ +\int_{0}^{\infty}\frac{\sqrt{\gamma^{HD}}e^{-\frac{\varepsilon_R+\varepsilon_D+\nu\varepsilon_R\varepsilon_D}{\varepsilon_R\varepsilon_D}\gamma^{HD}}}{\varepsilon_R}d\gamma^{HD}\Bigg].\end{aligned} \tag{3.88}$$

The expression above can be presented as

$$\bar{P}_{e_{E2E}}^{HD}=\bar{P}_{e_1}^{HD}+\bar{P}_{e_2}^{HD}+\bar{P}_{e_3}^{HD}, \tag{3.89}$$

where $\bar{P}_{e_1}^{HD}$ is given as

$$\bar{P}_{e_1}^{HD}=\frac{\varrho}{2}\sqrt{\frac{\nu}{\pi}}\int_{0}^{\infty}\frac{e^{-\nu\gamma^{HD}}}{\sqrt{\gamma^{HD}}}d\gamma^{HD}, \tag{3.90}$$

while $\bar{P}_{e_2}^{HD}$ is expressed as

$$\bar{P}_{e_2}^{HD} = \frac{\varrho}{2}\sqrt{\frac{\nu}{\pi}}\int_0^\infty \frac{e^{-\frac{\varepsilon_R+\varepsilon_D+\nu\varepsilon_R\varepsilon_D}{\varepsilon_R\varepsilon_D}\gamma^{HD}}}{\sqrt{\gamma^{HD}}}d\gamma^{HD}, \tag{3.91}$$

and $\bar{P}_{e_3}^{HD}$ is given as

$$\bar{P}_{e_3}^{HD} = \frac{\varrho}{2}\sqrt{\frac{\nu}{\pi}}\int_0^\infty \frac{\sqrt{\gamma^{HD}}e^{-\frac{\varepsilon_R+\varepsilon_D+\nu\varepsilon_R\varepsilon_D}{\varepsilon_R\varepsilon_D}\gamma^{HD}}}{\varepsilon_R}d\gamma^{HD}. \tag{3.92}$$

The integral in (3.90) can be solved using [123, Eq. (3.361.2)], which yields

$$\bar{P}_{e_1}^{HD} = \frac{\varrho}{2}. \tag{3.93}$$

Moreover, [123, Eq. (3.361.2)] can be exploited to solve (3.91), which results in

$$\bar{P}_{e_2}^{HD} = \frac{\varrho}{2}\sqrt{\frac{\nu\varepsilon_R\varepsilon_D}{\varepsilon_R+\varepsilon_D+\nu\varepsilon_R\varepsilon_D}}. \tag{3.94}$$

Furthermore, (3.92) is evaluated by utilizing the result in [123, Eq. (3.381.4)] such that

$$\bar{P}_{e_3}^{HD} = \frac{\varrho}{2}\sqrt{\frac{\nu}{\pi}}\sqrt{\frac{\varepsilon_D}{\varepsilon_R^2+\varepsilon_R\varepsilon_D+\nu\varepsilon_R^2\varepsilon_D}}. \tag{3.95}$$

Finally, the lower bound E2E ASER of the Af-HD-PLNC system can be obtained by substituting (3.93), (3.94) and (3.95) in (3.89) to give

$$\bar{P}_{e_{E2E}}^{HD} = \frac{\varrho}{2}\left(1+\sqrt{\frac{\nu\varepsilon_R\varepsilon_D}{\varepsilon_R+\varepsilon_D+\nu\varepsilon_R\varepsilon_D}}+\sqrt{\frac{\nu}{\pi}}\sqrt{\frac{\varepsilon_D}{\varepsilon_R^2+\varepsilon_R\varepsilon_D+\nu\varepsilon_R^2\varepsilon_D}}\right). \tag{3.96}$$

This expression will be utilized in the next section to obtain the lower bound E2E ASER of the AF-HD-PLNC system.

3.6.3 End-to-end Ergodic Capacity

In this subsection, we derive the E2E tight upper bound ergodic capacity of the proposed AF-FD-PLNC system. It is noteworthy that using the exact E2E SINR expression given by (3.13) in evaluating the ergodic capacity is not mathematically tractable, therefore, we are going to utilize the tight upper bound of the E2E SINR, (3.18), to evaluate the tight upper bound ergodic capacity for the proposed AF-FD-PLNC. Owing to the fact that the E2E ergodic capacity is dominated by the weakest link in the two-hop relay network, the E2E ergodic capacity of the

proposed system can be given as [127]

$$C_{erg}^{E2E} = \min(C_{erg}^{R}, C_{erg}^{D}), \tag{3.97}$$

where C_{erg}^{R} is given as [128]

$$C_{erg}^{R} = \int_{0}^{\infty} \frac{1}{1+\gamma} \left(1 - P_{\gamma_R}(\gamma)\right) d\gamma, \tag{3.98}$$

while C_{erg}^{D} is expressed as

$$C_{erg}^{D} = \int_{0}^{\infty} \frac{1}{1+\gamma} \left(1 - P_{\gamma_D}(\gamma)\right) d\gamma. \tag{3.99}$$

Moreover, $P_{\gamma_R}(\gamma)$ and $P_{\gamma_D}(\gamma)$ represent the CDF of the SINR at the relay and end nodes, respectively.

The ergodic capacity at the relay, C_{erg}^{R}, can be evaluated by using (3.32) to substitute $P_{\gamma_R}(\gamma)$ in (3.98), which yields

$$\begin{aligned} C_{erg}^{R} = &\int_{0}^{\infty} \frac{\varepsilon_R e^{-\frac{\gamma}{\varepsilon_R}}}{\varsigma_R \left(1+\gamma\right)\left(\frac{\varepsilon_R}{\varsigma_R}+\gamma\right)} d\gamma + \int_{0}^{\infty} \frac{\gamma e^{-\frac{\gamma}{\varepsilon_R}}}{\varsigma_R \left(1+\gamma\right)\left(\frac{\varepsilon_R}{\varsigma_R}+\gamma\right)} d\gamma \\ &+ \int_{0}^{\infty} \frac{\varepsilon_R \gamma e^{-\frac{\gamma}{\varepsilon_R}}}{\varsigma_R \left(1+\gamma\right)\left(\frac{\varepsilon_R}{\varsigma_R}+\gamma\right)^2} d\gamma. \end{aligned} \tag{3.100}$$

The above expression can be presented such as

$$C_{erg}^{R} = C_{erg_1}^{R} + C_{erg_2}^{R} + C_{erg_3}^{R}, \tag{3.101}$$

where $C_{erg_1}^{R}$ is given as

$$C_{erg_1}^{R} = \int_{0}^{\infty} \frac{\varepsilon_R e^{-\frac{\gamma}{\varepsilon_R}}}{\varsigma_R \left(1+\gamma\right)\left(\frac{\varepsilon_R}{\varsigma_R}+\gamma\right)} d\gamma, \tag{3.102}$$

while $C_{erg_2}^{R}$ is expressed such that

$$C_{erg_2}^{R} = \int_{0}^{\infty} \frac{\gamma e^{-\frac{\gamma}{\varepsilon_R}}}{\varsigma_R \left(1+\gamma\right)\left(\frac{\varepsilon_R}{\varsigma_R}+\gamma\right)} d\gamma, \tag{3.103}$$

and $C_{erg_3}^R$ is given as

$$C_{erg_3}^R = \int_0^\infty \frac{\varepsilon_R \gamma e^{-\frac{\gamma}{\varepsilon_R}}}{\varsigma_R \left(1+\gamma\right) \left(\frac{\varepsilon_R}{\varsigma_R}+\gamma\right)^2} d\gamma. \tag{3.104}$$

The integral in (3.102) is mathematically difficult to solve, thus, we exploit the partial fraction decomposition to present this integral in a simplified form such that

$$C_{erg_1}^R = \frac{\varepsilon_R}{\left(\varsigma_R - \varepsilon_R\right)} \int_0^\infty \frac{e^{-\frac{\gamma}{\varepsilon_R}}}{\frac{\varepsilon_R}{\varsigma_R}+\gamma} d\gamma + \frac{\varepsilon_R}{\left(\varepsilon_R - \varsigma_R\right)} \int_0^\infty \frac{e^{-\frac{\gamma}{\varepsilon_R}}}{1+\gamma} d\gamma. \tag{3.105}$$

The integrals in (3.105) can be solved using [123, Eq. (3.352.4)], which results in

$$C_{erg_1}^R = -\left[\frac{\varepsilon_R}{\left(\varsigma_R - \varepsilon_R\right)} e^{\frac{1}{\varsigma_R}} \mathrm{Ei}\left(-\frac{1}{\varsigma_R}\right) + \frac{\varepsilon_R}{\left(\varepsilon_R - \varsigma_R\right)} e^{\frac{1}{\varepsilon_R}} \mathrm{Ei}\left(-\frac{1}{\varepsilon_R}\right)\right], \tag{3.106}$$

where $\mathrm{Ei}\left(x\right)$ denotes the exponential integral function that is defined in [123, Eq. (8.211.1)] as

$$\mathrm{Ei}\left(x\right) = -\int_{-x}^\infty \frac{e^{-t}}{t} dt. \tag{3.107}$$

Analogous to (3.102) the integral in (3.103) can be simplified using partial fraction decomposition, which gives

$$C_{erg_2}^R = \frac{\varepsilon_R}{\varsigma_R \left(\varepsilon_R - \varsigma_R\right)} \int_0^\infty \frac{e^{-\frac{\gamma}{\varepsilon_R}}}{\frac{\varepsilon_R}{\varsigma_R}+\gamma} d\gamma + \frac{1}{\left(\varsigma_R - \varepsilon_R\right)} \int_0^\infty \frac{e^{-\frac{\gamma}{\varepsilon_R}}}{1+\gamma} d\gamma. \tag{3.108}$$

The result of [123, Eq. (3.352.4)] can be utilized to solve the integrals in (3.108) such that

$$C_{erg_2}^R = -\left[\frac{\varepsilon_R}{\varsigma_R \left(\varepsilon_R - \varsigma_R\right)} e^{\frac{1}{\varsigma_R}} \mathrm{Ei}\left(-\frac{1}{\varsigma_R}\right) + \frac{1}{\left(\varsigma_R - \varepsilon_R\right)} e^{\frac{1}{\varepsilon_R}} \mathrm{Ei}\left(-\frac{1}{\varepsilon_R}\right)\right]. \tag{3.109}$$

Moreover, partial fraction decomposition is employed to simplify the integral in (3.104), which gives

$$\begin{aligned} C_{erg_3}^R = {} & \frac{\varepsilon_R^2}{\varsigma_R \left(\varepsilon_R - \varsigma_R\right)} \int_0^\infty \frac{e^{-\frac{\gamma}{\varepsilon_R}}}{\left(\frac{\varepsilon_R}{\varsigma_R}+\gamma\right)^2} d\gamma + \frac{\varepsilon_R \varsigma_R}{\left(\varepsilon_R - \varsigma_R\right)^2} \int_0^\infty \frac{e^{-\frac{\gamma}{\varepsilon_R}}}{\frac{\varepsilon_R}{\varsigma_R}+\gamma} d\gamma \\ & - \frac{\varepsilon_R \varsigma_R}{\left(\varepsilon_R - \varsigma_R\right)^2} \int_0^\infty \frac{e^{-\frac{\gamma}{\varepsilon_R}}}{1+\gamma} d\gamma. \end{aligned} \tag{3.110}$$

The first integral in (3.110) can be solved by exploiting the result of [123, Eq. (3.353.3)], while [123, Eq. (3.352.4)] can be used to solve the second and third integrals, subsequently,

$C^R_{erg_3}$ is given as

$$C^R_{erg_3} = \frac{\varepsilon_R}{(\varepsilon_R - \varsigma_R)} + \frac{\varepsilon_R}{\varsigma_R(\varepsilon_R - \varsigma_R)} e^{\frac{1}{\varsigma_R}} \mathrm{Ei}\left(-\frac{1}{\varsigma_R}\right) + \frac{\varepsilon_R \varsigma_R}{(\varepsilon_R - \varsigma_R)^2} e^{\frac{1}{\varepsilon_R}} \mathrm{Ei}\left(-\frac{1}{\varepsilon_R}\right) - \frac{\varepsilon_R \varsigma_R}{(\varepsilon_R - \varsigma_R)^2} e^{\frac{1}{\varsigma_R}} \mathrm{Ei}\left(-\frac{1}{\varsigma_R}\right). \tag{3.111}$$

Finally, the ergodic capacity at the relay can be evaluated by substituting (3.106), (3.109) and (3.111) in (3.101), which produces

$$C^R_{erg} = \frac{\varepsilon_R}{(\varepsilon_R - \varsigma_R)} + \frac{\varepsilon_R \varsigma_R}{(\varepsilon_R - \varsigma_R)^2} \left[e^{\frac{1}{\varepsilon_R}} \mathrm{Ei}\left(-\frac{1}{\varepsilon_R}\right) - e^{\frac{1}{\varsigma_R}} \mathrm{Ei}\left(-\frac{1}{\varsigma_R}\right) \right] - \frac{1}{(\varsigma_R - \varepsilon_R)} e^{\frac{1}{\varepsilon_R}} \times \mathrm{Ei}\left(-\frac{1}{\varepsilon_R}\right) - \frac{\varepsilon_R}{(\varsigma_R - \varepsilon_R)} \left[e^{\frac{1}{\varsigma_R}} \mathrm{Ei}\left(-\frac{1}{\varsigma_R}\right) - e^{\frac{1}{\varepsilon_R}} \mathrm{Ei}\left(-\frac{1}{\varepsilon_R}\right) \right]. \tag{3.112}$$

On the other hand, using (3.34) to substitute $P_{\gamma_D}(\gamma)$ in (3.99) yields the ergodic capacity at the end nodes, which is given as

$$C^D_{erg} = \int_0^\infty \frac{\varepsilon_D e^{-\frac{\gamma}{\varepsilon_D}}}{(1+\gamma)(\varepsilon_D + \gamma\varsigma_D)} d\gamma. \tag{3.113}$$

The expression above can be simplified using partial fraction decomposition such that

$$C^D_{erg} = \frac{\varepsilon_D}{(\varsigma_D - \varepsilon_D)} \int_0^\infty \frac{e^{-\frac{\gamma}{\varepsilon_D}}}{\frac{\varepsilon_D}{\varsigma_D} + \gamma} d\gamma + \frac{\varepsilon_D}{(\varepsilon_D - \varsigma_D)} \int_0^\infty \frac{e^{-\frac{\gamma}{\varepsilon_D}}}{1+\gamma} d\gamma. \tag{3.114}$$

Moreover, the integrals in (3.114) can be solved by exploiting the result of [123, Eq. (3.352.4)], which produces

$$C^D_{erg} = -\left[\frac{\varepsilon_D}{(\varsigma_D - \varepsilon_D)} e^{\frac{1}{\varsigma_D}} \mathrm{Ei}\left(-\frac{1}{\varsigma_D}\right) + \frac{\varepsilon_D}{(\varepsilon_D - \varsigma_D)} e^{\frac{1}{\varepsilon_D}} \mathrm{Ei}\left(-\frac{1}{\varepsilon_D}\right) \right]. \tag{3.115}$$

Finally, the tight upper bound, E2E ergodic capacity for the proposed AF-FD-PLNC can be evaluated by substituting (3.112) along with (3.115) in (3.97). The obtained expression will be utilized in Section 3.7 to thoroughly study the impact of the residual SI after the active SIC on the achieved E2E ergodic capacity of the proposed AF-FD-PLNC.

Moreover, to meticulously study the throughput gain of the AF-FD-PLNC over the AF-HD-PLNC, the tight upper bound ergodic capacity expression of the AF-HD-PLNC is derived and presented in this subsection. First, the ergodic capacity at the relay of the AF-HD-PLNC system

can be computed by substituting (3.29) in (3.98), which yields

$$C_{erg}^{R_{HD}} = \int_0^\infty \frac{e^{-\frac{\gamma^{HD}}{\varepsilon_R}}}{(1+\gamma^{HD})} d\gamma^{HD} + \int_0^\infty \frac{\gamma^{HD} e^{-\frac{\gamma^{HD}}{\varepsilon_R}}}{\varepsilon_R (1+\gamma^{HD})} d\gamma^{HD}. \tag{3.116}$$

The first integral in (3.116) can be solved using [123, Eq. (3.352.4)], while [123, Eq. (3.383.10)] is exploited to evaluate the second integral in (3.116). Subsequently, $C_{erg}^{R_{HD}}$ is given as

$$C_{erg}^{R_{HD}} = \frac{e^{\frac{1}{\varepsilon_R}}}{\varepsilon_R} \Gamma(2) \Gamma\left(-1, \frac{1}{\varepsilon_R}\right) - e^{\frac{1}{\varepsilon_R}} \mathrm{Ei}\left(-\frac{1}{\varepsilon_R}\right). \tag{3.117}$$

Next, substituting (3.30) in (3.98) yields the expression of the ergodic capacity at the end nodes of the AF-HD-PLNC system, which is given as

$$C_{erg}^{D_{HD}} = \int_0^\infty \frac{e^{-\frac{\gamma^{HD}}{\varepsilon_D}}}{(1+\gamma^{HD})} d\gamma^{HD}. \tag{3.118}$$

The result of [123, Eq. (3.352.4)] can be utilized to solve the integral in (3.118) to give

$$C_{erg}^{D_{HD}} = -e^{\frac{1}{\varepsilon_D}} \mathrm{Ei}\left(-\frac{1}{\varepsilon_D}\right). \tag{3.119}$$

Finally, substituting (3.117) and (3.119) in (3.97) gives the E2E tight upper bound ergodic capacity of the AF-HD-PLNC such that

$$C_{erg}^{E2E_{HD}} = \min\left(\frac{e^{\frac{1}{\varepsilon_R}}}{\varepsilon_R} \Gamma(2) \Gamma\left(-1, \frac{1}{\varepsilon_R}\right) - e^{\frac{1}{\varepsilon_R}} \mathrm{Ei}\left(-\frac{1}{\varepsilon_R}\right), -e^{\frac{1}{\varepsilon_D}} \mathrm{Ei}\left(-\frac{1}{\varepsilon_D}\right)\right). \tag{3.120}$$

This expression will be utilized in the next section to evaluate the E2E tight upper bound ergodic capacity results of the AF-HD-PLNC system, which will be used as a benchmark to study the throughput gain that can be achieved by the proposed AF-FD-PLNC in the presence of residual SI.

3.7 Results

This section presents the analytical results of the proposed AF-FD-PLNC in the presence of residual SI. Furthermore, these analytical results is supported by simulation based results to validate the theoretical expressions that were derived in Sections 3.5 and 3.6. We consider an uncoded OFDM-based FD-TWRC system with two FD end nodes, A and B, exchange informa-

tion with the assistance of one FD relay node, R, over asymmetric Rayleigh fading frequency-selective channels, using AF relaying. The utilized OFDM system parameters are given in Table 3.1, while the average channel impulse responses utilized in the simulations are given in Tables 3.2 and 3.3. It worth mentioning that the average channel impulse response parameters given in Tables 3.2 and 3.3 are used to obtain the channels coefficients that are used in both the theoretical and simulation performance evaluation. Moreover Monte Carlo technique is used to obtain the simulation based outage probability, ASER and ergodic capacity.

Table 3.1: Simulation Settings.

Packet length	8192 (bit)
Number of subcarriers	4096
Length of cyclic prefix (CP)	128
Total Number of transmitted bits	819200000

Table 3.2: Channel model of the channel between node A and the relay.

Delay (ns)	0	110	190	410
Average Power (dB)	0.0	-9.7	-19.2	-22.8

Table 3.3: Channel model of the channel between node B and the relay.

Delay (ns)	0	200	800	1200	2300	3700
Average Power (dB)	0.0	-0.9	-4.9	-8.0	-7.8	-23.9

Table 3.4: The scenarios for residual self-interference for the proposed AF-FD-PLNC.

Scenario (Sc.)	$(\Lambda_{IR}, \Lambda_{IA}, \Lambda_{IB})$ dB
1	(0, 0, 0)
2	(5, 5, 5)
3	(10, 10, 10)

First, the analytical PDF of the E2E upper bound SINR was evaluated using the PDF expression that was obtained in Section 3.5.1, as illustrated in Fig. 4.8. The obtained results in Fig. 3.4 show the impact of the residual SI on the PDF of the E2E SINR, in particular the distribution of the SINR becomes more concentrated at the low SINR region as the amount of the residual SI increases. Next, Fig. 3.5 depicts the analytical E2E outage probability of the conventional

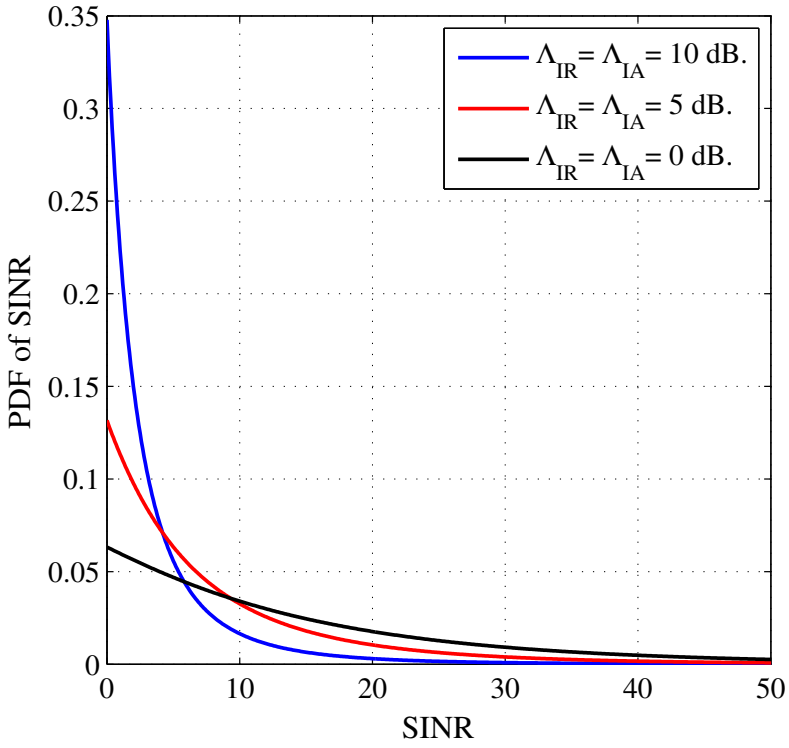

Figure 3.4: The PDF of the SINR at Node A after the SIC for AF-FD-PLNC with different levels of residual SI to noise ratio at SNR= 15 dB.

AF-HD-PLNC along with the proposed AF-FD-PLNC with three different scenarios of residual SI to noise ratio, these scenarios of residual SI to noise ratio vs. SNR after the SIC, whilst the SINR threshold, γ_{th}, was fixed at 15 dB. The considered residual SI to noise ratio scenarios are illustrated in Table 3.4. Moreover, the analytical outage probability results of the AF-FD-PLNC were validated by simulation based results as shown in Fig. 3.5. Comparing the outage probability results of the AF-HD-PLNC with those of the AF-FD-PLNC reveals that there is an SNR of 3.1, 6.3 and 10.5 dB, respectively, when the residual SI to noise ratio at each node ranges from 0 to 10 dB. These SNR penalties show the impact of the residual SI to noise ratio on the E2E outage probability performance of the proposed AF-FD-PLNC system. Hence, the network designers should consider these SNR penalties to maintain the communication quality while improving the network throughput using the FD mode.

The E2E tight lower bound ASER performance vs. SNR of the proposed AF-FD-PLNC system with three SI to noise ratio scenarios, which are depicted in Table 3.4, along with the E2E ASER performance vs. SNR of the AF-HD-PLNC system are shown in Fig. 3.6. Moreover, the analytical results in Fig. 3.6 were verified using exact simulation based E2E ASER performance. A closer inspection of Fig. 3.6 reveals that the analytical and the simulation ASER performance of the proposed AF-FD-PLNC show close match in the low SNR region, while they show a

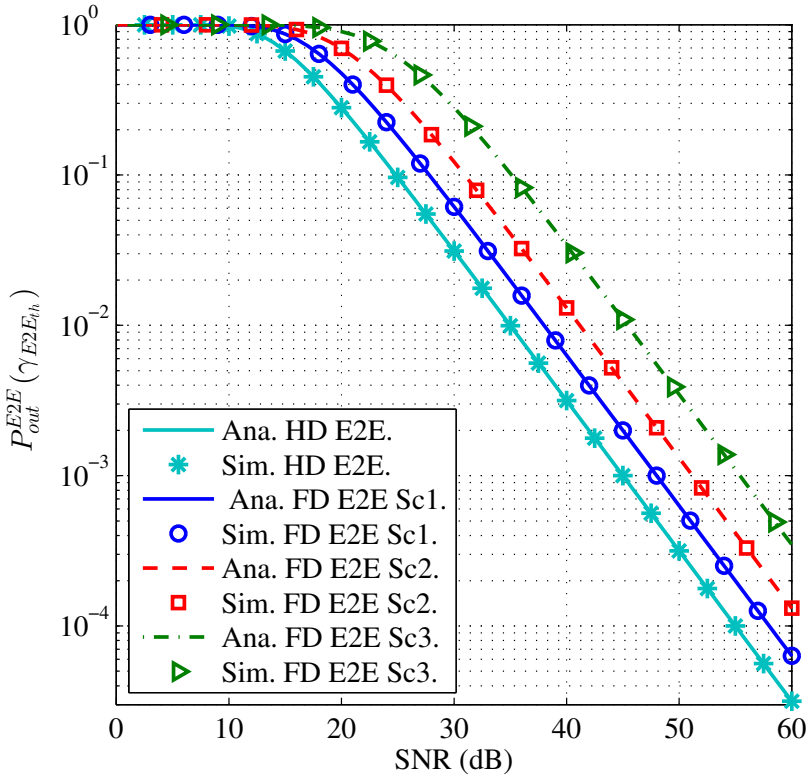

Figure 3.5: The E2E outage probability for AF-FD-PLNC with different levels of residual SI to noise ratio.

perfect match in the mid-high SNR region. Thus, the E2E ASER expression that was derived in Section 3.6 can be considered as a tight lower bound ASER expression. Furthermore, it can be observed from Fig. 3.6 that the ASER for the AF-HD-PLNC and AF-FD-PLNC with three considered scenarios residual SI to noise ratio reaches $10^{-}4$ at SNR equals 39.9, 43.1, 46.4, 50.2 dB, respectively. This gives a clear indication of the effect of the residual SI to noise ratio on the E2E ASER performance of the proposed AF-FD-PLNC.

Next, the tight upper bound ergodic capacity expression that was derived in Section 3.6.3 was used to evaluate the E2E upper bound ergodic capacity for the proposed AF-FD-PLNC as depicted in Fig. 3.7. Furthermore, the exact simulation-based E2E ergodic capacity of the proposed AF-FD-PLNC was obtained as illustrated in Fig. 3.7. These simulation results were included to validate the theoretical E2E ergodic capacity results. Careful inspection of Fig. 3.7 reveals that the upper bound E2E ergodic capacity results of the proposed AF-FD-PLNC system match closely the exact E2E simulation results, which verifies the E2E tight lower bound expression that was presented in Section 3.6.3. Moreover, the E2E ergodic capacity of the AF-HD-PLNC system was compared with the E2E ergodic capacity of the proposed AF-FD-PLNC with three residual SI to noise ratio scenarios that are illustrated in Table 3.4. This comparison

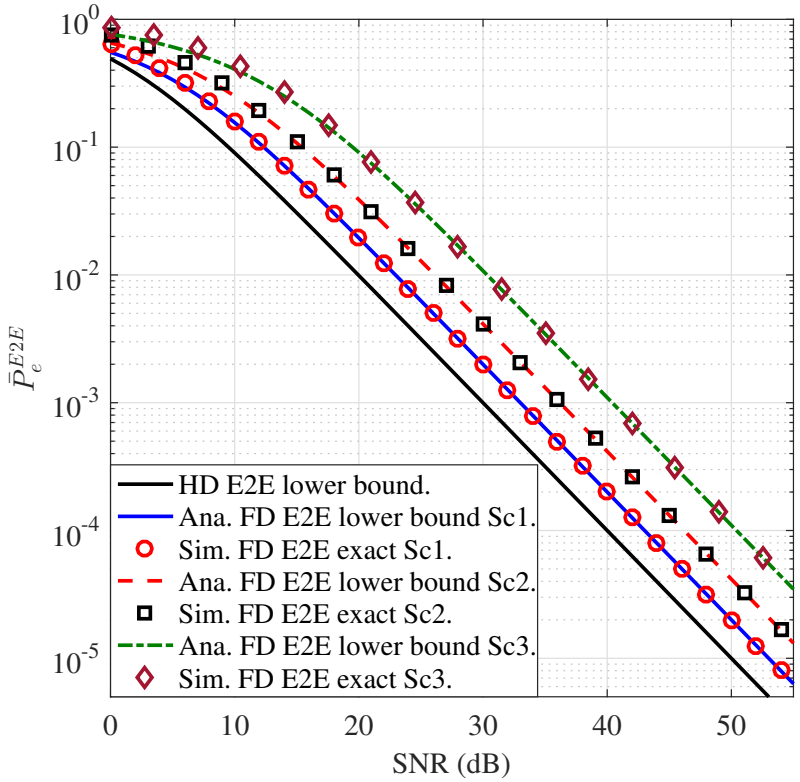

Figure 3.6: The E2E tight lower bound of the ASER for AF-FD-PLNC with different levels of residual SI to noise ratio.

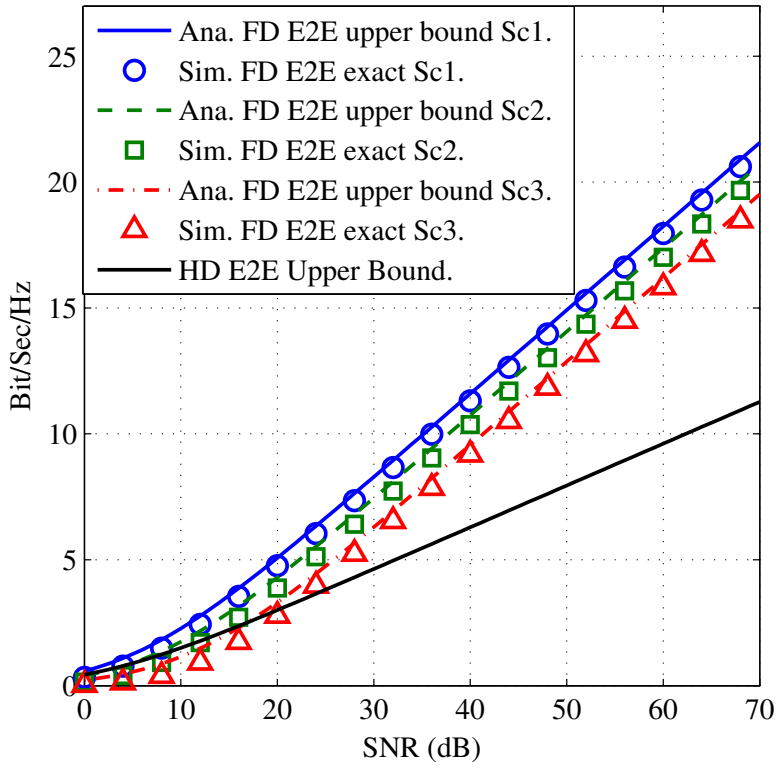

Figure 3.7: The average E2E ergodic capacity after the SIC for AF-FD-PLNC with different levels of residual SI to noise ratio.

has revealed that the proposed AF-FD-PLNC can double the ergodic capacity of the conventional AF-HD-PLNC when the SNR is larger than 25 dB and the residual SI to noise ratio is smaller than 0 dB. Furthermore, the ergodic capacity results in Fig. 3.7 show the effect of the residual SI to noise ratio on the E2E ergodic capacity performance of the proposed AF-FD-PLNC system.

3.8 Chapter Summary

In this chapter, we presented an OFDM based AF-FD-PLNC system, which is combined with a SIC scheme to mitigate the effect of the SI signal. This SIC comprises passive and active SIC schemes, which are integrated together to improve attained SI suppression. Moreover, the impact of the residual SI to noise ratio on the PDF of the SINR was examined and a closed-form expression of the PDF of the E2E SINR of the AF-FD-PLNC system was presented in this chapter. Next, closed-form expressions for the E2E outage probability and E2E lower bound ASER of the Af-FD-PLNC system were derived, presented and validated using extensive simulation studies. In particular, the theoretical E2E lower bound ASER results of the proposed system have shown a perfect match with the simulation based exact E2E ASER in the mid-high SNR region. An exact expression of the tight upper bound E2E ergodic capacity of the proposed system was introduced and supported using simulation results in this chapter. Furthermore, the ergodic capacity of the AF-FD-PLNC was evaluated in the presence of the residual SI and compared with that of the AF-HD-PLNC system. All of the derived theoretical expressions have been verified using simulation studies. Next, the derived E2E tight upper bound ergodic capacity expression for the proposed system was used to evaluate the E2E ergodic capacity of the AF-FD-PLNC. The obtained results of the AF-FD-PLNC system were compared with those of the conventional AF-HD-PLNC, which demonstrated the ergodic capacity gain of the proposed AF-FD-PLNC over the ergodic capacity of the traditional AF-HD-PLNC. In particular, the proposed AF-FD-PLNC can increase the ergodic capacity of AF-HD-PLNC by a factor of 2 when the SNR is higher than 25 dB and the SI to noise ratio is less than 0 dB. However, the E2E ASER and outage probability results have shown that there is an SNR penalty in the proposed AF-FD-PLNC system, which varies with the amount of the residual SI.

It is worth pointing out that the active SIC scheme, which is utilized in this chapter, exploits the perfect knowledge of the transceiver nodes transmitted signal in conjunction of the perfect CSI of the SI channel to effectively suppress the SI signal. Hence, the availability of the perfect CSI at each transceiver node is crucial to the performance of the active SIC scheme. However,

in practice, it is very challenging to obtain the perfect CSI. This has been identified as the key limitation of the proposed SIC technique. Thus, in the next chapter, we present an adaptive SIC scheme, which exploits the NLMS algorithm to effectively suppress the SI signal without the need to have the perfect CSI of the SI channel.

Chapter 4

An One-Timeslot Full-Duplex Two-Way Relay Channel System Exploiting Adaptive-SIC

4.1 Introduction

The implementation of an effective SIC scheme that can enable the in-band FD mode, i.e. the transceiver nodes transmit and receive simultaneously over the same frequency band, has attracted a massive research focus. Hence, recently number of different SIC schemes have been presented [7–11, 36, 129]. Chapter 3 presented an active SIC scheme, which requires the CSI of the SI channel to be available at each transceiver node. In this chapter, we introduce an adaptive SIC scheme that exploits the normalized least-mean-square (NLMS) algorithm to suppers the SI signal without the need for the CSI of the SI channel. This adaptive SIC scheme utilizes each nodes knowledge of its own transmitted signal in conjunction with the NLMS algorithm to construct a replica of the SI signal and subtract this replica from the received signal before the ADC. Subsequently, this SIC scheme diminishes the SI signal before the ADC, which prevents the ADC from being inundated with the SI signal.

The introduced adaptive SIC is integrated with a DNF-FD-PLNC system, to enable the FD communication mode by mitigating the SI signal. This DNF-PLNC comprises two end nodes, A and B, that exchange information with the aid of a DNF relay node R. The main motivation of the proposed DNF-FD-PLNC is to reduce the number of time slots required to attain one information packet exchange between the end nodes in the TWRC network that exploits the PLNC scheme. In general, a DNF-HD-PLNC scheme consists of two phases. During the

first phase both of the end nodes, A and B, simultaneously transmit their information to the relay node and the relay performs the denoising operation on the received superimposed signal [75, 76]. Therefore, this phase is called the uplink or multiple access (MA) phase. In the sitecond phase, the relay broadcasts the denoised signal to the end nodes [130]. This phase is called the downlink or broadcast (BC) phase. Hence, a DNF-HD-PLNC can accomplish one information packet E2E exchange between the end nodes A and B in two time slots, i.e. one time slot for each phase [72, 73, 130]. In the proposed DNF-FD-PLNC both of the phases. i.e. MA and BC, take place concurrently in one time slot, subsequent one time slot is sufficient to accomplish one information packet exchange between the end nodes.

In this chapter, we examine the performance of a DNF-FD-PLNC system for reciprocal asymmetric Rayleigh fading channels. Firstly, a closed-form expression for the distribution of the SINR at each node is derived. Secondly, an exact E2E outage probability expression for the proposed DNF-FD-PLNC system is presented. Thirdly, the analytical E2E ASER is derived. Finally, an E2E closed-form expression for the ergodic capacity for the proposed DNF-FD-PLNC system is presented. The obtained results reveal that the ergodic capacity is limited by the amount of residual SI. Moreover, these results confirm that the proposed DNF-FD-PLNC can achieve up to approximately double the throughput of the DNF-HD-PLNC for SNR levels greater than 20 dB and SI to noise ratio levels less than 0 dB.

The rest of the paper is organized as follows: Section 4.2 presents the DNF-FD-PLNC system. Section 4.3 illustrates the architecture of the adaptive SIC scheme. Section 4.4 thoroughly studies the performance of the adaptive SIC scheme. The impact of the imperfect CSI on the performance of the DNF-FD-PLNC system is investigated in Section 4.5. Section 4.6 provides the SINR for the DNF-FD-PLNC system. In Section 4.7, the expressions for the PDF of the SINR at each node along with the E2E outage probability expression for the DNF-FD-PLNC system are derived and presented. In Section 4.8, the E2E ASER expression for the DNF-FD-PLNC is derived. Section 4.9 investigates the E2E ergodic capacity for DNF-FD-PLNC and DNF-HD-PLNC systems. Section 4.10 presents the analytical and simulation results of the proposed system. Finally, the summary of this chaper is presented in Section 4.11.

4.2 System Model

This section presents the DNF-FD-PLNC system. We consider an uncoded quadrature phase shift keying (QPSK) TWRC network with three nodes, two FD end nodes, A and B, and one FD relay node, R. It is noteworthy, that QPSK modulation is considered in this work to simplify

the illustration of the DNF relaying scheme exploited in the proposed system. It can be seen from Fig. 5.1 that all nodes in the proposed system are equipped with two antennas dedicated to transmission and reception, respectively. This is a relatively low complexity approach as compared with the MIMO approaches as in [16] and [91]. Moreover, this is a more practical solution to mitigate SI than using a single antenna as in [131]. We assume that the end nodes intend to exchange information, yet, there is no direct path connecting them. Thus, they perform information exchange with the aid of node R, which acts as a relay as depicted in Fig. 5.1. Since all the nodes in the proposed DNF-FD-PLNC system can transmit and receive concurrently, the end nodes can exchange up to $2(I-1)$ packets in I time slots. In contrast, I information packets can be exchanged between the end nodes in I time slots in a DNF half-duplex physical-layer network coding (DNF-HD-PLNC) system.

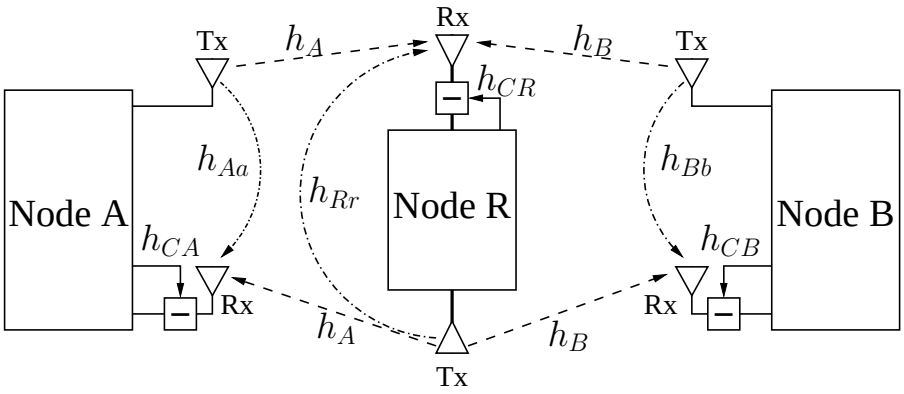

Figure 4.1: Full-duplex physical_layer network coding (FD-PLNC) system.

It is noteworthy that there are two types of channels in the proposed system, i.e. the self-interference channels between a node's TX and RX antennas and the channels between the source nodes and the relay, which are assumed to be quasi-static asymmetric and reciprocal frequency flat Rayleigh-fading channels. Reciprocal implies that the uplink and down-link channels are identical. Moreover, owing to the fact that in the full-duplex mode the nodes transmit and receive simultaneously using the same band, SI signal comprises the direct TX-to-RX antenna path signal and the signals reflected from the surrounding objects. Therefore, the SI channel is modelled as a multipath channel [92].

Given the data symbols at the end nodes are modulated using QPSK, $x_A = \mathcal{M}(S_A)$, $x_B = \mathcal{M}(S_B)$ are the transmitted signals from the two end nodes and $\mathcal{M}$ denotes the Gray mapping to a QPSK constellation. Moreover, at the relay node x_R is obtained from the received signal in the previous time slot using the DNF relaying scheme that was derived and introduced in [80]. This scheme starts with maximum-likelihood (ML) detection followed by two mappers, i.e. the denoising mapper, $\mathcal{DM}$, and the constellation mapper, $\mathcal{CM}$ [80]. Firstly, the ML detection is

performed as follows

$$(\hat{S}_A(n), \hat{S}_B(n)) = \underset{(q_1,q_2)\in\mathbb{Z}_4\times\mathbb{Z}_4}{\operatorname{argmin}} \mid y_R(n) - (h_A(n)\mathcal{M}(q_1) + h_B(n)\mathcal{M}(q_2)) \mid^2, \tag{4.1}$$

to obtain the estimates, $\hat{S}_A$ and $\hat{S}_B$. Secondly, the ML output is mapped to a network-coded dibits signal S_R using the denoising mapper $\mathcal{DM}$ as follows

$$S_R(n) = \mathcal{DM}(\hat{S}_A(n), \hat{S}_B(n)), \tag{4.2}$$

where $\mathcal{DM}$ is given as

$$\mathcal{DM}(\hat{S}_A(n), \hat{S}_B(n)) = \hat{S}_A(n) \oplus \hat{S}_B(n), \tag{4.3}$$

where $\oplus$ denotes a bit-wise XOR operation. The ML detection process followed by the denoising mapping process is referred to as PLNC denoising. Finally, the constellation mapper $\mathcal{CM}$ maps S_R to a QPSK modulated symbol. This mapping process is referred to as PLNC mapping and is given as

$$x_R(n) = \mathcal{CM}(S_R(n)). \tag{4.4}$$

This mapping operation is performed in a manner that enables the end nodes to extract the data transmitted by the other end node using the knowledge of their own transmitted data during the previous time slot.

The received signal at the relay node in the uplink is given as

$$y_R(n) = x_A(n)h_A(n) + x_B(n)h_B(n) + \sum_{l_R=0}^{L_R} h_{R_I}(l_R)x_R(n - l_R + 1) + w_R(n). \tag{4.5}$$

where h_A and h_B denote the channel coefficients between the relay and the end nodes, A and B, respectively, h_{R_I} represents the self-interference multipath channel coefficient between the TX and RX antennas at the relay, L_R represents the maximum delay spread of the channel between the TX and RX antennas at the relay. Furthermore, S_A and S_B are the digital dibits for the QPSK symbols and w_R represent the additive white Gaussian noise (AWGN) samples at the relay node exhibiting a complex-valued circular Gaussian distribution, whose PDF is

$\mathcal{CN}(0, N_0)$. Furthermore, the received signal at the end nodes takes the form of

$$y_D(n) = x_R(n)h_D(n) + \sum_{l_D=0}^{L_D} h_{D_I}(l_D)x_D(n - l_D + 1) + w_D(n), \tag{4.6}$$

where $D \in \{A, B\}$ whilst $D_I \in \{A_I, B_I\}$, w_D represents complex-valued AWGN with $\mathcal{CN}(0, N_0)$. h_{A_I} and h_{B_I} represent the self-interference multipath channel coefficients between the TX and RX antennas at the end nodes. Moreover, L_J denotes the maximum delay spread of the channel between the TX and RX antennas at the end nodes.

A FD-PLNC system is expected to double the throughput compared to the HD-PLNC system, yet this cannot be achieved unless the SI signal is significantly suppressed. This fact has raised the demand for an effective SIC system. Therefore, the proposed DNF-FD-PLNC system is combined with an hybrid self-interference cancellation system to mitigate the effect of the SI signal.

4.3 Adaptive Self-interference Cancellation

In this section, the DNF-FD-PLNC system is combined with a normalized least-mean-square (NLMS) adaptive self-interference cancellation (SIC) scheme. Since the SI channel is modelled as a multipath channel [92], the SI signal can be expressed as

$$SI(n) = \mathbf{h}_{J_I}^H \mathbf{x}(n), \tag{4.7}$$

where $J \in \{A, B, R\}$ while $J_I \in \{A_I, B_I, R_I\}$, $(.)^H$ denotes Hermitian transposition, $\mathbf{x}(n) = [x(n), ..., x(n - L_J + 1)]^T$ and $\hat{\mathbf{h}}_{\mathbf{J_I}} = \left[\hat{h}_{J_I}^1, ..., \hat{h}_{J_I}^{L_J}\right]^T$. Furthermore, L_J represents the maximum delay spread of the channel between the TX and RX antennas at each node.

As depicted in Figs. 4.2 and 4.3 each node exploits its perfect knowledge of its own transmitted signal to generate a replica of the SI signal, i.e. $cs(n)$, with the aid of an adaptive filter, $\hat{\mathbf{h}}_{\mathbf{J_I}}$, such that

$$cs(n) = \hat{\mathbf{h}}_{J_I}^H \mathbf{x}(n). \tag{4.8}$$

The length of the adaptive filter coefficients is set to be equal to the length of the channel between TX and RX antennas at each node, $\mathrm{L_J}$. The adaptive filter output, $cs(n)$, is then subtracted from the received signal to effectively mitigate the effect of the SI signal before the analog-to-digital converter (ADC) to prevent the ADC saturation. The residual self-interference

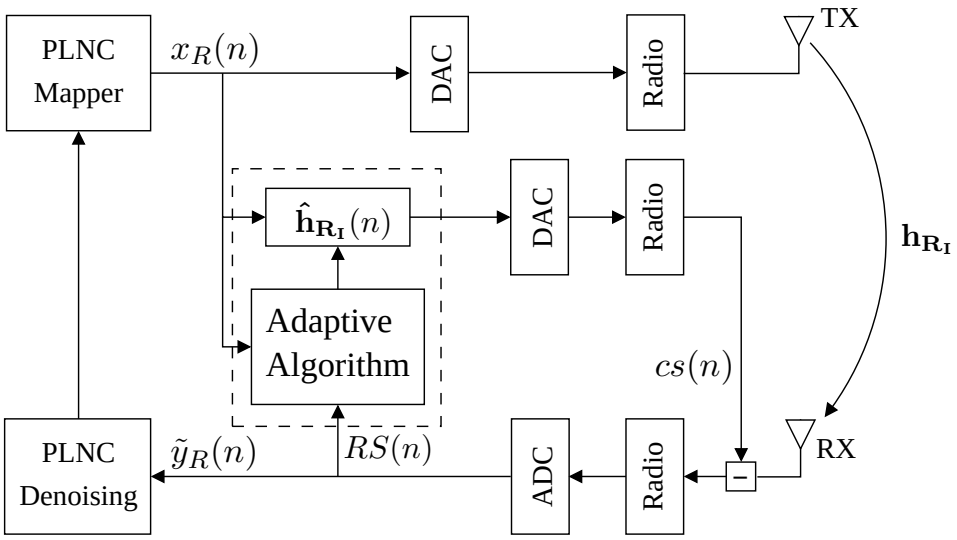

Figure 4.2: Architecture of the relay node of the DNF-FD-PLNC system combined with the adaptive SIC scheme.

(RS), resulting from subtracting cs(n) from SI(n) can be expressed as

$$RS(n) = SI(n) - cs(n). \tag{4.9}$$

In this paper, we consider the normalized least-mean-square (NLMS) algorithm to adjust the filter coefficients. Unlike the conventional least-mean-square (LMS) algorithm, NLMS does not suffer from a gradient noise amplification problem. It has been shown in [132], that the criterion for NLMS algorithm can be formulated as a constrained optimization one, where the updated tap-weight vector, $\hat{\mathbf{h}}_{\mathbf{J_I}}(n+1)$, is determined so as to minimize the squared Euclidean norm of the change,

$$\delta\hat{\mathbf{h}}_{J_I}(n+1) = \hat{\mathbf{h}}_{J_I}(n+1) - \hat{\mathbf{h}}_{J_I}(n), \tag{4.10}$$

subject to the constraint

$$\hat{\mathbf{h}}^H_{J_I}(n+1)\mathbf{x}(n) = SI(n). \tag{4.11}$$

Using the method of Lagrange multipliers, this constrained optimization problem can be converted into unconstrained one, thus its cost function can be expressed as

$$C(n)=||\delta\hat{\mathbf{h}}_{J_I}(n+1)||^2 + \mathrm{Re}\left[\lambda^*\left(SI(n) - \hat{\mathbf{h}}^H_{J_I}(n+1)\mathbf{x}(n)\right)\right], \tag{4.12}$$

where λ is the complex-valued Lagrange multiplier, asterisk represents complex conjugation

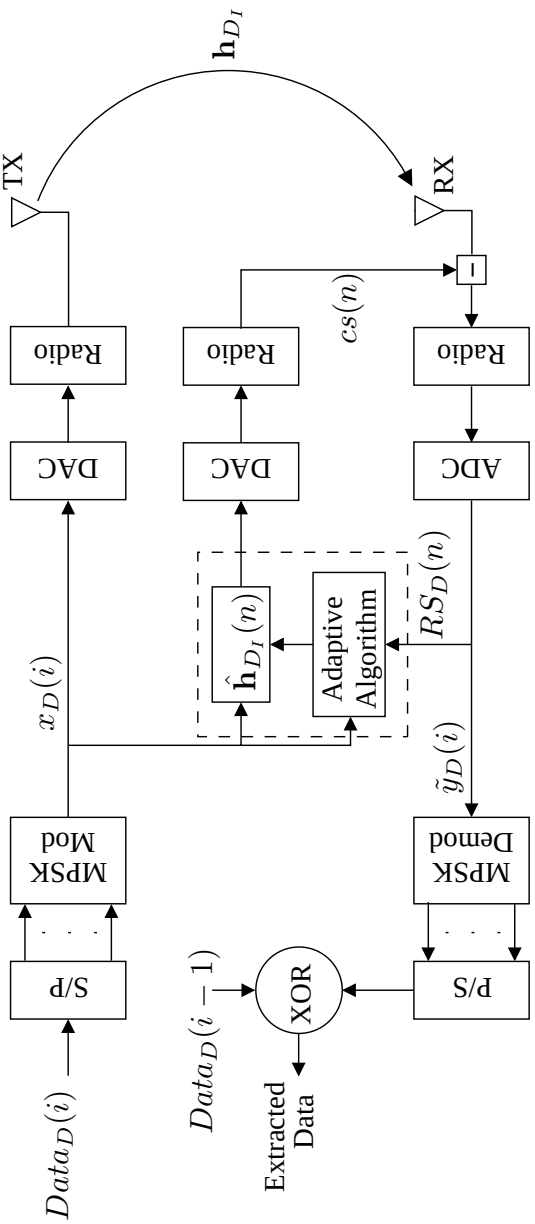

Figure 4.3: Architecture of the end node of the DNF-FD-PLNC system combined with the adaptive SIC scheme.

and $\mathrm{Re}[\cdot]$ denotes real-part operator. Using (4.10), to substitute $\delta\hat{\mathbf{h}}_{J_I}(n+1)$ in (4.12) gives

$$C(n) = \left(\hat{\mathbf{h}}_{J_I}(n+1) - \hat{\mathbf{h}}_{J_I}(n)\right)^H \left(\hat{\mathbf{h}}_{J_I}(n+1) - \hat{\mathbf{h}}_{J_I}(n)\right) + \mathrm{Re}\left[\lambda^* \left(SI(n) - \hat{\mathbf{h}}_{J_I}^H(n+1)\mathbf{x}(n)\right)\right]. \tag{4.13}$$

In order to find the optimum value of the updated weight vector the cost function, $C(n)$, differentiated with respect to $\hat{\mathbf{h}}_{J_I}^H(n+1)$, which results in

$$\frac{\partial C(n)}{\partial \hat{\mathbf{h}}_{J_I}^H(n+1)} = 2\left(\hat{\mathbf{h}}_{J_I}(n+1) - \hat{\mathbf{h}}_{J_I}(n)\right) - \lambda^*\mathbf{x}(n). \tag{4.14}$$

Setting this result equal to zero yields the optimum value of $\hat{\mathbf{h}}_{J_I}(n+1)$ as

$$\hat{\mathbf{h}}_{J_I}(n+1) = \hat{\mathbf{h}}_{J_I}(n) + \frac{1}{2}\lambda^* \mathbf{x}(n). \tag{4.15}$$

Using (4.15) to substitute $\hat{\mathbf{h}}_{J_I}(n+1)$ in (4.11) gives

$$SI(n) = \hat{\mathbf{h}}_{J_I}^H(n)\mathbf{x}(n) + \frac{1}{2}\lambda ||\mathbf{x}(n)||^2 \tag{4.16}$$

Then, solving for λ yields

$$\lambda = \frac{2RS(n)}{||\mathbf{x}(n)||^2}. \tag{4.17}$$

Using this result to substitute λ in (4.15) gives

$$\hat{\mathbf{h}}_{J_I}(n+1) = \hat{\mathbf{h}}_{J_I}(n) + \frac{1}{||\mathbf{x}(n)||^2}\mathbf{x}(n)RS^*(n). \tag{4.18}$$

To control the change in the tap weight from one adaptation cycle to the next one, a positive adaptation constant, $\tilde{\mu}$, is introduced, hence, (4.18) can be expressed as

$$\hat{\mathbf{h}}_{J_I}(n+1) = \hat{\mathbf{h}}_{J_I}(n) + \frac{\tilde{\mu}}{||\mathbf{x}(n)||^2}\mathbf{x}(n)RS^*(n). \tag{4.19}$$

Furthermore, to overcome the problem that may arise when the input vector, $\mathbf{x}(n)$, is small, i.e. dividing by a small value for the squared norm, $||\mathbf{x}(n)||^2$, (4.19) is modified such that

$$\hat{\mathbf{h}}_{J_I}(n+1) = \hat{\mathbf{h}}_{J_I}(n) + \frac{\tilde{\mu}}{\delta + ||\mathbf{x}(n)||^2}\mathbf{x}(n)RS^*(n), \tag{4.20}$$

where $0 < \delta \leq 1$.

4.4 Residual Self-Interference

This section investigates the performance of the adaptive SIC scheme and evaluates the properties of the residual SI signal after the adaptive SIC. First, we investigate the convergence of the residual SI signal after the adaptive SIC towards the noise floor. Fig. 4.4 illustrates the simulation based instantaneous power of the residual SI after the adaptive SIC for the first 10000 samples. Furthermore, Fig. 4.4 shows the instantaneous power of the residual SI that is obtained by subtracting the SI signal, which is generated using the NLMS filter, from the actual SI signal. A closer inspection of Fig. 4.4 reveals that the power of the residual SI reaches the level of the

noise floor after 2000 samples with mean $\simeq -120$ dB and standard deviation $\simeq 5$ dB.

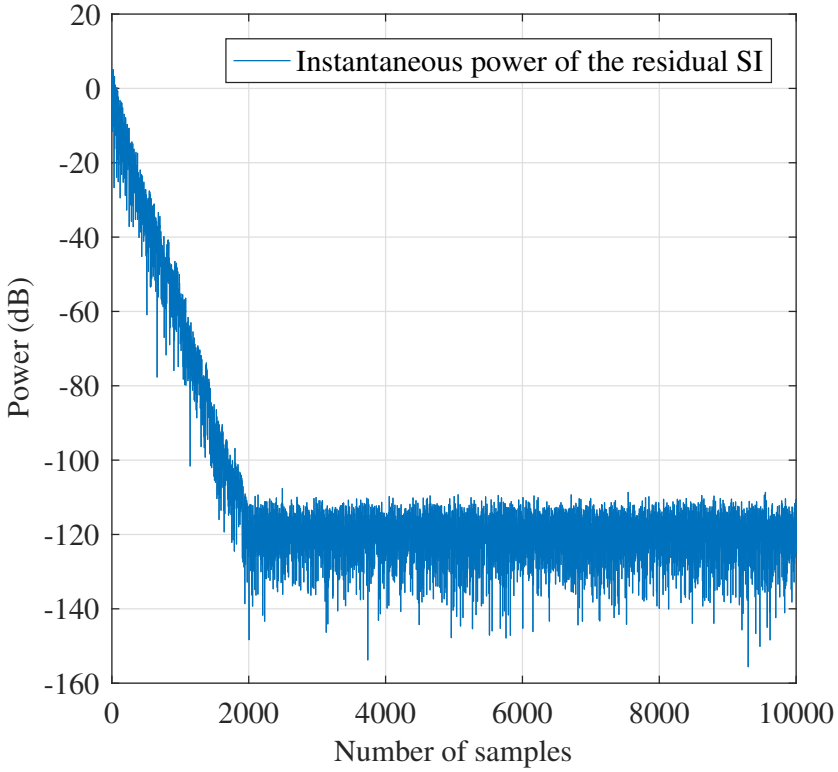

Figure 4.4: The power of the residual self-interference signal.

Moreover, Fig. 4.5 depicts the distribution of the magnitude residual SI, $|Rs|$, after the adaptive SI along with fitted complex Gaussian distribution. It can be observed form Fig. 4.5 that the residual SI signal follows the complex Gaussian distribution. Hence, in analysis it is fair to assume that the distribution of the residual SI exhibits a complex Gaussian distribution. The residual SI signal need to be included in the description of the received at each node. Subsequently, the received signal after self-interference cancellation will be given as

$$\tilde{y}_R(n) = x_A(i)h_A(n) + x_B(n)h_B(n) + RS_R(n) + w_R(n), \tag{4.21}$$

$$\tilde{y}_D(n) = x_R(n)h_D(n) + RS_D(n) + w_D(n), \tag{4.22}$$

where $D \in \{A, B\}$ and RS_J is modelled using a conditionally complex-valued Gaussian PDF, i.e. $\mathcal{CN}(0, \mho_J)$, with $\mho_J = \mathbf{E}\left[RS_J RS_J^{\dagger}\right]$, for $J \in \{A, B, R\}$, see Fig. 4.5.

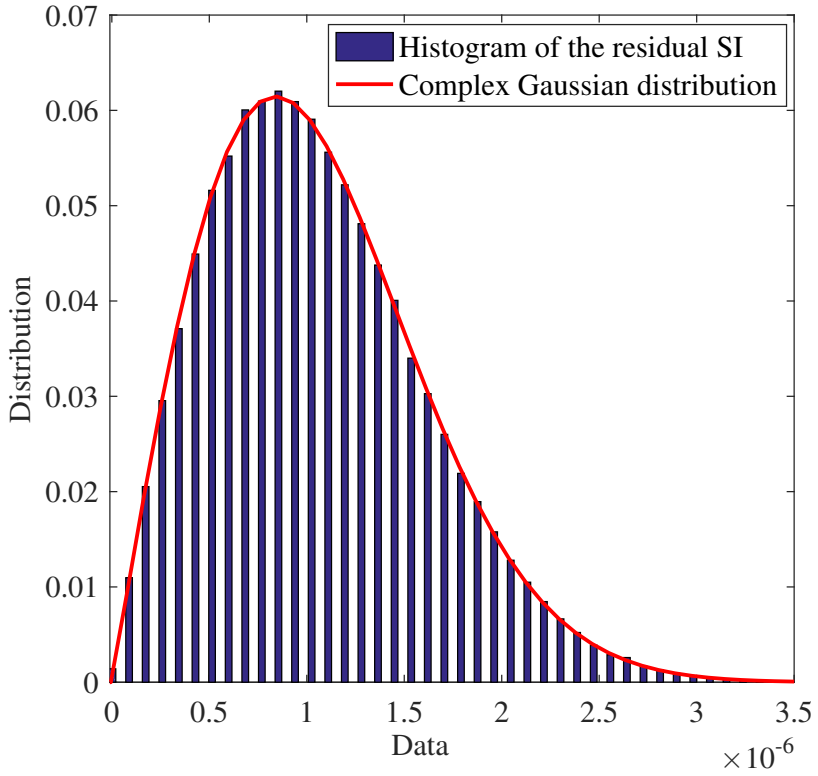

Figure 4.5: Histogram of $|RS_J|$ with fitted complex Gaussian distribution.

4.5 Signal-to-Interference-and-Noise Ratio (SINR)

It can be observed from (4.21) that the first two terms in the equation are the terms of interest and the rest are undesired terms considered as interference and/or noise. Consequently, the instantaneous signal-to-interference and noise ratio (SINR) at the relay can be written as

$$\gamma_R = \frac{|\sqrt{E_{b_A}}h_A + \sqrt{E_{b_B}}h_B|^2}{\mho_R + N_0}, \tag{4.23}$$

where E_{b_J} are the average bit energies for $J \in \{A, B, R\}$. It is worth noting the symbol indices have been dropped for clarity purposes. Since both end nodes are transmitting QPSK modulated signals with $E_{b_A} = E_{b_B}$, the instantaneous SINR can be re-written as

$$\gamma_R = \frac{E_{b_D}|h_A + h_B|^2}{\mho_R + N_0}. \tag{4.24}$$

Moreover, the signal-to-noise ratio (SNR) at the relay is given as $\Omega_R = E_{b_D}/N_0$ and the interference-to-noise ratio (INR) at the relay is given as $\Omega_{IR} = \mho_R/N_0$, which is assumed

to be a random variable. Hence, the instantaneous SINR at the relay can be given as

$$\gamma_R = \frac{\Omega_R |h_A + h_B|^2}{\Omega_{IR} + 1}. \tag{4.25}$$

The SNR at the end nodes is given as $\Omega_D = (E_{b_R}/N_0)$ and the INR at the end nodes is given as $\Omega_{ID} = (\mho_D/N_0)$, where Ω_{ID} is considered to be a random variable. Thus, the instantaneous SINR at the end nodes can be given as

$$\gamma_D = \frac{\Omega_D |h_D|^2}{\Omega_{ID} + 1}, \tag{4.26}$$

To simplify (4.25), $|h_A + h_B|^2$ is substituted by the random variable, Υ, therefore, the SINR at the relay can be rewritten as

$$\gamma_R = \frac{\Omega_R \Upsilon}{\Omega_{IR} + 1}. \tag{4.27}$$

It is clear that (4.27) can be represented as a combination of two independent random variables as follows

$$\gamma_R = \frac{\Omega_R \Upsilon}{\Omega_{IR} + 1} = \frac{y_R}{x_R + 1}. \tag{4.28}$$

The random variables x_R and y_R in (4.28) are given as $y_R = \Omega_R \Upsilon$ and $x_R = \Omega_{IR}$. Furthermore, (4.26) is a combination of two random variables, i.e.

$$\gamma_D = \frac{y_D}{x_D + 1}. \tag{4.29}$$

The random variables x_D and y_D in (4.29) are given as $y_D = \Omega_D |h_D|^2$ and $x_D = \Omega_{ID}$. Since all the channels and the residual SI exhibit a Rayleigh distribution, these random variables, i.e. x_J and y_J, follow Gamma distributions. Thus, the PDF of x_J is given as

$$p_{x_J}(x_J) = \frac{1}{\beta_J} e^{-\frac{x_J}{\beta_J}}, \tag{4.30}$$

where $J \in \{A, B, R\}$, $\beta_J = E\{x_J\}$. Furthermore, since both of the end nodes receives its signal from one node, i.e. the relay node, during the BC phase, the shape factor for $p_{y_D}(y_D)$ is $m_D = 1$, therefore, $p_{y_D}(y_D)$ is given as

$$p_{y_D}(y_D) = \frac{1}{\alpha_D} e^{-\frac{y_D}{\alpha_D}}, \tag{4.31}$$

where $D \in \{A, B\}$ and $\alpha_D = E\{y_D\}$. In contrast, as the relay node receives signals from both of the end nodes simultaneously, the shape factor for $p_{y_R}(y_R)$ is $m_R = 2$, therefore, $p_{y_R}(y_R)$ is given as

$$p_{y_R}(y_R) = \frac{y_R}{\alpha_R^2} e^{-\frac{y_R}{\alpha_R}}, \tag{4.32}$$

where $\alpha_R = \frac{1}{2}E\{y_R\}$.

4.6 Outage Probability

Since x_R and y_R are independent random variables, the PDF of the SINR can be expressed as the integral [122, Eq. (4.6)]

$$p_{\gamma_J}(\gamma_J) = \int_0^\infty (1 + x_J) p_{y_J}\big((1 + x_J)\gamma_R\big) p_{x_J}(x_J) dx_J. \tag{4.33}$$

Using (4.30) and (4.32) to substitute $p_{x_J}(x_J)$ and $p_{y_J}(y_J)$ in (4.33), the PDF of the SINR at the relay, $p_{\gamma_R}(\gamma_R)$ yields

$$p_{\gamma_R}(\gamma_R) = \frac{\gamma_R e^{-\frac{\gamma_R}{\alpha_R}}}{\alpha_R^2 \beta_R} \int_0^\infty (1 + x_R)^2 e^{-\frac{\gamma_R \beta_R + \alpha_R}{\alpha_R \beta_R} x_R} dx_R. \tag{4.34}$$

This integral can be presented as

$$\begin{aligned} p_{\gamma_R}(\gamma_R) = \frac{\gamma_R e^{-\frac{\gamma_R}{\alpha_R}}}{\alpha_R^2 \beta_R} \Bigg[& \int_0^\infty e^{-\frac{\gamma_R \beta_R + \alpha_R}{\alpha_R \beta_R} x_R} dx_R + \int_0^\infty 2 x_R e^{-\frac{\gamma_R \beta_R + \alpha_R}{\alpha_R \beta_R} x_R} dx_R \\ & + \int_0^\infty x_R^2 e^{-\frac{\gamma_R \beta_R + \alpha_R}{\alpha_R \beta_R} x_R} dx_R \Bigg]. \end{aligned} \tag{4.35}$$

The result of [123, Eq. (3.351.3)] can be exploited to solve the first integral, while the second and the third integrals can be solved using this formula $\int_{x=0}^\infty x^n e^{-\mu x} dx = n! \mu^{-n-1}$ for $[\mathbf{Re}\ \mu > 0]$ [123, Eq. (3.351.3)] to give the PDF of the SINR at the relay such that

$$p_{\gamma_R}(\gamma_R) = \frac{\gamma_R e^{-\frac{\gamma_R}{\alpha_R}}}{\alpha_R^2 \beta_R} \left[\frac{\alpha_R \beta_R}{\gamma_R \beta_R + \alpha_R} + 2 \left(\frac{\alpha_R \beta_R}{\gamma_R \beta_R + \alpha_R} \right)^2 + 2 \left(\frac{\alpha_R \beta_R}{\gamma_R \beta_R + \alpha_R} \right)^3 \right]. \tag{4.36}$$

On the other hand, the PDF of the SINR at the end nodes can be evaluated by utilizing (4.30)

and (4.31) to substitute $p_{x_J}(x_J)$ and $p_{y_J}(y_J)$ in (4.33), which gives

$$p_{\gamma_D}(\gamma_D) = \frac{e^{-\frac{\gamma_D}{\alpha_D}}}{\alpha_D\beta_D}\left[\int_0^\infty e^{-\frac{\gamma_D\beta_D+\alpha_D}{\alpha_D\beta_D}x_D}dx_D + \int_0^\infty x_D e^{-\frac{\gamma_D\beta_D+\alpha_D}{\alpha_D\beta_D}x_D}dx_D\right]. \tag{4.37}$$

Utilizing [123, Eq. (3.310)] and [123, Eq. (3.351.3)], i.e. $\int_{x=0}^\infty x^n e^{-\mu x}dx = n!\mu^{-n-1}$ for $[\mathbf{Re}\ \mu > 0]$, to solve the first and second integrals, respectively, results in

$$p_{\gamma_D}(\gamma_D) = \frac{e^{-\frac{\gamma_D}{\alpha_D}}}{\alpha_D\beta_D}\left[\frac{\alpha_D\beta_D}{\gamma_D\beta_D+\alpha_D} + \left(\frac{\alpha_D\beta_D}{\gamma_D\beta_D+\alpha_D}\right)^2\right]. \tag{4.38}$$

The outage probability is a performance metric that is used to measure the quality of the communication between the nodes. The outage probability is defined as the probability that the SINR falls below a certain threshold γ_{th} [125], and is given as

$$P^J_{out}(\gamma_{J_{th}}) \triangleq Pr\{\gamma_J \leq \gamma_{J_{th}}\} = \int_0^{\gamma_{J_{th}}} p_{\gamma_J}(\gamma_J)d\gamma_J. \tag{4.39}$$

Substituting (4.33) in (4.39) gives

$$P^J_{out}(\gamma_{J_{th}}) = \int_0^{\gamma_{J_{th}}}\int_0^\infty (1+x_J)p_{y_J}\big((1+x_J)\gamma_J\big)p_{x_J}(x_J)dx_J d\gamma_J. \tag{4.40}$$

Moreover, to compute the outage probability at the relay node, $P_{out_R}(\gamma_{R_{th}})$, (4.30) and (4.32) are used to substitute $p_{x_J}(x_J)$ and $p_{y_J}(y_J)$ in (4.40), which gives

$$P^R_{out}(\gamma_{R_{th}}) = \int_0^\infty \frac{(1+x_R)^2}{\alpha_R^2\beta_R}e^{-\frac{x_R}{\beta_R}}\int_0^{\gamma_{R_{th}}}\gamma_R e^{-\frac{1+x_R}{\alpha_R}\gamma_R}d\gamma_R dx_R. \tag{4.41}$$

This integral can be solved by exploiting the solution of the integral $\int_{x=0}^u xe^{-\mu x}dx = \frac{1}{\mu^2}[1 - e^{-\mu u}(1+\mu u)]$ for $[u > 0]$ [123, Eq. (3.351.3)] and $\int_{x=0}^\infty x^n e^{-\mu x}dx = n!\mu^{-n-1}$ for $[\mathbf{Re}\ \mu > 0]$ [123, Eq. (3.351.7)] to produce

$$\begin{aligned} P^R_{out}(\gamma_{R_{th}}) =& 1 - \frac{e^{-\frac{\gamma_{R_{th}}}{\alpha_R}}}{\beta_R}\left(\frac{\alpha_R\beta_R}{\gamma_{R_{th}}\beta_R+\alpha_R}\right) - \gamma_{R_{th}}\frac{e^{-\frac{\gamma_{R_{th}}}{\alpha_R}}}{\alpha_R\beta_R}\left(\frac{\alpha_R\beta_R}{\gamma_{R_{th}}\beta_R+\alpha_R}\right) \\ & - \gamma_{R_{th}}\frac{e^{-\frac{\gamma_{R_{th}}}{\alpha_R}}}{\alpha_R\beta_R}\left(\frac{\alpha_R\beta_R}{\gamma_{R_{th}}\beta_R+\alpha_R}\right)^2. \end{aligned} \tag{4.42}$$

Moreover, the outage probability at the end nodes is evaluated by using (4.38) to substitute

$p_{\gamma_J}(\gamma_J)$ in (4.39), which yields

$$P_{out}^{D}(\gamma_{D_{th}}) = \frac{1}{\beta_D}\int_0^{\gamma_{Dth}} \frac{e^{-\frac{\gamma_D}{\alpha_D}}}{\gamma_D + \frac{\alpha_D}{\beta_D}} d\gamma_D + \frac{\alpha_D}{\beta_D}\int_0^{\gamma_{Dth}} \frac{e^{-\frac{\gamma_D}{\alpha_D}}}{\Big(\gamma_D + \frac{\alpha_D}{\beta_D}\Big)^2} d\gamma_D. \tag{4.43}$$

The first and second integrals can be evaluated by exploiting [123, Eq. (3.352.1), Eq. (3.353.1), and Eq. (3.353.2)], respectively, to give

$$\begin{aligned} P_{out}^{D}(\gamma_{D_{th}}) = \frac{e^{\frac{1}{\beta_D}}}{\beta_D}\Bigg[\mathrm{Ei}\Big(-\frac{\gamma_{D_{th}}}{\alpha_D} - \frac{1}{\beta_D}\Big) - \mathrm{Ei}\Big(-\frac{1}{\beta_D}\Big)\Bigg] + \frac{\alpha_D}{\beta_D}\Bigg[\frac{\beta_D}{\alpha_D} + \frac{e^{\frac{1}{\beta_D}}}{\alpha_D}\mathrm{Ei}\Big(-\frac{1}{\beta_D}\Big) \\ - \frac{e^{-\frac{\gamma_{D_{th}}}{\alpha_D}}}{\gamma_{D_{th}} + \frac{\alpha_D}{\beta_D}} - \frac{e^{\frac{1}{\beta_D}}}{\alpha_D}\mathrm{Ei}\Big(-\frac{1}{\alpha_D}\big(\gamma_{D_{th}} + \frac{\alpha_D}{\beta_D}\big)\Big)\Bigg], \end{aligned} \tag{4.44}$$

where Ei is the exponential integral function defined as $\mathrm{Ei}(x) = \int_{-x}^{\infty} t^{-1}e^{-t}dt$ [123].

In contrast, for the DNF-HD-PLNC there is no SI, therefore, the SINR at the relay is given as [88, 99, 133]

$$\gamma_{HD_R} = \Omega_R \Upsilon, \tag{4.45}$$

while the SINR at the end nodes is expressed as node is given as

$$\gamma_{HD_D} = \Omega_D |h_D|^2. \tag{4.46}$$

Moreover, the PDF of the DNF-HD-PLNC SINR is given as

$$p_{\gamma_{HD_J}}(\gamma_{HD_J}) = \frac{\gamma_{HD_J}^{m_J-1}}{\Gamma(m_J)\alpha_{HD_J}^{m_J}} e^{\frac{-\gamma_{HD_J}}{\alpha_{HD_J}}}, \tag{4.47}$$

where $\alpha_{HD_J} = \frac{1}{m_J}E\{\gamma_{HD_J}\}$. Consequently, the outage probability at the relay in HD mode is given as

$$P_{out_{HD_R}}(\gamma_{HD_{Rth}}) = \int_0^{\gamma_{HD_{Rth}}} \frac{\gamma_{HD_R}}{\alpha_{HD_R}^2} e^{-\frac{\gamma_{HD_R}}{\alpha_{HD_R}}} d\gamma_{HD_R}. \tag{4.48}$$

This integral can be solved by exploiting the solution of the integral $\int_{x=0}^{u} xe^{-\mu x}dx = \frac{1}{\mu^2}[1 - e^{-\mu u}(1+\mu u)]$ for $[u > 0]$ [123, Eq. (3.351.7)], which yields

$$P_{out_{HD_R}}(\gamma_{HD_{Rth}}) = 1 - e^{-\frac{\gamma_{HD_{Rth}}}{\alpha_{HD_R}}}\Big[1 + \frac{\gamma_{HD_{Rth}}}{\alpha_{HD_R}}\Big]. \tag{4.49}$$

Furthermore, the outage probability at the end nodes in the HD mode is given as

$$P_{out_{HD_D}}(\gamma_{HD_{Dth}}) = \int_0^{\gamma_{HD_{Dth}}} \frac{e^{-\frac{\gamma_{HD_D}}{\alpha_{HD_D}}}}{\alpha_{HD_D}} d\gamma_{HD_D}, \tag{4.50}$$

which can be solved using [123, Eq. (3.310)]. Subsequently, the outage probability at the end nodes in the HD mode is obtained by solving (4.50), which gives

$$P_{out_{HD_D}}(\gamma_{HD_{Dth}}) = 1 - e^{-\frac{\gamma_{HD_{Dth}}}{\alpha_{HD_D}}}. \tag{4.51}$$

Finally, in order to calculate the exact E2E outage probability, three different scenarios have been considered. These scenarios are: (i) we assume that there is no outage during the MA phase, but there is outage during the BC phase; (ii) we assume that there is no outage during the BC phase, but there is outage during the MA phase; (iii) at low SNR levels, we assume that there is outage during the MA phase and during the BC phase. Subsequently, the exact E2E PLNC outage probability is given as

$$P_{out}^{E2E}(\gamma_{th}) = P_{out}^{D}(\gamma_{D_{th}}) + P_{out}^{R}(\gamma_{R_{th}}) - P_{out}^{R}(\gamma_{R_{th}}) P_{out}^{D}(\gamma_{D_{th}}), \tag{4.52}$$

where $D \in \{A, B\}$. To summarize, major contributions of this section are (4.36), (4.38), (4.42) and (4.44) all of which will be exploited in Section 4. 10 evaluate the E2E outage probability of the proposed DNF-FD-PLNC and PDF of the SINR at relay and the end nodes.

4.7 Average Symbol Error Rate

This section presents the E2E ASER, $\bar{P}_e$, of the DNF-FD-PLNC, which is obtained by averaging the instantaneous symbol error rate (SER), $P_e(\gamma)$, of the DNF-FD-PLNC over the instantaneous SINR (γ) as follows

$$\bar{P}_e^J = E[P_e^J(\gamma_J)] = \int_0^{\infty} P_e^J(\gamma_J) p_{\gamma_J}(\gamma_J) d\gamma_J. \tag{4.53}$$

The instantaneous symbol error rate can be evaluated using the Q-function as follows [99, 133]

$$P_e^J(\gamma_J) = aQ(\sqrt{2g\gamma_J}), \tag{4.54}$$

where a and g are modulation dependent constants, for example in M-PSK modulation these constants are given as $a = 2$ and $g \approx \sin^2(\frac{\pi}{M})$. Using (4.54) to substitute $P_{e_J}(\gamma)$ in (4.53) yields

$$\bar{P}_e^J = E\left\{P_e^J(\gamma_J)\right\} = a\int_0^\infty Q\Big(\sqrt{2g\gamma_J}\Big)p_{\gamma_J}(\gamma_J)d\gamma_J. \tag{4.55}$$

Recalling (4.30)-(4.32) along with (4.33) the ASER can be expressed as

$$\bar{P}_e^J = \frac{a}{\beta_J}\int_0^\infty \frac{e^{-\frac{x_J}{\beta_J}}}{\Gamma(m_J)\alpha_J^{m_J}}(1+x_J)^{m_J}\int_0^\infty \gamma_J^{m_J-1}Q\Big(\sqrt{2g\gamma_J}\Big)e^{-\frac{1+x_J}{\alpha_J}\gamma_J}d\gamma_J dx_J \tag{4.56}$$

In order to further simplify (4.56), Craig's expression is used instead of the Q function, i.e.

$$Q\Big(\sqrt{2g\gamma_J}\Big) = \frac{1}{\pi}\int_0^{\frac{\pi}{2}} \exp\Big(-\frac{2g\gamma_J}{2\sin^2\theta}\Big)d\theta. \tag{4.57}$$

Using (4.57) to substitute $Q(\sqrt{2g\gamma_J})$ in (4.56) yields

$$\begin{aligned}\bar{P}_e^J = \frac{a}{\Gamma(m_J)\beta_J}\int_0^\infty \frac{e^{-\frac{x_J}{\beta_J}}}{\alpha_J^{m_J}\pi}(1+x_J)^{m_J}\int_0^{\frac{\pi}{2}}\int_0^\infty \gamma_J^{m_J-1} \\ \times \exp\left(-\frac{g\alpha_J + (1+x_J)\sin^2\theta}{\alpha_J\sin^2\theta}\gamma_J\right)d\gamma_J d\theta dx_J.\end{aligned} \tag{4.58}$$

This integral can be simplified by exploiting the result of $\int_{\gamma=0}^\infty \gamma^n e^{-\mu\gamma}d\gamma = n!\mu^{-n-1}$ for $\mu > 0$, [123, Eq. (3.351.3)]. Subsequently, the ASER can be given as

$$\bar{P}_e^J = \frac{a}{\Gamma(m_J)\beta_J}\int_0^\infty e^{-\frac{x_J}{\beta_J}}\,\mathcal{I}_J\Big(\frac{\pi}{2}, \frac{g\alpha_J}{(x_J+1)}, m_J\Big)dx_J, \tag{4.59}$$

where $\mathcal{I}_J(\frac{\pi}{2}, \frac{g\alpha_J}{x_J+1}, m_J)$ is given as

$$\mathcal{I}_J(\frac{\pi}{2}, \frac{g\alpha_J}{x_J+1}, m_J) = \frac{1}{\pi}\int_0^{\frac{\pi}{2}}\Big(\frac{\sin^2\theta}{\sin^2\theta + \frac{g\alpha_J}{1+x_J}}\Big)^{m_J}d\theta. \tag{4.60}$$

The function $\mathcal{I}_J(\frac{\pi}{2}, \frac{g\alpha_J}{(x_J+1)}, m_J)$ can be decomposed using the results in [125, Section 5.4.4] as follows

$$\begin{aligned}\mathcal{I}_J(\frac{\pi}{2}, \frac{g\alpha_J}{x_J+1}, m_J) = \Big[\frac{1}{2} - \frac{\sqrt{\alpha_J g}}{2}\sum_{\mathcal{O}=0}^{m_J-1}\sum_{\mathcal{P}=0}^{\mathcal{O}} U_{\mathcal{O}\mathcal{P}}x_J^{\mathcal{P}} \\ \times\Big(\frac{1}{1+\alpha_J g + x_J}\Big)^{\mathcal{O}+\frac{1}{2}}\Big],\end{aligned} \tag{4.61}$$

where $U_{\mathcal{OP}} = \binom{2\mathcal{O}}{\mathcal{O}}\binom{\mathcal{O}}{\mathcal{P}}\left(\frac{1}{4}\right)^{\mathcal{O}}$. Using (4.61) to substitute $\mathcal{I}_J(\frac{\pi}{2}, \frac{g\alpha_J}{x_J+1}, m_J)$ in (4.59) yields

$$\bar{P}_e^J = \frac{a}{\Gamma(m_J)\beta_J}\int_0^\infty e^{-\frac{x_J}{\beta_J}}\Big[\frac{1}{2} - \frac{\sqrt{\alpha_J g}}{2}\sum_{\mathcal{O}=0}^{m_J-1}\sum_{\mathcal{P}=0}^{\mathcal{O}} U_{\mathcal{OP}} x_J^{\mathcal{P}} \times \Big(\frac{1}{1+\alpha_J g + x_J}\Big)^{\mathcal{O}+\frac{1}{2}}\Big]dx_J. \quad (4.62)$$

This equation contains the confluent hypergeometric function of the second kind, which is defined as [123, Eq.(9.211.4)]

$$\Psi(a;b;z) = \frac{1}{\Gamma(a)}\int_0^\infty e^{-zx}x^{a-1}(1+x)^{b-a-1}dx. \quad (4.63)$$

Consequently, the ASER is given as (4.64).

Consequently, ASER can be obtained by solving (4.55), which gives

$$\begin{aligned}\bar{P}_e^J =& \frac{a}{2} - \frac{a\sqrt{\alpha_J g}}{2\beta_J}\sum_{\mathcal{O}=0}^{m_J-1}\sum_{\mathcal{P}=0}^{\mathcal{O}}\binom{2\mathcal{O}}{\mathcal{O}}\binom{\mathcal{O}}{\mathcal{P}}\Big(\frac{1}{4}\Big)^{\mathcal{O}}\Gamma(\mathcal{P}+1)\Big(1+\alpha_J g\Big)^{\mathcal{P}-\mathcal{O}+\frac{1}{2}} \\ &\times \Psi(\mathcal{P}+1;\mathcal{P}-\mathcal{O}+\frac{3}{2};\frac{1}{\beta_J}(1+g\alpha_J)). \end{aligned} \quad (4.64)$$

The confluent hypergeometric function can be solved using the generalized hypergeometric function either by (4.65) [123, Eq. (9.210.2)], or (4.66) [134, Eq. (40)] for positive values of a and z

$$\Psi(a;b;z) = \frac{\pi}{\sin(\pi b)}\left[\frac{{}_1F_1(a;b;z)}{\Gamma(a-b+1)\Gamma(b)} - \frac{z^{1-b}{}_1F_1(a-b+1;2-b;z)}{\Gamma(a)\Gamma(2-b)}\right], \quad (4.65)$$

$$\Psi(a;a-b+1;z) = z^{-a}{}_2F_0(a,b;;-z^{-1}). \quad (4.66)$$

Furthermore, since there is no SI in the DNF-HD-PLNC the PDF of the SINR is given as (4.47), subsequently, the ASER for the DNF-HD-PLNC is given as

$$\bar{P}_e^{HD_J} = \frac{a}{\pi}\int_0^{\pi/2}\int_0^\infty \frac{\gamma_J^{m_J-1}}{\Gamma(m_J)\alpha_J^{m_J}}e^{-\frac{sin^2\theta+g\alpha_J}{sin^2\theta\alpha_J}}d\gamma d\theta. \quad (4.67)$$

This integral can be simplified by exploiting the result of $\int_{\gamma=0}^\infty \gamma^n e^{-\mu\gamma}d\gamma = n!\mu^{-n-1}$ for $\mu > 0$,

[123, Eq. (3.351.3)], which results in

$$\bar{P}_e^{HD_J} = \frac{a}{\pi}\int_0^{\frac{\pi}{2}} \Big(\frac{\sin^2\theta}{\sin^2\theta + g\alpha_J}\Big)^{m_J} d\theta. \tag{4.68}$$

This integral can be solved using the results in [125, Section 5.4.4]. Consequently, the ASER for the DNF-HD-PLNC is given as

$$\bar{P}_e^{HD_J} = \frac{a}{2} - \frac{a\sqrt{(g\alpha_J)}}{2}\sum_{\mathcal{O}=0}^{m_J-1}\binom{2\mathcal{O}}{\mathcal{O}}\Big(\frac{1}{4}\Big)^{\mathcal{O}}\Big(\frac{1}{1+g\alpha_J}\Big)^{\mathcal{O}+\frac{1}{2}}. \tag{4.69}$$

Finally, the exact E2E ASER is calculated by considering three different scenarios. These scenarios are: (i) symbols are detected with no errors at the relay node during the uplink (MA phase) but are detected with errors at the end nodes during the down-link (BC phase); (ii) symbols are detected with errors at the relay node during the uplink (MA phase) but are detected with no errors at the end nodes during the down-link (BC phase); (iii) at low SNR levels, symbols are detected with errors at the relay node during the uplink (MA phase) and at the end nodes during the down-link (BC phase). Subsequently, the exact E2E (E2E) PLNC ASER is given as

$$\bar{P}_e^{E2E} = \big(1-\bar{P}_e^R\big)\bar{P}_e^D + \big(1-\bar{P}_e^D\big)\bar{P}_e^R + \bar{P}_e^R\bar{P}_e^D, \tag{4.70}$$

where $D \in \{A, B\}$.

To encapsulate, the main contribution of this section is (4.64), which has needed complex mathematical derivations and will be used in Section 4.10 to obtain the E2E ASER of the proposed DNF-FD-PLNC.

4.8 The End-to-end Ergodic Capacity

This section presents the derivation of the E2E ergodic capacity of the proposed DNF-FD-PLNC, which can be obtained using the results of [135] as

$$C_{erg}^{E2E} = \min(C_{erg}^R, C_{erg}^D), \tag{4.71}$$

where C_{erg}^{R} and C_{erg}^{D} represent the ergodic capacity at the relay and the end nodes, respectively, and can be evaluated as

$$C_{erg}^{J} = \int_{0}^{\infty} \log_2(1+\gamma_J) p_{\gamma_J}(\gamma_J) d\gamma_J, \tag{4.72}$$

where $J \in \{A, B, R\}$ and $D \in \{A, B\}$.

The ergodic capacity at the relay node can be obtained by using (4.35) to substitute $p_{\gamma_J}(\gamma_J)$ in (4.72), which results in

$$C_{erg}^{R} = \int_{\gamma_R=0}^{\infty} \gamma_R \log_2(1+\gamma_R) e^{-\frac{1+x_R}{\alpha_R}\gamma_R} \int_{x_R=0}^{\infty} \frac{(1+x_R)^2}{\alpha_R^2 \beta_R} e^{-\frac{x_R}{\beta_R}} dx_R d\gamma_R. \tag{4.73}$$

This double integral can be rewritten as

$$\begin{aligned} C_{erg}^{R} = {} & \frac{\alpha_R^2}{\ln(2)(1+x_R)^2} \int_{\gamma_R=0}^{\infty} \gamma_R \ln(1+\frac{\alpha_R}{(1+x_R)}\gamma_R) e^{-\gamma_R} \\ & \times \frac{(1+x_R)^2}{\alpha_R^2 \beta_R} \int_{x_R=0}^{\infty} e^{-\frac{x_R}{\beta_R}} dx_R d\gamma_R, \end{aligned} \tag{4.74}$$

so that the solution of this integral can be obtained by exploiting [123, Eq. (4.337.5)] followed by integration by parts to solve (4.74), which yields the ergodic capacity at the relay node such that

$$\begin{aligned} C_{erg}^{R} = {} & \frac{1}{\ln(2)} \Bigg[1 + \Big(\frac{e^{\frac{1}{\alpha_R}}}{\alpha_R - \beta_R}\Big) \mathrm{Ei}\Big(\frac{-1}{\alpha_R}\Big) + \frac{\beta_R}{\alpha_R - \beta_R} + \Big(\frac{e^{\frac{1}{\alpha_R}} \alpha_R \beta_R}{(\alpha_R - \beta_R)^2}\Big) \mathrm{Ei}\Big(\frac{-1}{\alpha_R}\Big) \\ & - \Big(\frac{e^{\frac{1}{\beta_R}} \alpha_R \beta_R}{(\alpha_R - \beta_R)^2}\Big) \mathrm{Ei}\Big(\frac{-1}{\beta_R}\Big) - \Big(\frac{e^{\frac{1}{\alpha_R}} \alpha_R}{\alpha_R - \beta_R}\Big) \mathrm{Ei}\Big(\frac{-1}{\alpha_R}\Big) + \Big(\frac{e^{\frac{1}{\beta_R}} \alpha_R}{\alpha_R - \beta_R}\Big) \mathrm{Ei}\Big(\frac{-1}{\beta_R}\Big) \Bigg], \end{aligned} \tag{4.75}$$

where $\mathrm{Ei}\,(x)$ denotes the exponential integral function that is defined in [123, Eq. (8.211.1)] as $\mathrm{Ei}\,(x) = -\int_{-x}^{\infty} \frac{e^{-t}}{t} dt$.

Furthermore, using (4.37) to substitute $p_{\gamma_J}(\gamma_J)$ in (4.72) gives the ergodic capacity at the end nodes as

$$C_{erg}^{D} = \frac{1}{\ln(2)} \int_{0}^{\infty} \ln(1+\gamma_D) e^{-\frac{1+x_D}{\alpha_D}\gamma_D} \int_{0}^{\infty} \frac{(1+x_D)}{\alpha_D \beta_D} e^{-\frac{x_D}{\beta_D}} dx_D d\gamma, \tag{4.76}$$

which can be re-arranged as

$$C_{erg}^{D} = \frac{e^{\frac{1+x_D}{\beta_D}}}{\ln(2)} \int_{\gamma_D=1}^{\infty} \ln(\gamma_D) e^{-\frac{1+x_D}{\alpha_D}\gamma_D} \int_{x_D=0}^{\infty} \frac{(1+x_D)}{\alpha_D \beta_R} e^{-\frac{D}{\beta_D}} dx_D d\gamma_R. \tag{4.77}$$

so that the double integral can be solved using [123, Eq. (4.331.2)] and integration by parts to

result in the ergodic capacity at the end as

$$C_{erg}^{G}=\frac{\alpha_G}{(\alpha_G-\beta_G)\log(2)}\left[e^{\frac{1}{\beta_G}}\mathrm{Ei}(-\frac{1}{\beta_G})-e^{\frac{1}{\alpha_G}}\mathrm{Ei}(-\frac{1}{\alpha_G})\right]. \tag{4.78}$$

Finally, the E2E ergodic capacity of the proposed DNF-FD-PLNC system can be computed using (4.75) and (4.78) to substitute C_{erg}^{R} and C_{erg}^{D} in (4.71), respectively.

The E2E ergodic capacity for DNF-HD-PLNC system can be evaluated as

$$C_{HD}^{E2E}=\min(C_{HD}^{R},C_{HD}^{D}), \tag{4.79}$$

where C_{HD}^{R} and C_{HD}^{D} denote the ergodic capacity at the relay and end nodes, respectively, in the DNF-HD-PLNC, which can be computed as

$$C_{HD}^{J}=\int_{0}^{\infty}\log_2(1+\gamma_{HD_J})p_{\gamma_{HD_J}}(\gamma_{HD_J})d\gamma_{HD_J}. \tag{4.80}$$

The E2E ergodic capacity of at the relay in the DNF-HD-PLNC can be evaluated by using (4.47) to substitute $p_{\gamma_{HD_J}}(\gamma_{HD_J})$ in (4.80), which yields

$$C_{HD}^{R}=\int_{0}^{\infty}\log 2(1+\gamma_{HD_R})\frac{\gamma_{HD_R}}{\alpha_{HD_R}^{2}}e^{-\frac{\gamma_{HD_R}}{\alpha_{HD_R}}}d\gamma_{HD_R}. \tag{4.81}$$

This integral can be re-written as

$$C_{HD}^{R}=\frac{1}{\ln(2)}\int_{0}^{\infty}\gamma_{HD_R}\ln(1+\alpha_{HD_R}\gamma_{HD_R})e^{-\gamma_{HD_R}}d\gamma_{HD_R}, \tag{4.82}$$

so that this integral can be solved utilizing [123, Eq. (4.337.5)], which results in

$$C_{HD}^{R}=\frac{1}{\ln(2)}\left[1+e^{\frac{1}{\alpha_{HD_R}}}\mathrm{Ei}(-\frac{1}{\alpha_{HD_R}})\left(\frac{1}{\alpha_{HD_R}}-1\right)\right]. \tag{4.83}$$

Furthermore, using using (4.47) to substitute $p_{\gamma_{HD_J}}(\gamma_{HD_J})$ in (4.80) gives the ergodic capacity at the end nodes in the DNF-HD-PLNC as

$$C_{HD}^{D}=\int_{0}^{\infty}\log 2(1+\gamma_{HD_D})\frac{e^{-\frac{\gamma_{HD_D}}{\alpha_{HD_D}}}}{\alpha_{HD_D}}d\gamma_{HD_D}. \tag{4.84}$$

This integral can be solved utilizing [123, Eq. (4.337.2)], which yields

$$C_{HD}^{D} = -\frac{1}{\ln(2)} e^{\frac{1}{\alpha_{HD_D}}} \mathrm{Ei}(-\frac{1}{\alpha_{HD_D}}). \tag{4.85}$$

Finally, the E2E ergodic capacity for DNF-HD-PLNC can be evaluated using (4.83) and (4.83) to substitute C_{HD}^{R} and C_{HD}^{D} in (4.79), respectively.

In summary, the distinct contributions of this section are (4.75) and (4.78), which have demanded intricate mathematical derivations and will be utilized in Section 4.10 to evaluate the E2E ergodic capacity of the proposed DNF-FD-PLNC system.

4.9 Performance Studies

In this section, analytical and simulation based results for the proposed DNF-FD-PLNC system under investigation are presented and analyzed in the presence of residual self-interference (SI) and channel estimation errors. We consider an uncoded QPSK FD-TWRC network, where the full-duplex nodes, A and B, exchange information with the aid of a DNF full-duplex relay node, R, over quasi-static reciprocal asymmetric Rayleigh-fading channels.

First, the analytical SINR distribution of the DNF-FD-PLNC at the relay and the end nodes is evaluated and compared to the simulation based SINR distribution as depicted in Figs. 4.6, 4.7, 4.8 and 4.9, respectively.

Fig. 4.6, shows the effect of the residual SI on the PDF of the SINR at the relay node. It is evident from Fig. 4.6 that as the amount of the residual SI increases the distribution of the SINR is concentrated more in the low SNR region. In contrast, Fig. 4.7 illustrates the effect of the channel estimation errors on the PDF of the SINR at the relay node. A closer examination of Figs. 4.6 and 4.7 reveals that the effect of the channel estimation errors on the shape of the PDF of the SINR at the relay is less significant than the effect of the residual SI.

On the other hand, Figs. 4.8 and 4.9, show the effect of the residual SI and the effect of the channel estimation errors on the PDF of the SINR at node A. Inspecting Figs. 4.8 and 4.9, a similar pattern as in Figs. 4.6 and 4.7 can be observed, i.e., the mean of the PDF of the SINR is located in the low SNR region as the amount of the residual SI increases. Furthermore, the channel estimation errors have a less significant effect on the shape of the distribution of the SINR than the residual SI. It is worth highlighting that the PDF of the SINR at node B is essentially the same as to the shape of the PDF of the SINR at node A.

Moreover, the E2E outage probability of the proposed DNF-FD-PLNC system in the pres-

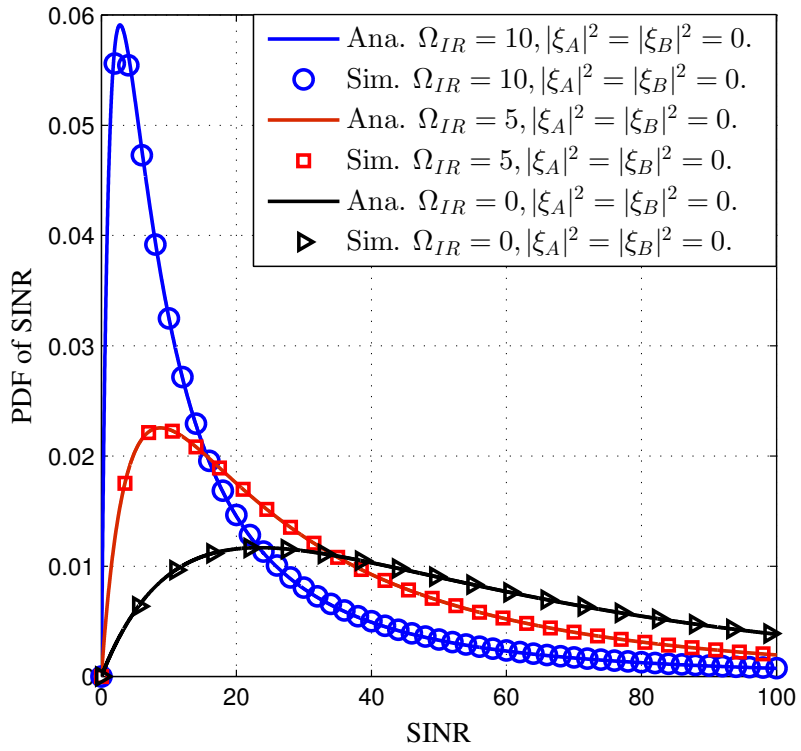

Figure 4.6: The PDF of the SINR at the relay after the adaptive SIC for the DNF-FD-PLNC system with different levels of residual SI at SNR Ω_R=15 dB.

ence of ICSI and residual SI was calculated and analyzed for nine different scenarios of residual SI, perfect and ICSI. These scenarios are illustrated in Table 4.1. The outage probability of the proposed DNF-FD-PLNC system was compared with the outage probability of DNF-HD-PLNC system as shown in Fig. 4.10.

Table 4.1: The scenarios for residual self-interference, perfect and imperfect channel state information (CSI) for the proposed DNF-FD-PLNC.

Scenario (Sc.)	Description	$(\lvert\xi_A\rvert^2,\lvert\xi_B\rvert^2)$	$(\Omega_{IR},\Omega_{IA},\Omega_{IB})$ (dB)
1	PCSI, Medium residual SI (RSI)	(0,0)	(0, 0, 0)
2	PCSI, High residual SI (RSI)	(0,0)	(5, 5, 5)
3	PCSI, V. high residual SI (RSI)	(0,0)	(10, 10, 10)
4	ICSI 1, Medium residual SI (RSI)	$(10^{-3},10^{-3})$	(0, 0, 0)
5	ICSI 1, High residual SI (RSI)	$(10^{-3},10^{-3})$	(5, 5, 5)
6	ICSI 1, V. high residual SI (RSI)	$(10^{-3},10^{-3})$	(10, 10, 10)
7	ICSI 2, Medium residual SI (RSI)	$(10^{-2},10^{-2})$	(0, 0, 0)
8	ICSI 2, High residual SI (RSI)	$(10^{-2},10^{-2})$	(5, 5, 5)
9	ICSI 2, V. high residual SI (RSI)	$(10^{-2},10^{-2})$	(10, 10, 10)

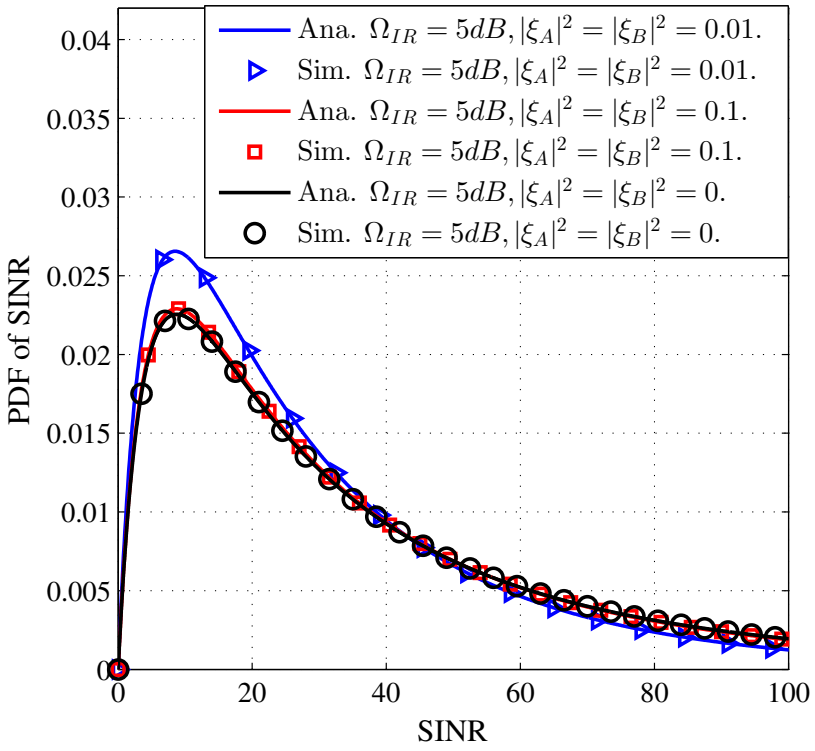

Figure 4.7: The PDF of the SINR at the relay after the adaptive SIC for the DNF-FD-PLNC system with different levels of channel estimation error at SNR Ω_R=15 dB.

Figs. 4.10 and 4.11 depict the E2E outage probability of the DNF-HD-PLNC system and the E2E outage probability of the proposed DNF-FD-PLNC system after the adaptive SIC as a function of SINR threshold, i.e. γ_{th}, for three different scenarios of residual SI and channel estimation errors, respectively, while the SNR was fixed at 15 dB. The first four curves in Fig. 4.10 depict the effect of the residual SI on the E2E outage portability of the PLNC system and illustrate the difference between the E2E outage probability of DNF-HD-PLNC, that is $\Omega_{IR} = \Omega_{IA} = \Omega_{IB} = 0$, with perfect CSI (PCSI) and the E2E outage probability of DNF-FD-PLNC with perfect CSI for three different scenarios of residual SI to noise ratio at each node, i.e. $\Omega_{IR} = \Omega_{IA} = \Omega_{IB} = 0,\ 5,\ 10$ dB, respectively.

A closer examination of Figs. 4.10 and 4.11, reveals an analogous behavior, namely, that the residual SI has more significant effect on the outage probability than the channel estimation errors. However, channel estimation errors cause an error floor in the high SNR region as can be seen from Fig. 4.12, where the relationship between the E2E outage probability of both the DNF-HD-PLNC system and the proposed DNF-FD-PLNC system using adaptive SIC versus the SNR for nine different scenarios is illustrated. The SINR threshold, γ_{th}, in this case was fixed at 15 dB. Comparing the first four curves in Fig. 4.12, that is DNF-HD-PLNC system and DNF-FD-PLNC system with PCSI for three scenarios of residual SI to noise ratio at each node,

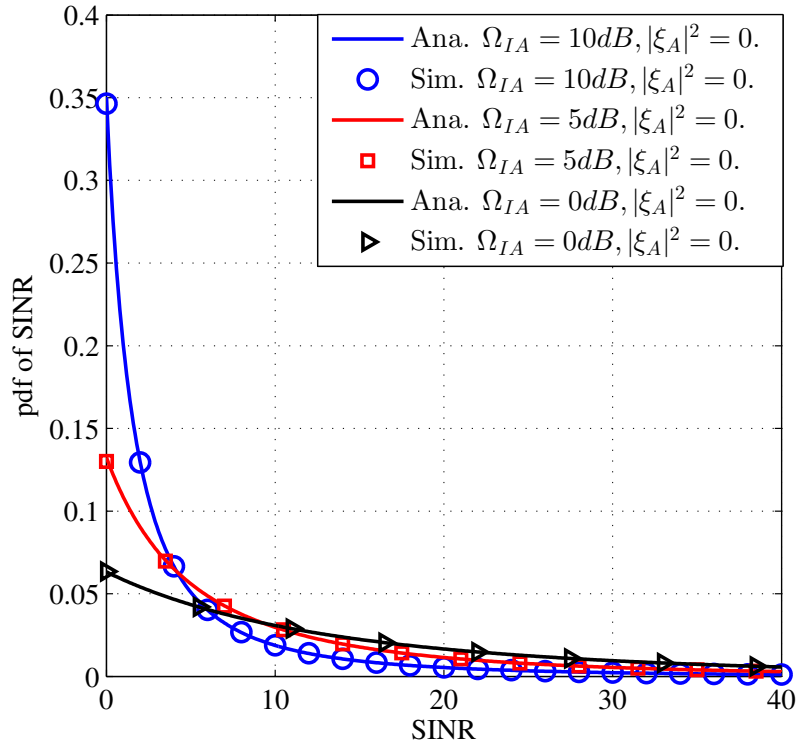

Figure 4.8: The PDF of the SINR at Node A after the adaptive SIC for the DNF-FD-PLNC system with different levels of residual SI at SNR Ω_R=15 dB.

i.e. $\Omega_{IR} = \Omega_{IA} = \Omega_{IB} = 0,\ 5,\ 10$ dB, respectively, it can be seen that $P_{out}^{E2E}(\gamma_{th})$ increases when the amount of the residual SI increases. For instance, for DNF-HD-PLNC system, that is PLNC system with no SI, and for the DNF-FD-PLNC system with $\Omega_{IR} = \Omega_{IA} = \Omega_{IB} = 0,\ 5,\ 10$ dB, to obtain $P_{out}^{E2E}(\gamma_{th}) = 10^{-3}$ requires an SNR level of 45, 48, 51.2 and 55.4 dB, respectively. Comparing the DNF-FD-PLNC system with DNF-HD-PLNC system it can be observed that there is 3, 6, 10 dB penalty in SNR when the SI to noise ratio is 0, 5, 10 dB, respectively.

Furthermore, the next three curves in Fig. 4.12 show that when the channel estimation errors, i.e. $|\xi_A|^2,\ |\xi_B|^2$, are equal to 10^{-3}, $P_{out}^{E2E}(\gamma_{th})$ exhibits an error floor of 3×10^{-2} for $\Omega_{IR} = \Omega_{IA} = \Omega_{IB} = 0,\ 5,\ 10$ dB, respectively. Moreover, the last three curves in Fig. 4.12 illustrate that due to the channel estimation errors the outage probability exhibits an error floor of 3×10^{-1}, when the channel estimation errors values are $|\xi_A|^2 = |\xi_B|^2 = 10^{-2}$ and $\Omega_{IR} = \Omega_{IA} = \Omega_{IB} = 0,\ 5,\ 10$ dB, respectively.

Next, in order to investigate the effect of ICSI and residual SI on the ASER performance of both the DNF-HD-PLNC and DNF-FD-PLNC systems, we present analytical and simulation based results computed for nine different scenarios that are illustrated in Table 4.1. Fig. 4.13 depicts the analytical and the simulation-based results of the DNF-HD-PLNC system and the

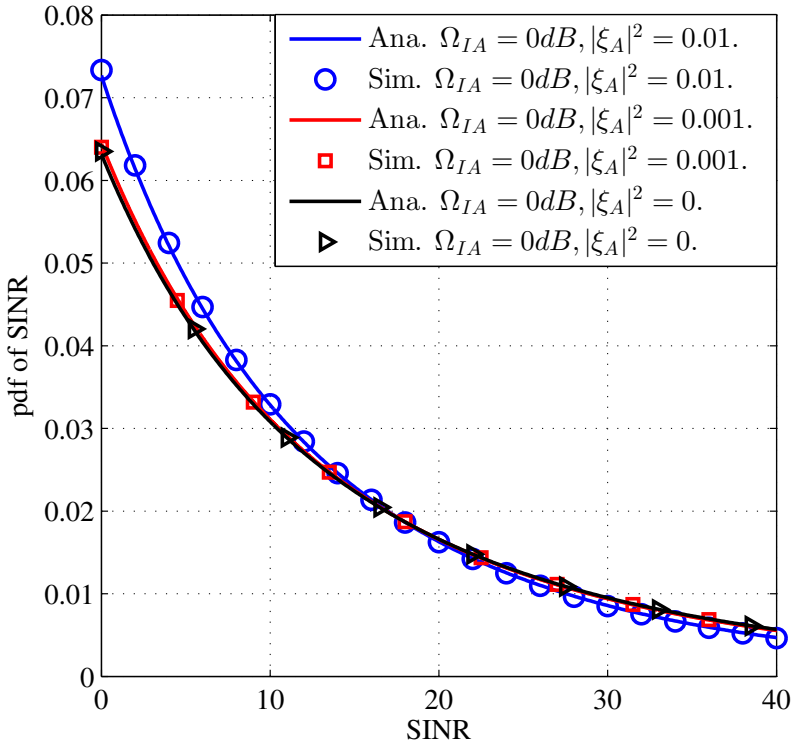

Figure 4.9: The PDF of the SINR at Node A after the adaptive SIC for the DNF-FD-PLNC system with different levels of channel estimation error at SNR Ω_R=15 dB.

proposed DNF-FD-PLNC system vs. SNR after the adaptive SIC. Examining the first four curves in Fig. 4.13, the effect of the residual SI on the ASER can be observed. It is evident that the ASER increases when the amount of the residual SI increases. It is clear from these curves that when the DNF-HD-PLNC system, i.e. no SI, and DNF-FD-PLNC system with three different scenarios of residual SI to noise ratio, which are $\Omega_{IR} = \Omega_{IA} = \Omega_{IB} = 0,\ 5,\ 10$ dB, are considered the ASER reaches 10^{-4} at SNR equals 40, 43, 46.2 and 50.4 dB, respectively. Thus, compared to the SI free case, there is a 3, 6 and 10 dB penalty in SNR when the SI to noise ratio is 0, 5 and 10 dB, respectively.

Moreover, inspecting the other six curves in Fig. 4.13, demonstrates the effect of the ICSI on the ASER. It can be observed from these curves that when $\Omega_{IR} = \Omega_{IA} = \Omega_{IB} = 0,\ 5,\ 10$ dB, respectively, the ASER shows error floors of 1×10^{-3} and 1×10^{-2} when $|\xi_A|^2$, $|\xi_B|^2$ values equal 10^{-3} and 10^{-2}, respectively. Such error floors are due to the channel estimation errors.

Finally, to show the throughput gain of the proposed DNF-FD-PLNC system over the conventional DNF-HD-PLNC system, we compared the E2E ergodic capacity of the DNF-FD-PLNC system C_{erg}^{E2E} and DNF-HD-PLNC system C_{HD}^{E2E}. Twelve different scenarios of residual SI to noise ratio, perfect and imperfect CSI were considered as shown in Figs. 4.14, 4.15 and 4.16. Fig. 4.14 illustrates C_{HD}^{E2E} and C_{erg}^{E2E} with perfect CSI and three different residual

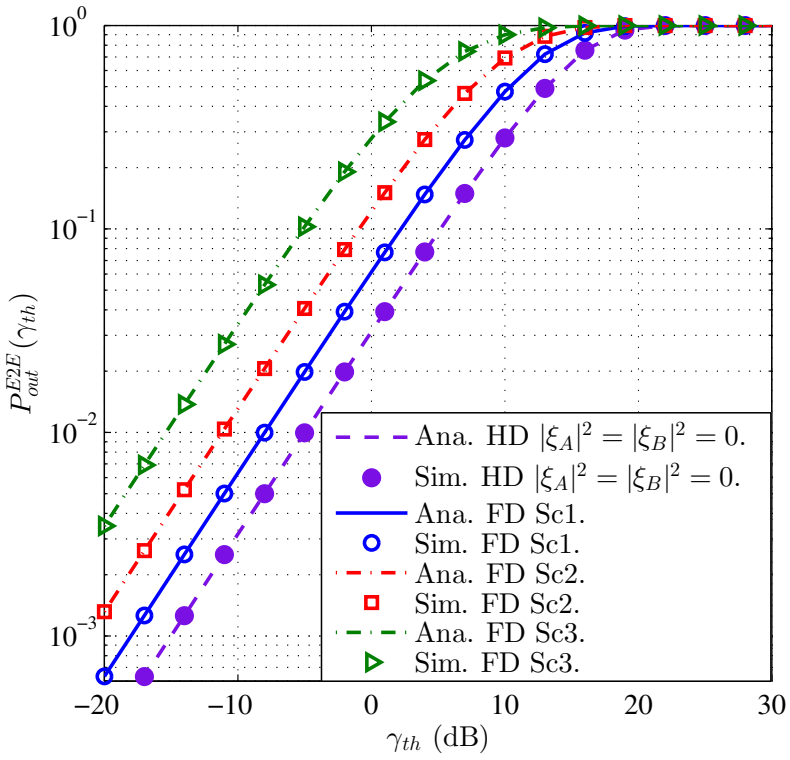

Figure 4.10: The analytical and simulation E2E outage probability for DNF-HD-PLNC and DNF-FD-PLNC systems after the adaptive SIC at SNR= 15 dB with perfect CSI and $\Omega_{IR} = \Omega_{IA} = \Omega_{IB} = \{0,\ 5,\ 10\}$ dB.

SI to noise ratios, namely 0, 5 and 10 dB. In contrast, Fig. 4.15 shows C_{HD}^{E2E} and C_{erg}^{E2E} with ICSI, i.e. $|\xi_A|^2 = |\xi_B|^2 = 10^{-3}$, and three different levels of residual SI to noise ratio, that are 0, 5 and 10 dB. On the other hand, Fig. 4.16 depicts C_{erg}^{E2E} and C_{erg}^{E2E} with ICSI, that is $|\xi_A|^2 = |\xi_B|^2 = 10^{-2}$, and three different levels of residual SI to noise ratio, that are 0 dB, 5 dB and 10 dB.

A closer inspection of Figs. 4.14, 4.15 and 4.16 reveals that the C_{erg}^{E2E} is not always double the C_{HD}^{E2E} as its gain is limited by the amount of the residual SI. Furthermore, as can be seen in these results, C_{erg}^{E2E} is less than C_{HD}^{E2E} when the amount of residual SI to noise ratio is 5 dB and the SNR is less than 10 dB, while C_{erg}^{E2E} is always higher than the C_{HD}^{E2E} when the SNR is more than 10 dB. Moreover, it can be observed that C_{erg}^{E2E} is less than C_{HD}^{E2E} when the amount of residual SI to noise ratio is 10 dB and the SNR is less than 20 dB, whereas C_{erg}^{E2E} is always more than the C_{HD}^{E2E} when the SNR is larger than 20 dB. Nevertheless, Figs 4.14, 4.15 and 4.16 suggest that C_{erg}^{E2E} is approximately double the C_{HD}^{E2E} when the SNR is larger than 30 dB.

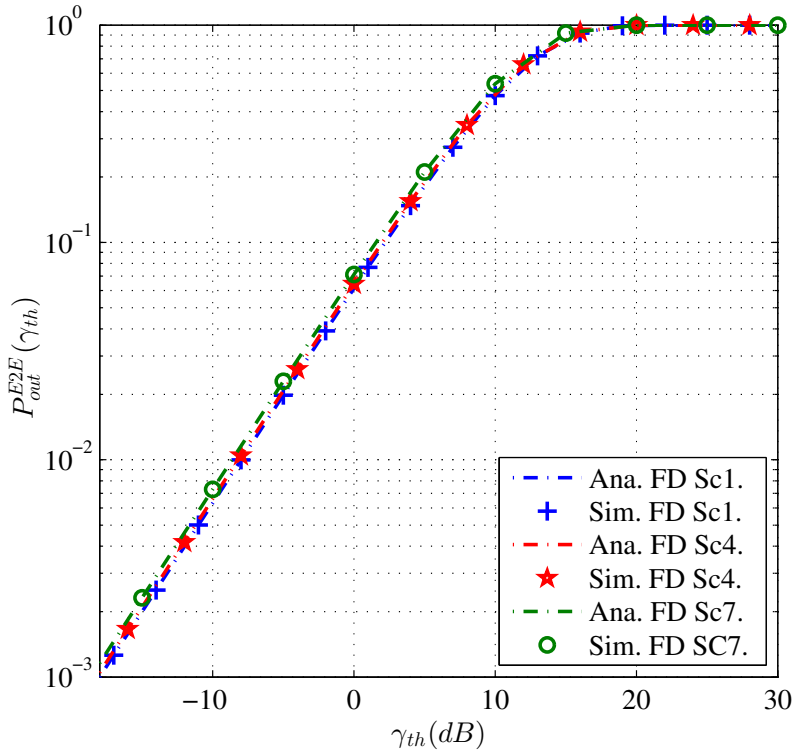

Figure 4.11: The analytical and simulation E2E outage probability for DNF-FD-PLNC system after the adaptive SIC at SNR= 15 dB with $\Omega_{IR} = \Omega_{IA} = \Omega_{IB} = 0$ dB and $|\xi_A|^2 = |\xi_B|^2 = \{0,\ 10^{-3},\ 10^{-2}\}$.

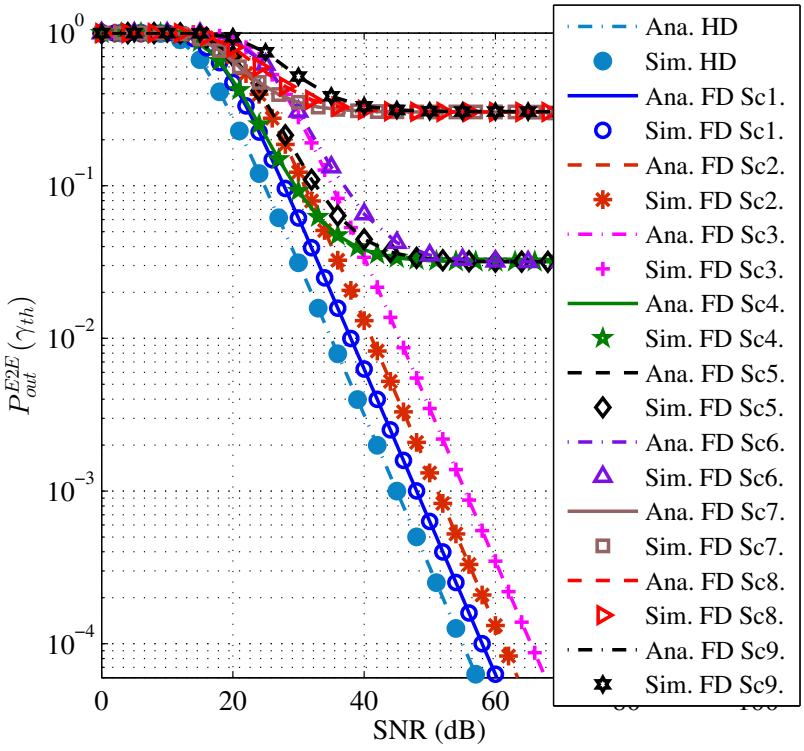

Figure 4.12: The analytical and simulation E2E outage probability for DNF-HD-PLNC and DNF-FD-PLNC systems after the adaptive SIC at γ_{th}=15 dB.

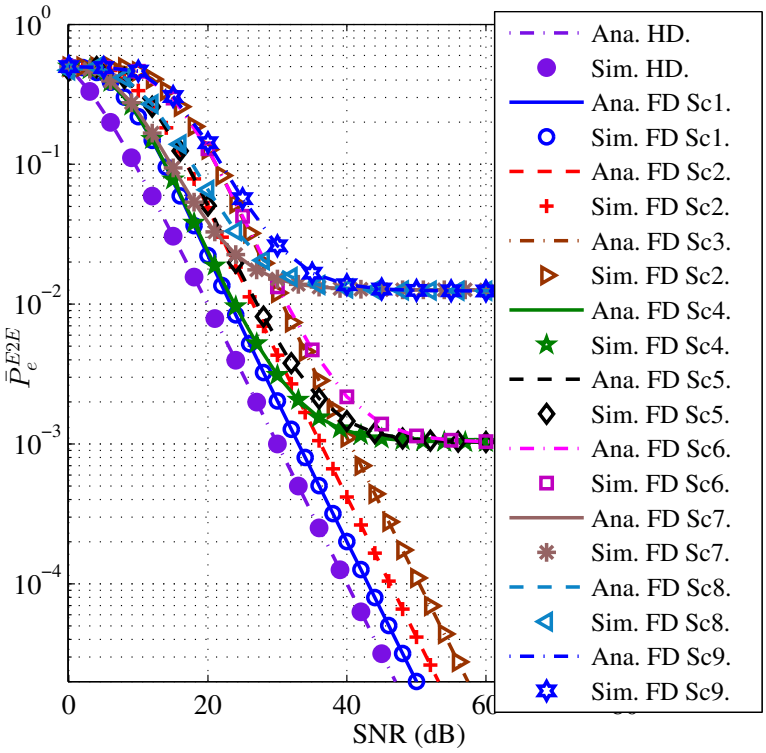

Figure 4.13: The analytical and simulation E2E ASER of the DNF-HD-PLNC and DNF-FD-PLNC systems after the adaptive self-interference cancellation.

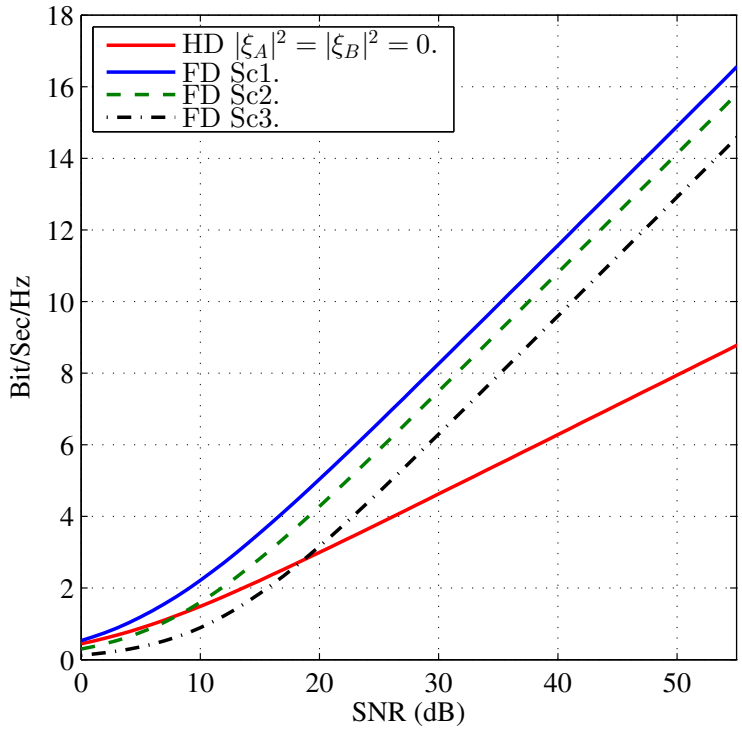

Figure 4.14: The E2E ergodic capacity for DNF-FD-PLNC system after the adaptive SIC with $|\xi_A|^2 = |\xi_B|^2$=0.

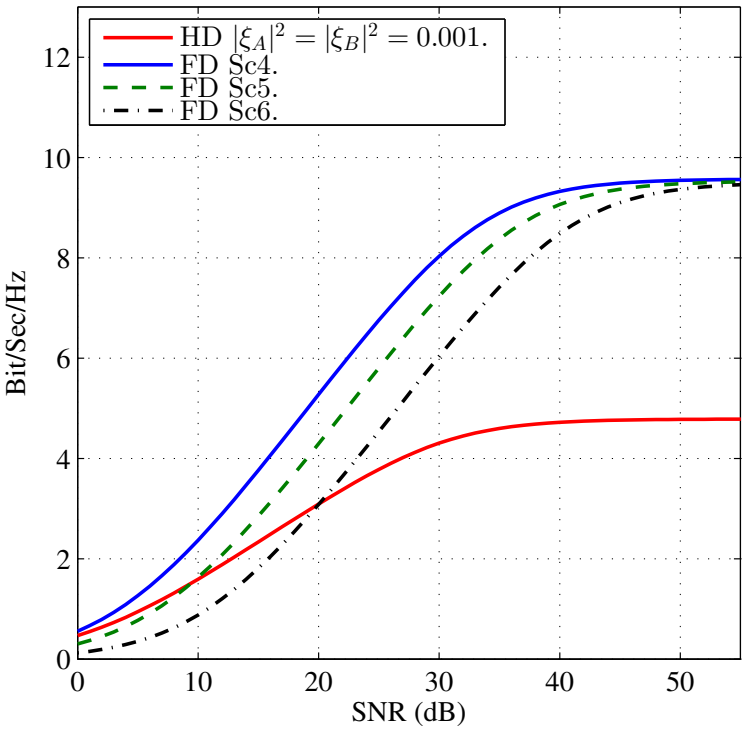

Figure 4.15: The E2E ergodic capacity for DNF-FD-PLNC system after the adaptive SIC with $|\xi_A|^2 = |\xi_B|^2$=10^{-3}.

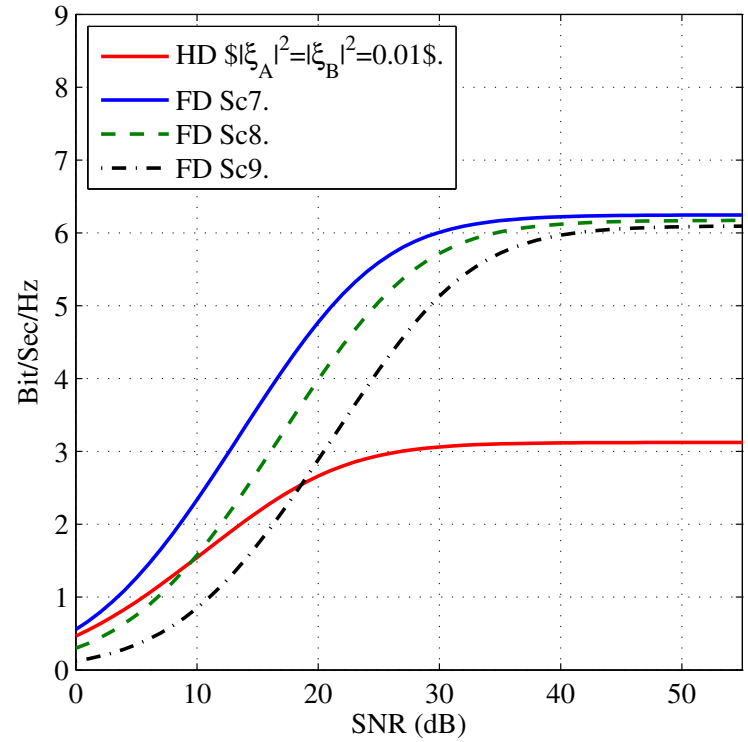

Figure 4.16: The E2E ergodic capacity for DNF-FD-PLNC system after the adaptive SIC with $|\xi_A|^2 = |\xi_B|^2$=10^{-2}.

4.10 Chapter Summary

In this chapter, we presented a DNF-FD-PLNC system for asymmetric frequency flat Rayleigh fading channels. Moreover, we introduced an adaptive SIC scheme that was integrated with the proposed DNF-FD-PLNC to effectively suppress the SI signal and enable the FD mode. The introduced adaptive SIC scheme exploits the NLMS algorithm to estimate the SI channel coefficients, which then utilized to construct a copy of the SI signal. The generated copy was then subtracted from the total received signal before the ADC to diminish the SI signal. The adaptive SIC has demonstrated the ability to suppress the SI signal to approximately the level of the noise floor. Furthermore, the performance of the DNF-FD-PLNC system in the presence of residual SI and channel estimation errors was investigated in this chapter. Initially, the analytical based PDF of the SINR at the end nodes and the relay was derived. Next, an exact closed-form expression for the E2E outage probability of the DNF-FD-PLNC was presented. Moreover, a closed-form expression for the E2E ASER of the QPSK DNF-FD-PLNC system was derived and the result was used to evaluate the analytical E2E ASER of the proposed system. The derived expressions for the PDF of the SINR, E2E outage probability and the E2E ASER were verified using extensive simulation studies. Finally, an exact E2E ergodic capacity expression for the DNF-FD-PLNC system was derived and used to evaluate the E2E ergodic capacity of the proposed DNF-FD-PLNC. Moreover, the obtained E2E ergodic capacity results of the DNF-FD-PLNC were compared with those of the DNF-HD-PLNC system. This comparison has shown that the ergodic capacity gain of the DNF-FD-PLNC system is limited by the amount of SI and the throughput of the DNF-FD-PLNC system is less than that of DNF-HD-PLNC when the residual SI to noise ratio is more than 10 dB and the SNR is less than 5 dB. Nevertheless, the analytical results have suggested that the proposed DNF-FD-PLNC system can increase the throughput of the conventional DNF-HD-PLNC system by a factor of approximately 2 for SNR level greater than 20 dB and SI to noise ratio levels less than 0 dB. Moreover, the analytical and simulation results have confirmed the feasibility of a DNF-FD-PLNC system with the aid of an adaptive self-interference cancellation scheme.

It is worth mentioning that the SIC schemes that have been introduced in this chapter and Chapter 3, perform the self-interference cancellation in the receive chain of transceiver node. Furthermore, these schemes require relatively complicated signal processing to construct a replica of the SI signal. Moreover, in Chapter 3 the proposed active SIC scheme needs two stages of self-interference cancellation, i.e. passive and active. Due to the fact that the main motivation of the SIC is to effectively diminish the SI signal before the ADC to protect the

signal of interest that is received from other transceiver nodes from being swamped by the SI signal, in the next chapter we will introduce a novel over-the-air SIC scheme. Unlike, the active and adaptive SICs the new SIC will be utilized in the transmit chain of each transceiver node, subsequently, the SIC is performed over-the-air before the ADC without the necessity to any further signal processing in the receive chain after the ADC.

Chapter 5

Full-Duplex Bi-Directional System With Spatial Self-Interference Cancellation Exploiting Generalized Nonsymmetric Eigenproblem

5.1 Introduction

In-band FD communication systems have attracted immense attention due to their ability to meet the 5G communication systems high-throughput requirements [22]. However, owing to the strong SI resulting from concurrently transmitting and receiving over the same frequency band, these 5G throughput requirements cannot be attained without a sufficient SIC [2, 136]. Consider that the transmit power at each node is 20 dBm and the receiver noise floor is -90 dBm. Moreover, according to the experimental results in [9] and [93], the attained passive suppression due to the distance between the TX and RX antennas is approximately 40 dB. Hence, the SI signal will be 70 dB above the noise floor, subsequently, an efficient SIC scheme is required to mitigate the SI to the level of the noise floor [136]. Thus, in recent years, a number of different SIC approaches have been introduced to tackle the SI problem. In this chapter, we will focus on the spatial SIC schemes that have been presented thus far. An FD relay system with spatial SIC approach that employs null-space projection (NSP) and zero-forcing (ZF) to diminish the SI signal was introduced and investigated in [97, 113, 114]. In this approach, the singular-value-decomposition (SVD) of the SI channel is exploited to design spatial filters that are used in the transmitting and receiving chains at each node to mitigate the SI signal.

It is worth pointing out that thus far all of the existing spatial SIC schemes require performing filtering and processing on the received signal after the ADC to mitigate the SI signal. This need for processing the received signal after the ADC is not advantages since the key motivation for the SIC is to diminish the SI signal before the ADC in order to prevent it from swamping the signal coming from other users. Hence, the main motivation of this work is to tackle this issue.

In this chapter, we present a new spatial SIC scheme, which employs the generalized non-symmetric eigenproblem (GNEP). The proposed SIC scheme is exploited in an OFDM based precoded full-duplex bi-directional (P-FD-BD) wireless communication system to effectively suppress the SI signal over-the-air before the ADC without the need for any further signal processing after the ADC. Thus, our approach is more pragmatic than the existing spatial SIC schemes. Moreover, in this Chapter, we consider the presence of transmit signal noise and thoroughly investigate its impact on the performance of the proposed GNEP SIC. Furthermore, closed-form expression for the PDF and cumulative distribution function (CDF) of the SINR, ASER and the outage probability of the (P-FD-BD) communication system are presented and validated using extensive simulation studies. The performance of the P-FD-BD system is meticulously studied by evaluating its outage probability, ASER, channel capacity, and CDF of the achieved data rate demonstrating the efficiency of the proposed GNEP SIC in suppressing the SI signal even in the presence of the transmit signal noise.

The rest of this chapter is organized as follows: Section 5.2 presents the system model of the P-FD-BD system along with the architecture of the GNEP SIC. The impact of the transmit signal noise on the performance of the GNEP SIC is studied in Section 5.3. Section 5.4 investigates the statistical analysis of the SINR for the P-FD-BD system. Moreover, the performance evaluation of the considered P-FD-BD system is thoroughly examined in Section 5.5. The analytical and simulation results of the P-FD-BD system are introduced in Section 5.6. Finally, the Summary of this chapter is presented in Section 5.7.

5.2 System and Signal Model

This section presents the P-FD-BD communication system along with the proposed GNEP SIC architecture. We consider a P-FD-BD based communication system that comprises two FD end nodes, N_a and N_b, communicating over frequency-selective channels in the presence of AWGN. In order to cancel the SI signal before the ADC, we introduce a second transmit antenna to enable the implementation of the GNEP SIC, which exploits the generalized nonsymmetric eigenproblem [137]. Hence, each node in the proposed system is equipped with two TX antennas and

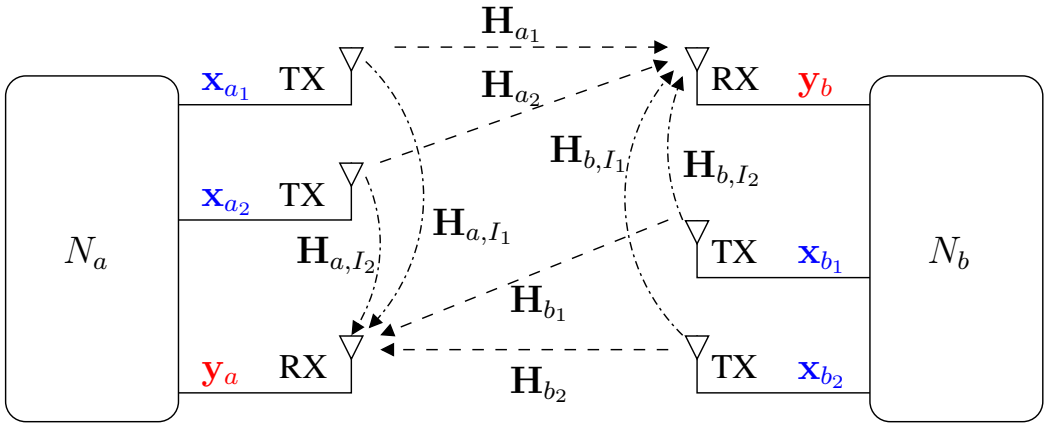

Figure 5.1: Full-duplex bi-directional communication system.

one RX antenna as depicted in Figs. 5.1 and 5.2. Without loss of generality, since both of the end nodes are identical, we focus on the received signal at node N_a, which receives the signal from node N_b and its SI signal. The received signal at node N_b is similar to that of node N_a. The received signal at node N_a after the ADC can be given as

$$\mathbf{y}_a = \mathbf{H}_{b_1}\mathbf{x}_{b_1} + \mathbf{H}_{b_2}\mathbf{x}_{b_2} + \mathbf{H}_{a,I_1}\mathbf{x}_{a_1} + \mathbf{H}_{a,I_2}\mathbf{x}_{a_2} + \mathbf{w}_a, \tag{5.1}$$

where $\mathbf{H}_{b_1}, \mathbf{H}_{b_2} \in \mathbb{C}^{M\times M}$ are the circulant channel matrices of the channels between node N_a and N_b, while $\mathbf{H}_{a,I_1}, \mathbf{H}_{a,I_2} \in \mathbb{C}^{M\times M}$ are the circulant channel matrices of the SI channels between the TX and RX antennas at node N_a, and $\mathbf{w}_a \in \mathbb{C}^{M\times 1}$ denotes the complex-valued additive white Gaussian noise (AWGN) vector with $\mathcal{CN}(0, N_0)$. Moreover, $\mathbf{x}_{a_1}, \mathbf{x}_{a_2} \in \mathbb{C}^{M\times 1}$ denote the signal transmitted from the first and second TX antennas at node N_a, respectively, whilst $\mathbf{x}_{b_1}, \mathbf{x}_{b_2} \in \mathbb{C}^{M\times 1}$ are the transmitted signals from the first and second TX antennas at node N_b, respectively. In general, the circulant channel matrix is given as

$$\mathbf{H} = \begin{bmatrix} h(0) & 0 & \dots & 0 & h(L) & \dots & h(1) \\ h(1) & h(0) & \ddots & & 0 & \ddots & \vdots \\ \vdots & h(1) & \ddots & & \ddots & \ddots & h(L) \\ h(L) & \vdots & \ddots & \ddots & & & 0 \\ 0 & h(L) & & \ddots & \ddots & & \vdots \\ \vdots & \ddots & \ddots & & \ddots & \ddots & \vdots \\ 0 & \dots & 0 & h(L) & & h(1) & h(0) \end{bmatrix}. \tag{5.2}$$

To cancel the SI, the following condition needs to be satisfied

$$\mathbf{H}_{a,I_1}\mathbf{x}_{a_1} + \mathbf{H}_{a,I_2}\mathbf{x}_{a_2} = 0. \tag{5.3}$$

In order to achieve this, we perform eigen-decomposition of the pair of SI channels, $\{\mathbf{H}_{a,I_1}, \mathbf{H}_{a,I_2}\}$, to obtain the eigenvalues, $\tilde{\mathbf{\Lambda}}_a \in \mathbb{C}^{M\times 1}$, and the eigenvectors matrix, $\mathbf{V}_a \in \mathbb{C}^{M\times M}$, by solving the GNEP [137]. The vector $\tilde{\mathbf{\Lambda}}_a = \text{diag}(\mathbf{\Lambda}_a)$ consists of the main diagonal elements of the eigenvalue matrix, $\mathbf{\Lambda}_a$, i.e., $\mathbf{\Lambda}_a = \mathbf{I}_M\tilde{\mathbf{\Lambda}}_a$. Furthermore, the eigenvectors matrix, $\mathbf{V}_a$, of the pair $\left(\mathbf{H}_{q_{I_1}}, \mathbf{H}_{q_{I_2}}\right)$ is given as

$$\mathbf{V}_a = \begin{bmatrix} | & & | \\ \mathbf{v}_{a,1} & \dots & \mathbf{v}_{a,M} \\ | & & | \end{bmatrix}, \tag{5.4}$$

where each column in $\mathbf{V}_a$, i.e. $\mathbf{v}_{a,i} \in \mathbb{C}^{M\times 1}$, represents the eigenvector corresponding to the i-th eigenvalue, $\lambda_{a,i}$ in $\tilde{\mathbf{\Lambda}}_a$.

Using the eigenvectors and eigenvalues matrices obtained from the GNEP, $\mathbf{V}_a$ and $\mathbf{\Lambda}_a$, the transmitted signal vectors can be given as

$$\mathbf{x}_{a_1} = \mathbf{V}_a\mathbf{x}_{p_a}, \tag{5.5}$$

$$\mathbf{x}_{a_2} = -\mathbf{V}_a\mathbf{\Lambda}_a\mathbf{x}_{p_a}, \tag{5.6}$$

$$\mathbf{x}_{b_1} = \mathbf{V}_b\mathbf{x}_{p_b}, \tag{5.7}$$

$$\mathbf{x}_{b_2} = -\mathbf{V}_b\mathbf{\Lambda}_b\mathbf{x}_{p_b}. \tag{5.8}$$

Substituting (5.5)-(5.8) into (5.1) results in

$$\begin{aligned} \mathbf{y}_a =& \mathbf{H}_{b_1}\mathbf{V}_b\mathbf{x}_{p_b} - \mathbf{H}_{b_2}\mathbf{V}_b\mathbf{\Lambda}_b\mathbf{x}_{p_b} + \mathbf{H}_{a,I_1}\mathbf{V}_a\mathbf{x}_{p_a} - \mathbf{H}_{a,I_2}\mathbf{V}_a\mathbf{\Lambda}_a\mathbf{x}_{p_a} + \mathbf{w}_a, \\ =& (\mathbf{H}_{b_1}\mathbf{V}_b - \mathbf{H}_{b_2}\mathbf{V}_b\mathbf{\Lambda}_b)\mathbf{x}_{p_b} + (\mathbf{H}_{a,I_1}\mathbf{V}_a - \mathbf{H}_{a,I_2}\mathbf{V}_a\mathbf{\Lambda}_a)\mathbf{x}_{p_a} + \mathbf{w}_a, \\ =& \mathbf{G}_b\mathbf{x}_{p_b} + \mathbf{\Xi}_a\mathbf{x}_{p_a} + \mathbf{w}_a, \end{aligned} \tag{5.9}$$

where we have defined $\mathbf{G}_b$ as

$$\mathbf{G}_b = \mathbf{H}_{b_1}\mathbf{V}_b - \mathbf{H}_{b_2}\mathbf{V}_b\mathbf{\Lambda}_b, \tag{5.10}$$

and $\mathbf{\Xi}_a$ as

$$\mathbf{\Xi}_a = \mathbf{H}_{a,I_1}\mathbf{V}_a - \mathbf{H}_{a,I_2}\mathbf{V}_a\mathbf{\Lambda}_a. \tag{5.11}$$

In this work, we utilize transmit precoding to simplify the receiver structure and avoid the need for a zero-forcing equalizer in the detection. Hence, the end nodes in the proposed system need to always have the CSI of the channels to be able perform the transmit precoding. Thus, $\mathbf{x}_{p_a}$ and $\mathbf{x}_{p_b}$ denote the output of the transmit precoding at each node, which can be accomplished by multiplying with the precoding matrices, $\mathbf{P}_a$ and $\mathbf{P}_b$, at each node designed as

$$\mathbf{P}_q = \beta_q \mathbf{G}_q^H \left(\mathbf{G}_q \mathbf{G}_q^H\right)^{-1}, \tag{5.12}$$

for $q \in \{a, b\}$. Moreover, $\beta_q \in \{\beta_a,\ \beta_b\}$ is the normalized factor, which is used to satisfy the total power constraint, ρ, such that

$$\mathbf{E}\left[||\mathbf{x}_{p_q}||^2\right] \leq \rho_q, \tag{5.13}$$

and is given as [138]

$$\beta_q = \sqrt{\frac{\rho_q}{\text{tr}\left[\left(\mathbf{G}_q \mathbf{G}_q^H\right)^{-1}\right]}}. \tag{5.14}$$

The resulting receiver structure is depicted in Fig. 5.2. The ZF transmit precoding that utilizes the Moore-Penrose pseudoinverse is employed in the proposed P-FD-BD system to reverse the impairments introduced by the channels. Hence, (5.9) can be rewritten as

$$\mathbf{y}_a = \mathbf{G}_b \mathbf{P}_b \mathbf{x}_{u_b} + \mathbf{\Xi}_a \mathbf{P}_a \mathbf{x}_{u_a} + \mathbf{w}_a, \tag{5.15}$$

where we have substituted $\mathbf{x}_{p_q} = \mathbf{P}_q \mathbf{x}_{u_q}$ with $\mathbf{x}_{u_q}$ being the buffered output of the OFDM modulator including cyclic prefix (CP). The buffer is introduced to reduce the computational and storage complexity required for the multiplication by the transmit precoding matrix, $\mathbf{P_a}$, and the SIC implementation, i.e. the matrix multiplications by $\mathbf{V}_a$ and $-\mathbf{V}_a\mathbf{\Lambda}_a$. In essence, the buffering stage converts the signal after IFFT and CP insertion, i.e. $\mathbf{x}_{cp_q} \in \mathbb{C}^{N+L_{cp}\times 1}$, into multiple blocks of $\mathbf{x}_{u_q} \in \mathbb{C}^{M\times 1}$, where N is the number of subcarriers in the OFDM symbol and L_{CP} denotes the CP length required to combat multipath induced inter-symbol interference (ISI). Moreover, the size of the buffer M is chosen such that $\max\{L_{a_1}, L_{a_2}, L_{b_1}, L_{b_2}, L_{a,I_1}, L_{a,I_2}, L_{b,I_1}, L_{b,I_2}\} \leq M$, where $L_{a_1}, L_{a_2}, L_{b_1}$ and L_{b_2} denote the excess delay spreads of the channels between the nodes, while $L_{a,I_1}, L_{a,I_2}, L_{b,I_1}$ and L_{b,I_2} are the excess delay spreads of the SI channels. Furthermore, $\mathbf{x}_{cp_q}$ is obtained by copying the last L_{CP} samples of the IFFT output signal, i.e. $\mathbf{x}_q$

and insert them at the beginning of $\mathbf{x}_q$, that is

$$\mathbf{x}_{cp_q} = [\mathbf{x}_q(N-L_{CP}), \ldots, \mathbf{x}_q(N-1), \mathbf{x}_q(0), \ldots, \mathbf{x}_q(N-1)]\,. \tag{5.16}$$

The IFFT output signal, $\mathbf{x}_q$, is given as

$$\mathbf{x}_q = \mathbf{F}^{\dagger}\mathbf{X}_q, \tag{5.17}$$

where $\mathbf{F}^{\dagger}$ is the Hermitian transpose of the discrete Fourier Transform (DFT) matrix, $\mathbf{F}$, which is given as

$$F_{m,n} = \frac{1}{\sqrt{N}} e^{-j2\pi\frac{mn}{N}}, \;\; \forall m, n = 0, 1, \ldots, N-1, \tag{5.18}$$

and $\mathbf{X}_q \in \mathbb{C}^{N\times 1}$ denotes the modulated information symbols. In practice, the number of subcarriers, N, is selected to be a power of 2, which in turn enables the DFT operation to be implemented using the Fast Fourier Transform (FFT).

Using (5.12) and (5.11) to substitute $\mathbf{P}_b$ and $\boldsymbol{\Xi}_a$ in (5.15) yields

$$\mathbf{y}_a = \beta_b \mathbf{x}_{u_b} + (\mathbf{H}_{a,I_1}\mathbf{V}_a - \mathbf{H}_{a,I_2}\mathbf{V}_a\boldsymbol{\Lambda}_a)\mathbf{P}_a\mathbf{x}_{u_a} + \mathbf{w}_a. \tag{5.19}$$

It can be observed from (5.19) that the SI term is given as

$$\boldsymbol{\psi}_a = (\mathbf{H}_{a,I_1}\mathbf{V}_a - \mathbf{H}_{a,I_2}\mathbf{V}_a\boldsymbol{\Lambda}_a)\mathbf{P}_a\mathbf{x}_{u_a}. \tag{5.20}$$

The key motivation behind the design of the proposed system as depicted in Fig. 5.2 is to mitigate effectively the SI induced by the FD mode. This can be achieved by constructing $\boldsymbol{\Lambda}_a$ and $\mathbf{V}_a$ so that

$$\mathbf{H}_{a,I_1}\mathbf{V}_a - \mathbf{H}_{a,I_2}\mathbf{V}_a\boldsymbol{\Lambda}_a = \mathbf{0}. \tag{5.21}$$

In the literature, (5.21) is referred to as the generalized nonsymmetric eigenproblem that in vector form satisfies [137]

$$\mathbf{H}_{a,I_1}\mathbf{v}_{a,i} - \lambda_{a,i}\mathbf{H}_{a,I_2}\mathbf{v}_{a,i} = \mathbf{0}. \tag{5.22}$$

Thus, finding $\boldsymbol{\Lambda}_a$ and $\mathbf{V}_a$ that satisfy (5.21), and utilizing them in the transmit chain of each transceiver node as illustrated in Fig. 5.2, results in suppressing the SI signal before the ADC. It is worth pointing out that unlike the existing spatial SIC methods, [97, 113, 114], our proposed spatial SIC scheme does not require any SIC signal processing stage in the receive chain after the ADC.

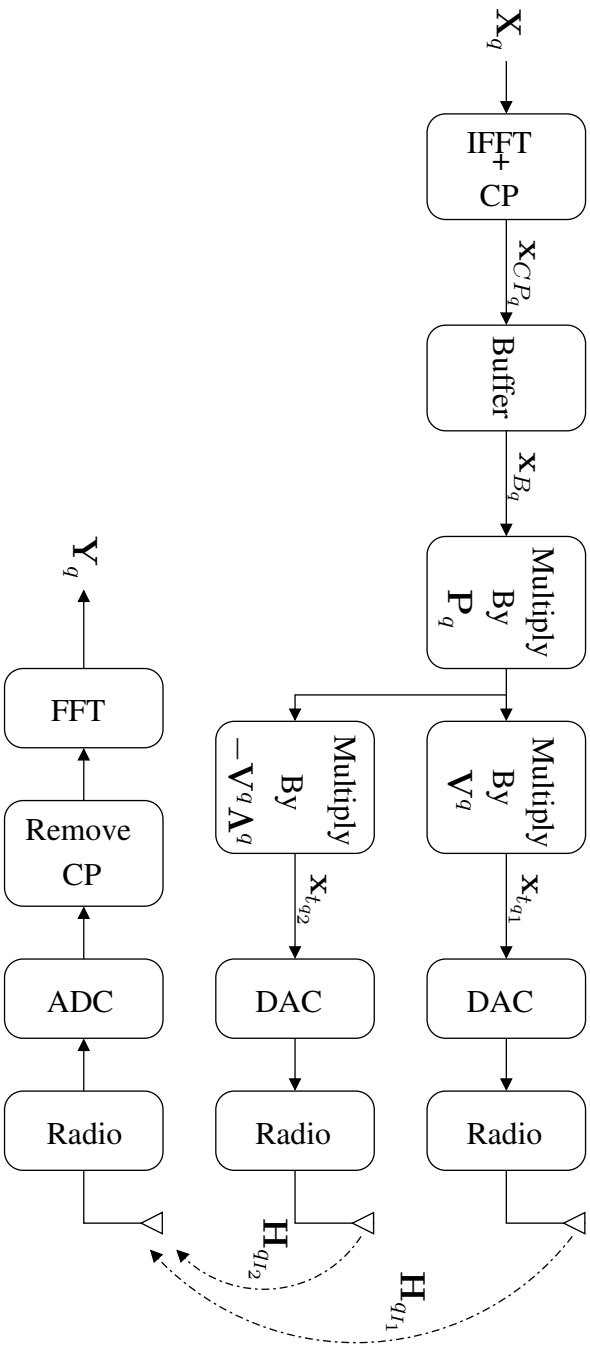

Figure 5.2: Architecture of each node in the proposed system.

The eigenvalues, $\tilde{\mathbf{\Lambda}}_a$, can be computed from (5.21) such that

$$\det\left(\mathbf{H}_{a,I_1} - \lambda_a \mathbf{H}_{a,I_2}\right) = 0, \tag{5.23}$$

this equation will result in an M-th order polynomial, $\phi(\lambda_a)$ exhibiting M distinct roots that correspond to M eigenvalues of the pair $(\mathbf{H}_{a,I_1}, \mathbf{H}_{a,I_2})$. Furthermore, each eigenvector, $\mathbf{v}_{a,i}$, corresponding to the i-th eigenvalue, $\lambda_{a,i}$, can be obtained by solving

$$\left(\mathbf{H}_{a,I_1} - \lambda_{a,i}\mathbf{H}_{a,I_2}\right)\mathbf{v}_{a,i} = 0. \tag{5.24}$$

It is worth pointing out that the generalized nonsymmetric eigenproblem can be evaluated using the QZ algorithm, which is a generalization of the QR algorithm [139] and [140]. The QZ algorithm factorizes the pair $(\mathbf{H}_{a,I_1}, \mathbf{H}_{a,I_2})$ such as

$$\mathbf{H}_{a,I_1} = \mathbf{Q}\mathbf{S}\mathbf{Z}^{\mathbf{H}}, \tag{5.25}$$

$$\mathbf{H}_{a,I_2} = \mathbf{Q}\mathbf{T}\mathbf{Z}^{\mathbf{H}}, \tag{5.26}$$

where $\mathbf{Q}$ and $\mathbf{Z}$ are unitary matrices, while $\mathbf{S}$ and $\mathbf{T}$ are upper quasitriangular matrices. Moreover, the generalized eigenvalues of the pair $(\mathbf{H}_{a,I_1}, \mathbf{H}_{a,I_2})$ can be obtained as

$$\lambda_{a,i} = \frac{\mathbf{S}_{ii}}{\mathbf{T}_{ii}}. \tag{5.27}$$

For more details related to the QZ algorithm, we refer the interested reader to [139], which introduced the QZ algorithm to solve the generalized eigenproblem. Moreover, the generalized eigenproblem can be evaluated using several available implementations; for instance, the LAPACK library has `qz.zggev()` and `qz.dggev()` functions that can be used to compute the generalized eigenproblem for complex and real matrices, respectively. It is worth mentioning that these LAPACK functions are utilized by the `eig()` function in MATLAB too.

5.3 Transmit Signal Noise

In this section, we address practical issues related to the transmit signal noise and its effect on the performance of the proposed GNEP SIC. In essence, the aim of the GNEP SIC is to mitigate the SI signal before it reaches the local receive chain by constructing the transmit signal so that the convolution between this transmit signal and the SI channels yields zero. However, the constructed transmit signal is subject to various practical implementation impairments, such as oscillator phase noise, digital-to-analog converter (DAC) imperfections and carrier frequency offset, amongst others [113]. The joint effect of these impairments is usually modelled as an uncorrelated, zero-mean, additive distortion noise such as $\mathcal{CN}(0, \sigma^2_{\boldsymbol{\xi}_{a_1}})$ and $\mathcal{CN}(0, \sigma^2_{\boldsymbol{\xi}_{a_2}})$ [113]. Thus, the noisy version of the transmit signals can be given as

$$\tilde{\mathbf{x}}_{a_1} = \mathbf{x}_{a_1} + \boldsymbol{\xi}_{a_1}, \tag{5.28}$$

$$\tilde{\mathbf{x}}_{a_2} = \mathbf{x}_{a_2} + \boldsymbol{\xi}_{a_2}, \tag{5.29}$$

where $\boldsymbol{\xi}_{a_1}$ and $\boldsymbol{\xi}_{a_2}$ denote the transmit signal noise on each transmit chain, respectively. Substituting (5.5) and (5.6) in (5.28) and (5.29), respectively, yields

$$\tilde{\mathbf{x}}_{a_1} = \mathbf{V}_a \mathbf{P}_a \mathbf{x}_{u_a} + \boldsymbol{\xi}_{a_1}, \tag{5.30}$$

$$\tilde{\mathbf{x}}_{a_2} = -\mathbf{V}_a \boldsymbol{\Lambda}_a \mathbf{P}_a \mathbf{x}_{u_a} + \boldsymbol{\xi}_{a_2}. \tag{5.31}$$

To model the effect of the transmit signal noise on the performance of the GNEP SIC, the SI related signal term in (5.20) should be substituted by (5.30) and (5.31), thus, yielding

$$\boldsymbol{\psi}_a = (\mathbf{H}_{a,I_1} \mathbf{V}_a - \mathbf{H}_{a,I_2} \mathbf{V}_a \boldsymbol{\Lambda}_a) \mathbf{P}_a \mathbf{x}_{u_a} + \boldsymbol{\xi}_a, \tag{5.32}$$

where $\boldsymbol{\xi}_a$ is the total noise resulting from the transmit signals distortion and is given as

$$\boldsymbol{\xi}_a = \mathbf{H}_{a,I_1} \boldsymbol{\xi}_{a_1} + \mathbf{H}_{a,I_2} \boldsymbol{\xi}_{a_2}. \tag{5.33}$$

Due to the fact that $\mathbf{V}_a$ and $\boldsymbol{\Lambda}_a$ were computed using the generalized nonsymmetric eigenproblem to satisfy (5.21), we obtain $\boldsymbol{\psi}_a = \boldsymbol{\xi}_a$, and the SI signal in (5.32) can be reduced to

$$\boldsymbol{\psi}_a = \mathbf{H}_{a,I_1} \boldsymbol{\xi}_{a_1} + \mathbf{H}_{a,I_2} \boldsymbol{\xi}_{a_2}, \tag{5.34}$$

which represents the residual SI signal.

5.4 Statistical Analysis of the Signal-to-Interference-and-Noise Ratio

This section evaluates the SINR of the proposed P-FD-BD communication system along with its statistical behaviour. After removing the CP and performing the FFT, the received signal in frequency domain is given as

$$\mathbf{Y}_a = \beta_b \mathbf{F} \mathbf{F}^{\dagger} \mathbf{X}_b + \boldsymbol{\Psi}_a + \mathbf{F} \mathbf{w}_a, \tag{5.35}$$

where

$$\boldsymbol{\Psi}_a = \mathbf{F} \boldsymbol{\xi}_a, \tag{5.36}$$

that is modelled using a conditionally complex Gaussian, i.e. $\mathcal{CN}(0, \Im)$ with $\Im = \mathbf{E}[\mathbf{\Psi}_a \mathbf{\Psi}_a^\dagger]$ Moreover, since $\mathbf{F}\mathbf{F}^\dagger = \mathbf{I}$, (5.35) can be simplified as

$$\mathbf{Y}_a = \beta_b \mathbf{X}_b + \mathbf{\Psi}_a + \mathbf{W}_a, \tag{5.37}$$

where $\mathbf{W}_a = \mathbf{F}\mathbf{w}_a$.

The SINR at the output of the FFT, $\mathbf{Y}_a$, at node N_a is given as

$$\gamma_a(n) = \frac{|\beta_b|^2 P_s}{\Im + \sigma_{W_a}^2}, \tag{5.38}$$

where n is the subcarrier index, $P_s = \mathbf{E}|\mathbf{X}_b(n)|^2$ is the information symbol energy, and $\sigma_{W_a}^2$ is the variance of the noise. Moreover, by dividing both the nominator and denominator of (5.38) by $\sigma_{W_a}^2$, we can rewrite (5.38) as

$$\gamma_a(n) = \frac{\Omega_a}{\Omega_{I_a} + 1}, \tag{5.39}$$

where

$$\Omega_a = \frac{|\beta_2|^2 P_s}{\sigma_{W_a}^2}, \tag{5.40}$$

and

$$\Omega_{I_a} = \frac{\Im}{\sigma_{W_a}^2}, \tag{5.41}$$

denote the signal-to-noise ratio (SNR) and self-interference-to-noise ratio (INR), respectively. A closer look at the SNR term, i.e. (5.40), reveals that this term is similar to the average SNR of the AWGN channel, hence, the PDF of this term is constant [99, 133], while Ω_{I_a}, (5.41), is assumed to be random . Moreover, the PDF of the INR term in (5.41) was empirically evaluated and supported by the theoretical PDF as illustrated in Fig. 5.3, which validated the assumption that the power of the residual SI exhibits a gamma distribution, that is

$$p_{\Omega_{I_a}}(\Omega_{I_a}) = \frac{\Omega_{I_a}}{(\eta_a)^2} e^{-\frac{\Omega_{I_a}}{\eta_a}}, \tag{5.42}$$

where $\eta_a = \mathbf{E}\{\Omega_{I_a}\}$.

It can be observed from (5.39) that the SINR of the proposed P-FD-BD system comprises the ratio of Ω_a divided by the term $\Omega_{I_a} + 1$, hence, to evaluate the PDF of the SINR we need to compute the PDF of $\Omega_{I_1} + 1$ first. Let $Z_{I_a} = \Omega_{I_a} + 1$, the PDF of Z_{I_a}, $p_{Z_{I_a}}(Z_{I_a})$, can be

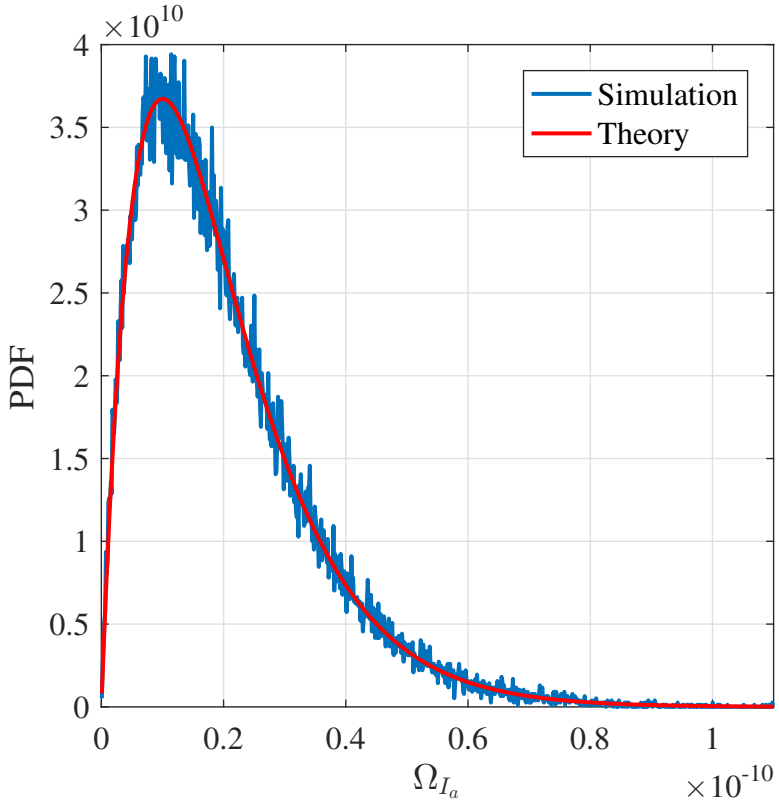

Figure 5.3: The PDF of power of the residual SI after the GNEP SIC, i.e. $|\mathbf{SI}|^2$.

obtained using the results in [141, Eq. (5.6)] such as

$$p_{Z_{I_a}}(Z_{I_a}) = \frac{(Z_{I_a}-1)}{(\eta_a)^2} e^{-\frac{(Z_{I_a}-1)}{\eta_a}}. \tag{5.43}$$

Moreover, (5.39) can be rewritten as

$$\gamma_a(n) = \frac{\Omega_a}{Z_{I_a}}, \tag{5.44}$$

and the PDF of the SINR in (5.44) can be obtained using the results in [141, Eq. (5.7)], i.e.

$$p_{\gamma_a}(\gamma_a) = \left(\frac{(\Omega_a)^2}{(\eta_a)^2(\gamma_a)^3} - \frac{\Omega_a}{(\eta_a)^2(\gamma_a)^2} \right) e^{\frac{1}{\eta_a}} e^{-\frac{\Omega_a}{\eta_a \gamma_a}}. \tag{5.45}$$

Furthermore, the CDF of the SINR is given as

$$P_{\gamma_a}(\gamma_a) = \int_0^{\gamma_a} p_{\gamma_a}(\gamma_a) d\gamma_a. \tag{5.46}$$

Substituting (5.45) in (5.46) results in

$$P_{\gamma_a}(\gamma_a) = \int_0^{\gamma_a} \frac{(\Omega_a)^2}{(\eta_a)^2(\gamma_a)^3} e^{\frac{1}{\eta_a}} e^{-\frac{\Omega_a}{\eta_a \gamma_a}} d\gamma_a - \int_0^{\gamma_a} \frac{\Omega_a}{(\eta_a)^2(\gamma_a)^2} e^{\frac{1}{\eta_a}} e^{-\frac{\Omega_a}{\eta_a \gamma_a}} d\gamma_a. \tag{5.47}$$

The integrals in (5.47) can be solved using [123, Eq. (3.471.1)]. Consequently, the CDF of the SINR is given as

$$P_{\gamma_a}(\gamma_a) = \left(1 + \frac{\Omega_a}{\eta_a \gamma_a}\right) e^{\frac{1}{\eta_a}} e^{-\frac{\Omega_a}{\eta_a \gamma_a}} - \frac{1}{\eta_a} e^{\frac{1}{\eta_a}} e^{-\frac{\Omega_a}{\eta_a \gamma_a}}. \tag{5.48}$$

The closed-form expression in (5.48) will be exploited in the next section to derive closed-form expressions for the outage probability and ASER of the proposed P-FD-BD system.

5.5 Performance Evaluation Metrics

In this section, important performance evaluation metrics of the proposed P-FD-BD wireless communication system are derived. These include, the outage probability, ASER, the ergodic capacity and the PAPR. These metrics will be utilized in the next section to understand the impact of the transmit signal noise on the performance of GNEP SIC and the entire system.

5.5.1 Outage Probability

The outage probability is widely used to measure the communication link quality and is defined as the probability that the value of the SINR, γ_a, falls below a certain threshold, γ_{th}, and can be evaluated as [125]

$$P_{out}(\gamma_{th}) = P\{\gamma_a \leq \gamma_{th}\} = P_{\gamma_a}(\gamma_{th}), \tag{5.49}$$

which is similar to the definition of the SINR CDF. Therefore, evaluating (5.48) at γ_{th} yields the outage probability, which is given as

$$P_{out}(\gamma_{th}) = \left[1 + \frac{\Omega_a}{\eta_a \gamma_{th}}\right] e^{\frac{1}{\eta_a}} e^{-\frac{\Omega_a}{\eta_a \gamma_{th}}} - \frac{1}{\eta_a} e^{\frac{1}{\eta_a}} e^{-\frac{\Omega_a}{\eta_a \gamma_{th}}}. \tag{5.50}$$

5.5.2 The Symbol Error Probability

The ASER performance of the proposed P-FD-BD communication system is evaluated by utilizing the formula [126, 142]

$$\bar{P}_{e_a} = \frac{\varrho}{2}\sqrt{\frac{\nu}{\pi}}\int_0^\infty \frac{e^{-\nu\gamma_a}}{\sqrt{\gamma_a}} P_{\gamma_a}(\gamma_a)d\gamma_a, \tag{5.51}$$

that exploits the CDF of the SINR, $P_{\gamma_a}(\gamma_a)$, which was evaluated in the previous section. Moreover, in (5.51), ϱ and ν are modulation dependent constants, for instance, for M-ary phase shift keying (M-PSK): $\varrho_{PSK} = 2$ and $\nu_{PSK} \approx \sin^2(\frac{\pi}{M})$, where M is the modulation order. Using (5.48) to substitute $P_{\gamma_a}(\gamma_a)$ in (5.51) yields

$$\begin{aligned}\bar{P}_{e,PSK_a} = \frac{\varrho_{PSK}}{2}\sqrt{\frac{\nu_{PSK}}{\pi}}e^{\frac{1}{\eta_a}}\Bigg[\int_0^\infty \frac{e^{-\nu_{PSK}\gamma_a}}{\sqrt{\gamma_a}}e^{-\frac{\Omega_a}{\eta_a\gamma_a}}d\gamma_a + \int_0^\infty \frac{\Omega_a e^{-\nu_{PSK}\gamma_a}}{\eta_a\gamma_a\sqrt{\gamma_a}}e^{-\frac{\Omega_a}{\eta_a\gamma_a}}d\gamma_a \\ - \int_0^\infty \frac{e^{-\nu_{PSK}\gamma_a}}{\eta_a\sqrt{\gamma_a}}e^{-\frac{\Omega_a}{\eta_a\gamma_a}}d\gamma_a\Bigg].\end{aligned} \tag{5.52}$$

The first and third integrals can be solved by exploiting [123, Eq. (3.471.15)], while the second integral can be evaluated using [123, Eq. (3.472.5)]. Subsequently, the ASER of the proposed P-FD-BD system is given as

$$\bar{P}_{e,PSK_a} = \frac{\varrho_{PSK}}{2}e^{\frac{1}{\eta_a}}e^{-2\sqrt{\frac{\Omega_a\nu_{PSK}}{\eta_a}}}\left[1 + \sqrt{\frac{\Omega_a\nu_{PSK}}{\eta_a}} - \frac{1}{\eta_a}\right]. \tag{5.53}$$

The Upper bound ASER for the M-ary quadrature amplitude modulation (M-QAM) can be obtained as [143]

$$\bar{P}_{e,QAM_a} \leq \frac{M-1}{M}\mathcal{M}_{\gamma_a}(-\nu_{QAM}), \tag{5.54}$$

where $\nu_{QAM} = \frac{3}{2(M-1)}$ and $\mathcal{M}_{\gamma_a}(-\nu_{QAM})$ is the moment generating function (MGF) of the SINR, which is given as [125]

$$\mathcal{M}_{\gamma_a}(-\nu_{QAM}) = \int_0^\infty e^{-\nu_{QAM}\gamma_a}p_{\gamma_a}(\gamma_a)d\gamma_a. \tag{5.55}$$

Substituting (5.45) in (5.55) results in

$$\mathcal{M}_{\gamma_a}(-\nu_{QAM}) = \frac{e^{\frac{1}{\eta_a}}}{(\eta_a)^2}\left[\int_0^\infty \frac{(\Omega_a)^2}{(\gamma_a)^3}e^{-\frac{\Omega_a}{\eta_a\gamma_a}}e^{-\nu_{QAM}\gamma_a}d\gamma_a \int_0^\infty \frac{\Omega_a}{(\gamma_a)^2}e^{-\frac{\Omega_a}{\eta_a\gamma_a}}e^{-\nu_{QAM}\gamma_a}d\gamma_a\right]. \tag{5.56}$$

These integrals can be solved using [123, Eq. (3.471.9)], which yields

$$\mathcal{M}_{\gamma_a}(-\nu_{QAM}) = e^{\frac{1}{\eta_a}}\left[\frac{2\Omega_a\nu_{QAM}}{\eta_a}K_{-2}\left(2\sqrt{\frac{\nu_{QAM}\Omega_a}{\eta_a}}\right)\right.$$
$$\left. - 2\sqrt{\frac{\Omega_a\nu_{QAM}}{(\eta_a)^3}}K_{-1}\left(2\sqrt{\frac{\nu_{QAM}\Omega_a}{\eta_a}}\right)\right]. \tag{5.57}$$

Hence, using (5.57) to substitute $\mathcal{M}_{\gamma_a}(-\nu_{QAM})$ in (5.54) gives the upper bound of the ASER for the M-QAM modulation such as

$$\bar{P}_{e,QAM_a} \leq \frac{(M-1)e^{\frac{1}{\eta_a}}}{M}\left[\frac{2\Omega_a\nu_{QAM}}{\eta_a}K_{-2}\left(2\sqrt{\frac{\nu_{QAM}\Omega_a}{\eta_a}}\right)\right.$$
$$\left. - 2\sqrt{\frac{\Omega_a\nu_{QAM}}{(\eta_a)^3}}K_{-1}\left(2\sqrt{\frac{\nu_{QAM}\Omega_a}{\eta_a}}\right)\right]. \tag{5.58}$$

Moreover, for the SI free P-FD-BD system, the SINR in (5.39) will be reduced to

$$\gamma_a(n) = \Omega_a, \tag{5.59}$$

which exhibits a constant PDF due to the utilization of transmit precoding. Hence, the analytical ASER of the M-PSK modulation for the SI free P-FD-BD system is evaluated as [99, 133]

$$\bar{P}_{e,PSK_a} = \varrho_{PSK}Q\left(\sqrt{2\Omega_a\nu_{PSK}}\right). \tag{5.60}$$

where $Q(.)$ denotes Q-function. Furthermore, the exact ASER of the M-QAM modulation for the SI free P-FD-BD system can be given as [99, 133]

$$\bar{P}_{e,QAM_a} = \frac{2(\sqrt{M}-1)}{\sqrt{M}}Q\left(\sqrt{\frac{3\Omega_a}{M-1}}\right). \tag{5.61}$$

The ASER results for the SI free scenario will provide in the next section a reference benchmark to measure the efficiency of the proposed GNEP SIC scheme.

5.5.3 Ergodic Capacity

In this section, we evaluate the upper bound ergodic capacity that can be achieved by the P-FD-BD system. In general, the ergodic capacity can be given as [133]

$$C = \int_0^\infty \log_2(1+\gamma_a) p_{\gamma_a}(\gamma_a) d\gamma_a. \tag{5.62}$$

By exploiting Jensen's inequality, (5.62) can be presented as [133]

$$\begin{aligned} C &= \int_0^\infty \log_2(1+\gamma_a) p_{\gamma_a}(\gamma_a) d\gamma_a = \mathbf{E}\left[\log_2(1+\gamma_a)\right] \\ &\leq \log_2(1+\mathbf{E}\left[\gamma_a\right]) = \log_2(1+\bar{\gamma}_a), \end{aligned} \tag{5.63}$$

where $\bar{\gamma}_a$ denotes the average SINR. Moreover, to provide a benchmark and meticulously investigate the performance of the proposed GNEP SIC, the ergodic capacity of the SI free P-FD-BD system is evaluated as

$$C = \log_2\left(1+\Omega_a\right). \tag{5.64}$$

5.5.4 Peak-to-Average Ratio (PAPR)

Due to the fact that the PAPR of the OFDM signal is the main concern of all of the OFDM system designers, it is crucial to examine the impact of the proposed GNEP SIC scheme in conjunction with the ZF precoding, which are used to construct the transmit signal, on the PAPR of the OFDM-based P-FD-BD system. The PAPR is defined as the ratio of the maximum power to average power of the time domain signal after the IFFT operation [144], which can be evaluated as [145–147]

$$PAPR = \frac{\max\limits_{0\leq k<NL-1} |x_{g_q}(k)|^2}{E\left\{|x_{g_q}(k)|^2\right\}}, \tag{5.65}$$

where $x_{g_q}(k)$ denotes the L-times oversampled IFFT output and is given as [147]

$$x_{g_q}(k) = \frac{1}{\sqrt{N}} \sum_n^{N-1} \mathbf{X}_q(n) e^{j2\pi\frac{nk}{N}}, \;\; 0 \leq k \leq LN-1. \tag{5.66}$$

In this paper, we examine the complementary cumulative distribution function (CCDF) of the PAPR, which represents the probability that the PAPR of a certain OFDM symbol is greater

than a given threshold and can be obtained such that [145]

$$\begin{aligned} P\left(PAPR > z\right) &= 1 - P\left(PAPR \leq z\right) \\ &= 1 - F\left(z\right)^{N} \\ &= 1 - \left(1 - \exp(-z)\right)^{N}. \end{aligned} \tag{5.67}$$

This expression is derived under the assumption that N is sufficient to ensure that N OFDM signal samples are mutually independent and uncorrelated [144–147].

5.6 Numerical Results

This section investigates the performance of the P-FD-BD OFDM system, which is combined with the proposed GNEP SIC scheme to effectively suppress the SI signal. We consider an FD bi-directional wireless communication system, which comprises two FD nodes that exchange information over frequency-selective channels. Moreover, in conjunction with the GNEP SIC, a ZF transmit precoding is employed at each node to invert the channels fading. Each node in the considered bi-directional network is equipped with two TX antennas and one RX antenna to enable the implementation of the proposed GNEP SIC.

First, the impact of the transmit signal noise on the performance of the introduced GNEP SIC has been evaluated. Fig. 5.4 depicts the average power of the SI signal after the SIC as a function of $\Delta_{a_s} = \mathbf{E}\left\{\boldsymbol{\xi}_{a_s}\right\}$, where $\Delta_{a_s} \in \{\Delta_{a_1}, \Delta_{a_2}\}$ and $\boldsymbol{\xi}_{a_s} \in \left\{\boldsymbol{\xi}_{a_1}, \boldsymbol{\xi}_{a_2}\right\}$, for the passive SIC, the proposed GNEP SIC and the combination of the passive and GNEP SIC. The passive SIC in this paper indicates the suppression that naturally results from the distance between the TX antennas and RX antenna at each node, and the experimental results in [9] have shown that 40 dB suppression can be attained from this kind of SIC. It can be observed from Fig. 5.4 that the power of the SI signal after the GNEP SIC varies with Δ_{a_s}. Moreover, Fig. 5.4 demonstrates the efficiency of GNEP SIC in suppressing the SI signal when Δ_{a_s} is less than 0.1.

Next, the impact of the transmit signal noise on the PDF of the SINR was evaluated for three different scenarios of average transmit signal noise, $\Delta_{a_1} = \Delta_{a_2} = 0.04,\ 0.05,\ 0.06$, as illustrated in Fig. 5.5. A closer inspection of Fig. 5.5 reveals that as the average transmit signal noise increases the distribution of the SINR becomes more concentrated in the low SINR region.

Fig. 5.6 illustrates the analytical and the simulation based ASER vs. SNR results using (4-QAM) modulation scheme of the P-FD-BD system for four different scenarios of Δ_{a_s}, $\Delta_{a_1} = \Delta_{a_2} = 0.04,\ 0.05,\ 0.06$ and 0.07, along with SI free scenario. Inspecting Fig. 5.6 shows that the

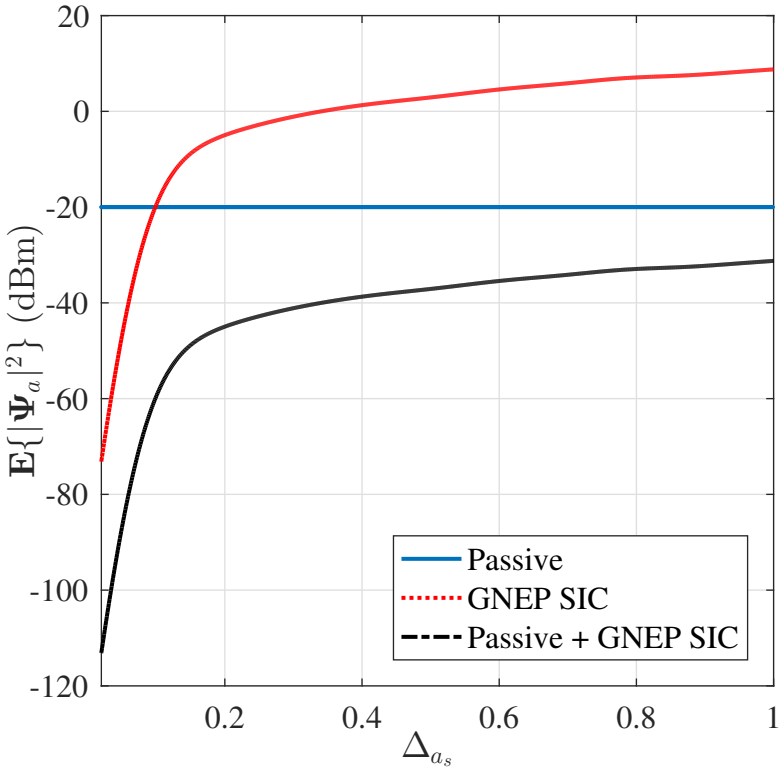

Figure 5.4: The average power of the SI signal after the proposed GNEP SIC Vs. the transmit signal noise power.

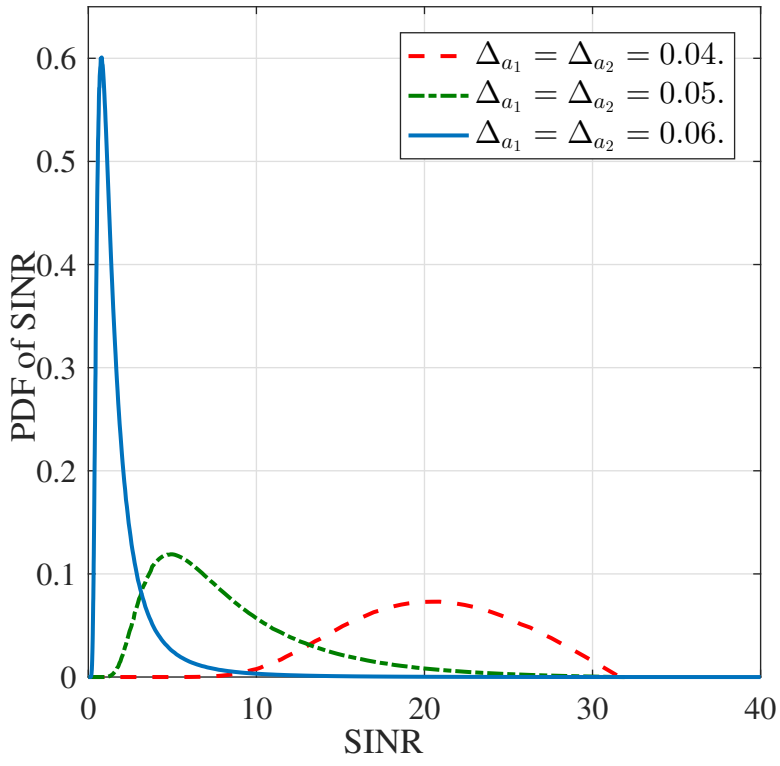

Figure 5.5: The PDF of the SINR of the P-FD-BD communication system with GNEP SIC.

ASER for these considered scenarios reaches 10^{-4} at SNR equals $11.4,\ 13.3,\ 21.7,\ 29.75,\ 35.55$ dB, respectively, which demonstrates the SNR penalty that comes with the transmit signal noise. This SNR penalty mainly results from the residual SI signal after the GNEP SIC. Moreover, the analytical upper bound and the exact simulation ASER results in Fig. 5.6 show a close match, which validates the upper bound ASER expression that has been derived in this paper. Furthermore, it can be observed from Fig. 5.6 that when $\Delta_{a_1} = \Delta_{a_2} = 0.04$ is considered the ASER performance of the P-FD-BD communication system is close to that of the SI free scenario, which indicates the efficiency of the proposed GNEP SIC in mitigating the SI signal. Next, the

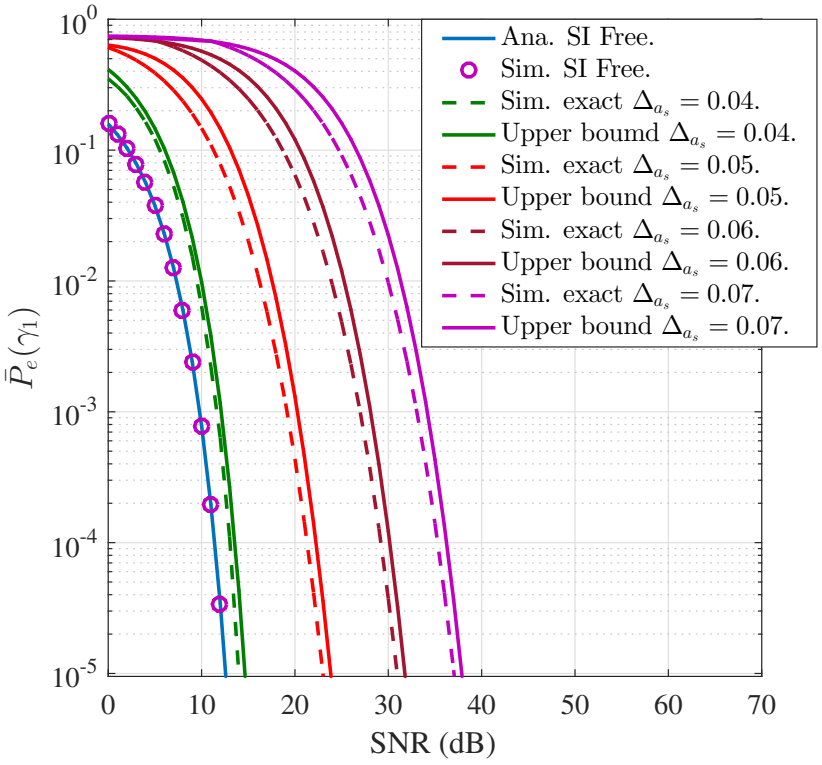

Figure 5.6: ASER Vs. SNR of the proposed P-FD-BD communication system with GNEP SIC using 4-QAM modulation scheme.

analytical BER result of the OFDM based P-FD-BD communication system was evaluated and supported by matching simulation results as illustrated in Fig. 5.7. Moreover, these BER results were compared with those of Alamouti space-time block code (STBC) system [148] with two TX antennas and one RX antenna and those of the coded FD-SIMO bi-directional system in [37] when one TX antenna and two RX antennas at each node scenario is considered to ensure a fair comparison, as depicted in Fig. 5.7. A closer at Fig. 5.7 reveals that the proposed system outperforms Alamouti STBC system and can attain 14 dB SNR gain. Furthermore, the results in Fig. 5.7 show that the coded FD-SIMO slightly outperforms our proposed system at the low SNR region, this comes from the error correction technique exploited in that work, while the

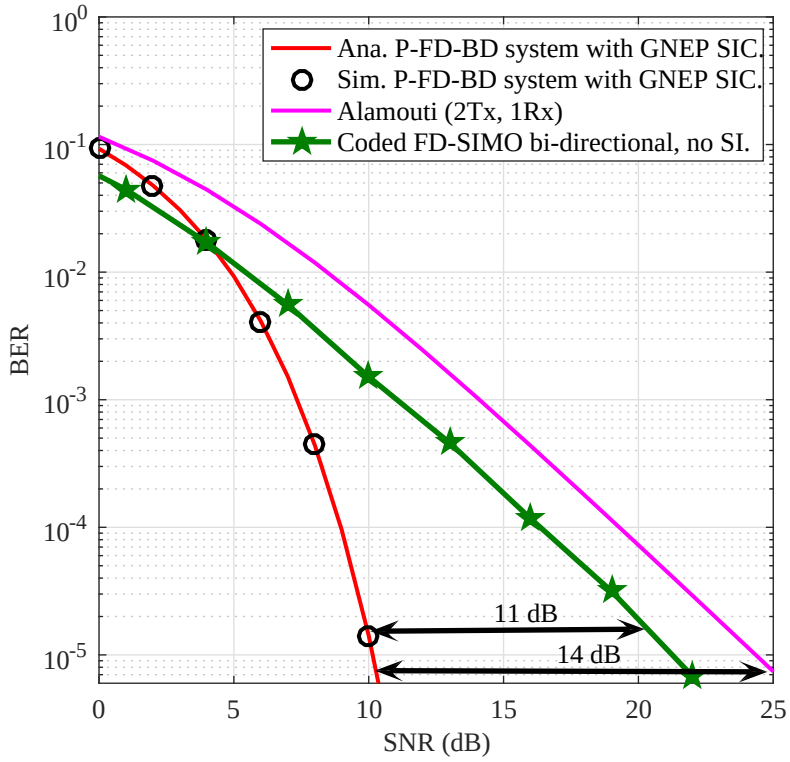

Figure 5.7: BER Vs. SNR of the proposed FD bi-directional communication system with GNEP SIC.

proposed system outperforms the coded FD-SIMO by 11 dB when the SNR is greater than 4 dB. It is worth pointing out that the comparison in Fig. 5.7 demonstrates the efficiency of the introduced GNEP SIC in suppressing the SI signal.

Figs. 5.8 and 5.9 show the analytical and simulation outage probability performance of the P-FD-BD communication system. Fig. 5.8 illustrates the outage probability performance of the considered system, $P_{out}(\gamma_{th})$, as a function of the SINR threshold, γ_{th}, for four different scenarios of Δ_{a_s}, $\Delta_{a_1} = \Delta_{a_2} = 0.04,\ 0.05,\ 0.06$ and 0.07. Moreover, Fig. 5.9 depicts the outage probability of the proposed P-FD-BD system vs. SINR performance for the same scenarios that were considered in Fig. 5.8. Inspecting Figs. 5.8 and 5.9 revels the match between the analytical and simulation results, which supports the derived outage probability expression. Furthermore, Figs. 5.8 and 5.9 show how the residual SI, which results from the average transmit signal noise, Δ_{a_s}, affects the outage probability performance of the P-FD-BD communication system.

The PAPR of the OFDM signal is one of the key performance indicators in all of the OFDM systems and the OFDM system designers aim to attain low PAPR. Hence, the PAPR performance of the proposed system was investigated by evaluating the CCDF of the PAPR of the OFDM signal before and after the ZF transmit precoding, and the GNEP SIC for different FFT points, i.e. $N = 256,\ 512,\ 1024$, as depicted in Fig. 5.10. Moreover, it can be observed from

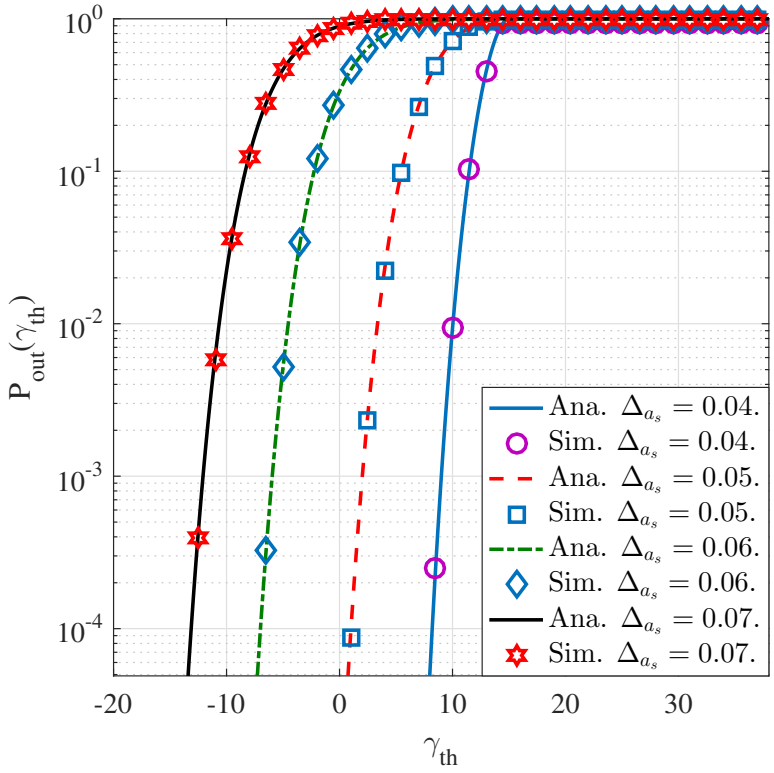

Figure 5.8: Outage probability Vs. γ_{th} of the P-FD-BD communication system with GNEP SIC.

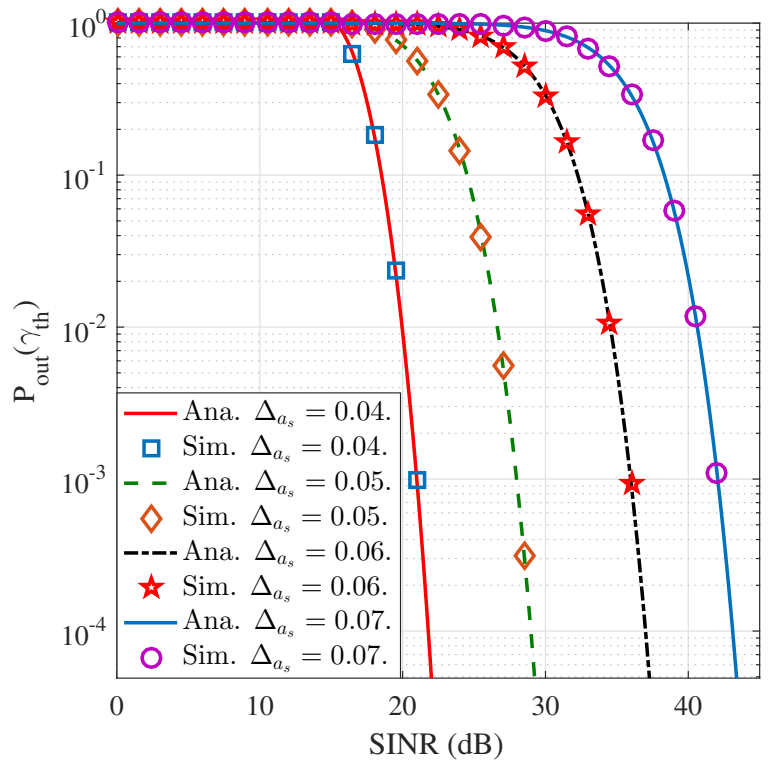

Figure 5.9: Outage probability Vs. SINR of the P-FD-BD communication system with GNEP SIC.

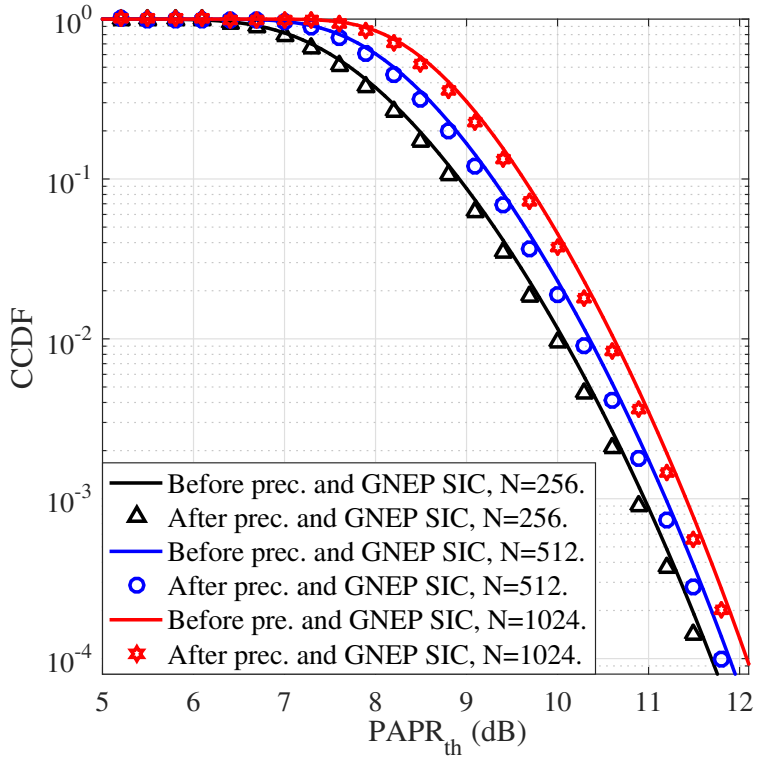

Figure 5.10: The CCDFs of the OFDM signal PAPR before and after applying the transmit precoding and GNEP SIC for different FFT points.

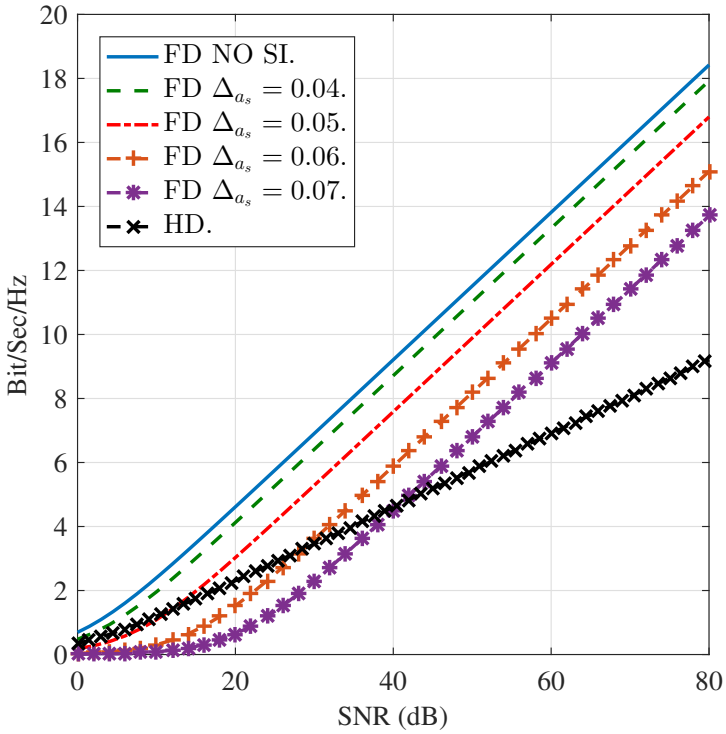

Figure 5.11: the average capacity of the P-FD-BD communication system with GNEP SIC for five different scenarios and that of the P-HD-BD communication system.

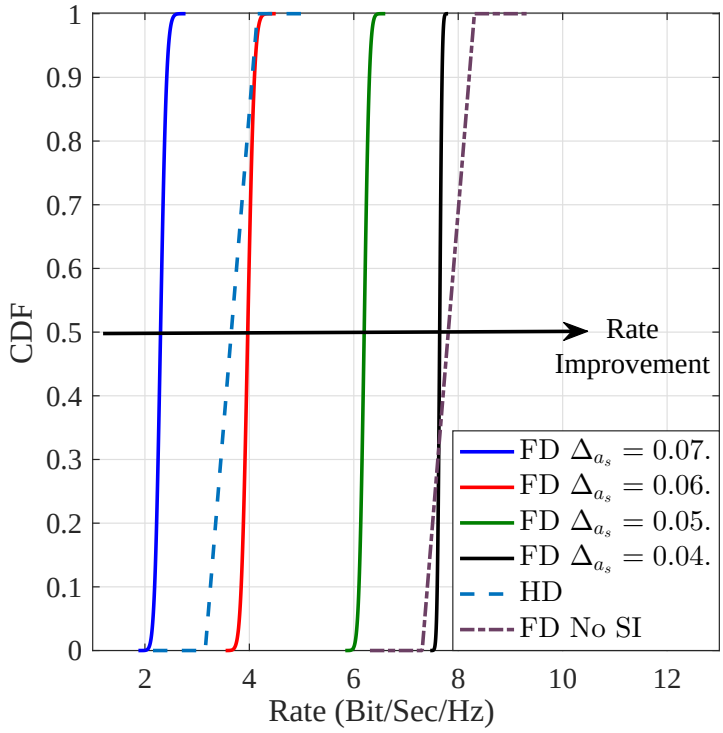

Figure 5.12: CDF of the data rate of the P-FD-BD communication system with GNEP SIC for five different scenarios of transmit signal noise and that of the P-HD-BD communication system, when the SNR is fixed at $\gamma_a = 25$ dB.

Fig. 5.10 that the CCDFs of the PAPR of the OFDM signal before and after the ZF transmit precoding and GNEP SIC show close match, which implies that the GNEP SIC and the ZF transmit precoding do not affect the PAPR of the OFDM signal.

The average channel capacity of the proposed P-FD-BD communication system has been evaluated for five different scenarios, i.e. SI free P-FD-BD system and P-HD-BD with $\Delta_{a_1} = \Delta_{a_2} = 0.04,\ 0.05,\ 0.06$ and 0.07, as depicted in Fig. 5.11. Furthermore, the capacity performance of the P-FD-BD communication system for the considered scenarios was compared with that of the P-HD-BD communication system to study the impact of the proposed GNEP SIC performance on the throughput gain that can be attained by each of the considered FD scenarios. Close inspection of the results in Fig. 5.11, shows that when $\Delta_{a_s} \leq 0.06$ and the SNR is larger than 30 dB the capacity of the P-FD-BD system is always higher than that of the P-HD-BD system. Furthermore, when $\Delta_{a_s} = 0.07$, the P-FD-BD system can attain higher capacity than the P-HD-BD system only when the SNR is more than 40 dB. Finally, Fig. 5.12 illustrates the CDF of the data rate of the P-FD-BD system for the same scenarios that were considered in Fig. 5.11, and that of the P-HD-BD system when the SNR was fixed at 25 dB. Moreover, Fig. 5.12 shows the rate improvement that can be accomplished by each of the FD scenarios compared with the P-HD-DB system when the SNR is fixed. In particular, the proposed P-FD-BD system attains

more data rate than the P-HD-BD system when $\Delta_{a_s} \leq 0.06$. Moreover, when $\Delta_{a_s} = 0.05$ scenario is considered the data rate is improved by 2 Bits/Sec/Hz, while the data rate of the P-FD-BD system shows a close match to data rate of the SI free scenario. These results show the ability of the proposed P-FD-BD to approximately double the throughput of the P-HD-BD. It is worth pointing out that the CDF of the data rate was obtained by averaging the ergodic capacity for a large number of transmission frames.

5.7 Chapter Summary

In this chapter, we considered an OFDM based P-FD-BD wireless communication system, which comprises two FD nodes that communicate over frequency selective channels. Moreover, we introduced a new spatial SIC scheme that exploits GNEP to solve the most challenging issue that is associated with FD mode, i.e. efficiently suppress SI signal and enable the FD mode. Unlike all the existing SIC scheme, in the introduced SIC scheme all the required signal processing are executed in the transmit chain of the transceiver nodes and no further signal processing is required in the receive chain of the transceiver nodes after the ADC. Furthermore, we considered the transmit signal noise as a practical limitation that affects the performance of the proposed GNEP SIC. The impact of the transmit signal noise on the performance of the GNEP SIC and the performance of the P-FD-BE wireless communication system was meticulously investigated. Moreover, the performance of the P-FD-BD system is thoroughly studied. First, the SINR expression of the P-FD-BD system was presented. Moreover, closed-form expressions for the PDF and CDF of the SINR along with exact outage probability and ASER expressions of the P-FD-BD system were introduced in this chapter. Moreover, These expressions were verified using simulation studies. Next, the effect of applying the GNEP SIC in conjunction with the transmit precoding on the PAPR of the OFDM signal was investigated in this chapter. The PAPR results have shown that the GNEP SIC and the transmit precoding do not affect the PAPR of the OFDM signal. Furthermore, the average capacity along with the CDF of the data rate of the P-FD-BD system were evaluated in this chapter. The results of the average capacity and the CDF of the data rate of the P-FD-BD system were compared with those of the P-HD-BD system and the comparison has confirmed the ability of the proposed P-FD-BD to approximately double the achieved data rate of the P-HD-BD system. Finally, the obtained results have demonstrated the efficiency of the introduced GNEP SIC even in the presence of the transmit signal noise.

Chapter 6

Conclusions and Future Work

6.1 Conclusions

In-band FD wireless communication technology in which the transceiver nodes have the ability to concurrently transmit and receive over the same frequency is the new frequency re-use strategy that can double the spectral efficiency and throughput of the HD out-of-band wireless communication systems. However, enabling the transceiver nodes to simultaneously transmit and receive over the same frequency band induces SI signal into the received signal at each node. This SI signal can severely degrade the performance of the FD systems due to the power difference between the SI signal and the signal of interest received from the distant nodes.

Thus, we have focused on the design of pragmatic FD transceiver nodes architectures, which are combined with effective SIC schemes to enable the FD mode. Moreover, we have investigated the feasibility of the FD systems to approximately double the throughput of the conventional HD systems. In essence, we have combined passive and active SIC techniques to diminish the SI signal in the proposed OFDM based AF-FD-PLNC system. The utilized passive SIC mechanism includes exploiting two 90° beamwidth antennas at each node dedicated for transmission and receptions, respectively, in conjecture with placing an RF observative shielding between the antennas. Moreover, we have investigated the residual SI signal on the outage probability, ASER, and ergodic capacity. Furthermore, closely match simulation-based results were used to verify the E2E outage probability, ASER, and ergodic capacity. In particular, the exact E2E simulation ergodic capacity results have shown a close match with the theoretical ergodic capacity results that were obtained using the derived E2E upper bound ergodic capacity expression. Moreover, the derive E2E lower bound expression of the ASER was used to obtain the E2E lower bound results, which have shown a close match with exact E2E simulation

based results in low SNR region. On the other hand, the E2E lower bound results have shown a perfect match with exact simulation based results in the mid-high SNR region. The obtained results have shown that the proposed OFDM based AF-FD-PLNC can approximately double the throughput of the AF-HD-PLNC when the SI to noise ratio is less than 5 dB and the SNR higher than 25 dB. It is noteworthy that when the SI to noise ratio is larger than 10 dB and the SNR is less than 20 dB the ergodic capacity performance of the AF-HD-PLNC system is better than that of the AF-FD-PLNC. Moreover, the SI channel estimation error has been identified as the key limitation of the utilized SIC scheme.

This has motivated us to develop an adaptive SIC scheme that can effectively suppress the SI signal to the level of the receiver noise floor. The proposed adaptive SIC scheme exploits the NLMS algorithm to obtain a perfect estimation of the SI channel, which is then exploited in conjunction with the perfect knowledge of the nodes transmitted signal to construct a replica of the SI signal. This replica has been passed through an auxiliary transmit chain, which is identical to the main transmit chain, in order to be subtracted from the overall received signal in the RF domain before the ADC. The obtained results have shown that residual SI power reaches the level of the noise floor after 2000 samples, which confirms the efficiency of the proposed SIC technique. Next, this adaptive SIC mechanism have utilized in the proposed DNF-FD-PLNC system to enable the FD mode. A meticulous performance analysis of the proposed system in the presence of the residual SI and channel estimation error was conducted. The obtained results have shown that the residual SI has more impact on the attained throughput gain of the proposed DNF-FD-PLNC over the DNF-HD-PLNC. Nevertheless, the E2E outage probability and ASER results of the proposed DNF-FD-PLNC exhibit an error floor in the presence of the channel estimation error. The exact expressions of the E2E outage probability, ASER, and ergodic capacity have been exploited to evaluate the theoretical E2E results. These results have shown a perfect match with the exact E2E simulation studies, which supports the derived expressions.

Motivated by the fact that the ultimate aim of designing an effective SIC scheme is to completely diminish the SI signal before it reaches the local receive chain, we introduced a novel over-the-air SIC scheme, which was combined with an OFDM base P-FD-BD wireless communication system. Each node in the proposed system was equipped with one RX antenna and two TX antennas. The extra TX antenna is utilized to enable the FD mode. Furthermore, the introduced SIC technique exploits the GNEP to adequately suppress the SI signal over-the-air before it arrives at the ADC. Moreover, the hardware impairments effects, such as oscillator phase noise, digital-to-analog converter (DAC) imperfections and carrier frequency offset, amongst

others, were addressed as the main limitations of the proposed SIC scheme. Nonetheless, the obtained results have shown the ability of the new SIC to suppress the SI signal to the level of the noise floor. Next, the derived performance metrics expressions of the proposed OFDM based P-FD-BD system were verified using matching Monte Carlo simulations. Furthermore, the obtained results have shown that the performance metrics, outage probability, ASER and ergodic capacity, of the proposed P-FD-BD system, can approximately match those of the SI free P-BD system. Finally, the PAPR results of the OFDM signal before and after the transmit precoding and the proposed SIC show a close match, which indicates that the proposed SIC along of the exploited ZF precoding do not affect the PAPR of the OFDM signal.

6.2 Future work

The promising results obtained from the three SIC schemes proposed in this thesis have demonstrated the feasibility of exploiting the FD mode improve the spectral efficiency and meet the throughput requirements of the next generation wireless communication systems. Nevertheless, further aspects and limitations of the FD, which have not considered in this work, need to be meticulously investigated in the future. Some of the aspects are outlined below along with proposals for that can be further researched in the future.

- An implementation of a practical hardware design for the proposed over-the-air SIC scheme. In this project, The proposed GNEP SIC was implemented using MATLAB functions. However, implementing this algorithm on DSP chip with fixed-point resolution will result in an efficient and pragmatic SIC processor, which can be exploited in the next generation communication devices.

- Develop a pragmatic FD-enabled underwater acoustic communication systems. In essence, minimum latency is essential for precise control of a micro remotely operated vehicle (ROV) that continuously transmits video to the base station. Hence, exploiting FD mode of communication will enable the ROV to have a bi-directional link with the base station that ensures simultaneous uplink and downlink communication. However, underwater acoustic channel (UAC) has a significant multipath phenomenon which results in sever frequency selective fading and signal distortion. Consequently, the Implementation of the SIC schemes for the UAC will be more challenging than those of the wireless channels.

- Use different transmit precoding techniques such as minimum mean square error (MMSE) to improve the performance of the P-FD-BD system proposed in this thesis. In general,

the performance of zero-forcing precoding is affected by the power of the AWGN in the low SNR region. The MMSE precoding technique considers the average power of the AWGN in the computation of the precoding matrix, which improves the performance of the system, especially in the low SNR region.

- Combine the proposed SIC schemes with FD Massive MIMO systems to further improve the attained performance.
- Study the effect of the co-channel interference (CCI) in conjunction with the impact of residual self-interference (SI) on the performance of the FD relay channel systems.
- Investigate the impact of inter-relay-interference (IRI) on the performance of FD multi-relay network.
- Combine the proposed systems with coding and error correction techniques in order to increase the robustness of the proposed systems to the residual SI, i.e. increase the system tolerance to more residual SI.

Appendix A

Special Functions

- Incomplete gamma function

$$\Gamma(\alpha, x) = \int_x^\infty e^{-t} t^{\alpha-1} dt. \tag{A.1}$$

- Parabolic cylinder function

$$D_p(z) = \frac{e^{-\frac{z^2}{4}}}{\Gamma(-p)} \int_0^\infty e^{-xz-\frac{x^2}{2}} x^{-p-1} dx, [\mathbf{Re}\, p < 0]. \tag{A.2}$$

- Whittaker function

$$W_{\lambda,\mu}(x) = \frac{\Gamma(-2\mu)}{\Gamma\left(\frac{1}{2}-\mu-\lambda\right)} M_{\lambda,\mu}(x) + \frac{\Gamma(2\mu)}{\Gamma\left(\frac{1}{2}+\mu-\lambda\right)} M_{\lambda,-\mu}(x). \tag{A.3}$$

- Whittaker function

$$M_{\lambda,\mu}(x) = x^{\mu+\frac{1}{2}} e^{\frac{-x}{2}} \Phi\left(\mu-\lambda+\frac{1}{2}, 2\mu+1; x\right), \tag{A.4}$$

$$M_{\lambda,-\mu}(x) = x^{-\mu+\frac{1}{2}} e^{\frac{-x}{2}} \Phi\left(-\mu-\lambda+\frac{1}{2}, -2\mu+1; x\right). \tag{A.5}$$

- Confluent hypergeometric function

$$\Phi(\alpha, \gamma; x) = \frac{2^{1-\gamma} e^{\frac{1}{2}x}}{B(\alpha, \gamma-\alpha)} \int_{-1}^1 (1-t)^{\gamma-\alpha-1} (1+t)^{\alpha-1} e^{\frac{1}{2}xt} dt. \tag{A.6}$$

- Beta function

$$B(x, y) = \int_0^1 t^{x-1} (1-t)^{y-1} dt. \tag{A.7}$$

- Exponential integral function

$$\mathrm{Ei}\,(x) = -\int_{-x}^{\infty} \frac{e^{-t}}{t} dt. \tag{A.8}$$

Appendix B

Jensen's inequality

For any concave function g [99],

$$\mathbf{E}[g(X)] \leq g(\mathbf{E}[X]). \tag{B.1}$$

Proof: The function g is concave if, for any x and z,

$$g(x) \leq g(z) + (x - z)g^{'}(z), \tag{B.2}$$

where $g^{'}(x)$ is the derivative of the function $g(x)$. Then, if we assume that $x = X$ and $z = \mathbf{E}[X]$, (B.2) can be rewritten as

$$g(x) \leq g(\mathbf{E}[X]) + (X - \mathbf{E}[X])g^{'}(\mathbf{E}[X]). \tag{B.3}$$

Taking the expectation on both sides results in

$$\mathbf{E}[g(x)] \leq g(\mathbf{E}[X]) + \mathbf{E}[(X - \mathbf{E}[X])]g^{'}(\mathbf{E}[X]) = g(\mathbf{E}[X]). \tag{B.4}$$

References

[1] Z. Zhang, K. Long, A. V. Vasilakos, and L. Hanzo, "Full-duplex wireless communications: Challenges, solutions, and future research directions," *Proceedings of the IEEE*, vol. 104, no. 7, pp. 1369–1409, July 2016.

[2] A. Sabharwal, P. Schniter, D. Guo, D. W. Bliss, S. Rangarajan, and R. Wichman, "In-band full-duplex wireless: Challenges and opportunities," *IEEE J. Sel. Areas Commun.*, vol. 32, no. 9, pp. 1637–1652, Sept 2014.

[3] X. Han, B. Huo, Y. Shao, C. Wang, and M. Zhao, "Rf self-interference cancellation using phase modulation and optical sideband filtering," *IEEE Photon. Technol. Lett.*, vol. 29, no. 11, pp. 917–920, June 2017.

[4] A. J. PAULRAJ, D. A. GORE, R. U. NABAR, and H. BOLCSKEI, "An overview of MIMO communications - A key to gigabit wireless," *Proc. IEEE*, vol. 92, no. 2, pp. 198–218, Feb 2004.

[5] Z. Zhang, X. Wang, K. Long, A. V. Vasilakos, and L. Hanzo, "Large-scale mimo-based wireless backhaul in 5g networks," *IEEE Wireless Commun.*, vol. 22, no. 5, pp. 58–66, October 2015.

[6] R. v. Nee and R. Prasad, *OFDM for wireless multimedia communications*. Artech House, Inc., 2000.

[7] J. I. Choi, M. Jain, K. Srinivasan, P. Levis, and S. Katti, "Achieving single channel, full duplex wireless communication," in *Proceedings of the sixteenth annual international conference on Mobile computing and networking*. ACM, 2010, pp. 1–12.

[8] M. Jain, J. I. Choi, T. Kim, D. Bharadia, S. Seth, K. Srinivasan, P. Levis, S. Katti, and P. Sinha, "Practical, real-time, full duplex wireless," in *Proceedings of the 17th Annual International Conference on Mobile Computing and Networking*. ACM, 2011, pp. 301–312.

[9] M. Duarte, C. Dick, and A. Sabharwal, "Experiment-driven characterization of full-duplex wireless systems," *IEEE Trans. Wireless Commun.*, vol. 11, no. 12, pp. 4296–4307, December 2012.

[10] E. Everett, A. Sahai, and A. Sabharwal, "Passive self-interference suppression for full-duplex infrastructure nodes," *IEEE Trans. Wireless Commun.*, vol. 13, no. 2, pp. 680–694, February 2014.

[11] E. Ahmed and A. Eltawil, "All-digital self-interference cancellation technique for full-duplex systems," *IEEE Trans. Wireless Commun.*, vol. 14, no. 7, pp. 3519–3532, July 2015.

[12] T. Riihonen, S. Werner, R. Wichman, and Z. Eduardo, "On the feasibility of full-duplex relaying in the presence of loop interference," in *IEEE 10th Workshop on Signal Processing Advances in Wireless Communications (SPAWC)*, June 2009, pp. 275–279.

[13] K. Haneda, E. Kahra, S. Wyne, C. Icheln, and P. Vainikainen, "Measurement of loop-back interference channels for outdoor-to-indoor full-duplex radio relays," in *Proceedings of the Fourth European Conference on Antennas and Propagation*, April 2010, pp. 1–5.

[14] K. Yamamoto, K. Haneda, H. Murata, and S. Yoshida, "Optimal transmission scheduling for a hybrid of full- and half-duplex relaying," *IEEE Commun. Lett.*, vol. 15, no. 3, pp. 305–307, March 2011.

[15] T. Riihonen, S. Werner, and R. Wichman, "Hybrid full-duplex/half-duplex relaying with transmit power adaptation," *IEEE Trans. Wireless Commun.*, vol. 10, no. 9, pp. 3074–3085, September 2011.

[16] I. Krikidis, H. Suraweera, P. Smith, and C. Yuen, "Full-duplex relay selection for amplify-and-forward cooperative networks," *IEEE Trans. Wireless Commun.*, vol. 11, no. 12, pp. 4381–4393, December 2012.

[17] H. A. Suraweera, I. Krikidis, and C. Yuen, "Antenna selection in the full-duplex multi-antenna relay channel," in *2013 IEEE International Conference on Communications (ICC)*, June 2013, pp. 4823–4828.

[18] K. Yang, H. Cui, L. Song, and Y. Li, "Joint relay and antenna selection for full-duplex af relay networks," in *2014 IEEE International Conference on Communications (ICC)*, June 2014, pp. 4454–4459.

[19] Y. Pan, J. Zhong, M. Lei, and M. Zhao, "Graph-based joint relay assignment and power allocation optimization for full-duplex networks," in *2015 IEEE 26th Annual International Symposium on Personal, Indoor, and Mobile Radio Communications (PIMRC)*, Aug 2015, pp. 1595–1599.

[20] M. G. Khafagy, M. S. Alouini, and S. Assa, "On the performance of future full-duplex relay selection networks," in *2015 IEEE 20th International Workshop on Computer Aided Modelling and Design of Communication Links and Networks (CAMAD)*, Sept 2015, pp. 11–16.

[21] M. Toka and O. Kucur, "Outage performance of dual hop full-duplex mimo relay networks with tas/mrc over rayleigh fading channels," in *2016 International Symposium on Wireless Communication Systems (ISWCS)*, Sept 2016, pp. 99–103.

[22] I. Dey and P. S. Rossi, "Probability of outage due to self-interference in indoor wireless environments," *IEEE Commun. Lett.*, vol. 21, no. 1, pp. 8–11, Jan 2017.

[23] A. Almradi and K. A. Hamdi, "On the outage probability of MIMO full-duplex relaying: Impact of antenna correlation and imperfect CSI," *IEEE Trans. Veh. Technol.*, vol. 66, no. 5, pp. 3957–3965, May 2017.

[24] D. W. Bliss, P. A. Parker, and A. R. Margetts, "Simultaneous transmission and reception for improved wireless network performance," in *2007 14th IEEE Workshop on Statistical Signal Processing*, Aug 2007, pp. 478–482.

[25] H. Ju, E. Oh, and D. Hong, "Improving efficiency of resource usage in two-hop full duplex relay systems based on resource sharing and interference cancellation," *IEEE Trans. Wireless Commun.*, vol. 8, no. 8, pp. 3933–3938, August 2009.

[26] T. Riihonen, S. Werner, and R. Wichman, "Spatial loop interference suppression in full-duplex mimo relays," in *2009 Conference Record of the Forty-Third Asilomar Conference on Signals, Systems and Computers*, Nov 2009, pp. 1508–1512.

[27] M. Duarte and A. Sabharwal, "Full-duplex wireless communications using off-the-shelf radios: Feasibility and first results," in *2010 Conference Record of the Forty Fourth Asilomar Conference on Signals, Systems and Computers*, Nov 2010, pp. 1558–1562.

[28] E. Everett, M. Duarte, C. Dick, and A. Sabharwal, "Empowering full-duplex wireless communication by exploiting directional diversity," in *2011 Conference Record of the Forty Fifth Asilomar Conference on Signals, Systems and Computers (ASILOMAR)*, Nov 2011, pp. 2002–2006.

[29] D. Korpi, M. Valkama, T. Riihonen, and R. Wichman, "Implementation challenges in full-duplex radio transceivers," in *Proc. XXXIII Finnish URSI Convention on Radio Science, Espoo, Finland*, 2013.

[30] D. Korpi, L. Anttila, V. Syrjl, and M. Valkama, "Widely linear digital self-interference cancellation in direct-conversion full-duplex transceiver," *IEEE J. Sel. Areas Commun.*, vol. 32, no. 9, pp. 1674–1687, Sept 2014.

[31] S. Huberman and T. Le-Ngoc, "Self-interference pricing-based mimo full-duplex precoding," *IEEE Wireless Commun. Lett.*, vol. 3, no. 6, pp. 549–552, Dec 2014.

[32] D. Korpi, Y. S. Choi, T. Huusari, L. Anttila, S. Talwar, and M. Valkama, "Adaptive nonlinear digital self-interference cancellation for mobile inband full-duplex radio: Algorithms and rf measurements," in *2015 IEEE Global Communications Conference (GLOBECOM)*, Dec 2015, pp. 1–7.

[33] J. Zhou, T. H. Chuang, T. Dinc, and H. Krishnaswamy, "Integrated wideband self-interference cancellation in the rf domain for fdd and full-duplex wireless," *IEEE J. Solid-State Circuits*, vol. 50, no. 12, pp. 3015–3031, Dec 2015.

[34] L. Laughlin, M. A. Beach, K. A. Morris, and J. L. Haine, "Electrical balance duplexing for small form factor realization of in-band full duplex," *IEEE Commun. Mag.*, vol. 53, no. 5, pp. 102–110, May 2015.

[35] K. E. Kolodziej, J. G. McMichael, and B. T. Perry, "Multitap rf canceller for in-band full-duplex wireless communications," *IEEE Trans. Wireless Commun.*, vol. 15, no. 6, pp. 4321–4334, June 2016.

[36] D. Korpi, J. Tamminen, M. Turunen, T. Huusari, Y. S. Choi, L. Anttila, S. Talwar, and M. Valkama, "Full-duplex mobile device: pushing the limits," *IEEE Commun. Mag.*, vol. 54, no. 9, pp. 80–87, September 2016.

[37] M. A. Ahmed and C. C. Tsimenidis, "A tight upper bound on the performance of iterative detection and decoding for coded full-duplex SIMO systems," *IEEE Commun. Lett.*, vol. 20, no. 3, pp. 606–609, March 2016.

[38] W. Chung, D. Hong, R. Wichman, and T. Riihonen, "Interference cancellation architecture for full-duplex system with gfdm signaling," in *2016 24th European Signal Processing Conference (EUSIPCO)*, Aug 2016, pp. 788–792.

[39] D. Korpi, M. Heino, C. Icheln, K. Haneda, and M. Valkama, "Compact inband full-duplex relays with beyond 100 db self-interference suppression: Enabling techniques and field measurements," *IEEE Trans. Antennas Propag.*, vol. 65, no. 2, pp. 960–965, Feb 2017.

[40] X. Han, B. Huo, Y. Shao, C. Wang, and M. Zhao, "Rf self-interference cancellation using phase modulation and optical sideband filtering," *IEEE Photon. Technol. Lett.*, vol. 29, no. 11, pp. 917–920, June 2017.

[41] D. Korpi, L. Anttila, and M. Valkama, "Nonlinear self-interference cancellation in mimo full-duplex transceivers under crosstalk," *EURASIP Journal on Wireless Communications and Networking*, vol. 2017, no. 1, p. 24, Feb 2017. [Online]. Available: https://doi.org/10.1186/s13638-017-0808-4

[42] J. G. Andrews, S. Buzzi, W. Choi, S. V. Hanly, A. Lozano, A. C. K. Soong, and J. C. Zhang, "What will 5G be?" *IEEE J. Sel. Areas Commun.*, vol. 32, no. 6, pp. 1065–1082, June 2014.

[43] S. Chen and J. Zhao, "The requirements, challenges, and technologies for 5G of terrestrial mobile telecommunication," *IEEE Commun. Mag.*, vol. 52, no. 5, pp. 36–43, May 2014.

[44] Y. Cai, Z. Qin, F. Cui, G. Y. Li, and J. A. McCann, "Modulation and multiple access for 5g networks," *arXiv preprint arXiv:1702.07673*, 2017.

[45] H. Lin, "Flexible configured ofdm for 5g air interface," *IEEE Access*, vol. 3, pp. 1861–1870, 2015.

[46] J. Rodriguez, *Fundamentals of 5G mobile networks*. John Wiley & Sons, 2015.

[47] R. K. Saha and C. Aswakul, "Fundamentals of 5G mobile network."

[48] Z. Zhao, M. Peng, Y. Ma, Y. Li, Y. Changqing, and Y. Wu, "Cooperative transmissions in 5G large-scale relay systems: How to keep a balance between performance and complexity?" *Journal of Signal Processing Systems*, vol. 83, no. 2, pp. 207–223, 2016.

[49] C. Zhang, J. Ge, J. Li, F. Gong, and H. Ding, "Complexity-aware relay selection for 5G large-scale secure two-way relay systems," *IEEE Trans. Veh. Technol.*, vol. 66, no. 6, pp. 5461–5465, June 2017.

[50] Y. Zhang, K. Xiong, P. Fan, H. C. Yang, and X. Zhou, "Space-time network coding with multiple af relays over nakagami- m fading channels," *IEEE Trans. Veh. Technol.*, vol. 66, no. 7, pp. 6026–6036, July 2017.

[51] C. Nam, C. Joo, S. G. Yoon, and S. Bahk, "Resource allocation in full-duplex ofdma networks: Approaches for full and limited csis," *Journal of Communications and Networks*, vol. 18, no. 6, pp. 913–925, Dec 2016.

[52] C. Liu, M. Ma, and B. Jiao, "A hybrid decode-and-forward relaying scheme for full duplex wireless relay networks," in *2016 IEEE 83rd Vehicular Technology Conference (VTC Spring)*, May 2016, pp. 1–5.

[53] W. Shin, J. B. Lim, H. H. Choi, J. Lee, and H. V. Poor, "Cyclic interference alignment for full-duplex multi-antenna cellular networks," *IEEE Trans. Commun.*, vol. 65, no. 6, pp. 2657–2671, June 2017.

[54] X. Tang, P. Ren, and Z. Han, "Distributed power optimization for security-aware multi-channel full-duplex communications: A variational inequality framework," *IEEE Trans. Commun.*, vol. PP, no. 99, pp. 1–1, 2017.

[55] M. Chung, M. S. Sim, D. Kim, and C. B. Chae, "Compact full duplex mimo radios in d2d underlaid cellular networks: From system design to prototype results," *IEEE Access*, vol. PP, no. 99, pp. 1–1, 2017.

[56] Y. He, X. Yin, and H. Chen, "Spatiotemporal characterization of self-interference channels for 60-ghz full-duplex communication," *IEEE Antennas Wireless Propag. Lett.*, vol. 16, pp. 2220–2223, 2017.

[57] D. Korpi, M. Heino, C. Icheln, K. Haneda, and M. Valkama, "Compact inband full-duplex relays with beyond 100 db self-interference suppression: Enabling techniques and field measurements," *IEEE Antennas Wireless Propag. Lett.*, vol. 65, no. 2, pp. 960–965, Feb 2017.

[58] A. Nosratinia, T. E. Hunter, and A. Hedayat, "Cooperative communication in wireless networks," *IEEE Commun. Mag.*, vol. 42, no. 10, pp. 74–80, Oct 2004.

[59] F. H. Fitzek and M. D. Katz, *Cooperation in wireless networks: principles and applications*. Springer, 2006.

[60] T. Cover and A. E. Gamal, "Capacity theorems for the relay channel," *IEEE Trans. Inf. Theory*, vol. 25, no. 5, pp. 572–584, September 1979.

[61] S. S. Ikki and M. H. Ahmed, "Performance analysis of incremental-relaying cooperative-diversity networks over rayleigh fading channels," *IET Communications*, vol. 5, no. 3, pp. 337–349, Feb 2011.

[62] S. S. Ikki and S. Aissa, "Performance analysis of amplify-and-forward relaying over weibull-fading channels with multiple antennas," *IET Communications*, vol. 6, no. 2, pp. 165–171, January 2012.

[63] R. Vaze and R. Heath, "On the capacity and diversity-multiplexing tradeoff of the two-way relay channel," *IEEE Trans. Inf. Theory*, vol. 57, no. 7, pp. 4219–4234, July 2011.

[64] S. Berger, *Coherent cooperative relaying in low mobility wireless multiuser networks*. Logos Verlag Berlin GmbH, 2010, vol. 10.

[65] B. Rankov and A. Wittneben, "Spectral efficient protocols for half-duplex fading relay channels," *IEEE J. Sel. Areas Commun.*, vol. 25, no. 2, pp. 379–389, February 2007.

[66] M. Xia and S. Aissa, "Cooperative af relaying in spectrum-sharing systems: Performance analysis under average interference power constraints and nakagami-m fading," *IEEE Trans. Commun.*, vol. 60, no. 6, pp. 1523–1533, June 2012.

[67] J. N. Laneman, D. N. C. Tse, and G. W. Wornell, "Cooperative diversity in wireless networks: Efficient protocols and outage behavior," *IEEE Trans. Inf. Theory*, vol. 50, no. 12, pp. 3062–3080, Dec 2004.

[68] M. Dohler and Y. Li, *Cooperative communications: hardware, channel and PHY*. John Wiley & Sons, 2010.

[69] Y.-W. P. Hong, W.-J. Huang, and C.-C. J. Kuo, *Cooperative communications and networking: technologies and system design*. Springer Science & Business Media, 2010.

[70] D. Zhou and W. Song, *Multipath TCP for User Cooperation in Wireless Networks*. Springer, 2014.

[71] K. R. Liu, *Cooperative communications and networking*. Cambridge university press, 2009.

[72] S. Zhang, S. C. Liew, and P. P. Lam, "Hot topic: physical-layer network coding," in *Proceedings of the 12th annual international conference on Mobile computing and networking*. ACM, 2006, pp. 358–365.

[73] S. C. Liew, S. Zhang, and L. Lu, "Physical-layer network coding: Tutorial, survey, and beyond," *Physical Communication*, vol. 6, pp. 4–42, 2013.

[74] S. Y. R. Li, R. W. Yeung, and N. Cai, "Linear network coding," *IEEE Trans. Inf. Theory*, vol. 49, no. 2, pp. 371–381, Feb 2003.

[75] T. Koike-Akino, P. Popovski, and V. Tarokh, "Denoising maps and constellations for wireless network coding in two-way relaying systems," in *IEEE Global Telecommunications Conference (GLOBECOM)*. IEEE, 2008, pp. 1–5.

[76] R. Chang, S.-J. Lin, and W.-H. Chung, "Symbol and bit mapping optimization for physical-layer network coding with pulse amplitude modulation," *IEEE Trans. Wireless Commun.*, vol. 12, no. 8, pp. 3956–3967, August 2013.

[77] P. Popovski and H. Yomo, "Physical network coding in two-way wireless relay channels," in *ICC '07. IEEE International Conference on Communications*, June 2007, pp. 707–712.

[78] R. H. Y. Louie, Y. Li, and B. Vucetic, "Practical physical layer network coding for two-way relay channels: performance analysis and comparison," *IEEE Trans. Wireless Commun.*, vol. 9, no. 2, pp. 764–777, February 2010.

[79] P. Popovski and H. Yomo, "The anti-packets can increase the achievable throughput of a wireless multi-hop network," in *ICC '06. IEEE International Conference on Communications*, vol. 9, June 2006, pp. 3885–3890.

[80] T. Koike-Akino, P. Popovski, and V. Tarokh, "Optimized constellations for two-way wireless relaying with physical network coding," *IEEE J. Sel. Areas Commun.*, vol. 27, no. 5, pp. 773–787, June 2009.

[81] T. Koike-Akino, P. Popovski, and V. Tarokh, "Optimized constellations for two-way wireless relaying with physical network coding," *IEEE Journal on Selected Areas in Communications*, vol. 27, no. 5, pp. 773–787, June 2009.

[82] T. Koike-Akino, P. Popovski, and V. Tarokh, "Denoising strategy for convolutionally-coded bidirectional relaying," in *2009 IEEE International Conference on Communications*, June 2009, pp. 1–5.

[83] J. H. Srensen, R. Krigslund, P. Popovski, T. K. Akino, and T. Larsen, "Physical layer network coding for fsk systems," *IEEE Commun. Lett.*, vol. 13, no. 8, pp. 597–599, August 2009.

[84] C. A. Schmidt, G. Gonzlez, F. Gregorio, J. E. Cousseau, T. Riihonen, and R. Wichman, "Compensation of ADC-induced distortion in broadband full-duplex transceivers," in *2017 IEEE International Conference on Communications Workshops (ICC Workshops)*, May 2017, pp. 1147–1152.

[85] A. Sabharwal, P. Schniter, D. Guo, D. W. Bliss, S. Rangarajan, and R. Wichman, "In-band full-duplex wireless: Challenges and opportunities," *IEEE J. Sel. Areas Commun.*, vol. 32, no. 9, pp. 1637–1652, Sept 2014.

[86] T. Riihonen, S. Werner, and R. Wichman, "Optimized gain control for single-frequency relaying with loop interference," *IEEE Trans. Wireless Commun.*, vol. 8, no. 6, pp. 2801–2806, June 2009.

[87] B. A. Jebur and C. Tsimenidis, "Performance analysis of OFDM-Based denoise-and-forward full-duplex PLNC with imperfect CSI," in *IEEE International Conference on Communication Workshop (ICCW)*, June 2015, pp. 997–1002.

[88] B. A. Jebur, C. C. Tsimenidis, and J. A. Chambers, "Tight upper bound ergodic capacity of an AF full-duplex physical-layer network coding system," in *2016 IEEE 27th Annual International Symposium on Personal, Indoor, and Mobile Radio Communications (PIMRC)*, Sept 2016, pp. 1–6.

[89] B. A. Jebur, C. C. Tsimenidis, M. Johnston, and J. Chambers, "Outage probability of an AF full-duplex physical-layer network coding system," in *2016 24th European Signal Processing Conference (EUSIPCO)*, Aug 2016, pp. 1828–1832.

[90] X. Cheng, B. Yu, X. Cheng, and L. Yang, "Two-way full-duplex amplify-and-forward relaying," in *IEEE Military Communications Conference, MILCOM*, Nov 2013, pp. 1–6.

[91] G. Zheng, "Joint beamforming optimization and power control for full-duplex mimo two-way relay channel," *IEEE Trans. Signal Process.*, vol. 63, no. 3, pp. 555–566, Feb 2015.

[92] D. Korpi, T. Riihonen, V. Syrjl, L. Anttila, M. Valkama, and R. Wichman, "Full-duplex transceiver system calculations: Analysis of ADC and linearity challenges," *IEEE Trans. Wireless Commun.*, vol. 13, no. 7, pp. 3821–3836, July 2014.

[93] D. Korpi, L. Anttila, and M. Valkama, "Feasibility of in-band full-duplex radio transceivers with imperfect rf components: Analysis and enhanced cancellation algorithms," in *2014 9th International Conference on Cognitive Radio Oriented Wireless Networks and Communications (CROWNCOM)*, June 2014, pp. 532–538.

[94] M. A. Khojastepour, K. Sundaresan, S. Rangarajan, X. Zhang, and S. Barghi, "The case for antenna cancellation for scalable full-duplex wireless communications," in *Proceedings of the 10th ACM Workshop on Hot Topics in Networks*. ACM, 2011, p. 17.

[95] X. Wang, W. Che, W. Yang, and W. Feng, "Antenna pair with self-interference cancellation for full duplex communication," in *2017 10th Global Symposium on Millimeter-Waves*, May 2017, pp. 44–46.

[96] T. Snow, C. Fulton, and W. J. Chappell, "Transmit-receive duplexing using digital beamforming system to cancel self-interference," *IEEE Trans. Microw. Theory Tech.*, vol. 59, no. 12, pp. 3494–3503, Dec 2011.

[97] H. A. Suraweera, I. Krikidis, G. Zheng, C. Yuen, and P. J. Smith, "Low-complexity end-to-end performance optimization in MIMO full-duplex relay systems," *IEEE Trans. Wireless Commun.*, vol. 13, no. 2, pp. 913–927, February 2014.

[98] C. R. Anderson, S. Krishnamoorthy, C. G. Ranson, T. J. Lemon, W. G. Newhall, T. Kummetz, and J. H. Reed, "Antenna isolation, wideband multipath propagation measure-

ments, and interference mitigation for on-frequency repeaters," in *IEEE SoutheastCon, 2004. Proceedings.*, March 2004, pp. 110–114.

[99] J. G. Proakis, *Digital communications*. McGraw-Hill Higher Education; London, 2001.

[100] M. Duarte, A. Sabharwal, V. Aggarwal, R. Jana, K. K. Ramakrishnan, C. W. Rice, and N. K. Shankaranarayanan, "Design and characterization of a full-duplex multiantenna system for wifi networks," *IEEE Trans. Veh. Technol.*, vol. 63, no. 3, pp. 1160–1177, March 2014.

[101] A. Sahai, G. Patel, C. Dick, and A. Sabharwal, "On the impact of phase noise on active cancelation in wireless full-duplex," *IEEE Trans. Veh. Technol.*, vol. 62, no. 9, pp. 4494–4510, Nov 2013.

[102] J. R. Krier and I. F. Akyildiz, "Active self-interference cancellation of passband signals using gradient descent," in *2013 IEEE 24th International Symposium on Personal Indoor and Mobile Radio Communications (PIMRC)*. IEEE, 2013, pp. 1212–1216.

[103] E. Antonio-Rodrguez, R. Lpez-Valcarce, T. Riihonen, S. Werner, and R. Wichman, "Adaptive self-interference cancellation in wideband full-duplex decode-and-forward mimo relays," in *2013 IEEE 14th Workshop on Signal Processing Advances in Wireless Communications (SPAWC)*, June 2013, pp. 370–374.

[104] T. Huusari, Y. S. Choi, P. Liikkanen, D. Korpi, S. Talwar, and M. Valkama, "Wideband self-adaptive rf cancellation circuit for full-duplex radio: Operating principle and measurements," in *2015 IEEE 81st Vehicular Technology Conference (VTC Spring)*, May 2015, pp. 1–7.

[105] D. Korpi, M. AghababaeeTafreshi, M. Piilila, L. Anttila, and M. Valkama, "Advanced architectures for self-interference cancellation in full-duplex radios: Algorithms and measurements," in *2016 50th Asilomar Conference on Signals, Systems and Computers*, Nov 2016, pp. 1553–1557.

[106] D. Korpi, L. Anttila, V. Syrjl, and M. Valkama, "Widely linear digital self-interference cancellation in direct-conversion full-duplex transceiver," *IEEE J. Sel. Areas Commun.*, vol. 32, no. 9, pp. 1674–1687, Sept 2014.

[107] J. Tamminen, M. Turunen, D. Korpi, T. Huusari, Y. S. Choi, S. Talwar, and M. Valkama, "Digitally-controlled RF self-interference canceller for full-duplex radios," in *2016 24th European Signal Processing Conference (EUSIPCO)*, Aug 2016, pp. 783–787.

[108] D. Liu, Y. Shen, S. Shao, Y. Tang, and Y. Gong, "On the analog self-interference cancellation for full-duplex communications with imperfect channel state information," *IEEE Access*, vol. 5, pp. 9277–9290, 2017.

[109] A. Koohian, H. Mehrpouyan, A. A. Nasir, S. Durrani, and S. D. Blostein, "Residual self-interference cancellation and data detection in full-duplex communication systems," in *2017 IEEE International Conference on Communications (ICC)*, May 2017, pp. 1–6.

[110] C. Campolo, A. Molinaro, A. O. Berthet, and A. Vinel, "Full-duplex radios for vehicular communications," *IEEE Commun. Mag.*, vol. 55, no. 6, pp. 182–189, 2017.

[111] X. Quan, Y. Liu, S. Shao, C. Huang, and Y. Tang, "Impacts of phase noise on digital self-interference cancellation in full-duplex communications," *IEEE Trans. Signal Process.*, vol. 65, no. 7, pp. 1881–1893, April 2017.

[112] J. Li, H. Zhang, and M. Fan, "Digital self-interference cancellation based on independent component analysis for co-time co-frequency full-duplex communication systems," *IEEE Access*, vol. 5, pp. 10 222–10 231, 2017.

[113] T. Riihonen, S. Werner, and R. Wichman, "Mitigation of loopback self-interference in full-duplex MIMO relays," *IEEE Trans. Signal Process.*, vol. 59, no. 12, pp. 5983–5993, Dec 2011.

[114] H. Q. Ngo, H. A. Suraweera, M. Matthaiou, and E. G. Larsson, "Multipair full-duplex relaying with massive arrays and linear processing," *IEEE J. Sel. Areas Commun.*, vol. 32, no. 9, pp. 1721–1737, Sept 2014.

[115] T. Riihonen, M. Vehkaper, and R. Wichman, "Large-system analysis of rate regions in bidirectional full-duplex mimo link: Suppression versus cancellation," in *2013 47th Annual Conference on Information Sciences and Systems (CISS)*, March 2013, pp. 1–6.

[116] L. Yang, K. Qaraqe, E. Serpedin, and M.-S. Alouini, "Performance analysis of amplify-and-forward two-way relaying with co-channel interference and channel estimation error," *IEEE Trans. Commun.*, vol. 61, no. 6, pp. 2221–2231, June 2013.

[117] L. Jimenez Rodriguez, N. Tran, and T. Le-Ngoc, "Performance of full-duplex AF relaying in the presence of residual self-interference," *IEEE J. Sel. Areas Commun.*, vol. 32, no. 9, pp. 1752–1764, Sept 2014.

[118] K. Alexandris, A. Balatsoukas-Stimming, and A. Burg, "Measurement-based characterization of residual self-interference on a full-duplex mimo testbed," in *IEEE 8th Sensor Array and Multichannel Signal Processing Workshop (SAM)*, June 2014, pp. 329–332.

[119] S. Ikki and S. Aissa, "Performance analysis of dual-hop relaying systems in the presence of co-channel interference," in *IEEE Global Telecommunications Conference (GLOBECOM)*, Dec 2010, pp. 1–5.

[120] N. Tran, L. Rodriguez, and T. Le-Ngoc, "Optimal power control and error performance for full-duplex dual-hop AF relaying under residual self-interference," *IEEE Commun. Lett.*, vol. 19, no. 2, pp. 291–294, Feb 2015.

[121] Z. Zhang, Z. Ma, M. Xiao, G. K. Karagiannidis, Z. Ding, and P. Fan, "Two-timeslot two-way full-duplex relaying for 5g wireless communication networks," *IEEE Trans. Commun.*, vol. 64, no. 7, pp. 2873–2887, July 2016.

[122] M. Ahsanullah, B. G. Kibria, and M. Shakil, *Normal and Student's t Distributions and Their Applications*. Springer, 2014.

[123] A. Jeffrey and D. Zwillinger, *Table of integrals, series, and products*. Academic Press, 2007.

[124] K. Hemachandra and N. Beaulieu, "Outage analysis of opportunistic scheduling in dual-hop multiuser relay networks in the presence of interference," *IEEE Trans. Commun.*, vol. 61, no. 5, pp. 1786–1796, May 2013.

[125] M. K. Simon and M.-S. Alouini, *Digital communication over fading channels*. John Wiley & Sons, 2005.

[126] Y. Chen and C. Tellambura, "Distribution functions of selection combiner output in equally correlated rayleigh, rician, and nakagami-m fading channels," *IEEE Trans. Commun.*, vol. 52, no. 11, pp. 1948–1956, Nov 2004.

[127] J. A. Hussein, S. S. Ikki, S. Boussakta, and C. C. Tsimenidis, "Performance analysis of opportunistic scheduling in dual-hop multiuser underlay cognitive network in the pres-

ence of cochannel interference," *IEEE Trans. Veh. Technol.*, vol. 65, no. 10, pp. 8163–8176, Oct 2016.

[128] D. Li, "Performance analysis of mrc diversity for cognitive radio systems," *IEEE Trans. Veh. Technol.*, vol. 61, no. 2, pp. 849–853, Feb 2012.

[129] M. Heino, D. Korpi, T. Huusari, E. Antonio-Rodriguez, S. Venkatasubramanian, T. Riihonen, L. Anttila, C. Icheln, K. Haneda, R. Wichman, and M. Valkama, "Recent advances in antenna design and interference cancellation algorithms for in-band full duplex relays," *IEEE Commun. Mag.*, vol. 53, no. 5, pp. 91–101, May 2015.

[130] P. Popovski and H. Yomo, "Physical network coding in two-way wireless relay channels," in *ICC '07. IEEE International Conference on Communications*, June 2007, pp. 707–712.

[131] J. Zhou, T. H. Chuang, T. Dinc, and H. Krishnaswamy, "Integrated wideband self-interference cancellation in the rf domain for fdd and full-duplex wireless," *IEEE J. Solid-State Circuits*, vol. 50, no. 12, pp. 3015–3031, Dec 2015.

[132] S. S. Haykin, *Adaptive filter theory*. Pearson Education India, 2008.

[133] A. Goldsmith, *Wireless communications*. Cambridge university press, 2005.

[134] A. Erdélyi, W. Magnus, F. Oberhettinger, F. G. Tricomi, and H. Bateman, *Higher transcendental functions*. McGraw-Hill New York, 1953.

[135] A. Hyadi, M. Benjillali, M. S. Alouini, and D. B. da Costa, "Performance analysis of underlay cognitive multihop regenerative relaying systems with multiple primary receivers," *IEEE Trans. Wireless Commun.*, vol. 12, no. 12, pp. 6418–6429, December 2013.

[136] L. Samara, M. Mokhtar, . zdemir, R. Hamila, and T. Khattab, "Residual self-interference analysis for full-duplex ofdm transceivers under phase noise and I/Q imbalance," *IEEE Commun. Lett.*, vol. 21, no. 2, pp. 314–317, Feb 2017.

[137] Z. Bai, J. Demmel, J. Dongarra, A. Ruhe, and H. van der Vorst, *Templates for the solution of algebraic eigenvalue problems: a practical guide*. SIAM, 2000.

[138] S. Wagner, R. Couillet, D. T. M. Slock, and M. Debbah, "Large system analysis of zero-forcing precoding in miso broadcast channels with limited feedback," in *2010 IEEE*

11th International Workshop on Signal Processing Advances in Wireless Communications (SPAWC), June 2010, pp. 1–5.

[139] C. B. Moler and G. W. Stewart, "An algorithm for generalized matrix eigenvalue problems," *SIAM Journal on Numerical Analysis*, vol. 10, no. 2, pp. 241–256, 1973.

[140] G. H. Golub and C. F. Van Loan, *Matrix computations*. JHU Press, 2012, vol. 3.

[141] A. Papoulis, *Probability, Random Variables, and Stochastic Processes*. McGraw Hill, 1991.

[142] J. A. Hussein, S. S. Ikki, S. Boussakta, and C. C. Tsimenidis, "Performance analysis of opportunistic scheduling in dual-hop multiuser underlay cognitive network in the presence of cochannel interference," *IEEE Trans. Veh. Technol.*, vol. 65, no. 10, pp. 8163–8176, Oct 2016.

[143] K. S. Ahn, "Performance analysis of mimo-mrc system in the presence of multiple interferers and noise over rayleigh fading channels," *IEEE Trans. Wireless Commun.*, vol. 8, no. 7, pp. 3727–3735, July 2009.

[144] Y. S. Cho, J. Kim, W. Y. Yang, and C. G. Kang, *MIMO-OFDM wireless communications with MATLAB*. John Wiley & Sons, 2010.

[145] S. H. Han and J. H. Lee, "An overview of peak-to-average power ratio reduction techniques for multicarrier transmission," *IEEE Wireless Commun.*, vol. 12, no. 2, pp. 56–65, April 2005.

[146] E. Al-Dalakta, A. Al-Dweik, A. Hazmi, C. Tsimenidis, and B. Sharif, "PAPR reduction scheme using maximum cross correlation," *IEEE Commun. Lett.*, vol. 16, no. 12, pp. 2032–2035, December 2012.

[147] T. Jiang and Y. Wu, "An overview: Peak-to-average power ratio reduction techniques for OFDM signals," *IEEE Trans. Broadcast.*, vol. 54, no. 2, pp. 257–268, June 2008.

[148] S. M. Alamouti, "A simple transmit diversity technique for wireless communications," *IEEE J. Sel. Areas Commun.*, vol. 16, no. 8, pp. 1451–1458, Oct 1998.